

# Geographia Technica



Technical Geography  
an International Journal for the Progress of Scientific Geography

**Volume 17, Geographia Technica No. 1/2022**

[www.technicalgeography.org](http://www.technicalgeography.org)

**Cluj University Press**

## Editorial Board

Okke **Batelaan**, Flinders University Adelaide, Australia  
Yazidhi **Bamutaze**, Makerere University, Kampala, Uganda  
Valerio **Baiocchi**, Sapienza University of Rome, Italy  
Gabriela **Biali**, "Gh. Asachi" University of Iasi, Romania  
Habib **Ben Boubaker**, University of Manouba, Tunisia  
Gino **Dardanelli**, University of Palermo, Italy  
Qingyun **Du**, Wuhan University, China  
Renata **Dulias**, University of Silesia, Poland  
Massimiliano **Fazzini**, University of Ferrara, Italy  
Edward **Jackiewicz**, California State University, Northridge CA, USA  
Shadrack **Kithiia**, University of Nairobi, Kenya  
Jaromir **Kolejka**, Masaryk University Brno, Czech Republic  
František **Križan**, Comenius University in Bratislava, Slovakia  
Muh Aris **Marfai**, Universitas Gadjah Mada, Yogyakarta, Indonesia  
Béla **Márkus**, University of West Hungary Szekesfehervar, Hungary  
Jean-Luc **Mercier**, Université de Strasbourg, France  
Igor **Patrakeyev**, Kyiv University of Construction and Architecture, Ukraine  
Cristian Valeriu **Patriche**, Romanian Academy, Iasi, Romania  
Dušan **Petrovič**, University of Ljubljana, Slovenia  
Hervé **Quénot**, Université de Rennes 2 et CNRS, France  
Sanda **Roșca**, Babes-Bolyai University of Cluj-Napoca, Romania  
José J. de **Sanjosé Blasco**, University of Extremadura, Spain  
Richard R. **Shaker**, Reyson University, Toronto, Canada  
Sarintip **Tantane**, Naresuan University, Phitsanulok, Thailand  
Gábor **Timár**, Eötvös University Budapest, Hungary  
Kinga **Temerdek-Ivan**, Babes-Bolyai University of Cluj-Napoca, Romania  
Yuri **Tuchkovenko**, Odessa State Environmental University, Ukraine  
Eugen **Ursu**, Université de Bordeaux, France  
Changshan **Wu**, University of Wisconsin-Milwaukee, USA  
Chong-yu **Xu**, University of Oslo, Norway

## Editor-in-chief

Ionel **Haidu**, University of Lorraine, France

## Editorial Secretary

Marcel Mateescu, Airbus Group Toulouse, France  
George Costea, Yardi Systemes, Cluj-Napoca, Romania

## Online Publishing

Magyari-Sáska Zsolt, "Babes-Bolyai" University of Cluj-Napoca, Romania

# **Geographia Technica**



**Technical Geography**

**an International Journal for the Progress of Scientific Geography**

**2022 – No. 1**

**Cluj University Press**

**ISSN: 1842 - 5135 (Printed version)**

**ISSN: 2065 - 4421 (Online version)**

© 2022. All rights reserved. No part of this publication may be reproduced or transmitted in any form or by any means, electronic or mechanical, including photocopy, recording or any information storage and retrieval system, without permission from the editor.

Babeş-Bolyai University  
Cluj University Press  
Director: Codruța Săcelean  
Str. Hașdeu nr. 51  
400371 Cluj-Napoca, România  
Tel./fax: (+40)-264-597.401  
E-mail: [editura@editura.ubbcluj.ro](mailto:editura@editura.ubbcluj.ro)  
<http://www.editura.ubbcluj.ro/>

Asociatia Geographia Technica  
2, Prunilor Street  
400334 Cluj-Napoca, România  
Tel. +40 744 238093  
[editorial-secretary@technicalgeography.org](mailto:editorial-secretary@technicalgeography.org)  
<http://technicalgeography.org/>

Cluj University Press and Asociatia Geographia Technica  
assume no responsibility for material, manuscript, photographs or artwork.



# Contents

## *Geographia Technica*

Volume 17, Issue 1, spring 2022

*An International Journal of Technical Geography*

ISSN 2065-4421 (Online); ISSN 1842-5135 (printed)

- IMPERVIOUS SURFACE TREND ANALYSIS AND ITS IMPACTS ON KOSOVO'S LANDSCAPE CHANGE FROM 2006 TO 2015**  
Ferat KRASNIQI & Florim ISUFI ..... 1  
DOI: 10.21163/GT\_2022.171.01
- INTEGRATING MULTISOURCE OF BATHYMETRY DATA FOR UPDATING BASEPOINT AND BASELINE POSITIONS OF MARITIME BOUNDARY**  
Ratna Sari DEWI, Tia Rizka Nuzula RACHMA, Ibnu SOFIAN, Nadya OKTAVIANI, Ayu Nur SAFI'I, SUPRAJAKA, Astrit RIMAYANTI & Eko ARTANTO ..... 18  
DOI: 10.21163/GT\_2022.171.02
- FACTORS INFLUENCING SOIL BEHAVIOR AND PROPERTIES OF MASS MOVEMENTS IN THE BLIMBING AREA, BRUNO DISTRICT, PURWOREJO REGENCY, CENTRAL JAVA, INDONESIA**  
Sari Bahagiarti KUSUMAYUDHA, Riskhy JUMADIL AKHIR & PURWANTO ..... 33  
DOI: 10.21163/GT\_2022.171.03
- MACHINE LEARNING FOR MAPPING SPATIAL DISTRIBUTION OF THICKNESS AND CARBON STOCK OF TROPICAL PEATLAND BASED ON REMOTE SENSING DATA: A CASE STUDY IN LAKE SENTARUM NATIONAL PARK, INDONESIA**  
Faizal MUSTHOFA, Wirastuti WIDYATMANTI, Sanjiwana ARJASAKUSUMA, Deha A. UMARHADI, Demetria A. PUTRI, Fahrudin F. RAHARJA & M. K. ARRASYID ..... 46  
DOI: 10.21163/GT\_2022.171.04
- INTEGRATION OF SENTINEL-1A SAR, HYDRO DYNAMIC AND TRAJECTORY MODEL OF OIL SPILL AT BALONGAN COASTAL WATER JAVA SEA, INDONESIA**  
Muhammad HELMI, Agus HARTOKO, Hifzhan HUSNA & Mochamad Indra Bayu ARDIANSYAH ..... 58  
DOI : 10.21163/GT\_2022.171.05
- ALGORITHMS IN MATLAB TO COMPUTE A LOCAL GEOID MODEL FOR GEOMATICS PURPOSES**  
Massimiliano PEPE ..... 77  
DOI : 10.21163/GT\_2022.171.06

**INTELLIGENT LOW-LEVEL WIND SHEAR ALERT PREDICTION SYSTEM  
BASED ON ANEMOMETER SENSOR NETWORK AND TEMPORAL  
CONVOLUTIONAL NETWORK (TCN)**

Muhammad RYAN, Adhi Harmoko SAPUTRO & Ardhasena  
SOPAHELUWAKAN ..... 92  
DOI: 10.21163/GT\_2022.171.07

**NIGHTTIME LIGHT EMISSIONS EXPLAIN THE DECLINE IN NO<sub>2</sub> DURING  
A COVID-19-INDUCED TOTAL LOCKDOWN IN FRANCE**

Kamill Dániel KOVÁCS ..... 104  
DOI: 10.21163/GT\_2022.171.08

**APPLICATION OF 3S TECHNOLOGY IN DISASTER RISK RESEARCH IN  
THE NORTHERN MOUNTAINOUS REGION OF VIETNAM**

Dieu Trinh NGUYEN & Quoc Lap KIEU ..... 116  
DOI: 10.21163/GT\_2022.171.09

**PHYSICAL DRIVERS OF THE 2013 MARINE HEATWAVE IN THE SEAS OF  
THE SOUTHERN JAVA-NUSA TENGGARA**

Tria MAULIDA, Anindya WIRASATRIYA, Dwi Haryo ISMUNARTI &  
Ardiansyah Desmont PURYAJATI ..... 129  
DOI : 10.21163/GT\_2022.171.10

**SPATIAL VARIATION OF NO<sub>2</sub> LEVELS DURING THE COVID-19  
PANDEMIC IN THE BALI TOURISM AREA**

I Nyoman SUNARTA & Moh SAIFULLOH ..... 140  
DOI: 10.21163/GT\_2022.171.11

**COMPARING CHOROPLETH AND GRADUATED SYMBOLS: HOW  
DIFFERENT MAP TYPES AFFECT PUBLIC UNDERSTANDING IN COVID-19  
MAP READING IN BADUNG REGENCY, BALI, INDONESIA**

Tri Tanami SUKRAINI, I Made Adi YASA & Putu Perdana Kusuma  
WIGUNA ..... 150  
DOI: 10.21163/GT\_2022.171.12

**3D MODELLING OF BULDINGS AND URBAN AREAS USING  
GRASSHOPPER AND RHINOCEROS**

Domenica COSTANTINO, Arianna GRIMALDI &  
Massimiliano PEPE ..... 167  
DOI: 10.21163/GT\_2022.171.13

## IMPERVIOUS SURFACE TREND ANALYSIS AND ITS IMPACTS ON KOSOVO'S LANDSCAPE CHANGE FROM 2006 TO 2015

Ferat KRASNIQI<sup>1</sup> , Florim ISUFI<sup>1\*</sup> 

DOI: 10.21163/GT\_2022.171.01

### ABSTRACT:

The growth of cities and human demands for a better life have influenced the transformation of land use from natural land or vegetation to an artificial area-impervious surface (IS). The IS is an important indicator to measure the process of urbanization and its impact on the ecological environment. This article aims to analyze the trends of impervious surface and exert influence on land cover/land use occupation based on High-Resolution Layers (HRL) of imperviousness time-series data from 2006 to 2015 obtained from the European Copernicus Programme for seven Kosovo's regions. For the spatiotemporal distribution of the IS changes to be expected, the overlay of the GIS method was utilized. The results show that the absolute and relative rate of IS increased in all Kosovo's districts in four time periods: 2006, 2009, 2012, and 2015. Whereas, in the three periods of impervious change: 2006 - 2009, 2009-2012, and 2012 – 2015 regional distinctions were distinguished, where Prishtina and Prizren regions occupy the most spatial increases of IS. To highlight the consumption of land cover/land use area by the IS increase change results of the periods 2009 -2012, and 2012 – 2015, five-first class categories of CORINE Land Cover inventory from 2012 and 2018 year utilized. In both periods, the most affected land cover class by IS increases was the artificial area, followed by agricultural area and forest and semi-natural area, where wetlands and water land cover classes showed no affection in all of Kosovo's regions.

**Keywords:** *impervious surface (IS), growth rate, change, land use, district.*

## 1. INTRODUCTION

We are witnessing that due to the extraordinary/rapid development of the economy and the continuous increase of the population, the surface of the Earth is continuing to be urbanized quite drastically (Liu et al., 2019). With this rapid socio-economic development, expected that, by 2050, the urban population will exceed the participation of 60% (UN, 2014), while, by 2092, this participation will approach 100% (Batty, 2011; Liu et al., 2019). As a result of this development, the demands for land space for urban human life have intensified to the maximum. Consequently, the transformation of land use/cover is in constant conflict and competition by human activity such as preserving the environment or building infrastructure, recreational areas, or agriculture, which can be changed and lead to create a new type of land use (Scalenghe & Marsan, 2009). As we all know, one of the characteristics – which is most prominent – of urbanization is the growth and expansion of impervious surfaces. Undoubtedly, such things forge our living environment under unprecedented pressure (Grimm et al., 2008; Seto et al., 2012; Weng, 2012). This land conversion often occurs from urban growth, which transforms the permeability of the soil from water to impervious (McMahon, 2007).

Impervious surfaces such as roads, sidewalks, parking lots, roofs, and others, which prevent water infiltration into the soil, are defined as anthropogenic materials (Weng, 2008). Such an expansion of these areas' highlights – in addition to the process of urbanization – also anthropogenic manifestations with their effects make our living environment change (Weng, 2012; Liu et al., 2019). In addition to the direct impact on the environment, the increase of soil sealing due to the urbanization process has raised numerous field-related studies. This increase of these surfaces causes the floods from water flows to intensify/frequent (Brun and Band, 2000), and the increased of the surface temperature

---

<sup>1</sup>Department of Geography, Faculty of Mathematical and Natural Sciences, University of Prishtina, Prishtina, Republic of Kosovo, [ferat.krasniqi@uni-pr.edu](mailto:ferat.krasniqi@uni-pr.edu), \*Corresponding author: [florim.isufi@uni-pr.edu](mailto:florim.isufi@uni-pr.edu)

becomes the reason for the use of materials that have small values of albedo – urban heat island effect (Yuan and Bauer, 2007). The awareness of the impacts of the urbanization process of the hydrological processes (Deng and Wu, 2013), climate changes (Boggs and Sun, 2011; Hao et al., 2015), and on human health (Gong et al., 2012) are shown to be fundamental factors for the investigation of the impervious surface dynamics. Paul and Meyer (2008) reported an influence of the impervious increase on physical (hydrology and geomorphology), chemical, biological and ecological streams urban landscape. The IS was treated as an essential environmental key indicator (Chester & Gibbons, 2007) for population density estimation (Morton & Yuan, 2009), changes in storm runoff (Miller, et al., 2014), water balance (Strohbach, et al., 2019) and quality (Schueler, 1994), and urban heat island (Weng, et al., 2004).

Numerous research methodologies were emerged to map impervious surfaces using whether low or high spatial resolution remotely sensed data. For instance, the Landsat-7 ETM+ and IKONOS and Digital Orthophoto Quadrangles (DOQ) imageries used for mapping large areas of impervious in the United States by applying regression tree (CART) algorithm (Yang, et al., 2003), the normalized spectral mixture analysis (NSMA) method used on Landsat TM and US census data (Morton & Yuan, 2009), pixel-based, segmentation based and a hybrid classification method applied on Quickbird high-resolution imagery (Lu, et al., 2011).

Remote sensing is considered a more suitable technique to extract and map IS compared to traditional methods due to many satellite-acquired image values such as multi-temporal image resolution, large covered scene area, and lower cost (Slonecker, et al., 2009). The medium-resolution image (like Landsat constellations) is widely endorsed to observe the urban spatial structure distributions due to their repeated measurement at moderate spatial resolution and orbit revisit time (Sexton, et al., 2013). In the last decades, the increase in open free source remotely sensed data and software policies has increased the ability to map and quantify the impervious area for a larger unit-continental unit. One such series of products covering 39 European countries and capture the percentage and change of soil sealing have been created under Copernicus Land Monitoring Service (CLMS) and is freely available for scientific purposes. Cooperation between the EEA and Swiss Federal Office for the Environment (FOEN) analyzed for the first time the extent of the urban sprawl over the period 2006 -2009 using the HRL imperviousness layer maps. The study involved 32 countries and revealed that the IS area could be used as a new indicator to monitor the urban sprawl (EEA-FOEN, 2016). The European Environment Agency (EEA) has created an online platform for time-series imperviousness changes based on impervious products. Every 3 years between 2006 and 2015, based on 100 m raster cell size of imperviousness change products for each country unit using data cube approach, aiming to measure the extent and dynamics of soil sealing caused by urban development and other artificial land use classes in Europe (EEA, 2020). The information on IS area differentiates between countries on administrative levels provided by this platform. The impervious change statistics analysis for Kosovo could be derived only per country unit. Based on the importance of the soil sealing trend, this study aims to highlight the spatial distribution of IS area changes for the seven regions units of Kosovo over 10 years (2006 - 2015) using GIS overlay methods and imperviousness time series data with 20m spatial resolution.

Moreover, the study addresses these three main questions:

1. What are the absolute and relative status and change of imperviousness layer in Kosovo and its regions?
2. What are the imperviousness change dynamics (trends) among seven regions, and why?
3. Which type of land cover or land use is more affected by the increase of impervious among the regions?

## 2. STUDY AREA

The Republic of Kosovo is located in the southeastern part of Europe respectively lies in the center of the Balkan Peninsula (**Fig. 1**). It borders Albania (south-west), Montenegro (northwest), Serbia (northeast), and Northern Macedonia (southeast) and has a total geographical area of 10905.25 km<sup>2</sup>. The territory lies between 41 ° 51 ' N to 43 ° 16' N latitudes and between 19 ° 59 ' E and 21 ° 47'

E longitude, characterized by different altitudes, from 270 m to 2656 m. The relief of Kosovo consists of mountains and plains. Mountains occupy 63% of the territory and are divided into peripheral mountains that form the framework of Kosovo and central mountains. The lowest point of Kosovo is located in the valley of the river Drini i Bardhë, on the border with Albania, and reaches an altitude of 270 m above sea level. The highest point is located in the west of Kosovo, in Gjeravica - 2,656 m. In terms of hydrography, Kosovo is divided into three river basins: Drini i Bardhë, Ibri, Morava e Binçës and Lepeneci. Kosovo Rivers flow into three marine catchments: the Black Sea, the Adriatic Sea, and the Aegean Sea. The climate of the Republic of Kosovo is mainly continental, resulting in summer warm and cold winters, with Mediterranean and continental influences (Kosovës, 2020). The state of Kosovo is characterized by a very young population structure, where the average age is 30.2 years. According to the census conducted in April 2011, the population is over 1.7 million inhabitants, where 61% of the population lives in rural areas.

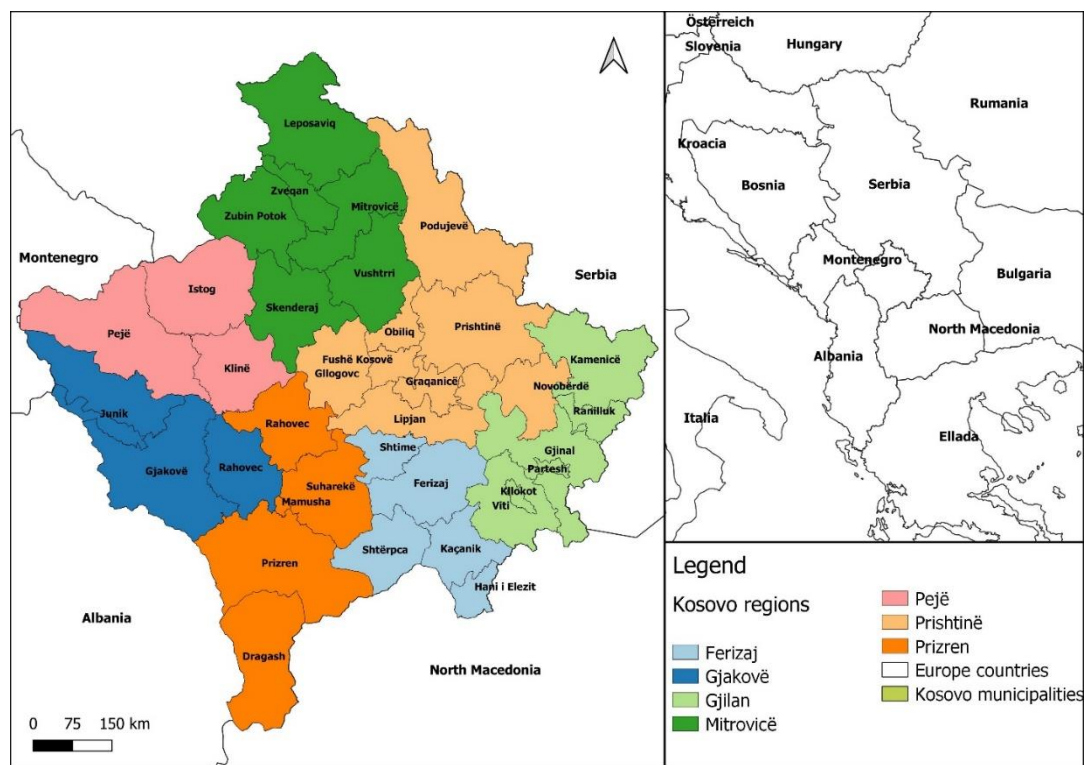


**Fig. 1.** Location of the Kosovo Republic in Balkan Peninsula and its administrative regional division.

The country is divided into seven administrative regions (**Fig. 1**). Data by size by region and estimated population from 2011 to 2015 are presented in **Table 1**. The name of the regions corresponds to the name of the regional centers, with Prishtina and Prizren regions being the most populated ones. Prishtina is the country's capital and is the largest regional economic, political, administrative, educational, and cultural center. Like any country that is in the phase of economic and demographic transition, Kosovo, respectively, these regional centers, have undergone significant spatial changes due to the growth of their urban area. In particular, changes had taken place in the last 20 years (after the 1999 war), namely, after 2008, when the country gained the right to state independence. The expansion of regional urban areas has been influenced by many factors, which can be related to the post-war migration of the rural population in the direction of urban areas to education, employment and then resulted in a permanent residence, the growth of rural settlements on the border with urban areas, development of inter-regional and state road infrastructure. The region of Prishtina

and Prizren is among the regions which have had the most significant increase in artificial areas, frequently uncontrolled, causing occupation and loss of fertile land. From 1981 to 2011, of the total population that had emigrated within the national borders between municipalities (196,429 inhabitants), most of them migrated towards Prishtina (45,905 inhabitants) or over 23.1% of its population, followed by the municipality of Prizren with 7.98% Ferizaj 6.79%, Gjilan with 5.31%, and Fushë Kosova with 4.74% (Kastrati, et al., 2014). Therefore, it is crucial to study the spatial distribution and changes of the impervious area of Kosovo, to better understand the trend and direction of urban development and its impact on transformation land use.

**Table 1.**  
**The size of the area and estimated population from 2011 to 2015 of Kosovo regions. Source: Kosovo Agency of Statistics, <https://ask.rks-gov.net/en/kosovo-agency-of-statistics>.**

Region		Area in km <sup>2</sup>	2011	2012	2013	2014	2015	Region's center
1.	Ferizaj	1 024	185695	189507	190299	186252	178754	Ferizaj
2.	Gjakova	1 236	196867	200348	200582	200956	201006	Gjakova
3.	Gjilan	1 331	181459	182991	182698	176700	166834	Gjilan
4.	Mitrovica	2 051	192637	235691	235386	231548	224420	Mitrovica
5.	Peja	1 366	174235	177854	177387	177266	176702	Peja
6.	Prishtina	2 157	477312	489975	493944	489846	480040	Prishtina
7.	Prizren	1 747	331620	339240	340335	342376	343848	Prizren
<b>Total</b>		<b>10, 912</b>	<b>1739825</b>	<b>1815606</b>	<b>1820631</b>	<b>1804944</b>	<b>1771604</b>	

### 3. DATA AND METHODS

The data utilized in this study comprise both raster and vector spatial datasets provided free of charge from Copernicus – European Union's Earth observation program. The imperviousness HRL (High- Resolution Layer) data time series are raster data format and contain information on imperviousness status and change layers. The imperviousness status layer captures the percentage form 0-100% of IS increase or decrease for the following four years: 2006, 2009, 2012, and 2015. Imperviousness change layers are classified thematic change products that map the most relevant categories of IS such as unchanged areas, new cover, loss of cover, and impervious degree increase and decrease for each of the 3-year periods: 2006-2009, 2009-2012, and 2012-2015 (**Table 2**). The imperviousness layers represent the spatial impermeability distribution of the soil per unit area. They are created using the semi-automatic classification method on NDVI calibrated products based on continuous multi-temporal seasonal image composites (3 per year) satellites (IRS-P6/ResourceSat-2 LISS-III, SPOT 5, and Landsat 8) with a spatial resolution of 20 x 20 m (LANGANKE, 2016). The CORINE Land Cover (CLC) time series inventory contains information on land cover/land use up to 44 classes at the three-level hierarchical category, using a Minimum Mapping Unit (MMU) of 25 hectares (ha) for area feature and a minimum width of 100 m for the linear feature (**Table 3**). The CLC Level 1 category compound of five class categories for this study includes artificial surfaces, agricultural areas, forest and semi-natural areas, wetlands, and water bodies are used.

**Table 2.**  
**Imperviousness products' main metadata information. Source: Copernicus – Land Monitoring Service (<https://land.copernicus.eu/pan-european>).**

Product type	Product name	Reference years	Pixel size	Projection	Tile ID
Status layers	IMD - Imperviousness degree	2006, 2009, 2012, 2015	20 m	EPSG:3035 (ETRS89, LAEA)	E50N20
Change layers	IMCC Imperviousness change classified	2006-2009, 2009-2012, 2012-2015	20 m	EPSG:3035 (ETRS89, LAEA)	E50N20

**Table 3.**  
**CORINE Land Cover inventories' main metadata information. Source: Copernicus – Land Monitoring Service (<https://land.copernicus.eu/pan-european>).**

Name	Year	Data type	Data format	Projection
Corine Land Cover - GeoPackage	2012	Vector	SQLite Database	EPSG:3035 (ETRS89, LAEA)
Corine Land Cover - GeoPackage	2018	Vector	SQLite Database	EPSG:3035 (ETRS89, LAEA)

After collecting the data described above, the first step was to pre-process the data for the study, such as clipping and re-projection. To exhale the absolute spatial distribution in IS pixel (2006, 2009, 2012, and 2015) and IS changes (2006-2009, 2009-2012, and 2012-2015) per each region, the GIS raster overlay method is employed, using QGIS tools. Overlay analysis is a GIS operation for overlaying the multiple layers of datasets representing different themes to identify layer relationships (Clarke, 1997). To produce the spatial distribution of the impervious surface in pixel, for each land cover category on each region, both vector and raster overlay analysis tools are applied on the CORINE Land Cover data set for 2012 and 2018. Then, the results of the GIS overlay analysis were exported to Excel spreadsheets for further analysis. From the data on the excel spreadsheet, the absolute (in km<sup>2</sup>) and relative (in percentage) area for the imperviousness status and change layers, annual IS change increase was calculated as well as land cover type consumption by IS per each region. This change was witnessed from the linear trend, calculated for the period 2006-2015. The linear trend equation can be represented by the equation (Pushka, 2008):

$$Y_t = A + BX \tag{1}$$

where:

$Y_t$  - the trend;

A - the value of the constant when X is zero;

B - the trend coefficient, which shows how much the dependent variable Y changes for a given period;

The parameters A and B are derived from two normal equations:

$$\Sigma Y = NA + B\Sigma X \tag{2}$$

$$\Sigma YX = A\Sigma X + B\Sigma X^2 \tag{3}$$

Degree of change (DCh), percentage of change (PCh), and annual rate increase (ARI) of IS area during each period time for each region were calculated based on the following formulas (Alawamy, Balasundram, Hanif, & Sung, 2020) :

$$Dch = (t1 - t2) \tag{4}$$

$$Pch = \frac{(t1-t2)}{Gt} * 100 \tag{5}$$

$$Ari = \frac{(t1-t2)}{(Gt*n)} * 100 \tag{6}$$

where:

- t1 - the imperviousness area of the region in the initial time;
- t2 - is the imperviousness area of the region at the final time;
- Gt - the sum of the total country imperviousness area, and
- n - the number of years between one period of change.

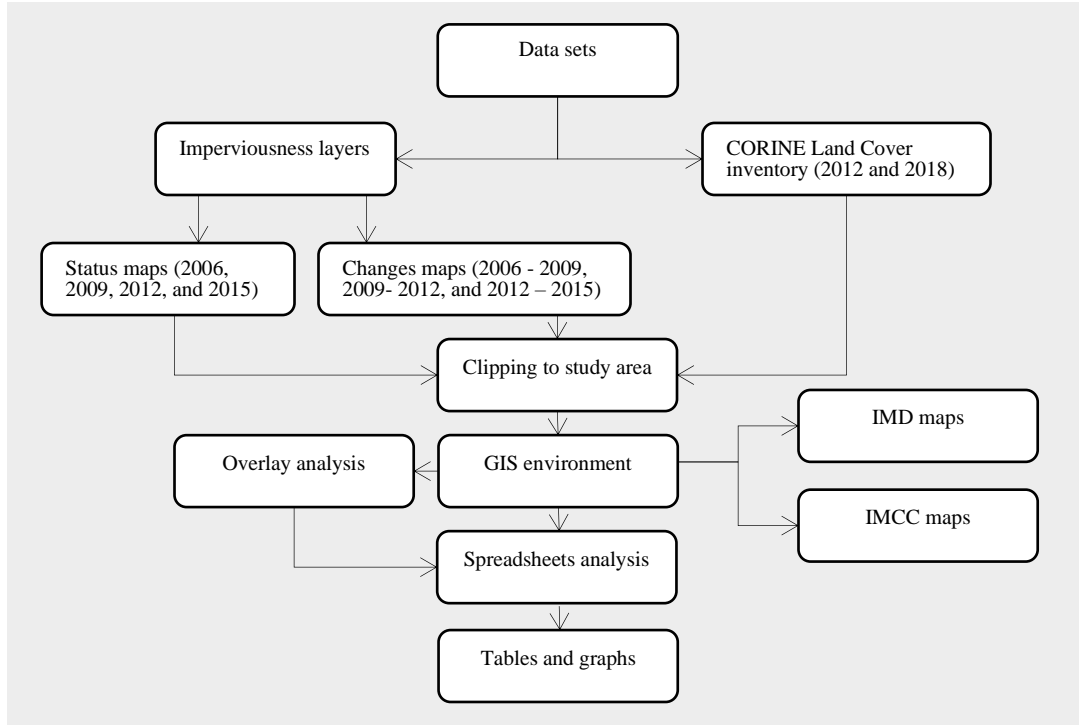


**Fig. 2.** Flowchart depicting methodology

## 4. RESULTS AND DISCUSSIONS

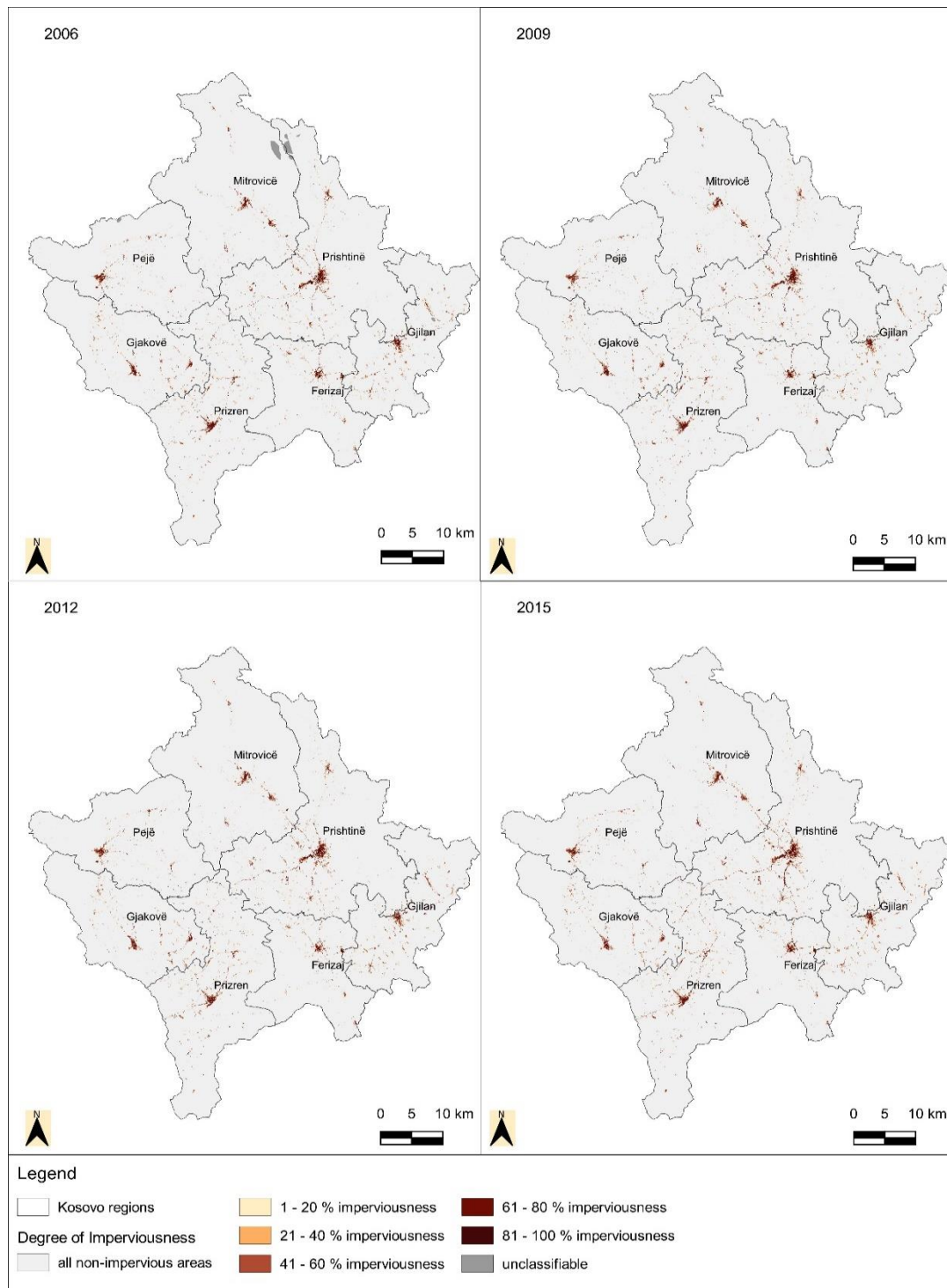
Based on the data and methodology applied, three types of results were obtained and analyzed in this study area: the degree of the impervious for the four-time periods (2006, 2009, 2012, 2015) in absolute and relative values, degree of impervious classes change (IMCC) in absolute and relative changes values and the annual increase of the impervious for the three periods of changes (2006-2009, 2009-2012, 2012-2015), and the consumption of land cover or use class category by the impervious trends for the two-period time of changes 2009-2012 and 2012-2015.

### 4.1. Degree of soil sealing from 2006 to 2015 (Degree of imperviousness = IMD)

The maps (**Fig. 3**) show the degree of soil sealing ranging from 0% to 100 % for all Kosovo regions. Light brown color (range 1-20) shows areas with a slight degree of imperviousness, while dark brown color (range 81 – 100%) shows an entirely impervious area of each region, indicating the trend of the impervious increase each year detected in all degree imperviousness time series products.

**Table 4** shows the absolute and relative distribution of soil impermeability for the study area for the period 2006 - 2015. From the tabular data, it can be estimated that IS has grown continuously in all regions. At the country level, the IS area increased from 225.80 km<sup>2</sup> to 250.42km<sup>2</sup> from 2006 to 2015. From 2006 to 2012, the IS area increased slowly, while from 2012 to 2015, the IS area increased quickly, from 234.90 km<sup>2</sup> to 250.42 km<sup>2</sup>.





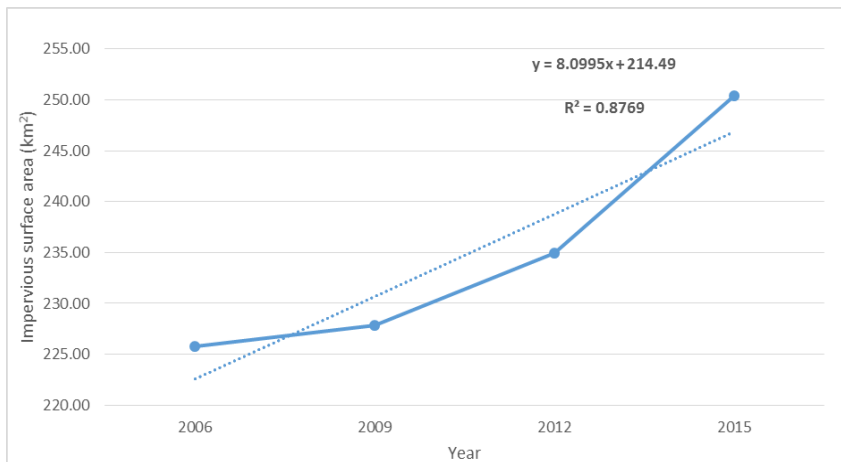
**Fig. 3.** Distribution of imperviousness degree rate in Kosovo and regions presented for four years (2006, 2009, 2012 and 2015).

Table 4.

## The absolute and relative soil sealing of the regions in the study area.

Region	2006		2009		2012		2015	
	Area (km <sup>2</sup> )	%	Area (km <sup>2</sup> )	%	Area (km <sup>2</sup> )	%	Area (km <sup>2</sup> )	%
Gjakova	27.56	0.25	27.66	0.25	27.8	0.3	28.01	<b>0.26</b>
Ferizaj	22.33	0.20	22.46	0.21	22.9	0.2	24.70	<b>0.23</b>
Peja	23.54	0.22	23.72	0.22	23.9	0.2	23.97	<b>0.22</b>
Prishtina	57.64	0.53	58.55	0.54	61.5	0.6	69.83	<b>0.64</b>
Mitrovica	23.07	0.21	23.22	0.21	23.7	0.2	24.43	<b>0.22</b>
Prizren	38.90	0.36	39.21	0.36	41.9	0.4	45.02	<b>0.41</b>
Gjilan	32.77	0.30	32.98	0.30	33.4	0.3	34.46	<b>0.32</b>
Grand Total	225.80	2.07	227.80	2.09	234.9	2.2	250.42	<b>2.30</b>

**Fig. 4** shows the linear trend and R<sup>2</sup> (R-Squared) calculated for IS in Kosovo from 2006 to 2015. The result of the calculated trend has the following values:  $Y = 8.0995x + 214.49$ . The trend coefficient  $B = 8.0995$  shows that for every three years, IS in Kosovo has increased by 8km<sup>2</sup>, while the value of the coefficient  $A = +214.49$  represents the constant for the period zero. The values of the linear trend model calculated in three-year intervals, from 2006 to 2015 are  $Y(2006) = 222.59$  km<sup>2</sup>,  $Y(2009) = 230.69$  km<sup>2</sup>,  $Y(2012) = 238.79$  km<sup>2</sup> and  $Y(2015) = 246.90$  km<sup>2</sup>. Based on these results, the projected value of IS growth for 2018 is  $Y(2018) = 254.99$  km<sup>2</sup>. The value of R-squared = 0.88 explains that the linear model regression has fit well our observation data.



**Fig. 4.** The trend of impervious surface area in Kosovo, from 2006 to 2015.

**Fig. 5** presents the IS area distribution of Kosovo's regions at different periods. In the initial year (2006), most changes occurred in the Prishtina region (57.64 km<sup>2</sup> or 0.53 %), followed by the Prizren region (38.90 km<sup>2</sup> or 0.36 %) and the Gjilan region (32.77 km<sup>2</sup> or 0.30 %). The other regions like Gjakova, Peja, Mitrovica, and Ferizaj share almost the same percentage of sealing on the country level.

The calculations for the imperviousness status layer of the second period (2009) indicate very little increase on both the absolute and relative values of the impervious with around two km<sup>2</sup> for the whole country. During this period, the most soil-sealed regions are Prishtina and Prizren, while in the other regions, the growth rate of impervious is relatively low. In the 2012 period, the impervious increased to 234.9 km<sup>2</sup> or 2.2 % for the whole country. Regional impervious increasing distinction occurs again in the region of Prishtina with 61.5 km<sup>2</sup> or 0.6 % and Prizren 41km<sup>2</sup> or 0.4% of the country area, while other regions show a slight IS growth (**Fig. 5**).

In the final year (2015), the biggest absolute IS increased to 250.42 km<sup>2</sup> or 2.30 % within the Republic of Kosovo. As seen in **Fig. 5**, except for Prishtina (69.98 km<sup>2</sup> or 0.64) and Prizren (45.02 km<sup>2</sup> or 0.41%) regions, a growth trend of IS increased in Ferizaj, Gjilan, and Mitrovica regions, while the Peja region indicates a very low IS growth rate.

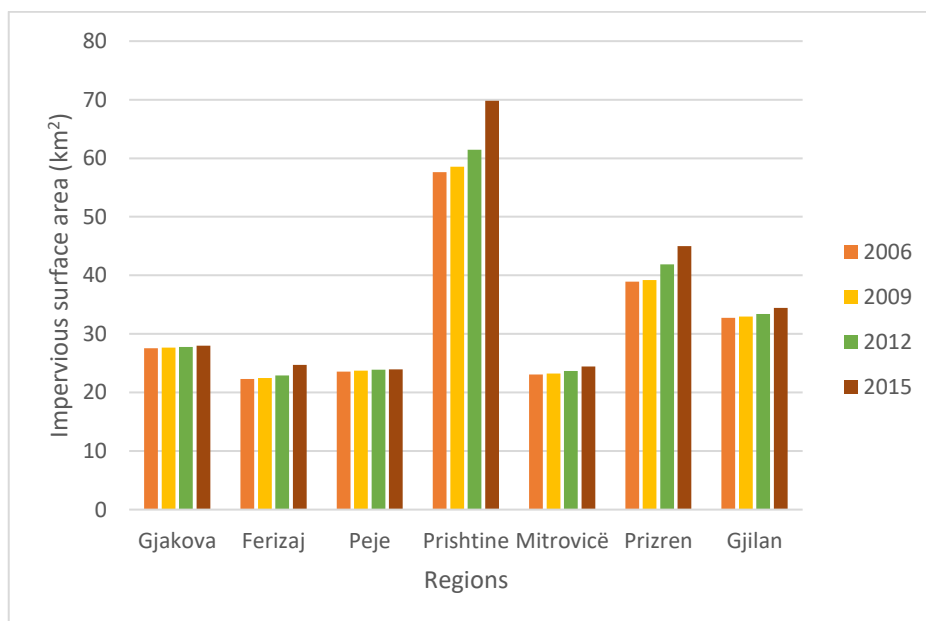


**Fig. 5.** The absolute increase of the IS in km<sup>2</sup> in Kosovo Region's from 2006 to 2015.

The IS growth rate in Kosovo and its regions continues to increase quickly. Based on the 2011 national population census data, 61% of the population is rural, while 39% is urban in Kosovo. Although, recently, there has been an improvement in the construction of road and water infrastructure in the deepest hilly-mountainous villages of the country, the migration of inhabitants continues towards the regional centers to better meet the living needs and opportunities for education and employment for the future. This has affected the growth of urban areas in each regional center, especially in Prishtina, which constantly attracts residents from border cities and all over the country. Examples of urban population lifestyle and their living change manner, as well as changes in economic activities of the population such as transport, trade, and tourism, may take to the construction of infrastructure and urban expansion, rather than the increase in the size of population (Scalenghe & Marsan, 2009). The new construction of highways, national and regional roads in Kosovo has increased the rate of IS area. The data calculated for the construction of the new highway in Kosovo show that from 2011 to 2020, about 137.2 km of highways were built (Krasniqi, et al., 2020), which has dramatically influenced the growth of the IS area and transformed the land use destination.

#### 4.2. Degree of imperviousness change (IMCC)

The classified impervious change maps (**Fig. 6**) indicate the spatial pattern of soil increase changes for the three periods over all regions of Kosovo. The colors presented in the IMCC legend indicate the attribute category of impervious classified changes. The white color represents the unchanged impervious areas with zero degrees: the red color indicates the new layer of increasing imperviousness area, which was zero on the first date of reference: the green color represents the degraded of the impervious surface, which was zero on the second reference date: the gray color represents the unchanged impervious surfaces between the two periods: the yellow color represents the increase of the imperviousness density in both the reference dates and color magenta - unclassified IS in any of the years, in the absence of raster data or cloud cover. However, a piece of more detailed information about the rate of the sealing of region's distinction is illustrated in **Table 5** and **Fig. 7**.

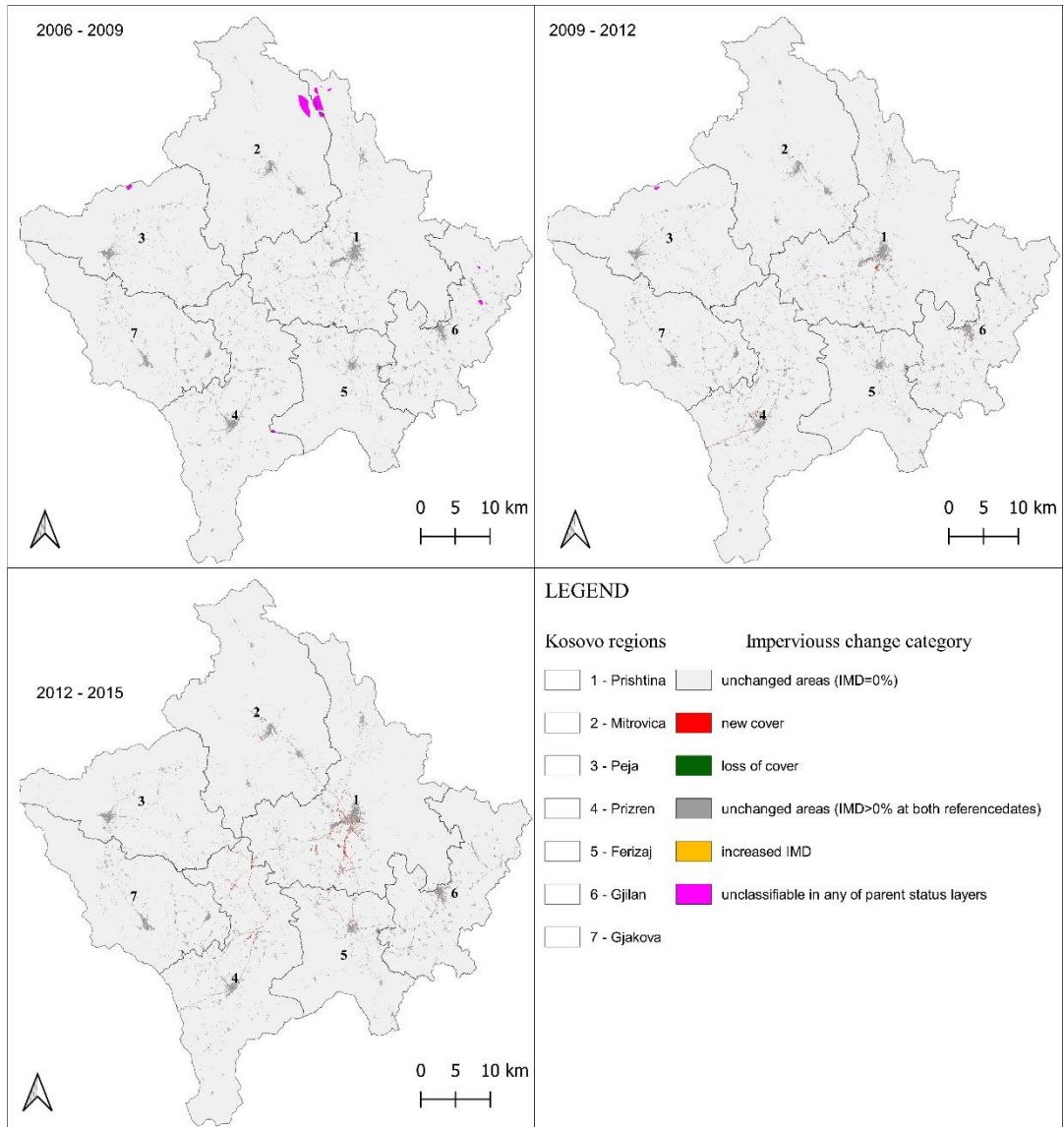


**Fig. 6.** The thematic classified impervious change in Kosovo regions for the three periods: 2006-2009, 2009-2012 and 2012-2015.

**Table 5** shows the statistics of imperviousness changes in three time periods; 2006-2009, 2009 – 2012, and 2012 -2015 according to each Kosovo region.

**Table 5.****The absolute, relative and annual sealing changes between 4-periods.**

Region	2006-2009			2009-2012			2012-15			2006-2015		
	Area (km <sup>2</sup> )	%	Annual %	Area (km <sup>2</sup> )	%	Annual %	Area (km <sup>2</sup> )	%	Annual %	Area (km <sup>2</sup> )	%	Annual %
Gjakova	0.1	0.04	0.01	0.12	0.05	0.02	0.23	0.1	0.03	0.45	0.20	0.06
Ferizaj	0.13	0.06	0.02	0.44	0.19	0.06	1.8	0.77	0.26	2.37	1.05	0.32
Peja	0.18	0.08	0.03	0.15	0.07	0.02	0.1	0.04	0.01	0.43	0.19	0.06
Prishtina	0.92	0.41	0.14	2.9	1.27	0.42	8.38	3.57	1.19	12.19	5.40	1.62
Mitrovica	0.15	0.07	0.02	0.44	0.19	0.06	0.77	0.33	0.11	1.36	0.60	0.18
Prizren	0.36	0.16	0.05	2.82	1.24	0.41	3.16	1.34	0.45	6.12	2.71	0.81
Gjilan	0.2	0.09	0.03	0.43	0.19	0.06	1.05	0.45	0.15	1.69	0.75	0.22
Total	2.04	0.9	0.3	7.3	3.21	1.07	15.49	6.59	2.2	24.62	10.90	3.28

**4.2.1. IMCC 2006-2009**

In the first period (2006 -2009), the absolute change was 2.04 km<sup>2</sup> or 0.90% of the total changes. The highest region in the degree of IS changes occurred in Prishtina with 0.92 km<sup>2</sup> or with an annual growth rate of 0.14%, followed by Prizren region with 0.36 km<sup>2</sup> or with a yearly growth rate of 0.05%, and other regions like Gjakova, Ferizaj, Peja, Mitrovica, and Gjilani, share almost the same absolute and their annual growth of rate changes ranging from 0.01 to 0.03 %.

**4.2.2. IMCC 2009-2012**

From 2009 to 2012, the absolute change was 7.3 km<sup>2</sup> or 3.21 % of the total changes in the second period of changes. Prishtina and Prizren regions experienced the most IS area changes: Prishtina with 2.90 km<sup>2</sup> or 1.27 %, followed by the Prizren region with 2.82 km<sup>2</sup> or 1.24 %. The characteristic of impervious surface changes in this period is that Ferizaj, Gjilan, and Mitrovica district show impervious surface area increase rate compared to the 2006-2012 period. While, Gjakova region is relatively the same, and Peja starts a small relative impervious surface decrease (**Fig. 7**).

**4.2.3. IMCC 2012-2015**

In the third period of impervious surface changes from 2012-2015, the absolute difference was 15.49 km<sup>2</sup> or 6.59 % of the total changes. The highest region in the degree of impervious changes is Prishtina with 8.38 km<sup>2</sup> or with an annual growth rate of 1.19%, followed by Prizren region with 3.16 km<sup>2</sup> or with a yearly growth rate of 0.45%, and other regions like Ferizaj, Gjilan, Mitrovica, Gjakova and Peja, share almost the same absolute and their annual growth of rate changes ranging (from 1.80km<sup>2</sup> to 0.10km<sup>2</sup> or 0.26 to 0.01 %). (**Fig. 7**).

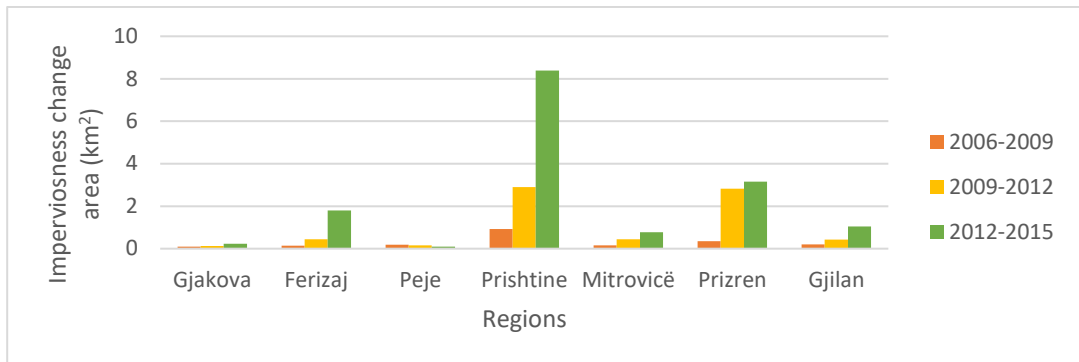


**Fig. 7.** Impervious surface changes are in km<sup>2</sup> of the regions for three periods.

#### 4.2.4. IMCC 2006-2015

**Fig. 8** presents the annual growth rate of IS changes. The annual growth of IS area at the national level from 2006 - 2015 is 24.62 km<sup>2</sup>, or 3.28 % of the annual rate IS area changes. The largest share of this change has the region of Prishtina with 12.19 km<sup>2</sup> or 1.62% of the territory, followed by the region of Prizren with 6.12 km<sup>2</sup> or 0.81%, Ferizaj shares 2.37 km<sup>2</sup> or 0.32 %, Gjilan 1.69 km<sup>2</sup> with 0.22% annual growth rate of IS changes, Mitrovica 1.36 km<sup>2</sup>, with 0.18 % annual growth rate of changes, while Gjakova and Peja regions, share the same annual growth rate of changes with 0.06 %.

The absolute and relative changes increase of the IS area in Kosovo continues to be prominent in the three periods of changes. In the regional aspect, except for the Peja region, which has a decrease in changes in IS, all other regions have a continuous increase. The decrease of changes in the region of Peja, can be related to its most extreme (peripheral) geographical position. The Prishtina region continues to have the largest increase of changes of the IS during the study period. In addition to the country's capital, Prishtina, in this region are located its neighboring cities such as Fushe-Kosova, Obiliq, Lipjan, Podujeva, Drenas, Gračanica, which have undergone a tremendous physical and spatial change. Based on the research "Increase of urban areas in Kosovo Municipalities" by the Institute for Spatial Planning of Kosovo (Nushi, Murseli, Nela, Kallaba, & Behrami, 2018), urban expansion is mainly done along national, regional, and local roads, especially when rural settlements have been very close to cities. In addition, such cases are the connection of Hajvali and Cagllavice with the city of Prishtina, the connection of the village of Uglare with the town of Fushë Kosova, and the internal connection of the town of Fushë Kosova with Prishtina.

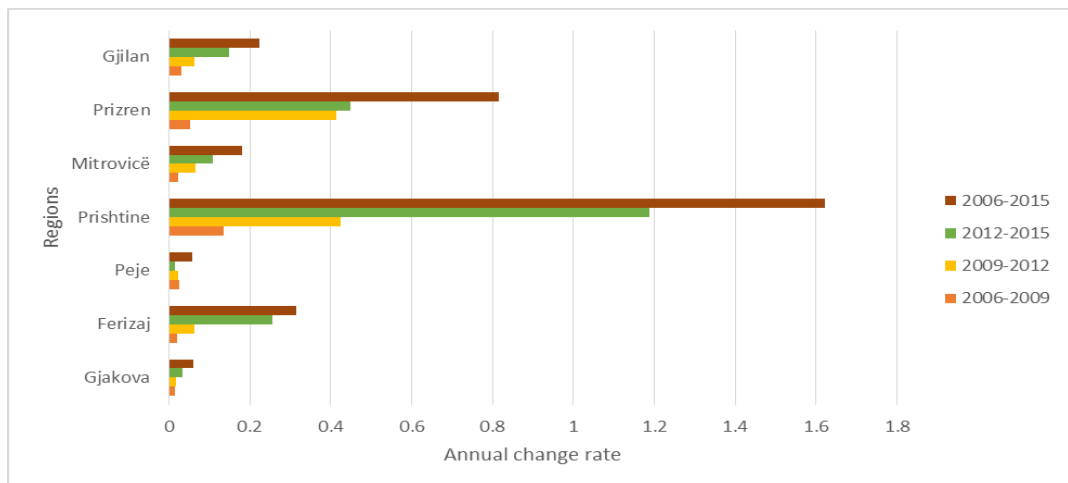


**Fig. 8.** The annual growth rate of IS changes of the regions for 4 time periods.

### 4.3. The impact of the impervious surface increase on land use

**Table 6** presents the absolute and relative area of three main category land cover classes occupied by impervious surface change expansion in the seven counties of Kosovo during the two periods (2009–2012 and 2012–2015). Artificial areas were the main land cover classes occupied by IS change in each period. The proportion of artificial area in the first period (2009–2012) was 70.26 % occupied by IS change increase, then in the second period (2012–2015) show a proportion decrease with 58.66 % of occupation by IS change increase. The proportion of agricultural area in the first period was 27.91% occupied by IS increase, then in the second period show an increase occupation by IS to 38.47%. As a third land cover class, forest, and semi-natural area, in the first period was 1.83% occupied by IS and increased slowly in the second period to 2.85%.

**Table 6.**  
The absolute and relative values of the land cover consumption by IS are increased during two periods of time series impervious changes in Kosovo regions.

Regions	2009 - 2012		2012 - 2015	
	Area km2	%	Area km2	%
<b>Ferizaj</b>	<b>0.44</b>	<b>6.00</b>	<b>1.80</b>	<b>11.62</b>
Artificial surfaces	0.29	3.92	0.96	6.20
Agricultural areas	0.15	2.00	0.83	5.33
Forest and semi-natural area	0.01	0.09	0.01	0.08
<b>Gjakova</b>	<b>0.12</b>	<b>1.65</b>	<b>0.23</b>	<b>1.51</b>
Artificial surfaces	0.03	0.38	0.09	0.59
Agricultural areas	0.08	1.14	0.14	0.89
Forest and semi-natural area	0.01	0.13	0.00	0.03
<b>Gjilan</b>	<b>0.43</b>	<b>5.93</b>	<b>1.05</b>	<b>6.76</b>
Artificial surfaces	0.35	4.78	0.49	3.17
Agricultural areas	0.08	1.11	0.53	3.44
Forest and semi-natural area	0.00	0.04	0.02	0.15
<b>Mitrovica</b>	<b>0.44</b>	<b>6.07</b>	<b>0.77</b>	<b>4.96</b>
Artificial surfaces	0.35	4.79	0.54	3.51
Agricultural areas	0.09	1.25	0.22	1.40
Forest and semi-natural area	0.00	0.03	0.01	0.05
<b>Peja</b>	<b>0.15</b>	<b>2.07</b>	<b>0.10</b>	<b>0.66</b>
Artificial surfaces	0.09	1.17	0.03	0.21
Agricultural areas	0.06	0.87	0.06	0.41
Forest and semi-natural area	0.00	0.03	0.01	0.03
<b>Prishtina</b>	<b>2.90</b>	<b>39.66</b>	<b>8.38</b>	<b>54.10</b>
Artificial surfaces	2.53	34.58	5.84	37.69
Agricultural areas	0.35	4.86	2.53	16.33
Forest and semi-natural area	0.02	0.22	0.01	0.08
<b>Prizren</b>	<b>2.82</b>	<b>38.62</b>	<b>3.16</b>	<b>20.40</b>
Artificial surfaces	1.51	20.64	1.13	7.29
Agricultural areas	1.22	16.68	1.65	10.67
Forest and semi-natural area	0.09	1.29	0.38	2.43
<b>Grand Total</b>	<b>7.30</b>	<b>100.00</b>	<b>15.49</b>	<b>100.00</b>

The graphic proportion area of each land cover class occupied by the increase of impervious surface changes in the two time-period of investigations for the seven districts of Kosovo is shown in **Fig. 9**. In the first period (2009-2012), artificial surfaces have been mostly occupied by the increase of impermeability in six of the regions, except the Gjakova region, where agricultural surfaces have the highest participation. The region of Prishtina has the highest percentage with 34.58% and the region of Prizren with 20.64%. Then, regions with more minor participation have Mitrovica (4.79%), Gjilan (4.78%), Ferizaj (3.92%), Peja (1.17), and Gjakova (0.38%). The region of Prizren (16.16%) has the largest occupation of the agricultural area due to the increase of the impervious surface, followed by regions such as Prishtina (4.86%), Ferizaj (2.0%), Mitrovica (1.25%), Gjakova (1.14%), Gjilan (1.11%), and Peja (0.87%). A smaller percentage of forest and the semi-natural area is affected by the impervious surface increase in this period. Prizren (with 1.29%) and Prishtina (with 0.22 %) districts occupy the largest proportion of this class. The other regions share the smaller percentage; Gjakova (0.13%), Ferizaj (0.09), Gjilani (0.04%), Mitrovica, and Peja with 0.03%.

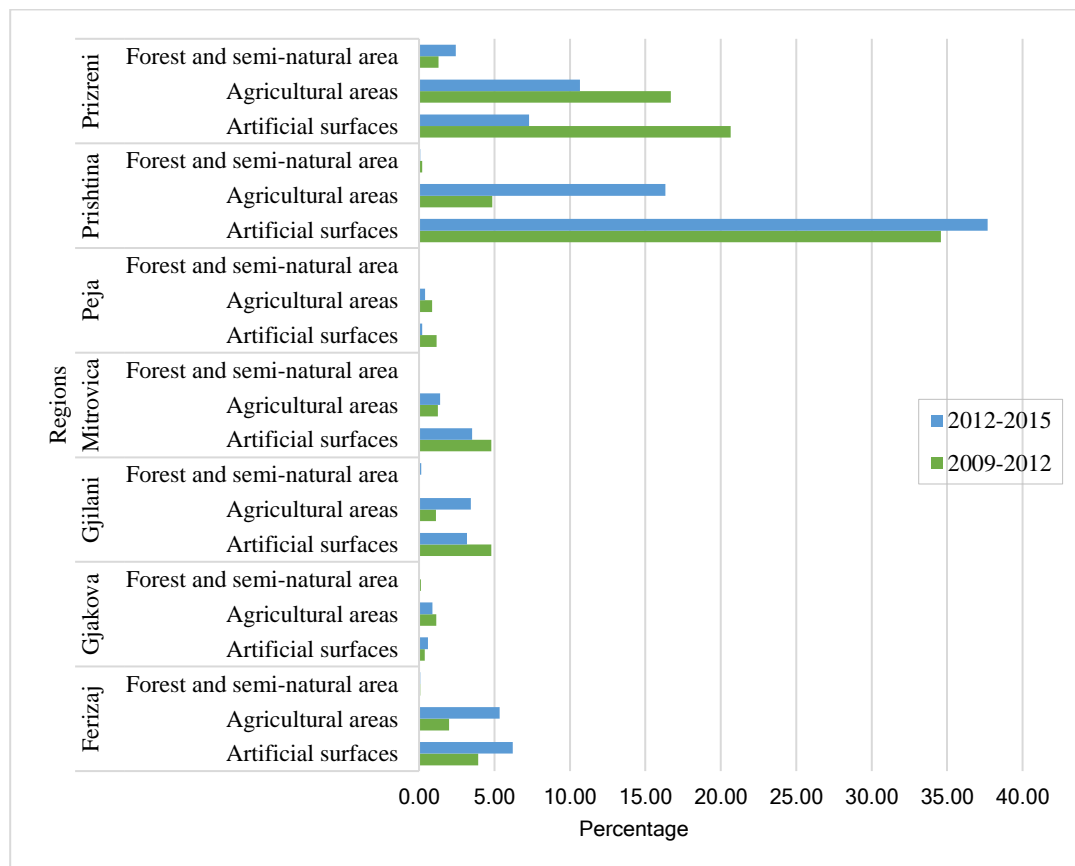


**Fig. 9.** Land cover consumption by IS are increases in Kosovo regions for to periods: 2009-2012 and 2012-2015.

In the second period (2012-2015) of impervious surface change, an increase and decrease great trend occupation of the artificial and agricultural land cover area experienced in Prishtina, Ferizaj, and Prizren districts. The district of Prishtina has the highest percentage occupation (with 37.69%) and continues to increase, followed by Prizren districts/region with 7.29% that show a decrease proportion comparing to the first period of impervious change.



A growth trend increases occupation of the artificial land cover area occurred in Ferizaj district with 6.20%. Then, regions with a smaller area of the artificial land cover proportion have Mitrovica (3.51%), Gjilan (3.17%), Gjakova (0.59%), and Peja (0.21). The region of Prishtina (16.33%) has the largest occupation of agricultural areas due to the increase of impervious surface are increased in this period, followed by Prizren district (7.29%), which had a decrease in the impervious surface area in this period, Ferizaj district (5.33%) which showed a fast impervious surface during this period and the other regions, Gjilan (3.44%), Mitrovica (1.40%), Gjakova (0.89%) and Peja (0.41%). An increased percentage occupation of forest and semi-natural area affected by impervious surface in this period. Prizren district occupies the largest proportion of this class (2.43 %), which increased this class's occupation during the second period. While the other districts and Prishtina (with 0.22 %) districts. The other regions share the smaller percentage; Gjilani (0.15%), Ferizaj and Prishtina (0.08%), Mitrovica (0.05%), Gjakova and Peja with 0.03%.

The reason why artificial surfaces have been occupied mainly by the increase of the impervious area in both periods taken in the analysis is due to the artificial surface class nomenclature and its definition and the increase of building density within cities and constructions along with existing buildings and roads. In the second period, 2012-2015, it is evident that the space and agricultural area begin to shrink more occupied by the impervious surface because one of the important reasons is that from 2011 begins the construction of highways in Kosovo and their extension has significantly reduced the area of fertile land. According to (Nizeyimana, et al., 2001), the expansion of cities tends to consume the best agricultural lands and affects the change of the boundary of the fertile land areas in the direction of the movement of lands with less productivity, such as hilly-mountainous areas.

## **5. CONCLUSION**

Rapid and uncontrolled urban growth has affected the development of the impervious area, bringing about chain changes in the living environment. Numerous studies have analyzed the IS spatial change increase in local and regional terms, caused by social and economic factors such as road infrastructure requirements and new recreational areas, new residential areas outside of the dense city area, and creation of economic and industrial zones, Etc. Because of these factors, the IS area, among other things, has disrupted the natural circulation of water, and their consequence is the flooding of rain.

In this study, the trend of the IS in the seven administrative districts of Kosovo is analyzed during the years 2006, 2009, 2012, and 2015 based on the time-series data of imperviousness High-Resolution Layers (HRL) downloaded free of charge by the European Copernicus Program. Also, the IS increase rate in the three periods of changes was discussed: 2006-2009, 2009-2012, and 2012-2015. The increase of IS areas is in constant conflict with the land use classes, especially agricultural ones. The findings of this study reveal the impact of IS changes of the two period-times 2009-2012, and 2012-2015, has affected the agricultural area shrinkage compared with the CORINE land cover inventories of the year 2012 and 2018.







Results show that during 9 years (2006-2015), the IS in Kosovo has increased to 24km<sup>2</sup> or an annual increase of changes to 3.28%. In the regional aspect, IS transformation has occurred in all administrative regions, except the Peja region, where there is a trend of IS decrease. The region of Prishtina continues to have a growing IS trend because this region is located in the capital of the country - Prishtina, where most of the tertiary and quaternary economic activities are concentrated. Furthermore, it was found that an increase in IS has had an effect on the narrowing of green spaces within urban areas and increased their boundary by consuming agricultural, forest, and semi-forest land. Spatial growth of land impermeability through regions provides important information to understand the growth rate of cities and their connection, sustainable regional urban planning in the future, environmental protection in general, and protection of water or natural plant reserves especially. Further studies at the city level may be conducted in the future, in case spatial data with higher resolution can be provided and other ancillary data to see in more detail the environmental impact of the IS increase.

## REFERENCES

- Alawamy, S. J., Balasundram, K. S., Hanif, M. H., & Sung, B. T. (2020). Detecting and Analyzing Land Use and Land Cover Changes in the Region of Al-Jabal Al-Akhdar, Libya Using Time-Series Landsat Data from 1985 to 2017. *Sustainability*, 24. <https://doi.org/10.3390/su12114490>
- Batty, M., 2011. When all the world's a city. *Environ Plan A* 43 (4), 765–772. <https://doi.org/10.1068/a43403>
- Brun, S.E., Band, L.E., 2000. Simulating runoff behavior in an urbanizing watershed. *Computers, Environment, and Urban Systems*. 24 (1), 5–22. [https://doi.org/10.1016/S0198-9715\(99\)00040-X](https://doi.org/10.1016/S0198-9715(99)00040-X)
- Boggs, J.L., Sun, G., 2011. Urbanization alters watershed hydrology in the Piedmont of North Carolina. *Ecohydrology* 4 (2), 256–264. <https://doi.org/10.1002/eco.198>
- Chester, L. A., & Gibbons, J. C. (2007). Impervious Surface Coverage: The Emergence of a Key. *Journal of the American Planning Association*, 62(2), 243 - 258. <https://doi.org/10.1080/01944369608975688>
- Clarke. (1997). *Getting Started with Geographic Information Systems* (Clarke, K ed.). New Jersey: Prentice-Hall.
- Deng, C., Wu, C., 2013. Examining the impacts of urban biophysical compositions on surface urban heat island: a spectral unmixing and thermal mixing approach. *Remote Sensing of Environment*. 131, 262–274. <https://doi.org/10.1016/j.rse.2012.12.020>
- EEA. (2020, 03 25). <https://www.eea.europa.eu/data-and-maps/indicators/imperviousness-change-2>. Retrieved from European Environment Agency: <https://www.eea.europa.eu/>
- EEA-FOEN, j. (2016). *Urban sprawl in Europe*. Luxembourg: European Environment Agency. <https://doi:10.2800/143470>
- Grimm, N.B., Faeth, S.H., Golubiewski, N.E., Redman, C.L., Wu, J., Bai, X., Briggs, J.M., 2008. Global change and the ecology of cities. *Science* 319 (5864), 756–760. <https://doi.org/10.1126/science.1150195>
- Gong, P., Yu, L., Li, C., Wang, J., Liang, L., Li, X., Ji, L., Bai, Y., Cheng, Y., Zhu, Z., 2016. A new research paradigm for global land cover mapping. *Annals of GIS*. 22 (2), 87–102. <https://doi.org/10.1080/19475683.2016.1164247>
- Hao, L., Sun, G., Liu, Y., Wan, J., Qin, M., Qian, H., Liu, C., Zheng, J., John, R., Fan, P., Chen, J., 2015. Urbanization dramatically altered the water balances of a paddy field dominated basin in southern China. *Hydrology and Earth System Sciences (HESS)*. <https://doi.org/10.5194/hessd-12-1941-2015>
- Kastrati, A., Sojeva, K., Maxharri, Z., Uka, S., Tara, R., & Gashi, D. (2014). *Migrimi Kosovar*. Prishtina: Agjencia e Statistikave të Kosovës.
- Kosovës, A. e. (2020). *Kosova në Shifra 2019*. Prishtinë: Agjencia e Statistikave të Kosovës (ASK). Retrieved from <https://ask.rks-gov.net/media/5686/kosova-n%C3%AB-shifra-2019.pdf>
- Krasniqi, I., Ulaj, R., Basha, I. T., Qevani, B., Kastrati, A., Rustemi, I., . . . Salihu, A. (2020). *Vjetari Statistikor i Republikës së Kosovës 2020*. Prishtinë: Agjencia e Statistikave të Kosovës.
- Langanke, T. (2016, 03 10). <https://land.copernicus.eu/pan-european/high-resolution-layers/imperviousness>. Retrieved from <https://land.copernicus.eu/>: <https://land.copernicus.eu/user-corner/technical-library/hrl-imperviousness-technical-document-prod-2015>
- Liu, C., Zhang, Q., Luo, H., Qi, S., Tao, S., Xu, H., & Yao, Y. (2019). An efficient approach to capture continuous impervious surface dynamics using spatial-temporal rules and dense Landsat time series stacks. *Remote Sensing of Environment*, 229, 114–132. <https://doi.org/10.1016/j.rse.2019.04.025>
- Lu, D., Hetrick, S., & Moran, E. (2011). Impervious surface mapping with Quickbird imagery. *International Journal of Remote Sensing*, 2519-2533. <https://doi.org/10.1080/01431161003698393>
- McMahon, G. (2007). Consequences of land-cover misclassification in models of impervious surface. *Photogrammetric Engineering and Remote Sensing*, 73(12), 1343-1353.
- Miller, D. J., Kim, H., & Klejdsen, R. T. (2014). Assessing the impact of urbanization on storm runoff in a peri-urban catchment using historical change in impervious cover. *Journal of Hydrology*, 59-70. <https://doi.org/10.1016/j.jhydrol.2014.04.011>
- Morton, A. T., & Yuan, F. (2009). Analysis of population dynamics using satellite remote sensing and US census data. *Geocarto International*, 24(2), 143-163. <https://doi.org/10.1080/10106040802460715>

- Nizeyimana, E. L., Petersen, G. W., Imhof, M. L., Sinclair Jr., H. R., Waltman, S. W., Reed-Margetan, D. S., . . . Russo, J. M. (2001). Assessing the Impact of Land Conversion to Urban Use on Soils with Different Productivity Levels in the USA. *Soil Science Society of America Journal*, 65(2), 391–402. <https://doi.org/10.2136/sssaj2001.652391x>
- Nushi, L., Murseli, R., Nela, N. N., Kallaba, M., & Behrami, V. (2018). *Rritja e zonave urbane në Komunitat e Kosovës*. Prishtina: Instituti për Planifikim Hapësinor.
- Paul, J. M., & Meyer, L. J. (2008). Streams in the Urban Landscape. *Annual Review of Ecology and Systematics*, 32(1), 207-231. [https://doi.org/10.1007/978-0-387-73412-5\\_12](https://doi.org/10.1007/978-0-387-73412-5_12)
- Pushka, A. (2008). *Metodat statistike dhe grafike në Gjeografi (Gjeostatistika)* (Third ed.). Prishtinë: University of Prishtina.
- Scalenghe, R., & Marsan, A. (2009). The anthropogenic sealing of soils in urban areas. *Landscape and Urban Planning*, 90(1-2), 1-10. <https://doi.org/10.1016/j.landurbplan.2008.10.011>
- Schueler, T. (1994). The Importance of imperviousness. *The Practice of Watershed Protection*, 100-111.
- Seto, K.C., Güneralp, B., Hutyra, L.R., 2012. Global forecasts of urban expansion to 2030 and direct impacts on biodiversity and carbon pools. *Proc. Natl. Acad. Sci. U. S. A.* 109 (40), 16083–16088. <https://doi.org/10.1073/pnas.1211658109>
- Sexton, J. O., Song, X.-P., Huang, C., Channan, S., Baker, M. E., & Townsched, J. R. (2013). Urban growth of the Washington, D.C.–Baltimore, MD metropolitan region from 1984 to 2010 by annual, Landsat-based estimates of impervious cover. *Remote Sensing of Environment*, 129(15), 42-53. <https://doi.org/10.1016/j.rse.2012.10.025>
- Slonecker, T. E., Jennings, B. D., & Garofalo, D. (2009). Remote sensing of impervious surfaces: A review. *Remote Sensing Reviews*, 20(3), 227-255. <https://doi.org/10.1080/02757250109532436>
- Strohbach, M. W., Döring, A. O., Möck, M., Sedrez, M., Mumm, O., Schneider, A.-K., . . . Schröder, B. (2019). The “Hidden Urbanization”: Trends of Impervious Surface in Low-Density Housing Developments and Resulting Impacts on the Water Balance. *Frontiers in Environmental Science*, 7, 1-10. <https://doi.org/10.3389/fenvs.2019.00029>
- United Nations (UN), 2014. World Urbanization Prospects: The 2014 Version-Highlights. Department of Economic and Social Affairs, New York.
- Weng, Q. (2008). *Remote Sensing of Impervious Surfaces*. NW: Taylor&Francis Group.
- Weng, Q., 2012. Remote sensing of impervious surfaces in the urban areas: requirements, methods, and trends. *Remote Sensing of Environment*. 117, 34–49. <https://doi.org/10.1016/j.rse.2011.02.030>
- Weng, Q., Lu, D., & Schubring, J. (2004). Estimation of land surface temperature–vegetation abundance relationship for urban heat island studies. *Remote Sensing of Environment*, 89(4), 467-483. <https://doi.org/10.1016/j.rse.2003.11.005>
- Yang, L., Huang, C., Homer, C. G., Bruce, W. K., & Michael, C. J. (2003). An approach for mapping large-area impervious surfaces: synergistic use of Landsat-7 ETM+ and high spatial resolution imagery. *Canadian Journal of Remote Sensing*, 29(2), 230 - 240. <https://doi.org/10.5589/m02-098>
- Yuan, F., Bauer, M.E., 2007. Comparison of impervious surface area and normalized difference vegetation index as indicators of surface urban heat island effects in Landsat imagery. *Remote Sensing of Environment*. 106 (3), 375–386. <https://doi.org/10.1016/j.rse.2006.09.003>

## INTEGRATING MULTISOURCE OF BATHYMETRY DATA FOR UPDATING BASEPOINT AND BASELINE POSITIONS OF MARITIME BOUNDARY

*Ratna Sari DEWI<sup>1\*</sup>* , *Tia Rizka Nuzula RACHMA<sup>1</sup>* , *Ibnu SOFIAN<sup>1</sup>* ,  
*Nadya OKTAVIANI<sup>1</sup>* , *Ayu Nur SAFTI<sup>1</sup>* , *SUPRAJAKA<sup>1</sup>* ,  
*Astrit RIMAYANTI<sup>1</sup>* and *Eko ARTANTO<sup>1</sup>*

DOI: 10.21163/GT\_2022.171.02

### ABSTRACT:

The research presents an alternative method to update the position of basepoints and baselines of maritime boundary especially for the area with lack of bathymetry data. We used multisource bathymetry data for instance the national bathymetry, the national digital elevation model, and echosounding measurement data. We then integrated them with satellite derived bathymetry to provide a dense depth point in shallow water. In this case, data limitation due to the difficulty in reaching for example the outermost location was overcome by using remote sensing technology. The spline interpolation-based method was successful to integrate those multisource data and obtained quite detail information and less noisy bathymetry data. Furthermore, the LAT and HAT coastlines were able to update the positions of basepoint and baseline in the study area. We developed a new maritime boundary consisting of a normal baseline and straight lines across the mouth of three rivers and integrate them with the existing archipelagic baselines. The results can be used as a basis knowledge to support negotiations in delimiting maritime boundaries so that a proportionate and equitable agreement with neighboring countries can be achieved.

**Key-words:** *Basepoints; Baselines; Coastlines; SDB; Gridding method; Maritime boundary.*

### 1. INTRODUCTION

Indonesia shares land and sea borders with other countries. Its maritime boundaries are divided into several maritime areas, including territorial sea, contiguous zone, the Exclusive Economic Zone, and continental shelf. To determine boundaries in these areas, defining basepoints and baselines is crucial since the baseline is the measurement reference for the boundary lines (Arsana, Rizos and Schofield, 2006). These basepoints and baselines are determined by Indonesia via Government Regulation ref. no. 38 of 2002 and Government Regulation ref. no. 37 of 2008 (Indonesian Government., 2002, 2008). Based on these regulations, archipelagic baselines are obtained from basepoints that are located in the low water line, namely the average position of the low water line (Indonesian Government., 2002). Based on NOAA (NOAA, 2021), the mean low water line (MLLW) is obtained from the average measurement of the lowest water level observed every day during the tidal datum period, which is 19 years. Nevertheless, with the current development of survey and mapping methodologies, there are various new methods that can be used to determine the position of these basepoints, especially when the availability of historical tide measurements is limited. Moreover, there is no internationally recognized standard method for determining the position of this archipelagic baselines (Specht, Specht, Waz, Dabrowski, *et al.*, 2019). However, the minimum quality of these measurements can be referred to in the IHO guidelines (IHO., 2008).

In the literature, measurement of basepoints and baselines can be carried out using various methods, including the tachymetric method (Specht *et al.*, 2017), through the LIDAR system

---

<sup>1</sup>Geospatial Information Agency, Jl. Raya Jakarta – Bogor KM.46, Cibinong, 16911, Indonesia,

\*Corresponding author: [dewi.rsd@gmail.com](mailto:dewi.rsd@gmail.com); [tia.rizka@big.go.id](mailto:tia.rizka@big.go.id); [ibnu.sofian@big.go.id](mailto:ibnu.sofian@big.go.id); [nadya.oktaviani@big.go.id](mailto:nadya.oktaviani@big.go.id); [ayu.nur@big.go.id](mailto:ayu.nur@big.go.id); [suprajaka@big.go.id](mailto:suprajaka@big.go.id); [astrit.rimayanti@big.go.id](mailto:astrit.rimayanti@big.go.id); [eko.artanto@big.go.id](mailto:eko.artanto@big.go.id).

(Sinclair, Stephenson and Barker, 2003), using UAVs (Specht, Specht, Waz, Dabrowski, *et al.*, 2019), and very high resolution imagery.

The use of UAVs and satellite imagery is primarily intended for very shallow waters, where ships cannot use echosounders because of the very shallow depths (Specht, Specht, Waz, Naus, *et al.*, 2019). Furthermore, it is stated that although the tachymetric method is the most accurate method, it is less effective because large coverage requires considerable time and cost (Specht, Specht, Waz, Dabrowski, *et al.*, 2019). Therefore, the use of remote sensing data has recently been increasingly developing in providing an alternative for mapping basepoints and baselines. This method will help the updating process since the position of these basepoints and baselines may be dynamic (Specht, Specht, Waz, Naus, *et al.*, 2019).

At present time, baselines at the study area has been developed by only connecting two basepoints due to limited data available in this location. Coastline surveys based on datums have never been carried out and bathymetric data around the site is also very minimal. Due to limited data availability to develop an accurate coastline position, the related baseline intersects part of the mainland as in **Fig. 1**. This study aims to develop an alternative method in determining an accurate position of basepoints and baselines of the Indonesian archipelago. We expect this method can be used as an alternative in determining the position of basepoints to complement Indonesia's maritime border data. The location of basepoints and baselines refers to the position of coastlines based on the lowest tidal datum (Lowest Astronomical Tide/LAT) and the highest tidal datum (Highest Astronomical Tide/HAT). This is in accordance with the Information Geospatial Law of Indonesia which mandates that Indonesia coastlines are categorized into three types of datum level: LAT, MSL and HAT (Geospatial Information Agency., 2011). Moreover, in 1997, to the member of IHO, Tidal Committee suggested the use of LAT as the reference for the chart datum. The LAT and HAT are calculated over at least 18.6 year period of harmonic constants derived from at least one year observation (FIG Commission 4 and 5., 2006). In addition, because of the difficulty in reaching the outermost location, the use of remote sensing data is expected to be able to overcome the problem of data limitations.

## 2. STUDY AREA

For the case study, a basepoint was selected, namely: TD.161B located in Cape Simansih, Siberut Island, part of Mentawai Islands, Indonesia. TD.161B is located at the coordinates of 01°40' 43" S and 98°52' 35" E. This basepoint is in the western part of Sumatra, facing the Indian Ocean and not bordering other countries. The closest basepoint to the TD.161B is TD.162 located in Cape Sakaladat, Siberut Island, and TD.161 in Sinyaunau Island (**Fig. 1**).

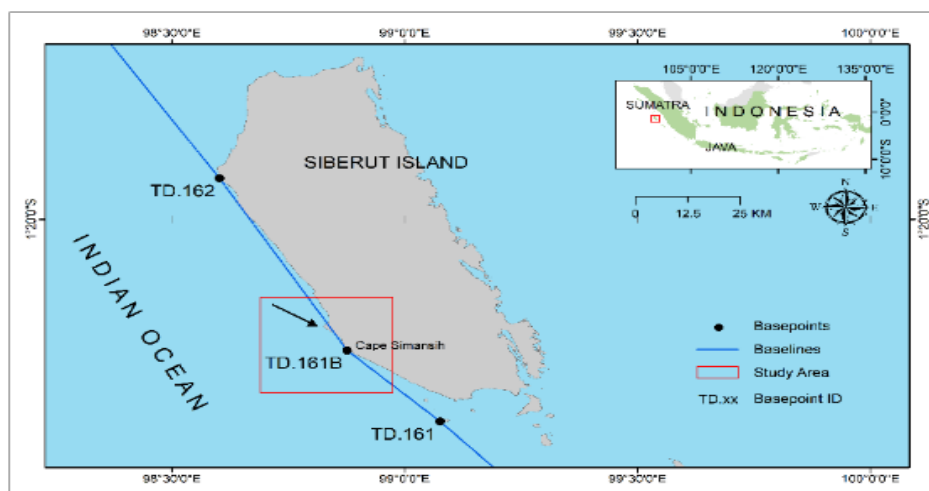


**Fig. 1.** Location of study area on a map of Indonesia including the location of existing basepoints and baselines. Black arrow shows the position at which the baseline intersects the mainland.

When checking the baseline carefully, we observed that the baseline intersects the land portion as indicated by black arrow in **Fig. 1**.

Tidal characteristics in the Mentawai Islands are dominated by semi-diurnal tides (Suparno., 2006) with wave height is ranging from 0.5 m up to 3 m depending on seasons (Dewi, Sugianto and Diponegoro, 2018). Siberut Island as the National Park Area is a biosphere reserve of UNESCO since 1981. It has a diversity of natural ecosystem such as coral reefs, seagrass beds and mangroves. On the other hand, Siberut has potential of disasters since this area is the meeting place of ocean and continental plates that is prone to earthquake and tsunami (Mustafa, 2010; Karim, 2011).

### 3. DATA AND METHODS

#### 3.1. Elevation and bathymetry data

Bathymetry data from various sources (see **Fig. 2**) were used in this experiment and described as follows:

- a) **National Digital Elevation Model (DEMNAS)**  
The National DEM is developed from multi data sources including IFSAR (5 m resolution), TERRASAR-X (5 m resolution) and ALOS PALSAR (11.25 m resolution) data. Further, the stereo-plotting mass point data is also incorporated in the process. The spatial resolution of DEMNAS is 0.27-arcsecond. It refers to the EGM2008 vertical datum (Geospatial Information Agency., 2018b).
- b) **Indonesian National Bathymetry Data (INBD)**  
National bathymetry is developed from the inversion of gravity anomaly data by using the altimetry data. Furthermore, sounding data from single beam and multibeam measurements are incorporated as well. The spatial resolution of the BATNAS data is 6arc-second and it refers to the MSL datum (Geospatial Information Agency., 2018b). The Geospatial Information Agency already has the National Bathymetry (INBD) data, which combines GEBCO data with several bathymetric measurements in only a few areas (Julzarika *et al.*, 2021).
- c) **Single Beam Echosounder Data (SBES)**  
For the study area, the best available data was from single beam echosounder (SBES) measurement provided by the Indonesia Geospatial Information Agency. The SBES survey was conducted in 2019. Since the data has been corrected for zero tidal influences, no additional tidal correction was needed. The depth information ranges from 1 m up to 29.9 m. **Table 1** presents the number of measurement points available within 2 m depth range. This SBES measurement data was used for two purposes: a) as an input when performing coastline model (gridding bathymetry and topography data); and b) as an input to build and validate the SDB model in extracting bathymetry information.
- d) **Satellite Derived Bathymetry Data (SDB)**  
SDB data were derived by performing Random Forest (RF) to Sentinel 2A. Further detail on the processing of the SDB model is available in Section 2.3.1.

**Table 1.**

**Number of measurement points within 2 m depth ranges for hydrographic data.**

Overall	>0 m	1–3 m	3–5 m	5–7 m	7–9 m	9–11 m	11–13 m	13–15 m	>15 m
97,971	N/A	6,645	4,593	7,119	24,770	26,465	22,576	3,847	1,956

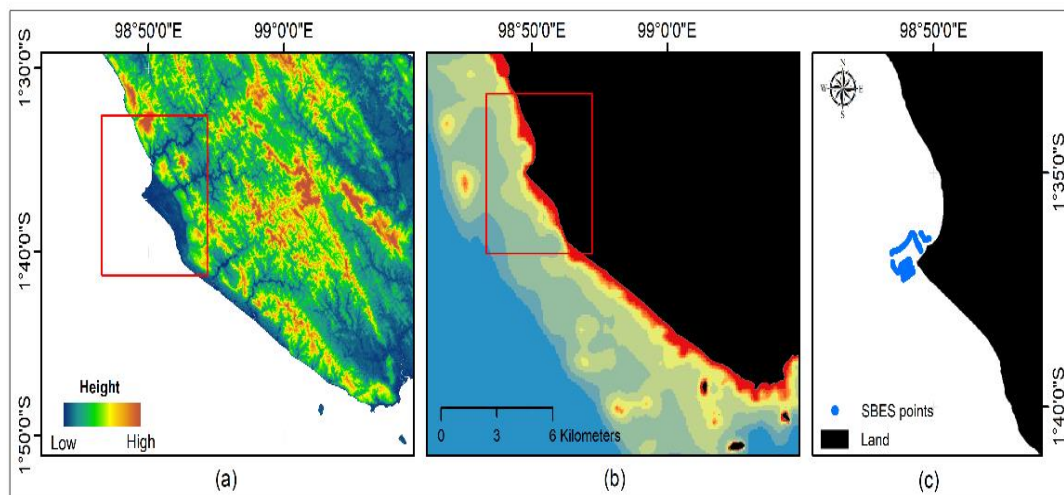


**Fig. 1.** The visualization of bathymetry data that were used for coastline model, namely a) composite of the national DEM; b) the Indonesian national bathymetry data; and c) SBES measurement points.

### 3.2. Tide gauge data

Hourly tides data observation was used in this research. The data were obtained from Mailepet tide gauge station in the southern part of Siberut Island located at the coordinates of 01°33' 49.7" S and 99°11' 49.2" E (Geospatial Information Agency., 2018a). The data which was made available from the Indonesian Geospatial Information Agency (Badan Informasi Geospasial) was recorded from 23 February 2011 up to 1 September 2020. The tide data was used in estimating the LAT and HAT position before performing coastline model.

### 3.3. Satellite image

Four bands of Sentinel 2A were used to extract bathymetry information from remote sensing data (satellite derived bathymetry). The spectral bands were consisting of blue (0.49  $\mu\text{m}$ ), green (0.56  $\mu\text{m}$ ), red (0.665  $\mu\text{m}$ ), and near infrared (0.842  $\mu\text{m}$ ) parts of the spectrum (ESA, 2015). For the study, we used level 2A format from the ESA website, i.e., Copernicus Open Access (ESA, 2020). The image was recorded on March 25th, 2019 with 10 m spatial resolution and in bottom of atmosphere reflectance (BoA) format. A standard radiometric and geometric correction has been applied to the image by the provider (ESA, 2015).

### 3.4. Other data

To compare the results of the method proposed in this study, we used topographic map of Siberut Island, the Indonesian archipelagic baseline, boundaries of territorial sea, contiguous zone, and the economic exclusive zone, Indonesian river data, and the existing basepoints of the surrounding area. Those data were obtained from the Geospatial Information Agency of Indonesia.

### 3.5. SDB model

To perform the SDB model, we used 80% of the SBES measurement data that was randomly selected as the training data. The remaining 20% of the SBES measurement was used for the testing data. For the next step, we applied Random Forest (RF) to derive depth information. We set the two parameters of RF, *mtry* and *ntree* to obtain the best accuracy (Breiman, 2001). The *ntree* values were set from 50–1,000 trees with intervals of 50. Meanwhile, the *mtry* values were tested from 1–10 with intervals of 1.



Furthermore, the validation of the SDB model was conducted by using 5-fold cross validation (H2O, 2021). In fact, for this research, we made experiment by assessing not only RF but also support vector machine (SVM), however, RF outperformed SVM. Therefore, in this study, we applied RF for the extraction of bathymetry from satellite images. For the detail information about RF, readers are suggested to check literatures (Manessa *et al.*, 2016; Sagawa *et al.*, 2019).

### 3.6. The LAT and HAT estimation for datum-based coastlines

T-TIDE package in MATLAB was employed to analyzed the tide gauge data (Pawlowicz, Beardsley and Lentz, 2002). Least squares harmonic analysis was applied by this package to identify the components and predictions of tide by using up to 71 tidal components. In this case, the harmonic analysis application is conducted by fitting the chosen harmonic constituents to the sea level observation. The following equation was used to estimate a tidal function by fitting the sea level observation (Bruce B. Parker, 2007; Siddig, Al-subhi and Alsaafani, 2019):

$$z(t) = z_0 + \sum_{i=1}^m f_i Z_i \cos(\omega_i t + u_i - k_i^*), \quad (1)$$

where:  $t$  is the time in serial hours,  $z(t)$  is a predicted water level at  $t$ ,  $z_0$  is the mean water level,  $f_i$  is a lunar node factor for the  $i^{th}$  constituent,  $Z_i$  is a mean amplitude for the  $i^{th}$  constituent over 18.6-year lunar node cycle,  $\omega_i$  is the frequency of the  $i^{th}$  constituent,  $u_i$  is the nodal phase for the  $i^{th}$  constituent,  $k_i^*$  is the phase of the  $i^{th}$  constituent for the period origin is utilized, and  $m$  is a number of constituents.

Nine-year observation data from 23 February 2011 up to 1 September 2020 were used in this study. The least squares method was applied to fit the trend which represents the general patterns of the time series observation over its period (Siddig, Al-subhi and Alsaafani, 2019). The LAT and HAT were calculated over a minimum period of 19 years which was during a full nodal period using the harmonic constant values derived from nine-year observations (FIG Commission 4 and 5., 2006; Thiébot, Guillou and Droniou, 2020). The LAT is defined as the lowest predicted tide level under average meteorological conditions and under any astronomical conditions. Meanwhile, the HAT is refers to the highest level of water that can be predicted under any combinations of astronomical situation (IHO., 2008; PCTMSL, 2014). For more information on the analysis of harmonic method, readers are suggested to check references (Ko *et al.*, 2018; Siddig, Al-subhi and Alsaafani, 2019).

### 3.7. Integrating elevation and bathymetry extracting coastlines

Gridding method was applied to integrate all various sources of data, including land elevation and bathymetry data so that the seamless digital elevation and bathymetry model could be obtained. Hell and Jakobsson (2011) developed the gridding method based on interpolation with spline tension at several resolutions determined by the source of data density. This method is found to be suitable when integrating various kinds of data for instance low-resolution National Bathymetry Data and high-resolution echo sounding measurements (Becker *et al.*, 2009; Hell and Jakobsson, 2011). In this study, a self-developed FORTRAN-based program based on the method proposed by Hell and Jakobsson (2011) was used to compile and develop the DEBM.

Coastline model can be developed in several ways (Boak and Turner, 2005; Dewi *et al.*, 2018), for example by classifying features on the coast using aerial photographs for instance the position of highest water line (Ford, 2013; NOAA, 2021). The coastline can also be built based on tide-coordinated coastline, for example, by referring to the mean high water line whose information is obtained, for example using LIDAR data or field measurements (Liu, 2008; Kim, Lee and Min, 2017). Furthermore, the coastline can also be generated by classifying beach features using remote sensing images, namely by extracting water and non-water pixels, for example from multispectral, radar and hyperspectral images (Al Fugura, Billa and Pradhan, 2011; Dewi, Bijker and Stein, 2017).



In this study, the second approach was adopted; coastline was extracted from an intersection between a seamless digital elevation and bathymetry model (DEBM) and the water level for i.e., the LAT and HAT as in Oktaviani et al., (2021). After performing gridding method, coastlines were generated by computing the intersection line between the seamless DEBM and water level for i.e., LAT and HAT obtained from the previous step. The concept of coastline developed in this study can be seen in Fig. 3.

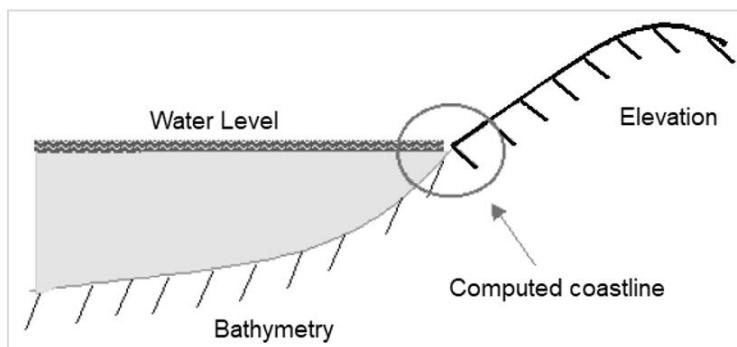


Fig. 2. Coastline estimated from an intersection between seamless digital elevation and bathymetry model and water level (modified from Li, Di and Ma (2004)).

### 3.8. Estimating basepoints, baselines and maritime boundaries

The LAT coastline was used as a reference in determining the basepoint while the HAT coastline was used to identify islands. To determine whether an object is an island, we referred to the definition provided by UNCLOS (United Nations Convention on the Law of the Sea) 1982 convention (United Nation, 1982). The mass of land which is visible during high and low tides is called an island/rock, however, when it is only visible during the low tide, it is called as low tide elevation (LTE). The first term is in line with the definition provided in UNCLOS Article 121 (United Nation, 1982): “An island is a naturally formed area of land, surrounded by water, which is above water at high tide”. The second term is described in Article 13: “A low-tide elevation is a naturally formed area of land which is surrounded by and above water at low tide but submerged at high tide”. Both concepts are visualized in Fig. 4.

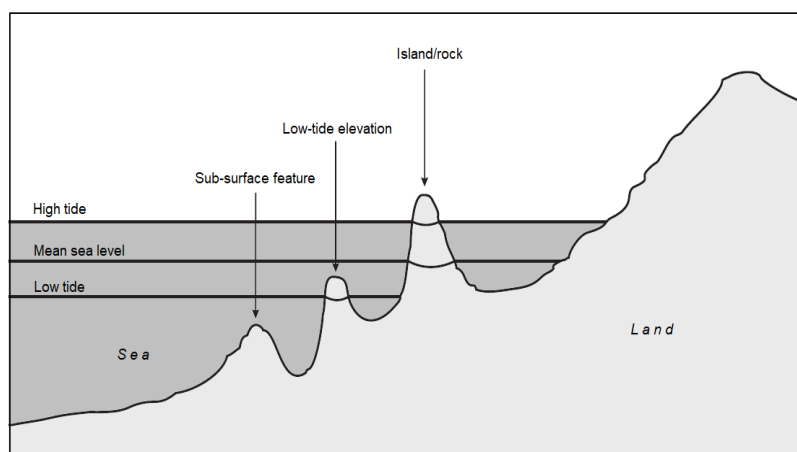
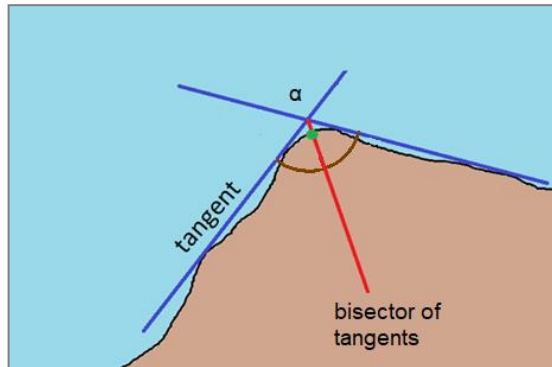


Fig. 3. The concept of island, low-tide elevation and sub-surface feature based on UNCLOS 1982 (modified from Schofield and Arsana (Schofield and Arsana, 2012)).

For this study, a method from Prescott and Schofield (2005) was adopted to estimate the basepoint location. The presence of any possible outermost island was assessed by using the HAT coastline and the position of the headland were assessed as well. In the next step, two straight lines were drawn on the side of the headlands and the angle formed by the intersection of both straight lines were measured. Furthermore, the measured angle was divided in half to create a bisector of tangents as a line that divides the angle equally. The intersection of this bisector of tangents line with the LAT coastline was then considered as basepoints (see **Fig. 5**).



**Fig. 4.** Locating the basepoint (green dot) at the position of the intersection between bisector of tangents line (red line) with the LAT coastline (modified from Prescott and Schofield (Prescott and Schofield, 2005)).

A baseline was created by joining the proposed basepoint resulted from this study with the available basepoints. For this purpose, given the situation of the study area, we generated a normal baseline and straight lines across the mouth of rivers. UNCLOS (United Nation, 1982) defines the normal baseline to measure the breadth of the territorial sea as the low-water line along the coast officially recognized by the government. Whereas, the closing of river mouth is conducted when a river flows directly into the sea. In this situation, we need to develop a straight line across the mouth of the river between points on the low-water line of its banks (United Nation, 1982). In this research, the position on the low-water line refers to the LAT coastline.

Lastly, the maritime boundary was developed by integrating the proposed baseline from this study with the existing archipelagic baselines from nearby basepoints (TD.161 and TD.162 as in **Fig. 1**). We compared the results with the existing baselines which was developed by joining the existing basepoints located at the low water line along the coast. They were determined by direct measurement via hydrographic survey at the nearshore area by the Indonesia Government. From the resulted baseline, we generated the boundary of territorial sea, contiguous zone and the exclusive economic zone. In fact, a state can develop four types of zones, namely: territorial sea, contiguous zone, continental shelf, and exclusive economic zone (Specht, 2019).

## 4. RESULTS

### 4.1. The result of SDB model and the estimation of LAT and HAT coastlines

**Fig. 6a** presents the results of the SDB model while **Fig. 6b** shows false color composite of Sentinel 2A as visual comparison. The estimated depth in the SDB model were from  $>0$  m up to less than 30 m, and the model clearly delineated land area of zero depth around the existing land and shallow water area representing by grey to white pixels in **Fig. 6b**.

The tidal harmonic constituents' analysis results are plotted in **Fig. 7**. The plot of tide gauge data is in blue, the predicted tide level is in orange and the residual of sea level is in red lines. The tidal analysis results show that water level observation fit with the predicted water level by using T-Tide model indicated by a small residual ranging from 20-30 cm.

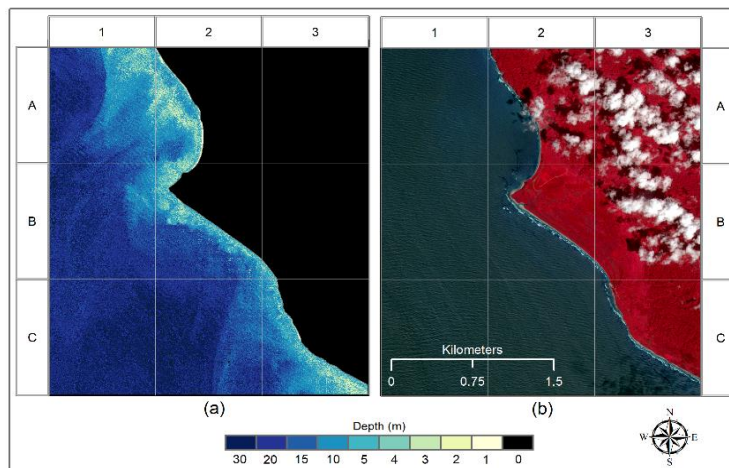


**Fig. 5.** Visualization of depth produced when performing RF in the study area; and (b) false colour composite of Sentinel 2A image (dark blue pixels are water; red pixels are vegetation and grey to white are very shallow water with submergence rocks).

This residual was classified as meteorological residual which is a non-tidal component resulted by removing regular tides in the analysis (Pugh, 1987). The model produced 71 tidal constituents which were further used to predict the water level in Siberut Island for 19 years. From the result in **Fig. 7**, the LAT was 26.77 cm while the HAT was 202.49 cm.

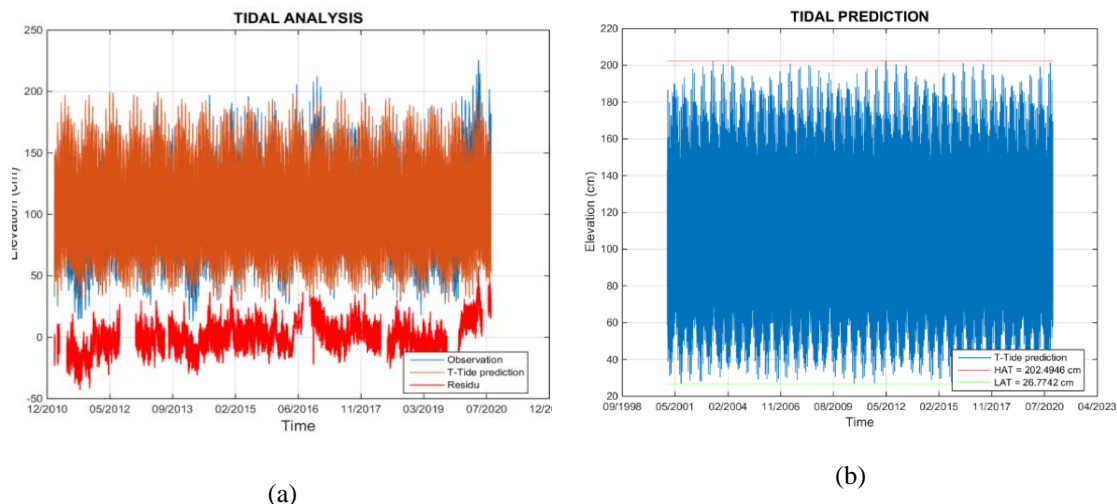


**Fig. 6.** (a) Hourly tide gauge data (blue line), the results of T-Tide prediction (orange line) and the residual of sea level (red line) as the results of tidal analysis; (b) Tidal prediction in blue line and the estimates of LAT (green line) and the HAT in red line. The x-axis is the time of measurement and y-axis is the sea level in cm.

#### 4.2. The result of elevation and bathymetry integration and coastline extraction

Integration results between elevation and bathymetry data using spline interpolation-based method (gridding method) is presented in **Fig. 8a**. Whereas, **Fig. 8b-c** show the visual comparison of the proposed result with other depth data, namely from SDB (**Fig. 8b**) and the national bathymetry data (**Fig. 8c**). The SDB model seems a bit noisy while the national bathymetry data has less detailed information. The integration of elevation and all available bathymetry data was successful in deriving quite detail information and less noisy bathymetry data as in **Fig. 8a**.

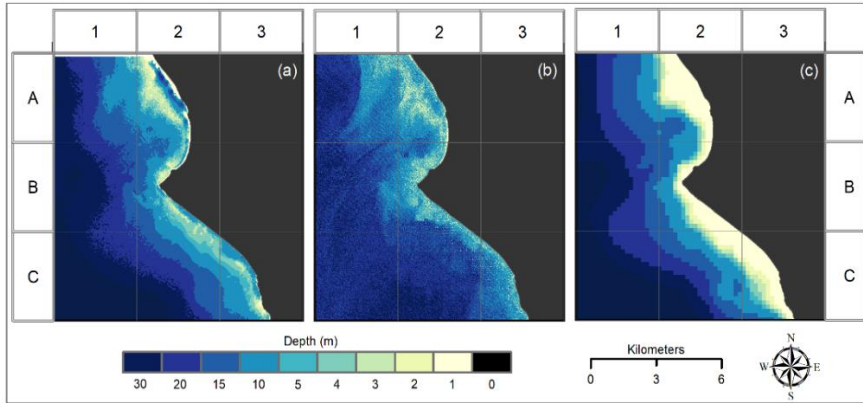


**Fig. 7.** The visualization of depth data comparison provided by (a) gridding method, (b) SDB model, and (c) the national bathymetry data

In the next step, we derived the LAT and HAT coastlines from the resulted bathymetry data. The results are provided in **Fig. 9** showing visual comparisons for coastlines generated by the national bathymetry data (black and magenta lines) and proposed coastlines from gridding method (yellow and toska lines). From the comparison in **Fig. 9**, it was obvious that coastlines resulted from the proposed method presented relatively smooth coastlines which were close to the shape of the land features. Whereas, rough coastlines from the national bathymetry data were due to lack of detailed depth information in shallow waters. In this case, we concluded that in locations where depth points maybe less dense, the resulting coastlines would be shifting. Hence, it was critical to have a dense depth point especially in shallow water to obtain an accurate coastline.

#### 4.3. The proposed basepoints, baselines and maritime boundary

The LAT and HAT coastlines presented in **Fig. 9** were used to update the position of basepoint and baseline in the study area.

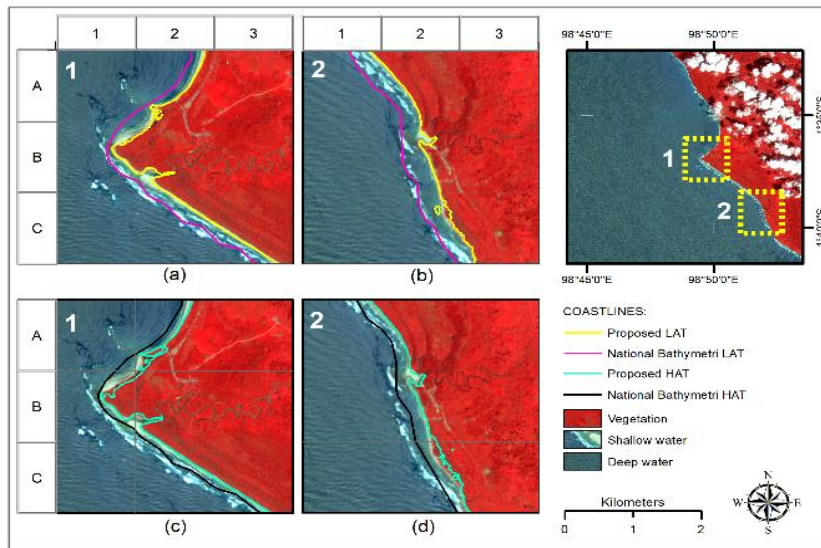


**Fig. 8.** The visualization of LAT (a-b) and HAT (c-d) coastlines. For each coastline type, comparisons are given for coastlines generated by the national bathymetry data (black and magenta lines), and proposed coastlines from gridding method (yellow and toska lines). False colour composite of Sentinel 2A is used as the background.

From visual inspection on the HAT coastline, we confirmed that there was no small island which was identify near the TD.161B. Therefore, we concluded that the baseline was still located at the Siberut Island. Meanwhile, by using the LAT coastline, we assessed the position of the new basepoint located in Cape Simansih approximately 171.58 m to the north of the existing point i.e. TD.161B (as in **Fig. 10b**).

After updating the basepoint, we obtained a new normal baseline (see red line in **Fig. 10a**). From the LAT coastlines, three rivers located nearby TD.161B were closed by straight lines across the mouth of the rivers (see **Fig. 10 c-e**). In this case, we proposed a new baseline position produced by integrating a normal baseline and straight lines across the mouth of rivers. **Fig. 10 a-b** show a visual comparison between the existing baseline and the new baseline resulted from the proposed method.

From the results, we can see that the proposed baseline was more accurate indicated by its position that was closely linked to the land. Finally, we updated the archipelagic baseline by connecting the updated TD.161B with the existing TD nearby namely: TD.161 and TD.162. Consequently, we updated new positions of Indonesia maritime boundary consisting of the boundaries of territorial, contiguous, and exclusive economic zones as in **Fig. 11a**. **Fig. 11b-d** present visual comparisons between the existing Indonesia maritime boundaries and the updated boundaries.

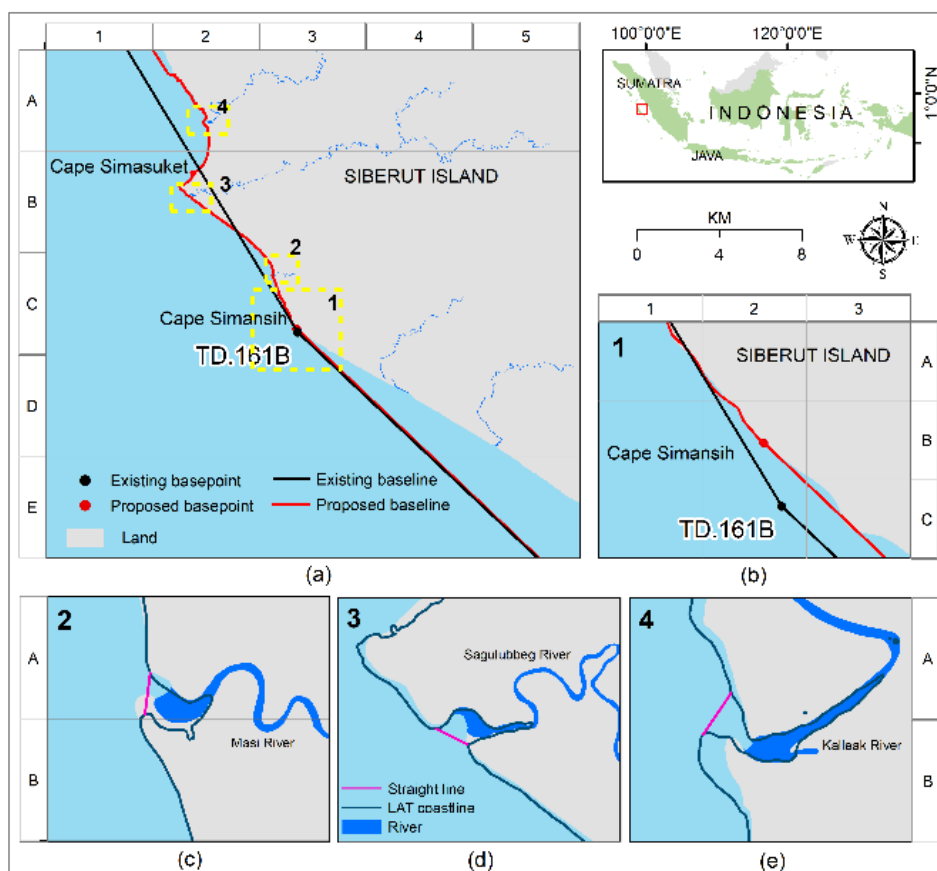


**Fig. 9.** (a) The visualization comparison of the existing basepoint TD161B (black dot) and the proposed basepoint (red dot) and zoom in to the location of TD.161B in Cape Simansih. (b) Magenta lines present straight lines develop to close mouth of rivers between points on the low-water line (the LAT coastlines in dark blue lines) of three rivers: (c) Masi River, (d) Sagulubbeg River, and (c) Kalleak River.

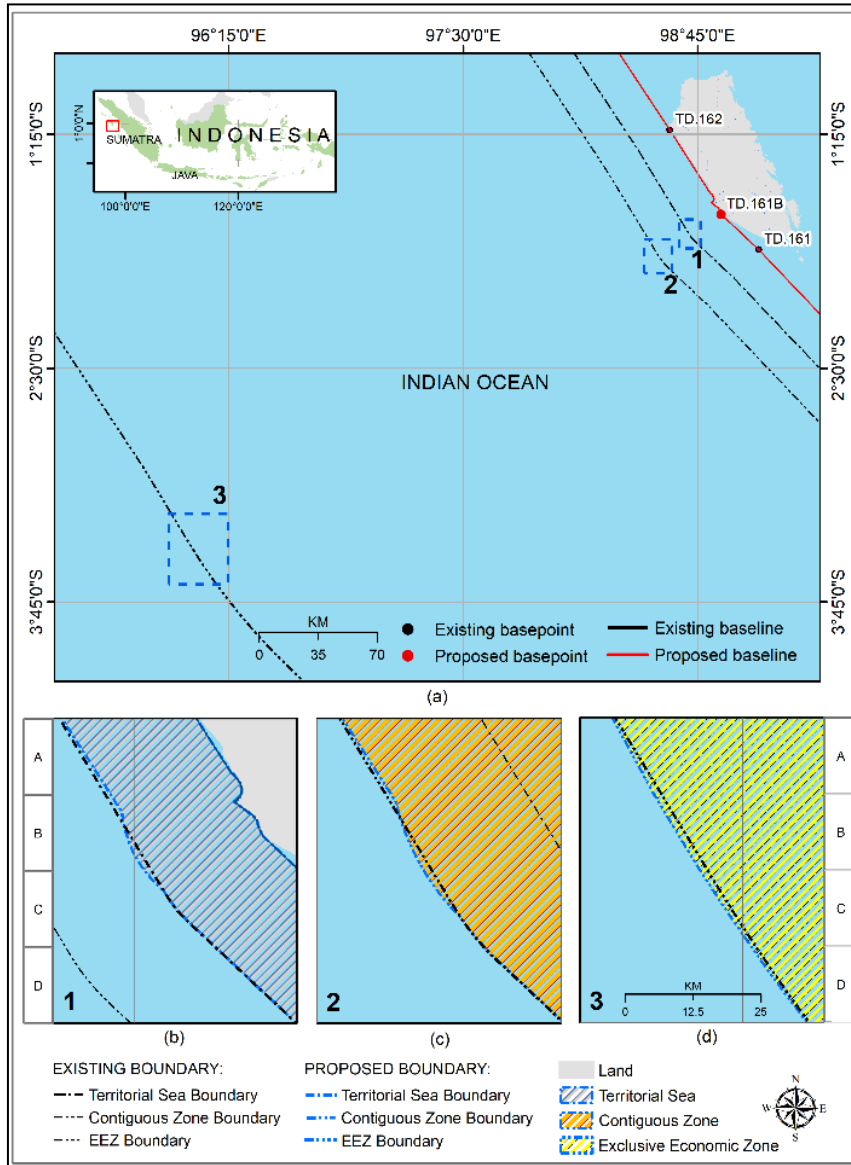


**Fig. 10.** (a) The visual comparison of the existing Indonesian maritime boundaries and the proposed boundaries and area for (b) territorial sea, (c) contiguous zone, (d) exclusive economic zone.

## 5. DISCUSSION

In this paper, we proposed an alternative method in determining position of basepoints and baselines in order to support the negotiations of Indonesia maritime boundaries. The proposed method was successful in updating the position of a basepoint and baseline in the study area by incorporating and integrating multisource of bathymetry data.

When performing the empirical SDB model to obtain bathymetry data, it was important to have a large amount of training data that represent variability of depth in related location (Geyman and Maloof, 2019; Sagawa *et al.*, 2019). The study area was characterized by high waves and strong winds making it difficult for surveyors to have an access and to conduct echo-sounding measurement.



Finding other alternatives to obtain training data is an opportunity for future research for example by using unmanned surface vehicles (Suhari *et al.*, 2017). However, high waves and winds at this area may hamper the implementation of such technology.

For this research, tide model was developed by using nine-year observations data producing 71 tidal components and the LAT and HAT were estimated over 19 years period. Parker (2007) stated that an accurate tide prediction is determined by the amplitude and epochs for the tidal components that can be calculated with a given length data time series. It implies that the longer the time series, the closer in frequency two tidal components can be solved for.

The LAT and HAT coastline can be calculated over a minimum period of 19 years using harmonic constants that are derived from the minimum of a one year observation (Ko *et al.*, 2018). However, the longer the observations, the smaller the standard deviation of each component and the better the prediction will be (Bruce B. Parker, 2007; Supriyono *et al.*, 2015).

We integrated bathymetry data by using gridding method. In this case, lower resolution of the national bathymetry data was stacked with a middle resolution of SDB model and a higher resolution of echo-sounding measurement points. The challenging part was in carrying out the stacking process involving various resolutions and in the same time suppressing gridding artifacts. Spline interpolation approach by adjusting an individual tension for each grid resolution was successful in maintaining small details in the bathymetry data and suppressing the artefacts caused by higher resolution data (Hell and Jakobsson, 2011). However, it required higher computational requirements.

The determination of basepoint and baseline positions was influenced by the presence of land features that may be identified during coastline extractions specifically when deriving the HAT coastline. In this case, the UNCLOS (United Nation, 1982) defined island as the naturally formed area of land which is above water during the high tide. Hence, it is important to define such features when generating the coastline since the presence of the island would determine how the basepoint and baseline would be developed.

## 6. CONCLUSIONS

This study presents an alternative method to determine the position of basepoints and baselines of the Indonesia maritime boundary which can also be applied to any other archipelagic countries. The use of remote sensing data and techniques was successful to overcome the problem of data limitation in the study area, especially ground survey data. In addition, the proposed method could be used to detect low tide elevation (LTE). In fact, an archipelagic countries are not able to use LTE as a basepoint, unless there is a permanent building on that certain location. However, the detected LTE information can be used to assist the planning of permanent buildings in the area.

Some challenges for the improvement of the method includes: a) to search for other alternative in obtaining training data when applying SDB model; and b) multitemporal observation maybe needed since the positions of these basepoint and baseline may vary in time. The method proposed in this study can be easily be adopted to any other locations. However, the procedures would be determined by the availability of data in the related locations.

The proposed basepoint obtained from this research is expected to be used as an input to update the existing basepoint. Furthermore, the proposed method from this research is also expected to be used as a basis to refine the whole existing baselines in Indonesia (as in Government Regulation ref. no. 38 of 2002 (Indonesian Government., 2002) and Government Regulation ref. no. 37 of 2008 (Indonesian Government., 2008)) so that an optimal configuration of the maritime boundaries can be obtained. Changes in the position of basepoints and baselines would certainly not change the previously agreed maritime boundary agreement as has been mentioned in the Vienna Convention Article 62 regarding *Fundamental change of circumstances* (United Nations, 1969) and the UNCLOS Article 51 (United Nation, 1982): "...an archipelagic State shall respect existing agreements with other States". Finally, in delimiting maritime boundaries with neighbouring countries, accurate basepoints and baselines are decisive factors to obtain an optimum maritime zone which provide a proportionate and equitable solution to both parties.

## ACKNOWLEDGMENTS

We would like to thank our colleagues from the Center for Marine and Coastal Environment Mapping and the Center for Geodesy and Geodynamic Control Network of the Indonesia Geospatial Information Agency for providing data, related documents, insight and expert inputs that greatly assisted this research.

## REFERENCES

- Arsana, I. M. A., Rizos, C. and Schofield, C. (2006) 'The Application of GIS in Maritime Boundary Delimitation A case study on the Indonesia-East Timor Maritime Boundary', in Abdul-Rahman, A., Zlatanova, S., and Coors, V. (eds) *Innovations in 3D Geo Information Systems*. Springer, Berlin, Heidelberg, pp. 695–719. doi: 10.1007/978-3-540-36998-1.
- Becker, J. J. *et al.* (2009) 'Global Bathymetry and Elevation Data at 30 Arc Seconds Resolution: SRTM30\_PLUS', *Marine Geodesy*, 32(4), pp. 355–371. doi: 10.1080/01490410903297766.
- Boak, E. H. and Turner, I. L. (2005) 'Shoreline Definition and Detection: A Review', *Journal of Coastal Research*, 214(1), pp. 688–703. doi: 10.2112/03-0071.1.
- Breiman, L. (2001) 'Random Forests', *Machine Learning*, 45(1), pp. 5–32. doi: 10.1023/A:1010933404324.
- Bruce B. Parker, P. D. (2007) *Tidal Analysis and Prediction, Sea-Level Science*. NOAA Special Publication NOS CO-OPS 3. doi: 10.1017/cbo9781139235778.007.
- Dewi, A., Sugianto, D. N. and Diponegoro, U. (2018) 'Analysis of Wave Deformation on Siberut Island, Mentawai Islands Regency, West Sumatra', *Journal of Oceanography*, 6(2), pp. 330–340.
- Dewi, R. S. *et al.* (2018) 'Transferability and upscaling of fuzzy classification for shoreline change over 30 years', *Remote Sensing*, 10(9). doi: 10.3390/rs10091377.
- Dewi, R. S., Bijker, W. and Stein, A. (2017) 'Comparing fuzzy sets and random sets to model the uncertainty of fuzzy shorelines', *Remote Sensing*. doi: 10.3390/rs9090885.
- ESA (2015) 'SENTINEL-2 User Handbook', *Sentinel-2 User Handbook*.
- ESA (2020) *Copernicus Open Access Hub*. Available at: <https://scihub.copernicus.eu/dhus/#/home>.
- FIG Commission 4 and 5. (2006) *FIG Guide on the Development of a Vertical Reference Surface for Hydrography, International Federation of Surveyors Publication*. Copenhagen. Available at: <http://www.fig.net/pub/figpub/pub37/pub37.pdf>.
- Ford, M. (2013) 'Shoreline changes interpreted from multi-temporal aerial photographs and high resolution satellite images: Wotje Atoll, Marshall Islands', *Remote Sensing of Environment*. doi: 10.1016/j.rse.2013.03.027.
- Al Fugura, A., Billa, L. and Pradhan, B. (2011) 'Semi-automated procedures for shoreline extraction using single RADARSAT-1 SAR image', *Estuarine, Coastal and Shelf Science*. doi: 10.1016/j.ecss.2011.10.009.
- Geospatial Information Agency. (2011) *Geospatial Information Law 04/2011*. Indonesia.
- Geospatial Information Agency. (2018a) *Daftar Stasiun (Tide Gauge Station)*. Available at: <http://ina-sealevelmonitoring.big.go.id/ipasut/data/station> (Accessed: 1 February 2020).
- Geospatial Information Agency. (2018b) *DEMNAS: Seamless Digital Elevation Model (DEM) dan Batimetri Nasional*. Available at: <https://tanahair.indonesia.go.id/demnas/#/>.
- Geyman, E. C. and Maloof, A. C. (2019) 'A Simple Method for Extracting Water Depth From Multispectral Satellite Imagery in Regions of Variable Bottom Type', *Earth and Space Science*. doi: 10.1029/2018EA000539.
- H2O (2021) *Cross Validation*. Available at: <https://docs.h2o.ai/h2o/latest-stable/h2o-docs/cross-validation.html> (Accessed: 2 June 2021).
- Hell, B. and Jakobsson, M. (2011) 'Gridding heterogeneous bathymetric data sets with stacked continuous curvature splines in tension', *Marine Geophysical Research*, 32(4), pp. 493–501. doi: 10.1007/s11001-011-9141-1.



- IHO. (2008) 'IHO Standards for Hydrographic Surveys (S-44) 5th Edition'.
- Indonesian Government. (2002) *Government Regulation 38/2002: List of Geographical Coordinates of the Points of the Base Line of the Indonesian Archipelago*. Indonesia.
- Indonesian Government. (2008) *Government Regulation 37/2008: Amendment to Government Regulation Number 38 of 2002 Concerning List of Geographic Coordinates of the Points of the Baseline Line of Indonesian Islands*. Indonesia.
- Julzarika, A. *et al.* (2021) 'Integration of the Latest Digital Terrain Model (DTM) with Synthetic Aperture Radar (SAR) Bathymetry', *J. Degrade. Min. Land Manage*, 8(3), pp. 2759–2777. doi: 10.15243/jdmlm.
- Karim, S. (2011) 'Geography of West Sumatra and Earthquake Natural Disaster'. Jurusan GeograJi Fakultas Ilmu Sosial Universitas Negeri Padang. Available at: [http://repository.unp.ac.id/17760/1/SUTARMAN\\_KARIM\\_68\\_11.pdf](http://repository.unp.ac.id/17760/1/SUTARMAN_KARIM_68_11.pdf).
- Kim, H., Lee, S. B. and Min, K. S. (2017) 'Shoreline change analysis using airborne LiDAR bathymetry for coastal monitoring BT - 2nd International Water Safety Symposium, IWSS 2016, June 22, 2016 - June 24, 2016', 33(Special Issue 79), pp. 269–273. doi: 10.2112/SI79-055.1.
- Ko, D. H. *et al.* (2018) 'Analysis on the estimation errors of the lowest and highest astronomical tides for the southwestern 2.5 GW offshore wind farm, Korea', *International Journal of Naval Architecture and Ocean Engineering*, 10(1), pp. 85–94. doi: 10.1016/j.ijnaoe.2017.03.004.
- Li, R., Di, K. and Ma, R. (2004) 'A comparative study of shoreline mapping techniques', in *GIS for Coastal Zone Management*. doi: 10.1201/9781420023428.ch3.
- Liu, H. (2008) 'Shoreline Mapping and Coastal Change Studies Using Remote Sensing Imagery and LIDAR Data', in *Remote Sensing and Geospatial Technologies for Coastal Ecosystem Assessment and Management*. doi: 10.1007/978-3-540-88183-4\_13.
- Manessa, M. D. M. *et al.* (2016) 'Satellite-Derived Bathymetry using Random Forest Algorithm and Worldview-2 Imagery', *Geoplanning: Journal of Geomatics and Planning: Vol 3, No 2 (2016): (October 2016)DO - 10.14710/geoplanning.3.2.117-126*. Available at: <https://ejournal.undip.ac.id/index.php/geoplanning/article/view/12047>.
- Mustafa, B. (2010) 'Analysis of the Nias earthquake and the West Sumatra earthquake and their similarities that do not cause a tsunami', *JURNAL ILMU FISIKA*, 2(1), pp. 44–50.
- NOAA (2021) *Mapping and Charting*. Available at: <https://tidesandcurrents.noaa.gov/mapping.html> (Accessed: 28 February 2021).
- Oktaviani, N. *et al.* (2021) 'Pemodelan Garis Pantai Menggunakan Metode Interpolasi Stacked Curve Spline Pemodelan Garis Pantai Menggunakan Metode Interpolasi Stacked Curve Spline Tension', (August). doi: 10.14710/teknik.
- Pawlowicz, R., Beardsley, B. and Lentz, S. (2002) 'Classical tidal harmonic analysis including error estimates in MATLAB using TDE', *Computers and Geosciences*, 28(8), pp. 929–937. doi: 10.1016/S0098-3004(02)00013-4.
- PCTMSL (2014) *Australian Tides Manual Special Publication No. 9*.
- Presscott, V. and Schofield, C. (2005) *The Maritime Political Boundary of the World*. Second Edi. Boston: Martinus Nijhoff Publishers.
- Pugh, D. T. (1987) *Tides, Surges and Mean Sea-Level*. Chichester, UK: John Wiley & Sons.
- Sagawa, T. *et al.* (2019) 'Satellite derived bathymetry using machine learning and multi-temporal satellite images', *Remote Sensing*. doi: 10.3390/rs11101155.
- Schofield, C. and Arsana, A. (2012) 'Climate change and the limits of maritime jurisdiction', in Warner, R. and Schofield, C. (eds) *Climate Change and the Oceans*. Massachusetts: Edward Elgar Publishing Limited, pp. 127–152.
- Siddig, N. A., Al-subhi, A. M. and Alsaafani, M. A. (2019) 'Tide and mean sea level trend in the west coast of the Arabian Gulf from tide gauges and multi-missions satellite altimeter', *Oceanologia*, 61(4), pp. 401–411. doi: 10.1016/j.oceano.2019.05.003.

- Sinclair, M. J., Stephenson, D. J. and Barker, R. M. (2003) 'Alaska Peninsula deployment of laser airborne bathymetric system', *Oceans Conference Record (IEEE)*, 2, pp. 770–779. doi: 10.1109/oceans.2003.178412.
- Specht, C. *et al.* (2017) 'Determination of the Territorial Sea Baseline - Measurement Aspect', *IOP Conference Series: Earth and Environmental Science*, 95(3). doi: 10.1088/1755-1315/95/3/032011.
- Specht, M., Specht, C., Waz, M., Dabrowski, P., *et al.* (2019) 'Determining the variability of the territorial sea baseline on the example of waterbody adjacent to the municipal Beach in Gdynia', *Applied Sciences (Switzerland)*, 9(18). doi: 10.3390/app9183867.
- Specht, M., Specht, C., Waz, M., Naus, K., *et al.* (2019) 'Methodology for performing territorial sea baseline measurements in selected waterbodies of Poland', *Applied Sciences (Switzerland)*, 9(15). doi: 10.3390/app9153053.
- Suhari, K. T. *et al.* (2017) 'Small ROV Marine Boat for Bathymetry Surveys of Shallow Waters – Potential Implementation in Malaysia', in *The International Archives of the Photogrammetry, Remote Sensing and Spatial Information Sciences*, pp. 201–208. doi: 10.5194/isprs-archives-XLII-4-W5-201-2017.
- Suparno. (2006) 'Surfing Tourism as the Prima Dona of Marine Environmental Services in the Mentawai Islands Regency, West Sumatra', *Jurnal Mangrove dan Pesisir*, VI(3), pp. 32–39.
- Supriyono *et al.* (2015) 'Tide Prediction Analysis and Calculation using Admiralty Method and Least Square Method (Case Study of Tarakan and Balikpapan Waters)', *Chart Datum*, 01 No.01, pp. 8–18.
- Thiébot, J., Guillou, S. and Droniou, E. (2020) 'Influence of the 18.6-year lunar nodal cycle on the tidal resource of the Alderney Race, France', *Applied Ocean Research*, 97(102107). doi: 10.1016/j.apor.2020.102107.
- United Nation (1982) *UNCLOS 1982, United Nation*. doi: 10.1080/00908329509546068.
- United Nations (1969) *Vienna Convention on the law of treaties, Treaty Series*. United Nations. doi: 10.4337/9781781006047.00014.

## FACTORS INFLUENCING SOIL BEHAVIOR AND PROPERTIES OF MASS MOVEMENTS IN THE BLIMBING AREA, BRUNO DISTRICT, PURWOREJO REGENCY, CENTRAL JAVA, INDONESIA

Sari Bahagiarti KUSUMAYUDHA<sup>1</sup> , Riskhy JUMADIL AKHIR<sup>1</sup> and PURWANTO<sup>1</sup>

DOI: 10.21163/GT\_2022.171.03

### ABSTRACT:

The Blimbing area, Bruno district of Purworejo Regency, Central Java, belongs to a susceptible area for mass movement. Its geomorphology expresses homoclinic hills, undulating plains, and denudated volcanic hills. The lithology is composed of sandstone of the Halang Formation and andesite breccia of the Peniron Formation. A study was conducted that aimed to examine the factors influencing soil behavior and mass movements in this area by applying an analytical descriptive method along with a field survey and surface mapping. There were eight slopes, namely Slope 1 to Slope 8, being examined and analysed. Slope 1 and Slope 5 are composed of high-plastic clay with very expansive properties. Slope 2 is occupied by high-plastic silt with slightly expansive properties. Slope 3, Slope 4, Slope 6, and Slope 7 comprise high-plastic silt with slightly expansive to very expansive properties, while Slope 8 is built of highly fractured rock, with a joint density of 0.36 m. Using the simplified Bishop method, it can be determined that Slope 1 to Slope 7 have safety factor values of 1.095, 1.369, 1.262, 1.128, 1.605, 1.095, and 0.961, respectively. Slope 8 has a rock mass rating (RMR) value of 38, which belongs to class IV (poor rock). It has the potential for wedge and toppling failures. Results of this study indicate that the existence of water in the slopes increases the load on the slopes by 15%, decreasing the cohesion force and reducing the friction angle values, especially when the water content is more than 70%. The type of soil is in the form of high-plastic clay and high-plastic silt that is slightly expansive to very expansive, with low permeability. Thus, water content and the very expansive soil are the main influencing factors for mass movements in the study area.

**Key-words:** Soil behaviour, Expansive clay, Poor rock, Water content, Mass movement.

## 1. INTRODUCTION

Soil/rock mass movements often occur in the Blimbing area and its surroundings in Bruno District, Purworejo Regency, Central Java, especially during the rainy season. The last landslide, which occurred in Tegalsari Village, resulted in 2 houses collapsing, 1 mosque, and 11 other houses threatened to move, with a total loss of more than 100 million rupiahs (BPS, 2021, Imam, 2021). The second rank of the landslide-prone areas in the Central Java province is the Purworejo Regency. It has an Indonesia Disaster Risk Index (IRBI) of 18<sup>th</sup> out of 496 regencies and cities in Indonesia that are classified into a high-risk category (Wicaksono, 2020, BPS, 2021).

The study area belongs to an area with an average heavy rainfall of more than 2000 mm/year (BMKG, 2021). Therefore, in order to identify and understand the factors influencing mass movement in the research area, it is necessary to study its soil behavior and characteristics so that the occurrence of mass movement can be anticipated, a countermeasure can be planned, and a mitigation model can be designed.

---

<sup>1</sup>Geological Engineering Department, Universitas Pembangunan Nasional Veteran Yogyakarta

\* Corresponding author: [saribk@upnyk.ac.id](mailto:saribk@upnyk.ac.id); [riskhyjumadil@upnyk.ac.id](mailto:riskhyjumadil@upnyk.ac.id); [purwanto\\_geotek@upnyk.ac.id](mailto:purwanto_geotek@upnyk.ac.id)

The research location is administratively situated in the Bruno district, Purworejo regency, Central Java province. Astronomically, it is positioned at the coordinates of  $X = 382000 \text{ mE} - 388000 \text{ mE}$  and  $Y = 91600000 \text{ mN} - 9168000 \text{ mN}$  (Universal Transverse Mercator, World Geodetic System 1984 in zone 49S), (**Fig. 1**). This research aims to examine the factors that influence soil behavior of mass movements in the study area.

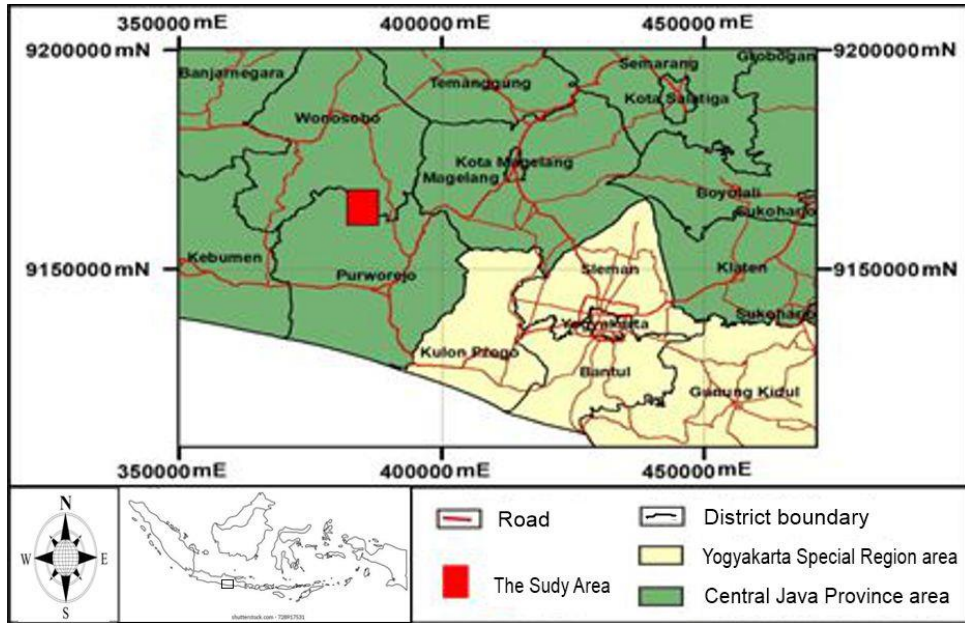


**Fig. 1.** Location map of the study area  
([www.mapsofworld.com/indonesia/provinces/jawa-tengah.html](http://www.mapsofworld.com/indonesia/provinces/jawa-tengah.html)).

## 2. METHOD OF STUDY AND DATA

This research applied an analytical-descriptive method with a field survey and surface mapping. Some undisturbed soil samples and rock samples were taken for laboratory testing and analysis. Sample testing and assessment in the laboratory included petrographic description; compressive strength tests for undisturbed soil samples, disturbed soil samples, rock samples, and unconfined compressive strength tests using the American Society for Testing and Material (ASTM D-2938-95) for rock mass rating (RMR). Determination of soil physical properties includes unit weight (ASTM D-2937), soil density (ASTM D-654-9), water content (ASTM D-2216-982), Atterberg limit (ASTM D-4318-89), permeability measurement (ASTM D-2434), soil shear strength analysis (ASTM D-3080-72), and sieve analysis (ASTM C-136-06) for classifying the soil types.

The Simplified Bishop method was used in determining the safety factor of the slope formed by soil, with the assumption that the sliding plane is circular in form and the movement is rotational (Kusumayudha & Ciptahening, 2016, Kusumayudha, et al., 2020). In order to determine the type of soil mass movement, Varnes classification is used (Varnes, 1978). The RMR (rock mass rating) method is used to analyse slopes composed of rocks (Bieniawski, 1989), as well as the Markland Method (Citrabhuwana et al., 2016). The Simplified Bishop Method uses Limit Equilibrium and utilizes a sectional approach where the forces acting on each slice are shown as in **Fig. 2** (Rajagukguk et al., 2014). In the RMR assessment, **Table 1** and **Table 2** were used (Bieniawski, 1989).

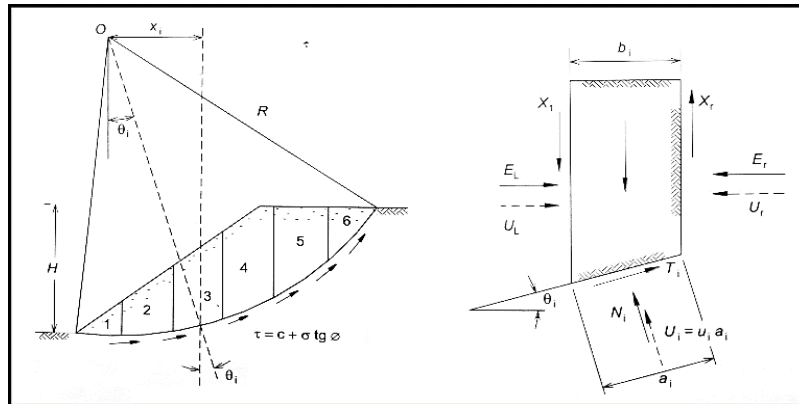


Fig. 2. Stress distribution in sliced soil slope (Rajagukguk, et.al., 2014).

Table 1.

Parameters and range of values of Rock Mass Rating (RMR), (Bieniawski, 1989).

Parameter	Range of Values								
Compressive strength (Mpa)	Values	>250	100-250	50-100	25-50	10-25	3-10	<3	
	Rating	15	12	7	4	2	1	0	
RQD (%)	Values	90 – 100	75 – 90	50 – 75	25 – 50	<25			
	Rating	20	17	13	8	3			
Joint Dencity	Values	>2	0.6 – 2	0.2 – 0.6	0.06 – 0.2	<0.006			
	Rating	20	15	10	8	5			
Joint Condition	Values	Very rough surfaces	Slightly rough surfaces	Slightly rough surfaces	Slicksided surfaces or Gouge <5 mm thick, or	Soft gough >5 mm thick, or			
		Not continuous	Separation <1 mm	Separation <1 mm	Separation 1 – 5 mm	Separation > 5 mm			
		No separation	Slightly weathered wall rock	Highly weathered walls	Continuous				
		Rating	30	25	20	10	0		
		Values	Completely dry	Damp	Wet	Dripping	Flowing		
		Rating	15	10	7	4	0		

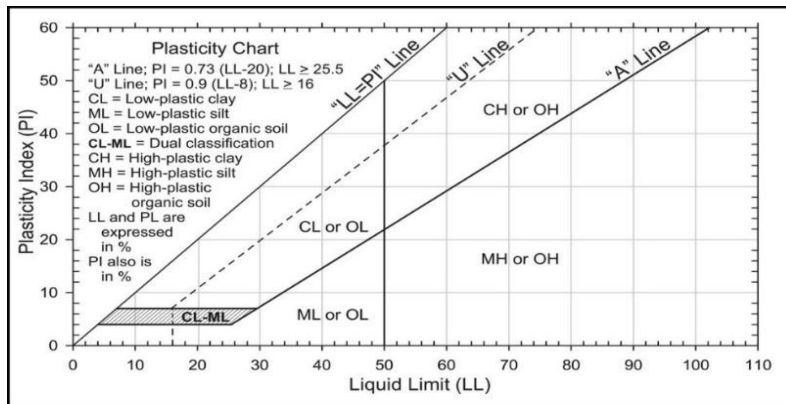
In determining the plasticity index (PI) of soil, the interpretation of the plastic and liquid limits is carried out using the Casagrande diagram (Fig. 3). To classify the soil type, it uses the American Association of State Highway and Transportation Officials (AASHTO) naming system (Hardiyatmo, 2014). Expansive properties, expansive soils, and swelling potentials are used to indicate soils that are prone to shrinkage and contain a lot of clay, especially the mineral of montmorillonite (Hardiyatmo, 2014). Based on their expansive properties, there are three groups of clay minerals (Nelson & Miller, 1991), namely kaolinite, non-expansive, mica-like, for example, illite and vermiculite, which can be expansive, and mildly developed illite, the smactite group, including montmotillonite, which is highly expandable or expansive (Duncan & Fasce, 1995).

Table 2.

Geomechanical classification of rock masses (Bieniawski, 1989).

Class	Description of Rock Mass	RMR (Sum of Rating Increments)
I	Very Good Rock	81 – 100
II	Good Rock	61 – 80
III	Fair Rock	41 – 60
IV	Poor Rock	21 - 40
V	Very Poor Rock	>20

The relationship between the degree of soil expansion and the plasticity index according to ASTM D-1883 is shown in **Table 3**. This table describes the association between the value of plasticity index, the degree of swelling of the soil when it contains water, and the percentage of its expansion. For example, if the plasticity index value of the soil is 0 to 10, the soil will be categorized as unexpansive, because the percentage of expansion is less than 2%. On the other hand, when the plasticity index value is greater than 20, then the soil is said to be very expansive or highly swelled, with a percentage expansion of more than 4%. Meanwhile, the relationship between the potency of clay expansion and the plasticity index (PI) is laid out in **Table 4** (Chen (1975).



**Fig. 3.** Casagrande Diagram (ASTM D-2487).

**Table 3.** Degree and % of the expansive due to the plasticity index (PI) (ASTM D-1883, vide Hardiyatmo, 2014).

Plasticity Index (ASTM D-424)	Degree of Expansive	Percent of expansive (ASTM D-1883)
0 – 10	Unexpansive	2% or less
10 - 20	Rather Expansive	2% - 4%
> 20	Very Expansive	>4%

**Table 4.** Relationship of the expansive potency and plasticity index (PI) (Chen, 1975).

Plasticity Index (PI)	Expansive Potency
> 35	Very High
20 – 55	High
10 – 35	Moderate
0 – 15	Low

### 3. RESULTS AND DISCUSSIONS

#### 3.1. Geomorphology and Geology

The Blimbing and surrounding area are included in the South Serayu Mountains (Van Bemmelen, 1949), a geoanticlinic ridge stretching from the west to the east for 100 km (**Fig. 4**). Using Van Zuidam's classification (1984), the geomorphology of the study area can be divided into homoclinic hills, undulating plains, and denuded volcanic hills. The homoclinic hills are in the middle part, occupying 12.80% of the study area, with slopes of 7%–140% (4°–55°) very steep. The lowest elevation is 200 m asl and the highest is 500 m asl. The undulating plain occupies 63.05% of the study area, with slopes of 2%–140% (2°–55°), very sloping–very steep. The lowest elevation is 187 m asl, and the highest is 597 m asl. The denudated volcanic hills are located in the southeast, occupying 21.8% of the study area, with slopes of 15%–140% (8°–55°), moderate to very steep.



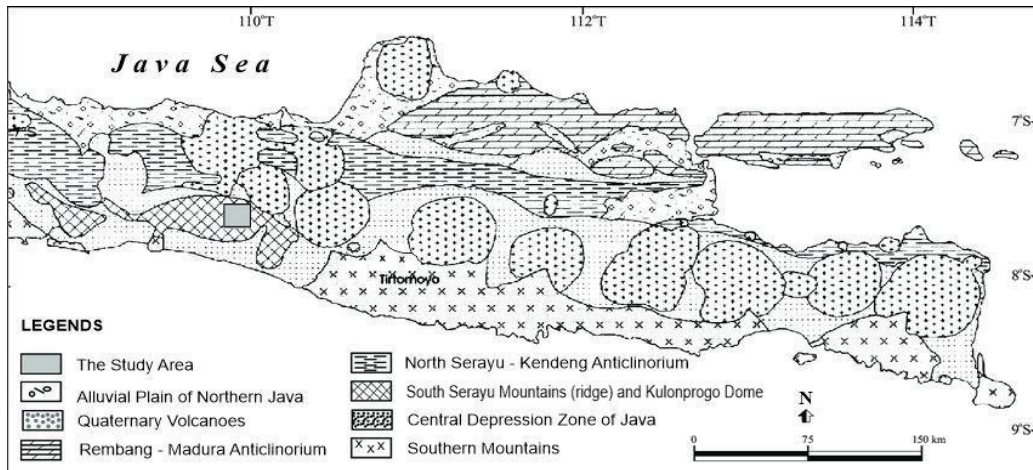


**Fig. 4.** The physiographic map of the Central - Eastern Java, and the study area belongs to the South Serayu Mountains (Van Bemmelen, 1949).

In the study area, there are two main rivers, namely Kali Jali and Kali Gowong, with relatively lateral erosion processes, so that the cross section of the rivers shows a "U" shape. Stratigraphically, the study area consists of alternating sandstones with claystones of the Halang Formation and volcanic andesite breccias of the Peniron Formation, in a conformable stratigraphical relationship (**Fig. 5**).

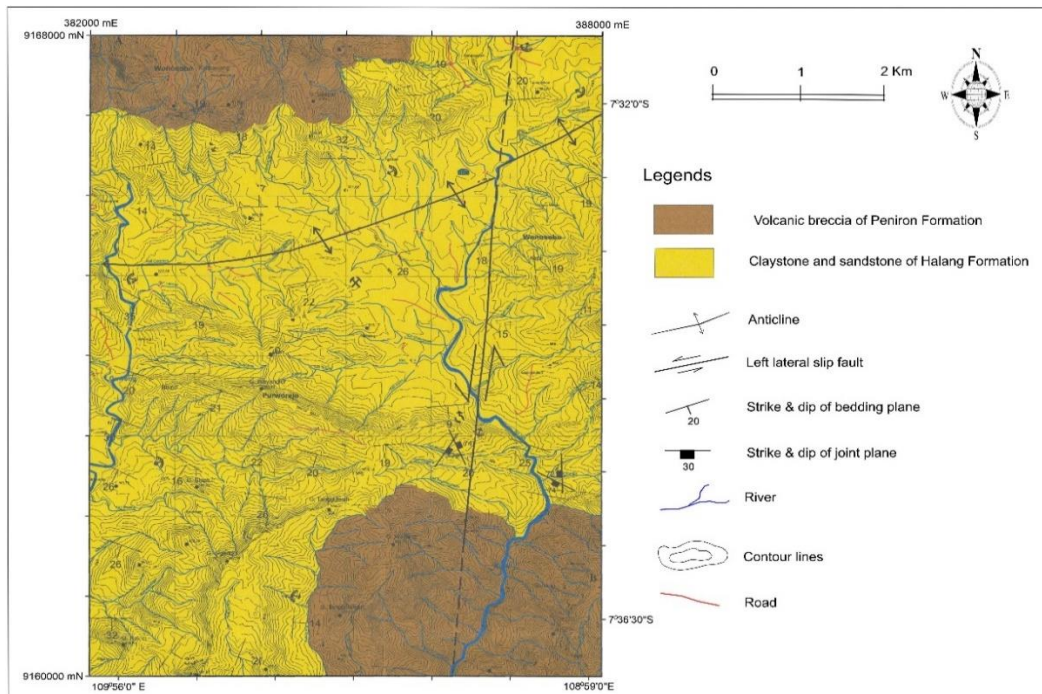


**Fig. 5.** Geological map of the study area.

The Halang Formation occupies 75.84% of the total study area, consisting of sandstone, claystone, carbonate sandstone, carbonate claystone, and polymixed breccia. The formation is late Miocene to early Pliocene epoch. The Peniron Formation consists of breccias with andesite fragments from the Pliocene epoch, which occupies the northwest and southeast areas of the study area.

There is a normal left-slip fault in the study area called the Blimbing Fault (**Fig. 5**). The fault plane is striking N6°E and dipping 70°, with a plunge of 5°, a bearing of 11°, and a rake of 32°. The general pattern of the shear joint is N118°E/72° and N173°E/74, while the distribution of principal stress is 1 = 0°, N318°E, 2 = 70°, N228°E, and 3 = 19°, N48°E.

### 3.2. Mass Movements

Mass movements in the study area can mostly be classified as landslides. Although most of the mass movements in the study area involve weathered soil, in some locations the slopes are composed of rock, and they also often have the potential to fail. In this study, seven representative slopes comprising soil, coded as LR1, LR2, LR3, LR4, LR5, LR6, LR7 (**Fig. 6 to Fig. 9**), and one slope consisting of rock (LR8), were analysed. The selection of the studied slopes is based on their potential threat to settlements and/or public roads if they move.



**Fig. 6.** Slope 1 (LR 1), left, and Slope 2 (LR 2), right.



**Fig. 7.** Slope 3 (LR 3), left, and Slope 4 (LR 4), right.



**Fig. 8.** Slope 5 (LR 5), left, and Slope 6 (LR 6), right.



**Fig. 9.** Slope 7 (LR 7), and the direction of movement (blue arrow).



Soil and rock samples for laboratory testing were also taken from those slopes. The results of soil physical properties testing are listed in **Table 5**.

**Table 5.**

**Physical properties of the soil composing Slope 1 (LR1) to Slope 7 (LR7), and the rock of Slope 8 (LR8).**

LR	Unit Weight (kg/m <sup>3</sup> )	Dry unit Weight (kg/m <sup>3</sup> )	Specific Gravity (gr/cm <sup>3</sup> )	Water Content (%)	Permeability (cm/s)	Atterberg Limit			Shear Strength	
						LL	PI	PI	C (kN/m <sup>2</sup> )	Φ (°)
1	1655.8	1113.1	2.43	46.35	5.5x10 <sup>-5</sup>	59	30	29	25	20
2	1301.5	663.45	2.21	822.04	7.63x10 <sup>-4</sup>	57	48	9	21	25
3	1552.54	1016.199	2.38	56.68	33.34x10 <sup>-4</sup>	51	34	18	36	21
4	2906.25	1666.14	2.34	80.47	5.85x10 <sup>-4</sup>	67	44	23	8	49
5	1637.5	1066.36	2.42	511.64	11.5x10 <sup>-4</sup>	59	31	28	25	34
6	1531.84	867.27	2.2	72.555	8.75x10 <sup>-4</sup>	79	43	35	11	43
7	1530.8	856.34	2.49	77.17	3.4x10 <sup>-4</sup>	57	37	20	14	30
8	UCS of Rock = 7.23 MPa									

The results of the soil consistency test in the form of plasticity index (PI) and liquid limit (LL) values were then plotted into the Casagrande diagram for determining the soil type (**Fig. 10**).

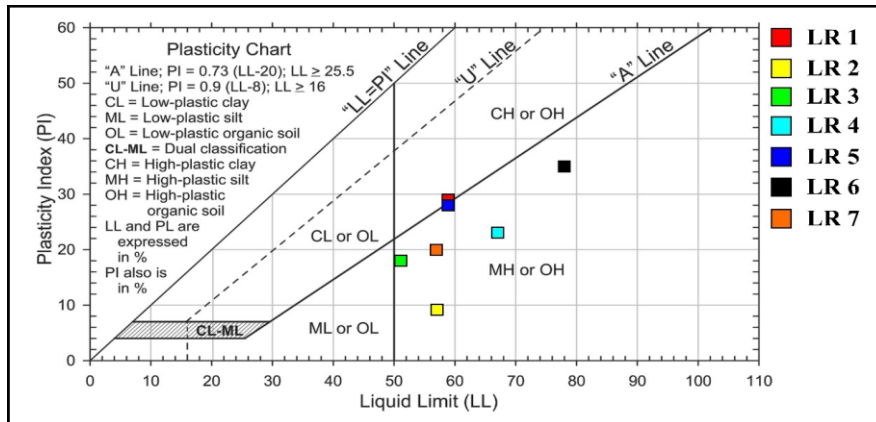


**Fig. 10.** The plots of liquid limit and plasticity index from LR1 to LR7 are used to determine the soil type. It shows that most of the soils are included in MH (high-plastic silt) or OH (high-plastic organic soil), except for LR1 and LR5, which belong to CH (high-plastic clay).

After being analysed, the soil samples taken from the representative slopes in the study area were classified using USCS and AASTHO classification as listed in **Table 6**.

**Table 6.**

**Soil type (USCS and AASTHO classification) of mass movements in the study area.**

Slope (LR)	USCS		AASTHO	PI	Expansive Degree	Expansive Potential	Clay Minerals
	Symbol	Name					
1	CH	High-plastic clay	A-7-5 (32)	29	Very Expansive	High	Smactite
2	MH	High-plastic silt	A-5 (13)	9	Not Expansive	Low	Kaolinite
3	MH	High-plastic silt	A-7-5 (19)	18	Rather Expansive	Medium	Mica-like
4	MH	High-plastic silt	A-7-5 (30)	23	Very Expansive	High	Smactite
5	CH	High-plastic clay	A-7-5 (32)	28	Very Expansive	High	Smactite
6	MH	High-plastic silt	A-7-5 (44)	35	Very Expansive	Very high	Smactite
7	MH	High-plastic silt	A-7-5 (22)	20	Rather Expansive	High	Mica-like

The expansive nature of soil depends on the type of clay content in it. By approaching ASTM (Chen, 1975; Nelson & Miller, 1991) from the value of the plasticity index (PI), the expansive properties of soil can be known (**Table 6**). Table 6 shows that in all of the representative slopes being studied, the types of soil constituents are very expansive, having the potential to expand, and some of them contain smactite clay. This is reinforced by the results of petrographic analysis of the Halang tuffaceous sandstone unit, which shows the large content of volcanic material, especially plagioclase. It is known that when plagioclase undergoes weathering, clay minerals will be formed. On the 7 representative slopes, the determination of the safety factor was carried out using the simplified bishop method (**Fig 11**). The overall results are described in detail in **Table 7**.

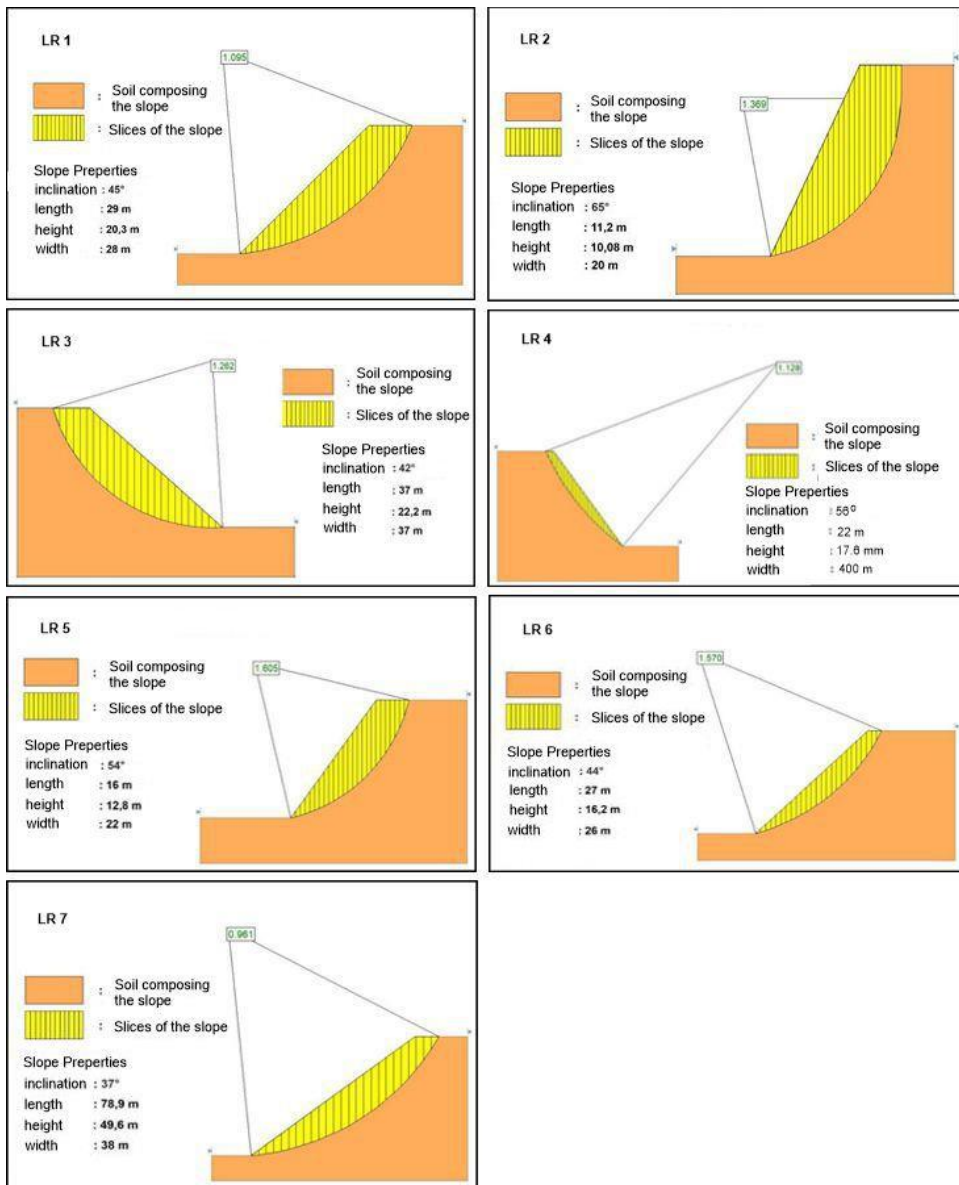


**Fig. 11.** Model of mass movements and factor of safety determination in the study area.

Table 7.

## Description of soil movements potential in the study area.

Slope (LR)	Location	Environment and Slope condition	Material	Soil properties	Safety Factor, Movement Type	
1	Jangkrikan village, 387754 mE 9167300 mN	Farming area, sloping 45°, slope length 29 m,	Tuffaceous sandstone of Halang Fm, intensively weathered, wet condition	CH, high plasticity, clay, A-7-5 (32), $\gamma = 1301,5$ kN/m <sup>3</sup> Expansive clay, smactite	C = 25 kN/m <sup>2</sup> ; $\phi = 20^\circ$ W = 46,35% K = 35x 10-4 cm/s	Fs = 1.095 Slump (Landslide) Slide direction N335oE
2	Jangkrikan village, main road side Kutoarjo – Bruno 387049 mE 9167841 mN	Settlement area, sloping 45°, slope length 29 m,	Tuffaceous sandstone of Halang Formation, intensively weathered, wet condition	MH, high plasticity, silt, A-5 (13), $\gamma = 1665,8$ kN/m <sup>3</sup> Expansive clay, smactite	C = 21 kN/m <sup>2</sup> ; $\phi = 25^\circ$ W = 82,04% K = 7.63 x 10-4 cm/s	Fs = 1.369 Slump (Landslide) Slide direction N15oE
3	Kaliwungu village, road side of Ngemplak – Krawan, 382508 mE 9165122 mN	Farming area, fruit trees, sloping 42°, slope length 37 m,	Tuffaceous sandstone of Halang Fm, intensively weathered, wet condition	MH, high plasticity, silt, A-7-5 (13), $\gamma = 1552,54$ kN/m <sup>3</sup> Expansive clay, smactite	C = 35 kN/m <sup>2</sup> ; $\phi = 21^\circ$ W = 56,68% K = 3.34 x 10-4 cm/s	Fs = 1.262 Slump (Landslide) Slide direction N 110oE
4	Suati – Sruwudadi Tengah, road side 384576 mE 9161165 mN	Farming area, sloping 56°, slope length 22 m,	Tuffaceous sandstone of Halang Fm, intensively weathered, wet condition	MH, high plasticity, silt, A-7-5 (30), $\gamma = 2906,25$ kN/m <sup>3</sup> Expansive clay, smactite	C = 8 kN/m <sup>2</sup> ; $\phi = 49^\circ$ W = 46,35% K = 35x 10-4 cm/s	Fs = 1.128 Slump (Landslide) Slide direction N115oE
5	Brunosari village, main road side 382813 mE 9162569 mN	Farming area, sengon trees, sloping 54°, slope length 16 m,	Tuffaceous sandstone of Halang Fm, weathered but there is rock debris, moistured condition	CH, high plasticity, clay, A-7-5 (32), $\gamma = 1637,5$ kN/m <sup>3</sup> Expansive clay, smactite	C = 25 kN/m <sup>2</sup> ; $\phi = 34^\circ$ W = 51,64% K = 11.5 x 10-4 cm/s	Fs = 1.605 Slump (Landslide) Slide direction
6	Kaliwungu village, road side 382813 mE 9162569 mN	Farming area, sloping 45°, slope length 29 m,	Tuffaceous sandstone of Halang Fm, intensively weathered, wet condition	MH, high plasticity. silt, A-7-5 (32), $\gamma = 1665,8$ kN/m <sup>3</sup> Expansive clay, smactite	C = 25 kN/m <sup>2</sup> ; $\phi = 20^\circ$ W = 51,64% K = 11,5 x 10-4 cm/s	Fs = 1.570 Slump (Landslide) Slide direction
7	Tegalsari village, main road side Kutoarjo – Bruno 385599 mE 9163143 mN	Threatening 12 houses, sloping 37°, slope length 78.3 m,	Tuffaceous sandstone of Halang Fm, intensively weathered, wet condition,	MH, high plasticity, silt, A-7-5 (22), $\gamma = 1530,8$ kN/m <sup>3</sup> Expansive clay, illite	C = 14 kN/m <sup>2</sup> ; $\phi = 30^\circ$ W = 77.1% K = 3.4 x 10-4 cm/s	Fs = 0.961 Slump (Landslide) Slide direction

The next example of the slope to be investigated is LR8. It is located beside the road connecting Blimbing village and Somoleter village and next to the Blimbing fault geological structure. On this slope, mass movement potential is in the direction of N20°E and threatens the road body. Administratively, the slope belongs to Somoleterkrajan hamlet, Somoleter village. The UTM coordinates are 386564 mE and 9163143 mN. The morphology at this location has a slope of 63°. In the unit composed of the Halang tuffaceous sandstone unit, the position of the groundwater table is not clearly found, but in the joint set of the rock, there are water drops. It indicates that the rock is saturated with water. The land use at this location is shrubs. This type of potential mass movement can be categorized as a rockslide. A rock mass rating has been carried out on this slope, and the results show that the rocks that make up the slope have a total score equal to 38. It means that the material composing the slope can be classified as poor rock. (**Table 8**).

**Table 8.****Rock mass rating of slope 8 (LR 8).**

Parameter	Assessment	Rating
Rock Strength	7.231 MPa	2
RQD	33.50%	8
Joint Spacing	0.36 m	10
Joint Condition	Opening of 1 – 5 mm	10
Groundwater Condition	Wet and saturated	7
Total Score / Class		38 / Poor Rock

There are discontinuity planes at this location with the strike and dip of joint set 1 (JS1) N203°E/82°, joint set 2 (JS2) N226°E/72°, joint set 3 (JS) N80°E/21°, the slope face is N280°E/63°, and the friction angle is 25°. The plot of this data for Markland analysis is shown in **Fig. 12**.

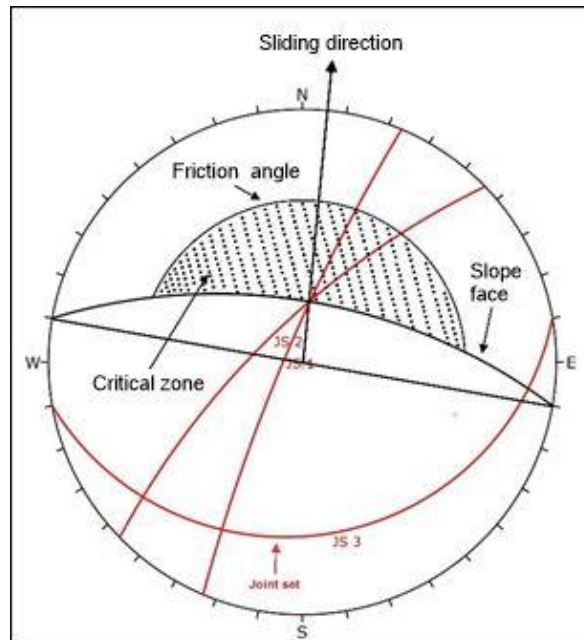


**Fig. 12.** The stereonet plot of LR 8, showing failure potencies of wedge type through the interception of JS2 and JS4, and toppling through JS 3.

The result of the stereonet plot and markland analysis demonstrate that the slope is not safe and the type of landslide potential is wedge and toppling failures. As well as the strike of the discontinuity plane, which is represented by the joint set of 3 forming an angle of 20° toward the strike of the slope, so that it will form a toppling landslide.

### 3.3. Soil Behavior and Characteristics

In this study, the formation that has the highest potential to be eroded is the Halang Formation, which consists of mainly clayey sandstone and claystone. Based on the results of laboratory analysis that showed the permeability values are very low, it can be inferred that the speed of water movement in the lithology composing the slopes being studied is very slow. This will trigger the existence of hydrostatic pressure in terms of pore pressure to weaken the shear strength of the slope (Kusumayudha, et al, 2020).

The soil cohesion ( $c$ ) values of the investigated slopes range from 8 KN/m<sup>2</sup> to 25 KN/m<sup>2</sup>, and the internal friction angle ( $\phi$ ) values extent from 20° to 49°. The types of soil are high plastic clay and high plastic silt with slightly expansive potential to very expansive, so that it will cause swelling when the water content is high and be able to form cracks if it loses its water content. The permeability ranges from  $3.410^{-4}$  to  $5.510^{-5}$  and the water content ranges from 46.35% to 80.47%. This shows that the speed of water movement in the body of the slopes is very low. With this very slow motion, the presence of water in the soil will cause hydrostatic pressure in the pores of the material. In turn, this condition will increase the weight force, reduce the cohesion force ( $c$ ) value, and reduce the friction angle ( $\phi$ ) (Fig. 13, Fig. 14, Fig. 15), thereby increasing the potential for mass movements in the area.

On slopes made up of rocks, such as LR8, the uniaxial compressive strength value of the rock is 7,231 Mpa, indicating that this rock is very weak (Hoek & Bray 1997). The result of the rock mass rating (RMR) on this slope is 38, which is classified as poor rock in class IV. Of course, poor rock has a higher potential to fail. Based on the Markland method, the potential failure types are wedge and toppling.

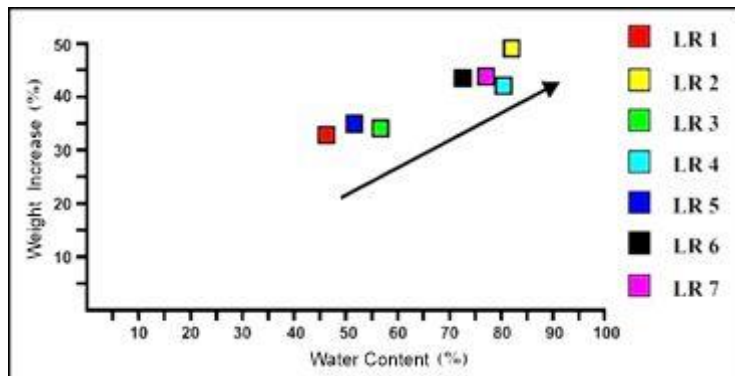


**Fig. 13.** The plots of water content and percent weight increase of the soil sample, showing the correlation of water content and weight increase. The higher the water content, the greater the percentage of the soil weight increase.

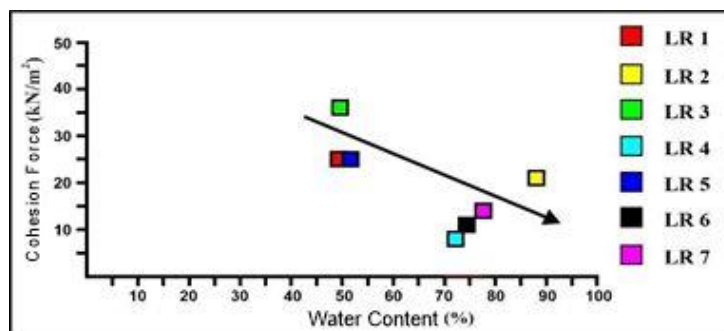


**Fig. 14.** The plots of water content and cohesion force value of the soil sample, showing the correlation of water content and cohesion force ( $c$ ). The higher the water content, the lower the cohesion force.

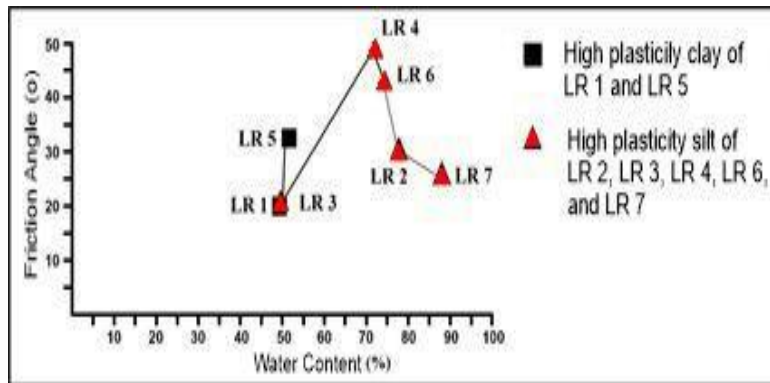


**Fig. 15.** The plots of water content and friction angle ( $\alpha$ ) value of the soil sample, showing that when the water content is higher than 70%, the friction angle will decrease.

The results of this study demonstrate that the factors influencing soil behavior in the occurrence of mass movement are the type of clay mineral (smactite group) and the amount of water content in the soil. Thus, the information on soil properties is very important to be understood by stakeholders in managing landslide-prone areas. Soil which is very expansive with high water content, low cohesion force, and low friction angle value will decrease its shear strength and therefore is susceptible to landslides. By knowing the soil behavior and characteristics in the area, the potential for mass movements in the area can be detected early, anticipation can be made, and countermeasures can be planned in the framework of designing a landslide disaster mitigation model.

## 5. CONCLUSIONS

Based on the results of the study, the following conclusions can be drawn:

The geomorphology of the research area consists of homoclinic hills, undulating wavy plains, and denudated volcanic hills. The lithology of the study area comprises sandstone units of the Halang Formation, from the late Miocene, and andesite breccia of the Peniron Formation, from the Pliocene epoch, with conformable stratigraphic relationships. There is a normal left slip fault, called the Blimbing Fault, striking N6°E and dipping 70°.

Slope 1 (LR1) and Slope 5 (LR5) are composed of high-plastic clay with very expansive properties. Slope 2 (LR2) is a high-plastic silt with non-extensive properties. Slope 3 (LR3), Slope 4 (LR4), Slope 6 (LR6), and Slope 7 (LR7) are high-plastic silt with slightly expansive to very expansive properties. Using the simplified Bishop method, the safety factor of slopes composed of soil (LR1 to LR7) is 1.095, 1.369, 1.262, 1.128, 1.605, 1.570, and 0.961, respectively, with slump or landslide type of movement. Slope 8 (LR8) has many discontinuities with a joint density of 0.36 m. The RMR value is 38, which belongs to rock mass class IV, or poor rock. The potential for movement is in the form of wedges and toppling types.

The effect of soil water content is to increase the load of the slopes by 15%, decreasing the cohesion value ( $c$ ), and reducing the friction angle ( $\alpha$ ). The friction angle decreases when the water content is more than 70%. The types of soil are high-plastic clay and high-plastic silt with smactite mineral, slightly expansive to very expansive. The velocity of water movement on the slope is very low, making the slope more conducive for ground or mass movements to occur.

Factors influencing soil behavior in the occurrence of mass movement are the type of clay mineral (smactite group) and the amount of water content in the soil. This study indicates that information on soil behavior and characteristics is important to stakeholders for landslide-prone area management, especially for anticipating and countermeasure planning in the framework of landslide disaster mitigation.

## ACKNOWLEDGEMENT

This study was held with the support of the Geological Engineering Department of Universitas Pembangunan Nasional Veteran Yogyakarta. In relation to that, the authors express their high appreciation and deep gratitude to the institution for its backing in the operation of this study.

## REFERENCES

- Bieniawski, Z. T. (1989). *Engineering rock mass classifications : a complete manual for engineers and geologists in mining, civil, and petroleum engineering*. Wiley-Interscience.
- BMKG (Badan Meteorologi Klimatologi dan Geofisika), (2021). Peta distribusi curah hujan bulan Januari 2021 Jawa Tengah. Semarang: [online] (<http://iklimjateng.info/index.php/informasi-iklim/informasi-iklim-2/informasi-iklim-5>).
- BPS (Badan Pusat Statistik), (2020). Jumlah Kejadian Bencana Alam Menurut Kabupaten/Kota di Provinsi Jawa Tengah. Jawa Tengah: [online] (<https://jateng.bps.go.id/indicator/152/511/1/jumlah-kejadian-bencana-alam-menurut-kabupaten-kota-di-provinsi-jawa-tengah.html>).
- Citrabhuwana, B.N.K., Kusumayudha S.B., and Purwanto, (2016). Geology and slope stability analysis using markland method on road segment of Piyungan-Patuk, Sleman, Gunungkidul Regencies, Yogyakarta Special Region, Indonesia, *International Journal of Economic and Environmental Geology*, vol. 7, no. 1, pp 16-21, [www.econ-environ-geol.org](http://www.econ-environ-geol.org).
- Duncan, C. I., and Fasce, J. (1992). Soil and Foundations For Architects and Engineers. (E. M. Walters, Ed) (Second Edition). Texas: *Springer Science+Business Media*, LLC, pp, 23-32.
- Hardiyatmo, H. C. (2014). Mekanika Tanah 1 (Ke Tujuh). Yogyakarta: Gadjah Mada University Press, pp, 3, 39, 48, 51, 329.
- Hoek, E., and Bray, J. (1997). *Rock Slope Engineering* (Revised Second Edition). London: Institution Of Mining and Metallurgy, pp, 150, 182.
- Imam, A. N., (2021). Tanah Bergerak di Bruno, 2 rumah roboh, belasan lainnya terancam longsor. Purworejonews.com. [online] (<http://purworejonews.com/tanah-bergerak-di-bruno-2-rumah-roboh-belasan-lainnya-terancam-longsor/>).
- Kusumayudha, S. B., and Ciptahening, A. N. (2016). Correlation Between Tectonic Environment and Characteristics of Mass Movement (Landslides): A Case Study From Java, Indonesia. *The Jurnal of Geology Resource and Engineering*. 4(2). 1-17, [www.davidpublisher.com](http://www.davidpublisher.com), <http://eprints.upnyk.ac.id/id/eprint/9028>
- Kusumayudha, S.B., Ciptahening, A.N., Purwanto, H.S., Kristanto, W.A.D, Nugroho, N.E. (2020). Slope Movement Characteristic and Models based on Engineering-geological Properties of the Menoreh Hills, Purworejo Regency, Central Java, Indonesia, *AIP Conference Proceedings* 2245, 070014 (2020); <https://doi.org/10.1063/5.0010201>
- Nelson, J. D., and Miller, D. J. (1991). *Expansif Soils*. Colorado: John Wiley & Sons, Inc, p, 12.
- Rajagukguk, O.C.P., Tarigan, A.E., dan Monintja, S. 2014. Analisis Kestabilan Lereng Dengan Metode Fillenius (Studi Kasus: Kawasan Citraland sta. 1000 m). *Jurnal Sipil Statik*, 2(3). 140-147.
- Van Bemmelen, R. W. (1949). *The Geology of Indonesia* (Vol. IA). Netherlands: Government Printing Office, p, 26.
- Van Zuidam, R. A. (1984). *Guide To Geomorphologic Aerial Photographic Interpretation And Mapping*. Enschede the Netherlands: ITC, p, 43.
- Varnes, D. J. (1978). Slope Movement Type and Processes, Special Report 176; *Landslide; Analisis and Control* (Schuster, R.L. and Krizek, R.J.), Washington, D.C: Transport Research Board, National Research Council, p, 11.
- Wicaksono, B. A. (2020). Purworejo Masuk Wilayah Risiko Rawan Bencana di Jateng. M.medcom.id. [Online] (<https://m.medcom.id/nasional/daerah/3NOqy83k-purworejo-masuk-wilayah-risiko-rawan-bencana-di-jateng>).



# MACHINE LEARNING FOR MAPPING SPATIAL DISTRIBUTION OF THICKNESS AND CARBON STOCK OF TROPICAL PEATLAND BASED ON REMOTE SENSING DATA: A CASE STUDY IN LAKE SENTARUM NATIONAL PARK, INDONESIA

Faizal MUSTHOFA<sup>1</sup>, Wirastuti WIDYATMANTI\*<sup>1</sup>, Sanjiwana ARJASAKUSUMA<sup>1</sup>, Deha A. UMARHADI<sup>1</sup>, Demetria A. PUTRI<sup>2</sup>, Fahrudin F. RAHARJA<sup>3</sup>, and M. K. ARRASYID<sup>4</sup>

DOI: 10.21163/GT\_2022.171.04

## ABSTRACT:

Indonesia is one of the countries with the largest area of tropical peatlands in the world. These wide peatlands have a vital role in the carbon cycle and carbon storage in huge quantities, thus strict conservation in the area is necessary. One effort to carry out conservation is to understand the spatial distribution of carbon stock in peatlands. This study aims to map the spatial distribution of carbon stock based on peat thickness modeling using machine learning algorithms, i.e., Random Forest (RF), Quantile Regression Forests (QRF), and Cubist. A case study was conducted in a part of Lake Sentarum National Park, Indonesia where human interference is still limited. Digital elevation model (DEM) and synthetic aperture radar (SAR) data were included as the input variables. The results showed that RF performed the best among other models to estimate peat thickness (mean = 1.877 m) with an RMSE (root mean square error) of 0.483 m and an  $R^2$  of 0.786. DEMs are the most important parameters in our analysis compared to SAR data. Based on the best model, we estimated the total volume of 5,112,687 m<sup>3</sup> in the study area, produced at 12.5 m resolution, which was then converted to a total of carbon stock at  $0.337 \pm 0.106$  Mt carbon.

**Key-words:** Peat thickness, Carbon stock, Machine learning, Remote Sensing, Tropical peatland.

## 1. INTRODUCTION

The role of tropical peatlands is vital in the global carbon cycle considering their immense carbon-rich ecosystems (Dargie et al., 2017; Page et al., 2011). Ninety percent (404.5 Mha) of peatlands worldwide are located in boreal and temperate zones (Yu et al., 2010), however, the carbon content of tropical peatlands is greater than high latitude peatlands (Bourgeau-Chavez et al., 2018). Thus, tropical peatlands could store up to 104.7 GtC from their limited coverage (90-170 Mha) (Ribeiro et al., 2021). Nearly half of tropical peatlands are situated in South-East Asia (43%; 24.8 Mha) (Dargie et al., 2017; Page et al., 2011). Tropical peatlands are widely distributed in three major Indonesian islands including Sumatra, Kalimantan, and Papua, with a total area of 13.43 Mha (Anda et al., 2021). This area undoubtedly provides carbon storage in a huge quantity (Mitra et al., 2005), while on the other hand, it has a large potential as a carbon emission source due to the conversion to agricultural and plantation purposes (Umarhadi et al., 2021).

---

<sup>1</sup> Department of Geography Science Information, Faculty of Geography, Universitas Gadjah Mada, Indonesia, [faizal.musthofa@mail.ugm.ac.id](mailto:faizal.musthofa@mail.ugm.ac.id), Corresponding author\* [wwidyatmanti@ugm.ac.id](mailto:wwidyatmanti@ugm.ac.id), [sanjiwana.arjasakusuma@ugm.ac.id](mailto:sanjiwana.arjasakusuma@ugm.ac.id), [deha.agus.u@mail.ugm.ac.id](mailto:deha.agus.u@mail.ugm.ac.id)

<sup>2</sup> Faculty of Forestry, Universitas Gadjah Mada, Indonesia, [demetriaalika2018@mail.ugm.ac.id](mailto:demetriaalika2018@mail.ugm.ac.id)

<sup>3</sup> Department of Mechanical Engineering, Vocational School, Universitas Gadjah Mada, Indonesia, [fahrudinfrida@mail.ugm.ac.id](mailto:fahrudinfrida@mail.ugm.ac.id)

<sup>4</sup> Department of Economy, Faculty of Economy and Bussines, Universitas Gadjah Mada, Indonesia, [arraysid103@gmail.com](mailto:arraysid103@gmail.com)



Tropical peat formation is mainly resulted from the accumulation of decomposed rainforest plant debris (branches, leaves, roots, and trunks) for million years (Rieley & Page, 2016), leading to the abundance of carbon content and thus considered as organic soils. The development of peatlands in South-East Asia started in the Pleistocene era (26,000 yr BP) for the inland peatlands (Page et al., 2004), followed by the formation in the coastal and sub-coastal area in the Holocene period (5,000-6,000 yr BP) (Supardi et al., 1993). The accumulation process continues to form a dome where is bordered by the sea, rivers, and/or in the depression area enclosed by levees (Melling, 2016). The mound of peat dome is indistinct in a gradient of about  $1 \text{ m km}^{-1}$  on the surface with higher elevation toward the center of the dome (Anderson, 1964). This indicates the thickness of peat is related to the higher accumulation, hence it stores a larger amount of carbon.

Considering the importance of peatlands, mapping the distribution of peat thickness and soil carbon stock is a part of efforts to mitigate disasters and climate change, especially in reducing carbon emissions. Moreover, the governance on peatlands is based on peat thickness whether it can be used for cultivation or should be fully conserved, with a threshold of 3 m thickness in Indonesia (Dohong et al., 2018). The most common method to spatially predict peat thickness is geostatistics by interpolating the thickness or depth data collected in the field (Altdorff et al., 2016; Jaenicke et al., 2008; Keaney et al., 2013; Silvestri et al., 2019), however, the density and distribution of samples highly influence the results. Spatial modeling has been utilized taking the high correlation between peat thickness and surface elevation using empirical methods such as linear regression (Holden & Connolly, 2011), yet it is challenging to accommodate the elevation variability of the underlying mineral substrate (Silvestri et al., 2019). The use of multivariate data coupled with machine learning methods can achieve an accurate peat thickness estimation and allow the evaluation of variables' importance in the modeling (Rudiyanto et al., 2018).

Previous research explored the prediction of peat thickness using 14 machine learning models based on environmental variables including elevation, terrain parameters, and distance from rivers and/or sea, as well as radar and optical satellite imageries in Bengkalis Island, where vast peat degradation peatland has occurred (Rudiyanto et al., 2018). The variables used considered the factors contributing to the development of soils that consist of peat properties, organisms including human activities, relief, and geographical position (McBratney et al., 2003; Rudiyanto et al., 2018). Our study demonstrated peat thickness estimation in undisturbed peat swamp forest in Lake Sentarum National Park, Borneo Island. We adopted the previous study by exploring multi variables and evaluating machine learning methods (i.e., Random Forest, Quantile Regression Forest, and Cubist) to produce high-resolution peat thickness (12.5 m). Moreover, spatial information of carbon stock was derived based on peat thickness, bulk density, and carbon content.

## **2. STUDY AREA**

Lake Sentarum National Park (LSNP) is a national park in the middle of Borneo Island, Indonesia, located in the floodplain of Kapuas River upstream. Peat swamp forest covers 16% of the national park and is considered one of the oldest Indonesian peat swamps alongside Putussibau peatlands (> 30000 yr BP) (Anshari et al., 2001; Giesen & Anshari, 2018; Ruwaimana et al., 2020). The study was conducted in the Kerinung Forest (3,627.93 ha;  $0^{\circ}43'48''$ – $0^{\circ}49'4.49''$ N and  $112^{\circ}1'24''$ – $112^{\circ}21'54''$ E) of LSNP, just about 100 km northward from Equator line. This work focused on the smaller area in Kerinung Forest with a total area of 272.3 ha ( $0^{\circ}45'21''$ N and  $112^{\circ}1'49''$ E) as shown in **Fig. 1**.

As a basin, the water sources to LSNP flow from hills and plateaus in the surroundings. Temperatures range from  $25^{\circ}\text{C}$ – $44^{\circ}\text{C}$  with rainfall between 3000-5000 mm. Soil types in the LSNP are generally divided into two large groups, namely sediments and organosols on land and sand and clay in hilly areas (Giesen, 1987). The level of peat maturity in Kerinung Forest consists of various levels including fibric, hemic, and sapric.

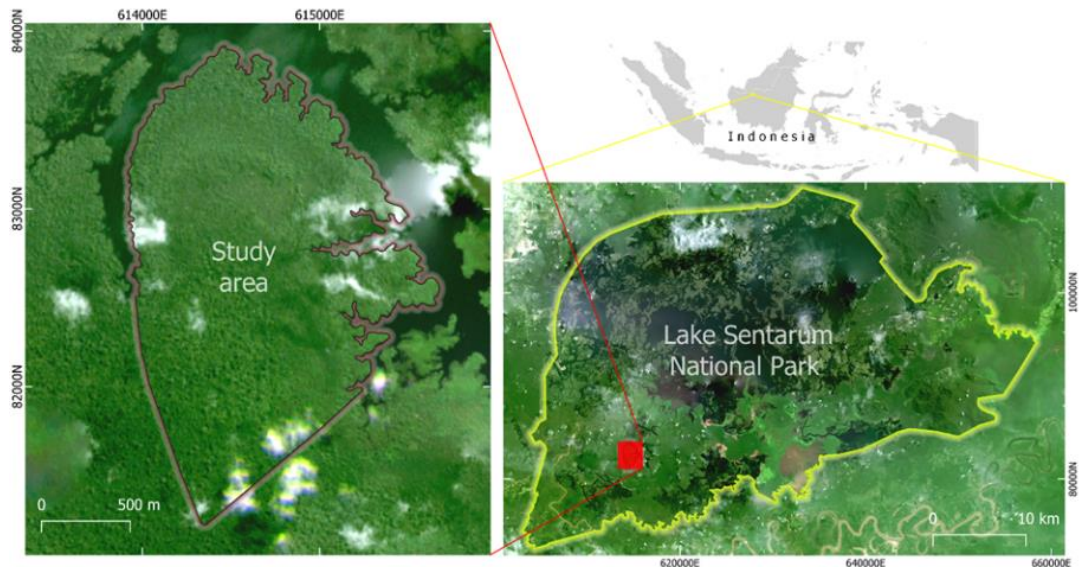


**Fig. 1.** Study area located in Kerinung Forest inside Lake Sentarum National Park, Indonesia. Planet© imagery is used for the visualization.

### 3. MATERIALS AND METHODS

#### 3.1. Field Data

Peat thickness data in the field were collected using peat soil drilling tools on 7-17 September 2019. Samples were determined by a transect method with a gap of 200 m between each plot. A total of 36 sites were plotted and the measurement was conducted 4-9 times in the center of the plot and surroundings to cover 236 samples in total. The number of repetitions is based on consideration of the thickness of the peat and the time taken for sampling. The deeper the peat thickness, the less the sampling repetition. A handheld Garmin GPSMAP 64s receiver was used to obtain the coordinates for each sample point by a single point positioning. GPSMAP 64s receives locations obtained from GPS and GLONASS at high sensitivity with a quad-helix antenna (<https://www.garmin.com/en-US/p/140022>). The device can provide a horizontal accuracy of up to 3 m (Hil, 2020).

#### 3.2. Spatial data

We refer to Rudiyanto et al., 2018 for parameter selection used in peat thickness modeling. This study used the parameter of elevation and synthetic aperture radar (SAR) images as both data contributed the highest in the estimation (Rudiyanto et al., 2018).

##### 3.2.1. Elevation data

Digital elevation model (DEM) is one of the crucial parameters in modeling the thickness of peat (Rudiyanto et al., 2018) because the surface of the elevation model can determine the location where the peat dome is known (Jaenicke et al., 2008). The thickness can be generally figured out from the shape of the peat dome, showing that the closer to the peat dome, the deeper the thickness is. We used DEMs retrieved from two sources, i.e., Indonesian National DEM (DEMNAS) and ALOS DEM. DEMNAS is a high resolution (8.25 m) national elevation dataset compiled from TERRASAR-X (5 m), Airborne Interferometric Synthetic Aperture Radar (IFSAR; 5 m), and ALOS PALSAR (11.25 m), added with stereo-plotting data (Geospatial Information Agency, 2018). In the study area, IFSAR acquired in 2005 was used as the source of DEMNAS. ALOS PALSAR (Advanced Land Observing Satellite-Phased Array-Type L-Band Synthetic Aperture Radar) Radiometrically Terrain Corrected (RTC) DEM was also used that has a spatial resolution of 12.5 m.

### 3.2.3. Synthetic aperture radar data

Synthetic aperture radar (SAR) images used in this study consist of two different sensors, i.e., Sentinel-1 and ALOS PALSAR, representing C and L-band, respectively. Sentinel-1 works at a frequency of 5.405 GHz (wavelength = 5.6 cm), capturing the same location on Earth's surface frequently every 6 days, thanks to its satellite constellation: Sentinel-1A and Sentinel-1B. The images were obtained from the Alaska Satellite Facility (ASF) Distributed Active Archive Center (DAAC) services and Google Earth Engine (GEE) cloud computing platform acquired in 2019. The images fetched from ASF DAAC were at Radiometric Calibration of S-1 Level-1, while images from GEE were provided at terrain correction level. ALOS PALSAR has a longer wavelength (24 cm; frequency = 1.27 GHz) than Sentinel-1. The image is freely available downloaded from ASF DAAC with an acquisition time in 2011. Both Sentinel-1 and ALOS PALSAR respectively provide dual-polarization (VV-VH and HH-HV) with a slight difference of spatial resolution (10 and 12.5 m). Supplementing the individual polarization, some image transformations were also included, i.e., ratio, mean, and difference (**Table 1**). The total spatial data inputs used for the modeling are 13 image layers.

**Table 1.**

**Equations of image transformations used for Sentinel-1 and ALOS PALSAR.**

Image transformation	Sentinel-1	ALOS PALSAR
Ratio	VV/VH	HH/HV
Mean	$(VV + VH) / 2$	$(HH + HV) / 2$
Difference	VV-VH	HH-HV

### 3.3. Peat thickness modeling

The methods used to obtain a peat thickness model are divided into several machine learning regressions. These algorithms include Random Forest (RF) (Breiman, 2001), Quantile Regression Forests (QRF) (Meinshausen, 2006), and Cubist (Kuhn et al., 2021) – all of them is non-parametric regression methods. Non-parametric regression is getting more prominent to describe geographical phenomena using Earth observation data and it has the capability to deal with non-linear complexity, however, it may allow overfitting the training dataset (Houborg & McCabe, 2018; Verrelst et al., 2015). RF is a tree-based ensemble learning method that the results are generated from the aggregations of numerous classifiers (Liaw & Wiener, 2002). Many bootstrap samples are firstly drawn from the given training dataset, then a tree is evolved by the bootstrap sample with modifications: at each node, randomly sample  $m_{try}$  (number of random variables in each tree) of the predictors and choose the best split from among those variables (Liaw & Wiener, 2002). QRF is the generalization of the random forest by modeling the conditional quantiles of an outcome of interest as a function of covariates without an assumption of normal distribution (Meinshausen, 2006; Wei et al., 2019).

Cubist is a rule-based regression based on the Model Tree approach according to the works by (Quinlan, 1992) and (Quinlan, 1993). The tree grows where the endpoint leaf contains a linear regression model (Kuhn et al., 2021; Zhou et al., 2019). Then a series of “if-after-after” rules are created, where the rule has an associated multivariate linear model, afterwards, the value is predicted from the corresponding model after the set of covariates satisfies the conditions of the rule (Zhou et al., 2019).

The performance of the three machine learning methods has been tested and achieved considerable accuracy to map tropical peat thickness (Rudiyanto et al., 2018). Field data of peat thickness were used as the reference which was then split into training (80%) and test samples (20%). Training data were used for peat depth modeling, while test data were to test the performance of the model developed from training data. The performance of modeling was evaluated using 10-fold cross-validation.

All processing was conducted using RStudio with Caret Package that provides numerous machine learning methods including those used in this study, i.e., RF, QRF, and Cubist. Variable importance was also calculated describing the calculation of the relationship between the predictor and outcome by individually permuting individual predictor and assessing the effect when the corresponding predictor is negated (Kuhn & Johnson, 2013). The importance score is relative, where the first (most important) variable is scaled to have a maximum value of 100 and the others range between 0 and 100. The score approaching 100 indicates the closeness to the first variable, and vice versa. Peat thickness models were evaluated using K-Fold Cross Validation to measure the coefficient of determination ( $R^2$ ) and root mean square error (RMSE) values in order to find the best model.

### 3.4. Carbon stock calculation

To generate the spatial distribution of carbon stock, it is necessary to derive a map model of peat thickness with the best model result. The value of carbon stock is calculated based on the algorithm as follows:

$$C_{\text{stock}} = C_v \times V \quad (1)$$

where  $C_{\text{stock}}$  denotes carbon stock (Mg),  $C_v$  denotes carbon density ( $\text{Mg m}^{-3}$ ), and  $V$  denotes volume ( $\text{m}^3$ ).

Volume is a multiplication thickness (m) and between area ( $\text{m}^2$ ), where the area is calculated based on the pixel size of raster data ( $12.5 \times 12.5$  m). Thickness is obtained from the best model based on the accuracy comparison of the results of machine learning algorithms. Carbon density used in this study refers to a field measurement by Warren et al., (2012) conducted in 4 sites of LSNP. The carbon density is  $0.0659 \pm 0.0208 \text{ Mg m}^{-3}$ , resulted from the multiplication between carbon content ( $50.7 \pm 2.2$  %) and bulk density ( $0.131 \pm 0.043 \text{ Mg m}^{-3}$ ) (Warren et al., 2012).

## 4. RESULTS AND DISCUSSION

### 4.1. Peat thickness models

A total of 13 variables for the inputs of machine learning algorithms are presented in **Fig. 2**. In general, the inputs consist of elevation (2 variables), backscatter values (6 variables), and SAR image transformation (5 variables). Field data of peat thickness were used for reference in the learning process. The total of field samples is 237, i.e., 190 samples (80%) for modeling and 47 samples (20%) for testing. The input variables and training sample for references were processed using three machine learning regressions: RF, QRF, and Cubist, and evaluated using 10-fold cross-validation.

The results of peat thickness modeling are shown in **Fig. 3**. Visually, three models have similar spatial distribution, showing the thicker peatlands in the middle and south of the study area, while lower thickness towards the edge of the dome. However, some thicker peats were found between thinner peats, showing that the thickness is not always gradual following the relative position to the edge. For more detail, Cubist model showed the patchy areas for high thickness. As shown in **Fig. 4**, high thickness values are observed in Cubist model, showing the potential of overestimation. Overall, the mean values of RF and Cubist models are similar, i.e., 1.877 and 1.816 m, respectively. The mean value of QRF model is lower (1.640 m), indicating the underestimated values.

The accuracy of the models was assessed using coefficient of determination ( $R^2$ ) and RMSE (**Table 2**). The RMSE value is related to the corresponding  $R^2$  of each model. RF outperformed the other two algorithms with an RMSE of 0.483 m and  $R^2$  of 0.786, followed by QRF model (RMSE = 0.544 m;  $R^2 = 0.729$ ). The accuracy of Cubist is significantly lower than the other two models with an RMSE of 0.756 m ( $R^2 = 0.514$ ). As likely other tree model approaches, overfitting problems may occur in Cubist model as well (Noi et al., 2017), despite several studies also reporting its outperformance compared to other methods (Dias et al., 2021; Houborg & McCabe, 2018; Zhou et al., 2019).

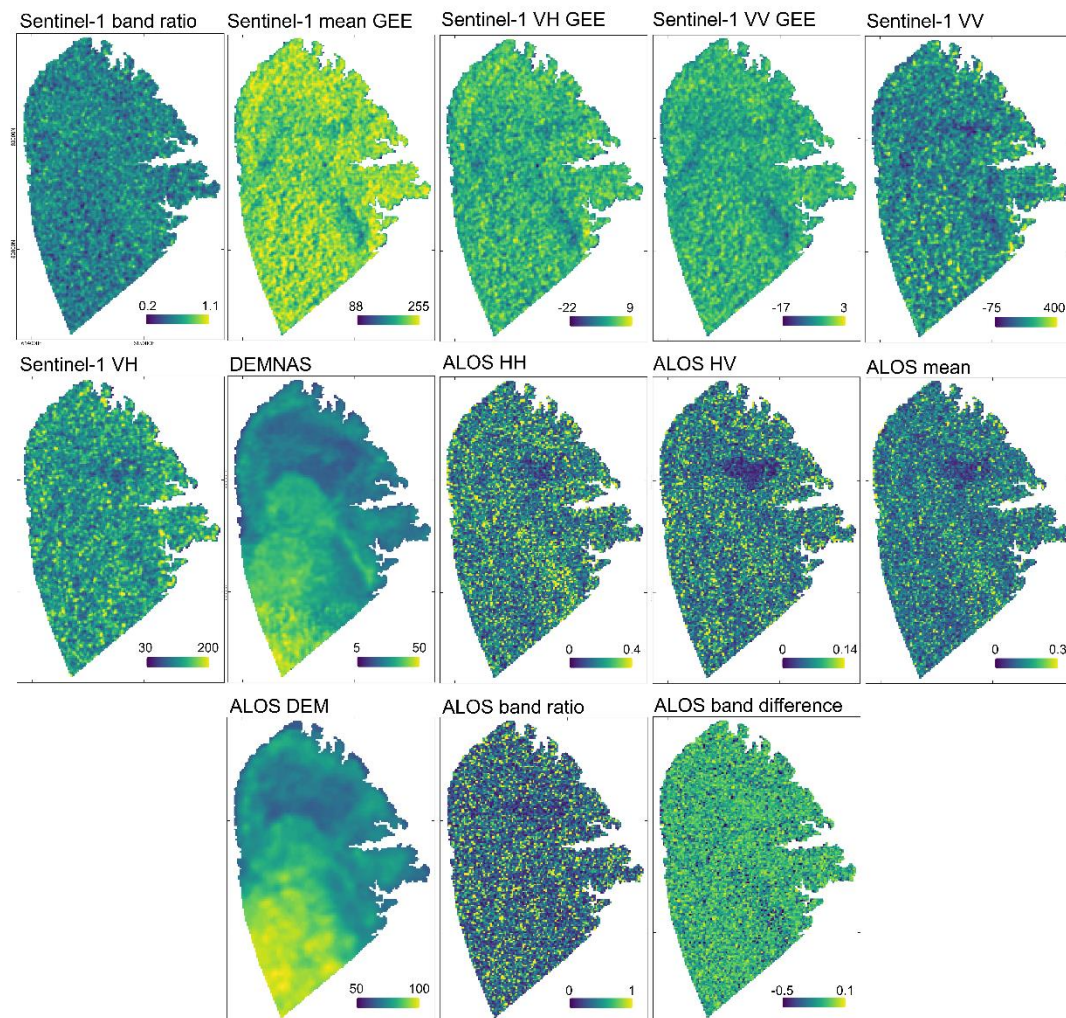


**Fig. 2.** Parameters used in peat thickness modeling.

Based on RMSE values, all of our models achieved an overall error of less than 0.6 m. This accuracy is much higher than the previous study with a range of RMSE between 1.8 to 2.8 m (Rudiyanto et al., 2016). It is mainly due to the undisturbed peatlands in our study area, compared to highly degraded peatlands in a previous study in Bengkalis Island (Rudiyanto et al., 2016). The variability was less complex than degraded peatlands, where anthropogenic variables such as land cover need to be considered in the modeling. Therefore, our methods can be adapted to cover a larger area in undegraded tropical peatlands.

The mean peat thickness value based on the RF model (mean = 1.877 m) is far below the average peat thickness mapped by Ruwaimana et al., (2020) at  $5.16 \pm 2.66$  m in Upper Kapuas Basin, where includes LSNP area. The high discrepancy is mainly due to the small area chosen for this study that does not cover a whole peat dome. The thicker peat is possibly located in the middle of the dome that is not mapped in this study. Spatial information of peat thickness is crucial to be the evidence to determine whether the peatlands can be used for cultivation or should be protected. According to the Ministerial Regulation No. 14 of 2017 concerning Inventory and Determination of the Function of Peat, peatlands with thickness less than 3 m are allowed for development, whereas conservation should be implemented for above 3 m thick peatlands.



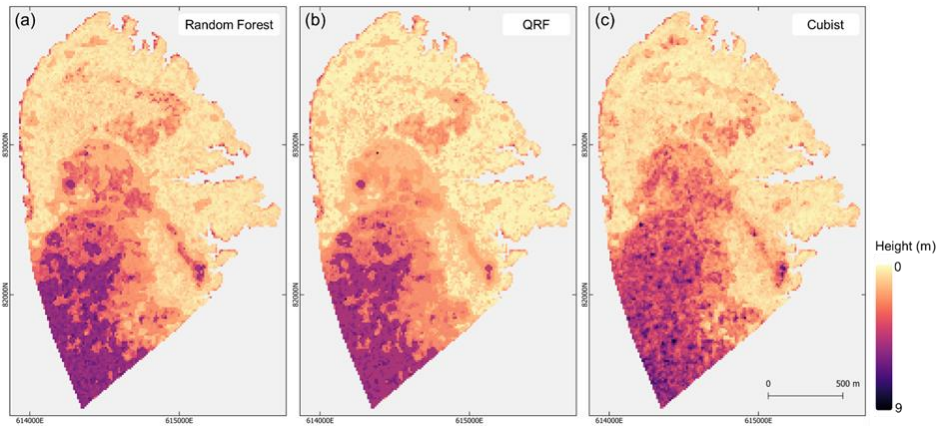


**Fig. 3.** Peat thickness modeled by (a) Random Forest, (b) Quantile Regression Forests, and (c) Cubist.

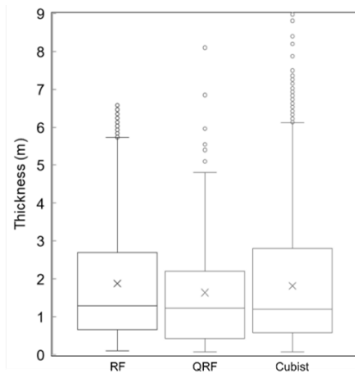


**Fig. 4.** Boxplots showing the distribution of thickness estimates based on machine learning models.

**Table 2.**  
**Root mean square error (in meter) and coefficient of determination values of peat thickness models.**

Methods	Root mean square error (RMSE)	Coefficient of determination ( $R^2$ )
Random Forest	0.483	0.786
Quantile Regression Forests	0.544	0.729
Cubist	0.756	0.514

Based on our results, 79.18% of the areas have a thickness of less than 3 m. However, it could not be generalized for the entire LSNP, since we only took a small area for the case study. Moreover, LSNP is a national park that was regulated to be a protected area, hence any land conversion is restricted regardless of the peat thickness.

#### 4.2. Variable importance for peat thickness modeling

The importance level of variables used in modeling can be seen in **Fig. 5**. The variable of DEMNAS is highest among the others in all models (RF, QRF, and Cubist), followed by ALOS DEM. DEMNAS dominated the most in RF model, where the importance values of other variables are less than 10. In QRF model, ALOS DEM still contributed high in the modeling that exhibits the importance value of 50. The more distributed importance is shown by Cubist modeling. Despite DEMNAS and ALOS DEM representing surface elevation (Julzarika & Harintaka, 2019), both still achieved the highest importance. The differences of both DEM data are the sources and spatial

resolution. ALOS DEM is the up-sampled data from 1 arc-second (30 m) Shuttle Radar Topography Mission (SRTM) DEM acquired in 2000 (Alaska Satellite Facility, 2019). The IFSAR data used for generating DEMNAS has a higher spatial resolution, i.e., 5 m which was then resampled to 8.25 m to seamlessly produce a national DEM, with a more recent acquisition date in 2005. Therefore, DEMNAS could attain a higher score of variable importance than ALOS DEM.

The superior importance of DEM follows research conducted by Rudiyanto et al., (2018) that elevation is one of the important parameters in modeling peat thickness. Visually, a positive relationship was also observed that the higher the height, the thicker the peat. The general characteristic of peatlands in South-East Asia is a convex-dome shape, describing the higher elevation towards the center of the dome (Takada et al., 2016). Since peatlands were formed in the depression area, peats could be concentrated in the center and a biconvex form was shaped. However, further investigation should be conducted since the mounds of underlying mineral soils may vary while the elevation of peat domes is smoother (Nasrul et al., 2020).

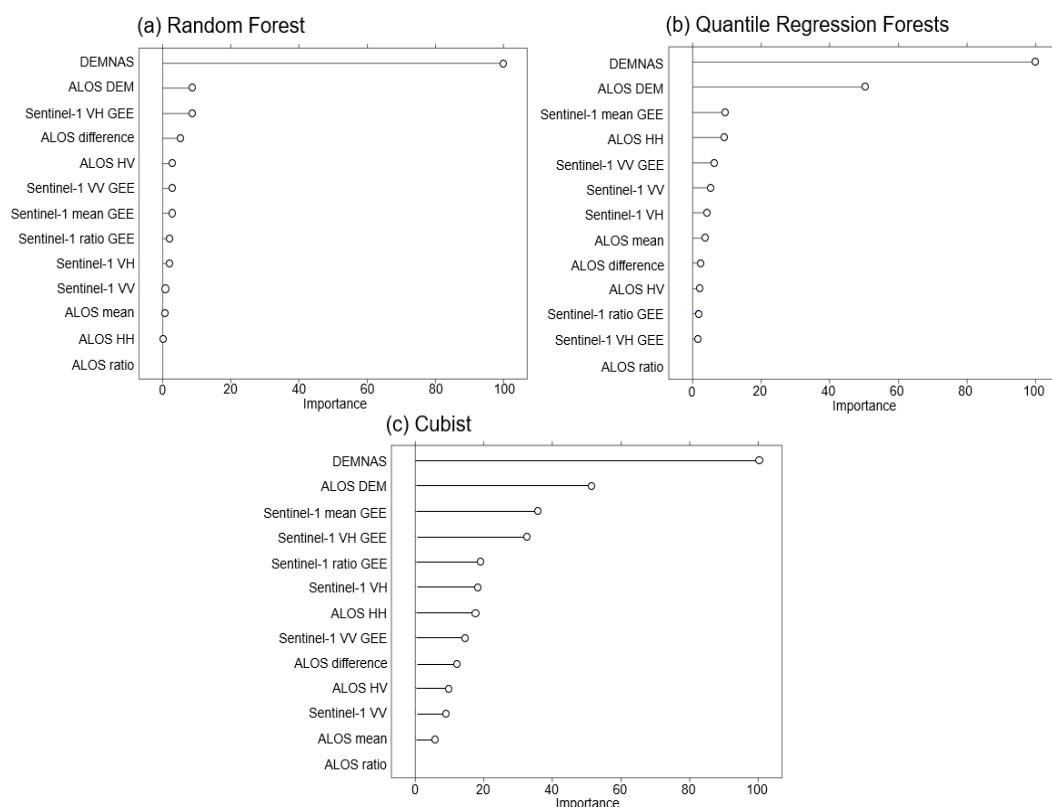
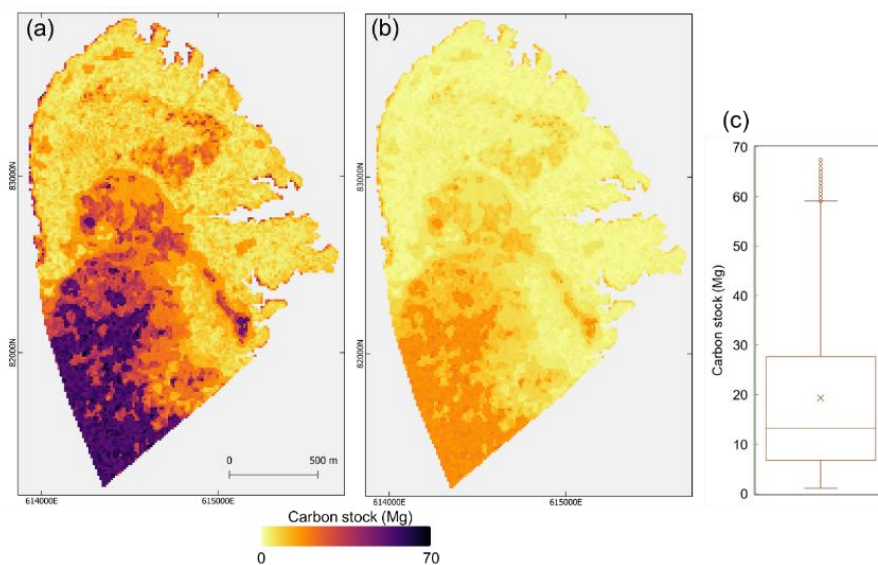


Fig. 5. Variable importance in (a) Random Forest, (b) Quantile Regression Forests, and (c) Cubist models.

The backscatter value of the radar image is less influential in modeling the thickness of the peat because the radar images (C- and L-band for Sentinel-1 and ALOS PALSAR, respectively) are unable to penetrate the vegetation coverage on the peatland. Overall, although working at C-band, the importance values of Sentinel-1 are higher than ALOS PALSAR, even the ratio calculation of ALOS data has zero importance in all models. For instance, P-band SAR data could penetrate deeper to the forest floor, yet the P-band satellite is currently under development (Meyer, 2019). BIOMASS mission carrying P-band (Quegan et al., 2019) and NISAR with S- and L-band (Rosen & Kumar, 2021) that will be launched in upcoming years should be considered for future studies in peat thickness modeling.

### 4.3. Estimating spatial distribution of below-ground carbon stock

Carbon stock was calculated using Equation 1 with the input of the best peat thickness model derived from RF regression. **Fig. 6** illustrates the estimated below-ground carbon stock derived from the best model (Random Forest) of peat thickness (**Fig. 6a**), presented with the standard deviation map (**Fig. 6b**) and the boxplot showing the data distribution (**Fig. 6c**). Visually, the spatial distribution of carbon stock is the same as the peat thickness with different values as illustrated in **Fig. 6a**. The total volume of peat in the study area is 5,112,687 m<sup>3</sup> considering the pixel size of 12.5 m. The standard deviation of the carbon stock estimate was also quantified to show the uncertainty and variability (**Fig. 6b**). A total of  $0.337 \pm 0.106$  Mt below ground carbon was predicted in the study area. Calculated based on the total area (272.33 ha), carbon concentration reached  $1237.2 \pm 390.5$  Mg ha<sup>-1</sup>. This value is half the best estimate of peat carbon concentration in the country at 2772 Mg ha<sup>-1</sup> (Page et al., 2011), mainly because of the low depth peat of the chosen study area. The whole Upper Kapuas Basin was estimated to store  $2790 \pm 1440$  Mg of carbon in every hectare (Ruwaimana et al., 2020). This motivates future studies to apply a similar method to upscale the area covering at least one peat dome.



**Fig. 6.** (a) Estimated carbon stock, (b) its standard deviation based on peat thickness model, and (c) a boxplot presenting the data distribution.

## 5. CONCLUSION

We demonstrated machine learning methods for peat thickness mapping using elevation data and synthetic aperture radar (SAR) satellite imageries. Random Forest (RF) regression outperformed the results of Quantile Random Forests (QRF) and Cubist methods based on accuracy assessment with an RMSE of 0.483 m and an R<sup>2</sup> of 0.786. Among 13 variables, two elevation data (i.e., DEMNAS and ALOS DEM) are the most important features to model peat thickness. The longer wavelength of SAR data (e.g., P-band) should be explored to see the significance compared to C- and L-band data that did not show considerable contributions to the modeling. Based on the best method (RF regression), our results showed the mean peat thickness is 1.877 m with a total peat volume at 5,112,687 m<sup>3</sup>. We estimated a total carbon of  $0.337 \pm 0.106$  Mt in the study area with a carbon concentration of  $1237.2 \pm 390.5$  Mg ha<sup>-1</sup>. The low carbon concentration per area is due to the low peat depth in the selected study area that does not cover the whole peat dome.



## REFERENCES

- Alaska Satellite Facility. (2019). *ALOS PALSAR – Radiometric Terrain Correction*. <https://asf.alaska.edu/data-sets/derived-data-sets/alos-palsar-rtc/alos-palsar-radiometric-terrain-correction/>
- Altdorff, D., Bechtold, M., van der Kruk, J., Vereecken, H., & Huisman, J. A. (2016). Mapping peat layer properties with multi-coil offset electromagnetic induction and laser scanning elevation data. *Geoderma*, *261*, 178–189. <https://doi.org/10.1016/j.geoderma.2015.07.015>
- Anda, M., Ritung, S., Suryani, E., Sukarman, Hikmat, M., Yatno, E., Mulyani, A., Subandiono, R. E., Suratman, & Husnain. (2021). Revisiting tropical peatlands in Indonesia: Semi-detailed mapping, extent and depth distribution assessment. *Geoderma*, *402*, 115235. <https://doi.org/10.1016/j.geoderma.2021.115235>
- Anderson, J. A. R. (1964). The structure and development of the peat swamps of Sarawak and Brunei. *J Trop Geogr*, *18*, 7–16.
- Anshari, G., Peter Kershaw, A., & van der Kaars, S. (2001). A Late Pleistocene and Holocene pollen and charcoal record from peat swamp forest, Lake Sentarum Wildlife Reserve, West Kalimantan, Indonesia. *Palaeogeography, Palaeoclimatology, Palaeoecology*, *171*(3–4), 213–228. [https://doi.org/10.1016/S0031-0182\(01\)00246-2](https://doi.org/10.1016/S0031-0182(01)00246-2)
- Bourgeau-Chavez, L. L., Endres, S. L., Graham, J. A., Hribljan, J. A., Chimner, R. A., Lillieskov, E. A., & Battaglia, M. J. (2018). Mapping Peatlands in Boreal and Tropical Ecoregions. In *Comprehensive Remote Sensing* (pp. 24–44). Elsevier. <https://doi.org/10.1016/B978-0-12-409548-9.10544-5>
- Breiman, L. (2001). Random Forests. *Machine Learning*, *45*(1), 5–32. <https://doi.org/10.1023/A:1010933404324>
- Dargie, G. C., Lewis, S. L., Lawson, I. T., Mitchard, E. T. A., Page, S. E., Bocko, Y. E., & Ifo, S. A. (2017). Age, extent and carbon storage of the central Congo Basin peatland complex. *Nature*, *542*(7639), 86–90. <https://doi.org/10.1038/nature21048>
- Dias, S. H. B., Filgueiras, R., Fernandes Filho, E. I., Arcanjo, G. S., Silva, G. H. da, Mantovani, E. C., & Cunha, F. F. da. (2021). Reference evapotranspiration of Brazil modeled with machine learning techniques and remote sensing. *PLOS ONE*, *16*(2), e0245834. <https://doi.org/10.1371/journal.pone.0245834>
- Dohong, A., Aziz, A. A., & Dargusch, P. (2018). Carbon emissions from oil palm development on deep peat soil in Central Kalimantan Indonesia. *Anthropocene*, *22*, 31–39. <https://doi.org/10.1016/j.ancene.2018.04.004>
- Geospatial Information Agency. (2018). *DEMNAS*. <https://tanahair.indonesia.go.id/demnas/#/>
- Giesen, W. (1987). *Giesen (1987)—Danau Sentarum Wildlife Reserve- Inventory Ecology and Management Guidelines*. World Wildlife Fund.
- Giesen, W., & Anshari, G. Z. (2018). Danau Sentarum National Park (Indonesia). In C. M. Finlayson, G. R. Milton, R. C. Prentice, & N. C. Davidson (Eds.), *The Wetland Book* (pp. 1841–1850). Springer Netherlands. [https://doi.org/10.1007/978-94-007-4001-3\\_44](https://doi.org/10.1007/978-94-007-4001-3_44)
- Hil, G. (2020). Better Management Through Measurement: Integrating Archaeological Site Features into a GIS-Based Erosion and Sea Level Rise Impact Assessment—Blueskin Bay, New Zealand. *The Journal of Island and Coastal Archaeology*, *15*(1), 104–126. <https://doi.org/10.1080/15564894.2018.1531331>
- Holden, N. M., & Connolly, J. (2011). Estimating the carbon stock of a blanket peat region using a peat depth inference model. *CATENA*, *86*(2), 75–85. <https://doi.org/10.1016/j.catena.2011.02.002>
- Houborg, R., & McCabe, M. F. (2018). A hybrid training approach for leaf area index estimation via Cubist and random forests machine-learning. *ISPRS Journal of Photogrammetry and Remote Sensing*, *135*, 173–188. <https://doi.org/10.1016/j.isprsjprs.2017.10.004>
- Jaenicke, J., Rieley, J. O., Mott, C., Kimman, P., & Siegert, F. (2008). Determination of the amount of carbon stored in Indonesian peatlands. *Geoderma*, *147*(3–4), 151–158. <https://doi.org/10.1016/j.geoderma.2008.08.008>
- Julzarika, A. & Harintaka. (2019). Indonesian DEMNAS: DSM or DTM? *2019 IEEE Asia-Pacific Conference on Geoscience, Electronics and Remote Sensing Technology (AGERS)*, 31–36. <https://doi.org/10.1109/AGERS48446.2019.9034351>

- Keaney, A., McKinley, J., Graham, C., Robinson, M., & Ruffell, A. (2013). Spatial statistics to estimate peat thickness using airborne radiometric data. *Spatial Statistics*, 5, 3–24. <https://doi.org/10.1016/j.spasta.2013.05.003>
- Kuhn, M., & Johnson, K. (2013). *Applied Predictive Modeling*. Springer New York. <https://doi.org/10.1007/978-1-4614-6849-3>
- Kuhn, M., Weston, S., Keefer, C., Coulter, N., & Quinlan, R. (2021). Package “Cubist” (0.3.0) [R].
- Liaw, A., & Wiener, M. (2002). Classification and regression by randomForest. *R News*, 2(3), 18–22.
- McBratney, A. B., Mendonça Santos, M. L., & Minasny, B. (2003). On digital soil mapping. *Geoderma*, 117(1–2), 3–52. [https://doi.org/10.1016/S0016-7061\(03\)00223-4](https://doi.org/10.1016/S0016-7061(03)00223-4)
- Meinshausen, N. (2006). Quantile Regression Forests. *Journal of Machine Learning Research*, 7, 983–999.
- Melling, L. (2016). Peatland in Malaysia. In M. Osaki & N. Tsuji (Eds.), *Tropical Peatland Ecosystems* (pp. 59–73). Springer Japan. [https://doi.org/10.1007/978-4-431-55681-7\\_4](https://doi.org/10.1007/978-4-431-55681-7_4)
- Meyer, F. (2019). *Spaceborne Synthetic Aperture Radar: Principles, Data Access, and Basic Processing Techniques*. <https://doi.org/10.25966/EZ4F-MG98>
- Mitra, S., Wassmann, R., & Vlek, P. L. G. (2005). An appraisal of global wetland area and its organic carbon stock. *Current Science*, 88(1), 25–35.
- Nasrul, B., Maas, A., Utami, S. N. H., & Nurudin, M. (2020). The relationship between surface topography and peat thickness on Tebing Tinggi Island, Indonesia. *Mires and Peat*, 26, 1–21. <https://doi.org/10.19189/MaP.2019.OMB.StA.1811>
- Noi, P., Degener, J., & Kappas, M. (2017). Comparison of Multiple Linear Regression, Cubist Regression, and Random Forest Algorithms to Estimate Daily Air Surface Temperature from Dynamic Combinations of MODIS LST Data. *Remote Sensing*, 9(5), 398. <https://doi.org/10.3390/rs9050398>
- Page, S. E., Rieley, J. O., & Banks, C. J. (2011). Global and regional importance of the tropical peatland carbon pool. *Global Change Biology*, 17(2), 798–818. <https://doi.org/10.1111/j.1365-2486.2010.02279.x>
- Page, S. E., Wüst, R. A. J., Weiss, D., Rieley, J. O., Shoty, W., & Limin, S. H. (2004). A record of Late Pleistocene and Holocene carbon accumulation and climate change from an equatorial peat bog (Kalimantan, Indonesia): Implications for past, present and future carbon dynamics. *Journal of Quaternary Science*, 19(7), 625–635. <https://doi.org/10.1002/jqs.884>
- Quegan, S., Le Toan, T., Chave, J., Dall, J., Exbrayat, J.-F., Minh, D. H. T., Lomas, M., D’Alessandro, M. M., Paillou, P., Papathanassiou, K., Rocca, F., Saatchi, S., Scipal, K., Shugart, H., Smallman, T. L., Soja, M. J., Tebaldini, S., Ulander, L., Villard, L., & Williams, M. (2019). The European Space Agency BIOMASS mission: Measuring forest above-ground biomass from space. *Remote Sensing of Environment*, 227, 44–60. <https://doi.org/10.1016/j.rse.2019.03.032>
- Quinlan, J. R. (1993). *Combining instance-based and model-based learning*. 236–243.
- Quinlan, J. R. (1992). *Learning with continuous classes*. 92, 343–348.
- Ribeiro, K., Pacheco, F. S., Ferreira, J. W., Sousa-Neto, E. R., Hastie, A., Krieger Filho, G. C., Alvalá, P. C., Forti, M. C., & Ometto, J. P. (2021). Tropical peatlands and their contribution to the global carbon cycle and climate change. *Global Change Biology*, 27(3), 489–505. <https://doi.org/10.1111/gcb.15408>
- Rieley, J., & Page, S. (2016). Tropical Peatland of the World. In M. Osaki & N. Tsuji (Eds.), *Tropical Peatland Ecosystems* (pp. 3–32). Springer Japan. [https://doi.org/10.1007/978-4-431-55681-7\\_1](https://doi.org/10.1007/978-4-431-55681-7_1)
- Rosen, P. A., & Kumar, R. (2021). NASA-ISRO SAR (NISAR) Mission Status. *2021 IEEE Radar Conference (RadarConf21)*, 1–6. <https://doi.org/10.1109/RadarConf2147009.2021.9455211>
- Rudiyanto, Minasny, B., Setiawan, B. I., Arif, C., Saptomo, S. K., & Chadirin, Y. (2016). Digital mapping for cost-effective and accurate prediction of the depth and carbon stocks in Indonesian peatlands. *Geoderma*, 272, 20–31. <https://doi.org/10.1016/j.geoderma.2016.02.026>
- Rudiyanto, Minasny, B., Setiawan, B. I., Saptomo, S. K., & McBratney, A. B. (2018). Open digital mapping as a cost-effective method for mapping peat thickness and assessing the carbon stock of tropical peatlands. *Geoderma*, 313, 25–40. <https://doi.org/10.1016/j.geoderma.2017.10.018>
- Ruwaimana, M., Anshari, G. Z., Silva, L. C. R., & Gavin, D. G. (2020). The oldest extant tropical peatland in the world: A major carbon reservoir for at least 47 000 years. *Environmental Research Letters*, 15(11), 114027. <https://doi.org/10.1088/1748-9326/abb853>
- Silvestri, S., Knight, R., Viezzoli, A., Richardson, C. J., Anshari, G. Z., Dewar, N., Flanagan, N., & Comas, X. (2019). Quantification of Peat Thickness and Stored Carbon at the Landscape Scale in Tropical Peatlands: A Comparison of Airborne Geophysics and an Empirical Topographic Method. *Journal of Geophysical Research: Earth Surface*, 124(12), 3107–3123. <https://doi.org/10.1029/2019JF005273>

- Supardi, Subekty, A. D., & Neuzil, S. G. (1993). General geology and peat resources of the Siak Kanan and Bengkalis Island peat deposits, Sumatra, Indonesia. In *Geological Society of America Special Papers* (Vol. 286, pp. 45–62). Geological Society of America. <https://doi.org/10.1130/SPE286-p45>
- Takada, M., Shimada, S., & Takahashi, H. (2016). Tropical Peat Formation. In M. Osaki & N. Tsuji (Eds.), *Tropical Peatland Ecosystems* (pp. 127–135). Springer Japan. [https://doi.org/10.1007/978-4-431-55681-7\\_8](https://doi.org/10.1007/978-4-431-55681-7_8)
- Umarhadi, D. A., Widyatmanti, W., Kumar, P., Yunus, A. P., Khedher, K. M., Kharrazi, A., & Avtar, R. (2021). Tropical peat subsidence rates are related to decadal LULC changes: Insights from InSAR analysis. *Science of The Total Environment*, 151561. <https://doi.org/10.1016/j.scitotenv.2021.151561>
- Verrelst, J., Camps-Valls, G., Muñoz-Marí, J., Rivera, J. P., Veroustraete, F., Clevers, J. G. P. W., & Moreno, J. (2015). Optical remote sensing and the retrieval of terrestrial vegetation bio-geophysical properties – A review. *ISPRS Journal of Photogrammetry and Remote Sensing*, 108, 273–290. <https://doi.org/10.1016/j.isprsjprs.2015.05.005>
- Warren, M. W., Kauffman, J. B., Murdiyarto, D., Anshari, G., Hergoualc’h, K., Kurnianto, S., Purbopuspito, J., Gusmayanti, E., Afifudin, M., Rahajoe, J., Alhamd, L., Limin, S., & Iswandi, A. (2012). A cost-efficient method to assess carbon stocks in tropical peat soil. *Biogeosciences*, 9(11), 4477–4485. <https://doi.org/10.5194/bg-9-4477-2012>
- Wei, Y., Kehm, R. D., Goldberg, M., & Terry, M. B. (2019). Applications for Quantile Regression in Epidemiology. *Current Epidemiology Reports*, 6(2), 191–199. <https://doi.org/10.1007/s40471-019-00204-6>
- Yu, Z., Loisel, J., Brosseau, D. P., Beilman, D. W., & Hunt, S. J. (2010). Global peatland dynamics since the Last Glacial Maximum. *Geophysical Research Letters*, 37(13). <https://doi.org/10.1029/2010GL043584>
- Zhou, J., Li, E., Wei, H., Li, C., Qiao, Q., & Armaghani, D. J. (2019). Random Forests and Cubist Algorithms for Predicting Shear Strengths of Rockfill Materials. *Applied Sciences*, 9(8), 1621. <https://doi.org/10.3390/app9081621>

## INTEGRATION OF SENTINEL-1A SAR, HYDRO DYNAMIC AND TRAJECTORY MODEL OF OIL SPILL AT BALONGAN COASTAL WATER JAVA SEA, INDONESIA

Muhammad HELMI<sup>1</sup>, Agus HARTOKO<sup>2\*</sup>, Hifzhan HUSNA<sup>1</sup>  
and Mochamad Indra Bayu ARDIANSYAH<sup>1</sup>

DOI: 10.21163/GT\_2022.171.05

### ABSTRACT:

Oil spill is a crucial issue for marine ecosystems, it is necessary to develop such a comprehensive and accurate oil spill detection and mitigation plan for counter measure. Balongan coastal water, Java Sea is an oil loading, unloading and refinery station. The study aims to determine the wide extent area, volume and monsoonal trajectory and volume of the oil spill in Balongan coastal water. The new paradigm of this study is the integration of 58 sets of Sentinel-1A SAR data analysis had resulted to 11 data sets confirmed with oil spill events. Then used as spatial reference, date, tide data and classification of oil spill to develop numeric trajectory model using hydrodynamic GNOME software. The numerical trajectory model for oil spill was running up from day-0 to 10 days or 240 hours period. Sea surface current during transition-1 April to May 2019 range 0.038-0.045 m.s<sup>-1</sup>, wind speed range 2.53-3.28 m.s<sup>-1</sup>. Sea surface current during the east monsoon of September 2019 0.191 m.s<sup>-1</sup>, wind speed 4.33 m.s<sup>-1</sup>. Sea surface current during transition-2 October to November 2019 range 0.139-0.214 m.s<sup>-1</sup>, wind speed range 3.16-4.33 m.s<sup>-1</sup>. Sea surface current during the west monsoon of December 2019 to February 2020 in the range of 0.251-0.369 m.s<sup>-1</sup>, wind speed range 2.59-4.42 m.s<sup>-1</sup>. Sea surface current and wind direction in Balongan coastal water Java Sea is predominantly to the northwest direction during the transition-1 April to May 2019 and east season September 2019. Wind and sea surface current during the transition-2 of October to November 2019 and December 2019 – February 2020 is predominantly to the southeast direction. Period of transition-1 April to May 2019 wide of oil spill range 42.80-113.40 km<sup>2</sup> and volume range 29.95-79.38 barrel of light crude oil. During the east monsoon of September 2019 is the lowest oil spill with wide area of 23.25 km<sup>2</sup> and smallest oil spill volume of 11.62 barrel of diesel oil. During transition-2 period October to November 2019 wide area range 65.54-78.66 km<sup>2</sup> volume range 39.07-45.88 barrel of diesel oil and light crude oil. During the west monsoon December 2-19 to February 2020 wide area range 27.08-107.90 km<sup>2</sup> volume range 13.54-82.37 km<sup>2</sup> of medium crude oil, light crude oil and diesel oil. Oil spill after 5 days or 120 hours trajectory model, wide area range of 12.10-57.07 km<sup>2</sup>, and most events during the transition-1 and the east monsoon were dispersing out after 10 days or 240 hours. Oil spill trajectory model after 10 days or 240 hours period wide area range 19.98-144.85 km<sup>2</sup> happened during the transition-2 November to December 2019. Evaporation rate during 10 days trajectory model is in the range of 21.5-56.9 % after 120 hours.

**Key-words:** Sentinel-1A, SAR, Hydrodynamic, Oil spill, Spatial, Temporal, Trajectory

### 1. INTRODUCTION

Oil spill is a mixture of oil, hydrocarbon and drilling cuts such as 'oil-based mud' and seawater. Which can harm to the coastal ecosystems, also both direct and indirect economic losses and long-term adverse effects of the above element interactions (Liu *et al.*, 2015).

---

<sup>1</sup>Department of Oceanography, Faculty of Fisheries and Marine Science and Center of Excellent for Science and Technology (PUI), Center for Coastal Disaster Mitigation and Rehabilitation Studie (CoREM), Diponegoro University, Indonesia, [muhammadhelmi69@gmail.com](mailto:muhammadhelmi69@gmail.com), [hifzhanhusna98@gmail.com](mailto:hifzhanhusna98@gmail.com), [indrabayuardiansyah04@gmail.com](mailto:indrabayuardiansyah04@gmail.com)

<sup>2</sup>Department of Aquatic Resource Management. Faculty of Fisheries and Marine Science. Diponegoro University, Indonesia. \* Corresponding author: [agushartoko.undip@gmail.com](mailto:agushartoko.undip@gmail.com)

Oil spill can cause adverse impacts and damage to mangroves, marine invertebrates, seabirds, marine mammals, as well as the composition of microbial communities. Socio-economic impacts can also be evaluated because they disrupt the water quality for aquaculture and coastal tourism. Public health can also be threatened because of the possible impact into the human food chain (Zhang *et al.*, 2019; Kingston 2022). The existing oil spill trajectory simulation is using 2D-hydrodynamic modelling using the General NOAA Operational Modeling Environment (GNOME) considering that the model has its high predictive accuracy. The modelling is based on Lagrangian discrete elements which allow the simulation of oil spill behavior (spots) during the breakdown process which includes dispersion, evaporation, dispersion, and advection (Balogun *et al.*, 2021). Qiao *et al.* (2019) examined the three-dimensional oil spill modeling to simulate and project the short- and long-term trajectories of oil slicks and oil-contaminated water leaking from debris in the Ryukyu Island Chain, Tsushima Strait, on the southern and eastern coasts of Japan. This research used the data of seawater temperature, ocean currents, wind and surface waves using the Lagrangian method which has been successfully applied to produce oil spill trajectory models. Various previous study with the use of 2D-hydrodynamics using GNOME conducted by Heidaria *et al.*, (2019), Naz *et al.*, (2021) and Balogun *et al.*, (2021). In conducting the hydrodynamic modelling using GNOME simulation to determine the trajectory of oil spills and effect of seasonal wind direction in the form of wind rose.

The previous 2D-hydrodynamic modelling study more focused on the trajectory of oil spills, but not yet to the volume of oil spills. To fill in the gaps of the previous research, this study will implement an integrated approach to the use of SAR radar data and hydrodynamic modeling and ultimately the volume of the oil spill. Synthetic Aperture Radar (SAR) satellite is a versatile sensor that can be operated in any weather and time of day or night (Fletcher, 2012; Josaphat and Nobuyoshi, 2016; Rajendran *et al.*, 2021). SAR data is commonly used to monitor oil spills at sea where the microwave beam is emitted by the sensor and the received signal is reflected into the backscatter object features (Fan *et al.*, 2015). In this case, the best method is using the digital number or spectral signature by means of the threshold spectral value analysis to detect the dark object as the oil spill, and spatial-temporal analysis approach (Cantona *et al.*, 2019; Chaturvedi *et al.*, 2020; Fan *et al.*, 2015; Li *et al.*, 2019). Balongan coastal water, Indramayu Regency Java Sea is extensively used for oil refinery, and distribution processed crude oil activities and gas companies. Crude oil supply activities to the Balongan refinery generally use oil tankers originating from Riau province, Sumatera. The oil tankers or carrier ships are moored at the mooring facilities, namely Single Point Mooring (SPM) with the Jetty Cargo facility. Through SPM, crude oil carried by transport ships is unloaded and transported to the Balongan oil refinery. This makes Balongan coastal water becomes a highly oil spill risk coastal water (Sinurat *et al.*, 2016). A comprehensive study is needed to determine the distribution of the oil spill trajectory to determine further policies in dealing with especially to estimate how and where the oil can spread (Heidaria *et al.*, 2019). The analysis represents the observed natural phenomena in the spatial and temporal dimensions where the data considered the spatial dependencies between the observed areas and its correlation of one or several time periods image data.

The new paradigm in study is aimed to apply integration of processed Sentinel-1A SAR to determine the initial, actual and wide area of the oil spill and 10 days trajectory modelling or spatial distribution pattern after the initial oil spills and ultimately analysis the volume of oil spills using GNOME method for four monsoons period namely transition-1 (March-April-May), the east monsoon (June-July-August, September), transition-2 (October-November) and west monsoon (December-January-February). The result of study can provide comprehensive data and information on oil spills to the oil companies and operators, environmentalists, and researchers in carrying out mitigation efforts and handling strategies. The spatial numerical model in this study can be adapted and implemented in other areas where oil spills frequently occur.

## 2. STUDY AREA

The study area is located in Balongan coastal water, Indramayu Regency Java sea, with coordinates of 6°14'2.72" - 6°28'50.96" South Latitude and 108°20'38.84" - 108°35'40.24" East Longitude (**Fig. 1**). The field study was conducted for one year from April 2019 to April 2020.

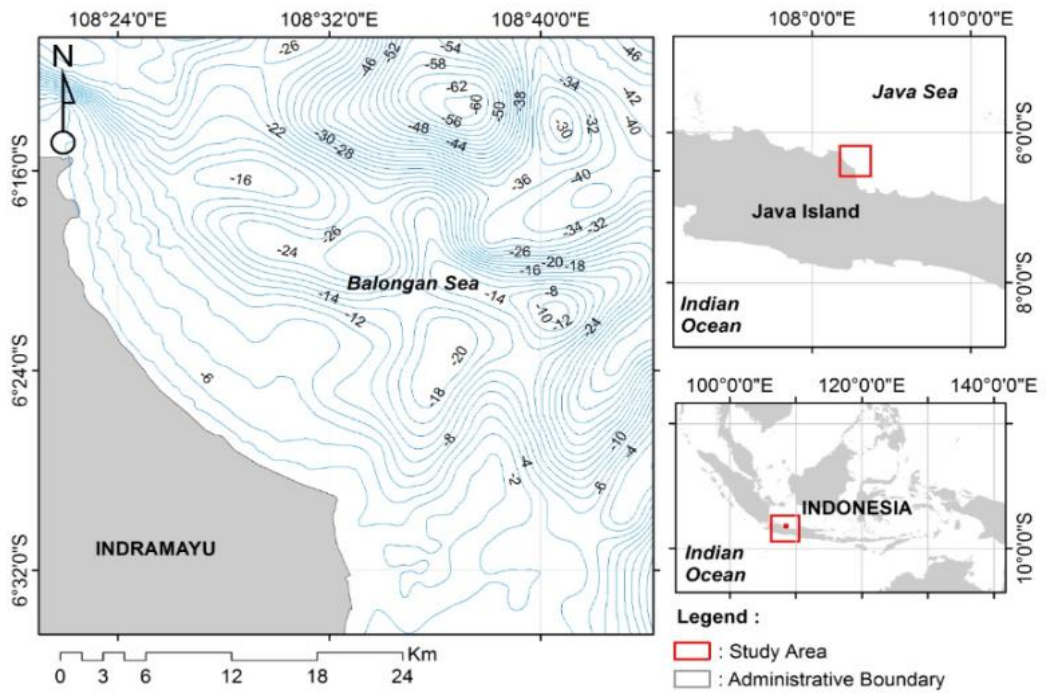


Fig. 1. Map of the study area and bathymetry.

### 3. DATA AND METHODS

#### 3.1. Data

##### 3.1.1. Wind and Current Data

The horizontal wind direction and wind speed data was obtained from the European Centre for Medium Range Weather Forecasts (ECMWF-<https://www.ecmwf.int>) and represent for 12-months period, starting from April 2019 – March 2020. The obtained wind data was then processed into the components of wind speed of u-component and v-component. After obtaining the direction and total wind speed, the data was displayed in the form of wind rose using WRPlot software. Data of sea surface current was collected from the Hybrid-Coordinate Ocean Model (HYCOM - <https://www.hycom.org>) for one year period. The initial current data was firstly arranged using Microsoft Excel software by selecting the data collection time, coordinates, depth, u-component and v-component. The work was continued using GIS data processing application for the interpretation of the vector direction and velocity of the sea surface current. To produce the total current speed or velocity and direction, the u and v data were compiled and grouped using Ms. Excel. The processed wind data was then used as input data in the modelling of sea surface current speed and direction, and ultimately used for the oil spills hydrodynamic modell using GNOME software to produce the oil spill trajectory modell.

##### 3.1.2. Oil Properties

Oil properties served was used as input for the model for the distribution of oil spills (**Table 1**). The data was in the form of oil, which was distributed through SPM (Single Point Mooring) and Loading Jetties of the state owned PT. Pertamina RU VI Balongan oil refinery. The data on oil loading and unloading activities at Balongan coastal water is used to build the spatial model and assist in analysing the results of oil spill detection. This data was obtained from the oil and gas loading and unloading schedule from PT. Pertamina RU VI Balongan. The data of ship coordinates, ship loading capacity and ship sailing time were used in analysing the type and source of the oil spill.

**Table 1.**  
**Oil Properties (Sun *et al.* 2016; Yu. *et al.*, 2018)**

Oil Properties	Diesel	Light Crude Oil	Medium Crude Oil
API gravity (deg)	44	31	26
Molecular average weight	194	199	262
Saturation (±1 wt %)	84	71	52
Aromatic (±1 wt %)	12	15	27
Resins (±1 wt %)	4	14	21
n-C7 Asphaltene stability	-	<i>stable</i>	<i>stable</i>
Wax Appearance	18	27	25
Temperature (±1 °C)			
Wax content (wt %)	-	3.1	2.1
SARA analysis at 65 °C.			

### 3.2. Oil Spill Spatial Distribution

Sentinel-1A SAR is a dual-polarization image data with specifications VV (vertical transmit and vertical receive) and VH (vertical transmit and horizontal receive) Level-1 Ground Range Detected (GRD) obtained from Copernicus Open Access Hub (<https://scihub.copernicus.eu/>). This data represent the period of April 2019 to March 2020, was processed using the SNAP 6.0 application with image correction stages which included geometric, radiometric, and speckle filtering (noise correction). Oil spill detection was carried out using the adaptive threshold method. This method processed dark objects, which are an indication of an oil spill, using the Oil Spill Detection Tool, which is part of the Ocean Application in the SNAP application (Li, 2019). The spatial Sentinel-1A SAR image data was first geometrically corrected to the World Geodetic System, namely WGS 1984 (Hartoko *et.al*, 2016; Hartoko *et.al*, 2019; Fitriyanto *et al.*, 2019). The process of detecting dark objects, which is an indication of an oil spill, used the adaptive threshold method on the Oil Spill Detection tool. If the maximum intensity value is below the average plus a predetermined standard deviation, it can be used to set an adaptive threshold. This limit is used to avoid oil spill detection errors (false negative). After the value was analysed, it would be tested using a quartic function and a negative exponential function as in the equation 1 and 2 below:

$$Y = -6.3401 \times 106X_4 + 0.00073027X_3 - 0.029919X_2 + 0.50015X - 2.6381 \tag{1}$$

$$Y = 7.4199 e^{-0.18212X} \tag{2}$$

where X is the value of the original pixel

Y is the value of the dark pixel value representing for the oil spill object.

The use of these functions would result several referred areas that were originally suspected of being an oil spill zone but are actually negative because these areas are not included in the threshold criteria (Mera *et al.*, 2012; Cantorna, 2019; Chaturvedi *et.al*, 2020).

### 3.3. Oil Spill Volume

The detection of an oil spill that has been carried out in an interpretation of the dark spot spectrally detected as an oil spill area from the Sentinel-1A SAR data. The data interpretation stage was carried out over a period of 12 months, which was in April 2019 - March 2020. The image was processed using the SNAP application and then it produced a map of the oil spill for each month. Total of 11 image detected with oil spill were obtained from total of 58 processed images. These results represents for the temporal and spatial of oil spill in area of Balongan coastal water. The classification of oil types was determined based on the plot profile value of each pixel in the image. By integrating it with the loading and unloading schedule of ships at Balongan coastal water, the type of oil spill could be determined from PT PERTAMINA Balongan. This thickness value would imply to the classification the oil spill as in **Table 2**. Using the oil type and thickness and the wide extent of

the oil spill could determine the total volume of oil spill. Each image detected with oil spill through Sentinel image processing integrated with classification of oil spill. The volume data was important because it was needed as input data in hydrodynamic modelling of oil spill trajectory.

**Table 2.**  
**Classification of oil spill thickness according to Sun *et al.* (2016).**

Plot Value (dB)	Thickness ( $\mu\text{m}$ )	Oil Type
-15 – (-20)	$\leq 50$	Diesel
-20 – (-25)	50-200	Light Crude Oil
-25 – (-30)	200-1000	Medium Crude Oil

### 3.4. Oil Spill Trajectory Using Hydrodynamic Numerical Model

Oil spill numeric spatial modelling was generally built using the GNOME application with the TxBLEND hydrodynamic model. This model uses the sea surface current data from the Hybrid-Coordinate Ocean Model (HYCOM) and wind data from the European Centre for Medium Range Weather Forecasts (ECMWF). The process was continued with the oil spill modelling by entering the oil properties and oil spill volume obtained from the spatial model image analysis for the period April 2019 to March 2020 that had been carried out previously. Sea surface current and oil spill model simulations were carried out for 48 hours (2 days), 96 hours (4 days), 144 hours (6 days), 192 hours (8 days) and 240 hours (10 days). Sea surface current modelling produced the **u**-velocity and **v**-velocity. The model is a representation of state, object, and event of the oil spill. The representation must be realized in a simple form, by eliminating or minimizing complex variables that are not directly related to the model (Susanti *et al.*, 2019).

Processing the TxBLEND model in GNOME applied the continuity equation, momentum equation and diffusion equation to solve water transport and circulation patterns. The following equations were used to built the spatial numerical model on the trajectory of oil spills in the seawater:

$$\frac{\partial^2 \xi}{\partial t^2} + G \frac{\partial \xi}{\partial t} - \nabla \cdot \left\{ \nabla \cdot (H \vec{V} \vec{V}) + gH \nabla \xi + \frac{gH^2}{2\rho} \nabla \rho + f \times H \vec{V} - HA \right\} + (G - \tau) \nabla \cdot (H \vec{V}) - H \vec{V} \cdot \nabla \tau = G \cdot (r - e) \quad (3)$$

$$\frac{\partial q_i}{\partial t} + \frac{\partial u q_i}{\partial x_i} + \frac{\partial v q_i}{\partial x_i} + gH \frac{\partial \xi}{\partial x_i} + \tau q_i = r_i \quad (4)$$

$$\frac{\partial C}{\partial t} + u \frac{\partial C}{\partial x} + v \frac{\partial C}{\partial y} - \frac{\partial}{\partial x} \left( D_x \frac{\partial C}{\partial x} \right) - \frac{\partial}{\partial y} \left( D_x \frac{\partial C}{\partial y} \right) = s \quad (5)$$

where  $\xi$  defines the water level elevation,

$\tau$  is the basic friction,

$r_i$  is the wind stress and the Coriolis parameter,

$s$  is the substance concentration  $C$ ,

$G$  is the law of continuity.

The sea surface current divergence was calculated from the surface current data (Nordam *et al.*, 2019; Wirasatriya *et al.*, 2020). The spatial modelling of the oil spill trajectory was analysed based on the numerical transformation of current and tidal data (Hartoko *et al.*, 2016; Hartoko *et al.*, 2019). Oil spill modelling is generally done using GNOME software with eularian-lagrangian hydrodynamic model. This equation approach is a simulation involving large and small particles in the sea surface water and examining the mass and momentum of the spilled oil (Remyalekhsmi and Hedge, 2013). This modelling used the data base maps of the Global Custom Maps Generator on NOAA, surface current data of the Hybrid-Coordinate Ocean Model (HYCOM) and wind data of the Global Forecast System (GFS). Then proceed with oil spill modelling by inputting the oil properties and oil spill volume obtained from the analysis for the period April 2019 to April 2020 that was carried out previously.



The following formula of Eulerian-Lagrangian particle tracking method, where  $L$  defines as the initial position of the particle at  $t_0 + \Delta t$ ,  $L_0$  is the position of the particle at  $t_0$ , and  $V_t$  is the speed of movement of the oil particles (Yang *et al.*, 2013).

$$L = L_0 + \int_{t_0}^{t_0 + \Delta t} V_t(t_0, y(t_0), t_0) dt \tag{6}$$

The particle velocity movement method was applied as follows, where  $V_t$  is the current speed at  $t$ ,  $V_w$  is the wind speed at  $t$  and  $\alpha V_w$  is a linear current driven by the wind carried out by the GNOME model (Yang *et al.*, 2013).

$$V = V_t + \alpha V_w \tag{7}$$

### 3.5. Oil Volume Estimation After Degradation and Evaporation

The estimated volume of an oil spill could be determined using oil property data (oil characteristic) and wind data, both are processed using the ADIOS 2 (Automated Data Inquiry for Oil Spills) application. Data of oil volume were obtained with integration of oil type and thickness, wind data, current data and wide area. Then the data became input data that was simulated to determine the volume of oil spills from the first day the oil spilled into the waters until the next 5 days. The volume of the oil spill was influenced by salinity, SST, density, wind, waves, and surface currents. These factors will affect the volume of oil which experience the process of dispersion, evaporation, emulsification, spreading, benzene contamination, sinking to the bottom of the water, leakage rate, heat burning due to atmospheric temperature. To determine the evaporation rate of an ADIOS 2 spill, the Pseudo Component (PC) evaporation model was used, with the equation used in the model as follows:

$$\left(\frac{dV}{dt}\right)_j \propto \frac{U^3 V (P_v v f_m)_j}{d} \tag{8}$$

where  $j$  determines a certain PC,  $f_m$  is the variable molar fraction of the pseudo component,  $V$  is the volume of oil,  $U$  is the wind speed, and  $d$  is the thickness. The relative molar volume is  $v$  (Lehr *et al.*, 2002).

## 4. RESULTS

### 4.1. Wide Area and Volume of Oil Spill

Total of 58 sets processed Sentinel-1A SAR image data had been analyzed representing the period of April 2019 to March 2020, had resulted to 11 images indicates with oil spill (**Table 3, Figures 2, 3, 4 and 5**). These results represent for the temporal and spatial of oil spill in area of Balongan coastal water. The classification of oil types was determined based on the plot profile cluster of pixel value of each 11 image. The dark spots spectral value detected with oil spill found during the transition-1 in Sentinel-1A SAR data recorded on April 8, 2019 wide area of oil spill is 88.30 km<sup>2</sup> volume 61.81 barrel. Sentinel-1A SAR image data of April 16, 2019 with wide area of 113.40 km<sup>2</sup> volume 79.38 barrel, data of May 26, 2019 with wide area of 42.80 km<sup>2</sup> volume 29.95 barrel all with category of light crude oil. The category of diesel oil spill were found in Sentinel-1A SAR data during the east monsoon September 11, 2019 with wide area of 23.25 km<sup>2</sup> and volume 11.62 barrel. Sentinel-1A SAR data during the transition-2 of October 13, 2019 wide area of 78.66 km<sup>2</sup> volume 39.33 barrel and Sentinel-1A SAR data in November 10, 2019 wide area of 78.13 km<sup>2</sup> volume 39.07 barrel of diesel oil category and data of November 18, 2019 wide area 65.54 volume 45.88 barrel of light crude oil. The Sentinel-1A SAR image data during the west monsoon of December 12, 2019, was recorded with category of medium crude oil spill with wide area of 91.52 km<sup>2</sup> volume 82.37 barrel. Data of December 16, 2019 wide area 107.90 km<sup>2</sup> volume 75.53 barrel. Data in January 9, 2020 wide area 56.70 km<sup>2</sup> volume 28.35 barrel and data in February 14, 2020 wide area of 27.08 km<sup>2</sup> volume 13.54 barrel.

**Table 3.**  
**The date, season, wide area and volume of oil spill based on Sentinel-1A SAR data.**

No	Date Detected	Monsoon	Wide Area Detected (km <sup>2</sup> )	Volume Detected (barrel)	Oil Type Detected
1	08/04/2019	Transt-1	88.30	61.81	Light crude oil
2	16/04/2019	Transt-1	113.40	79.38	Light crude oil
3	26/05/2019	Transt-1	42.80	29.95	Light crude oil
4	11/09/2019	East monsoon	23.25	11.62	Diesel oil
5	13/10/2019	Transt-2	78.66	39.33	Diesel oil
6	10/11/2019	Transt-2	78.13	39.07	Diesel oil
7	18/11/2018	Transt-2	65.54	45.88	Light crude oil
8	12/12/2019	West monsoon	91.52	82.37	Medium crude oil
9	16/12/2019	West monsoon	107.90	75.53	Light crude oil
10	09/01/2020	West monsoon	56.70	28.35	Diesel oil
11	14/02/2020	West monsoon	27.08	13.54	Diesel oil

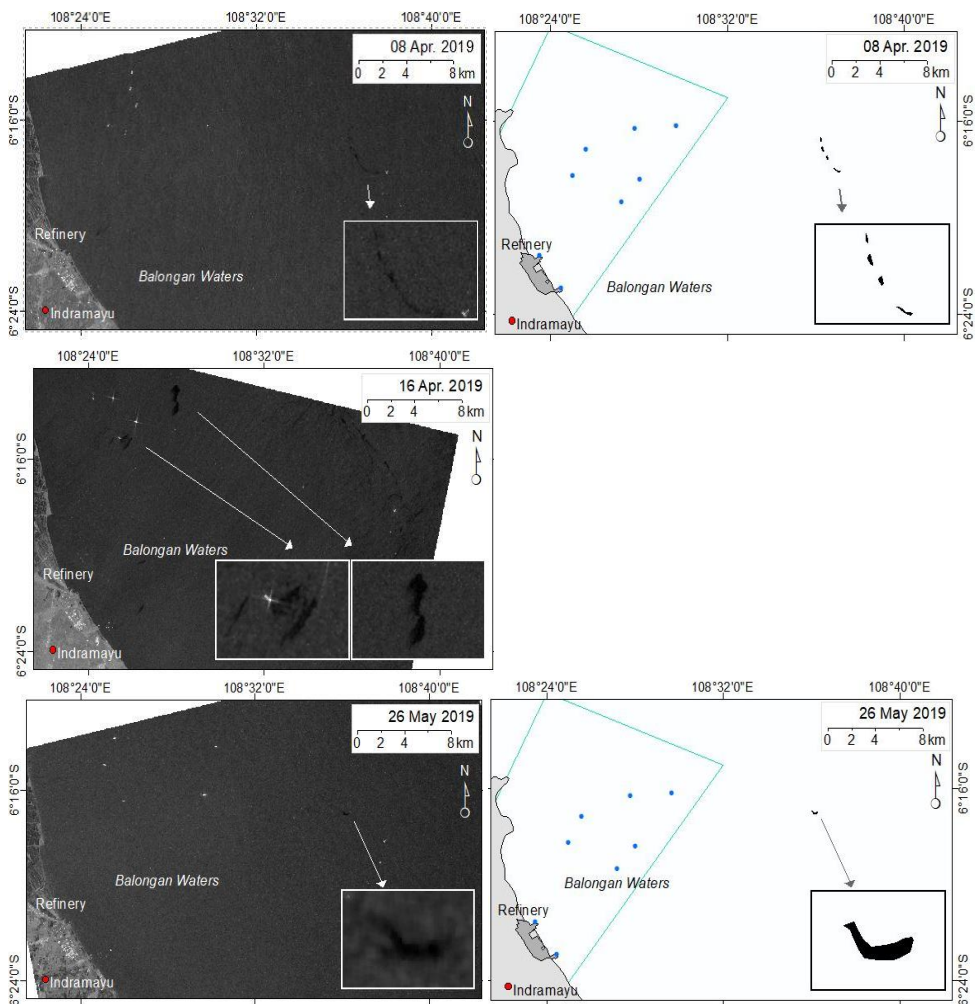


**Fig. 2.** Oil Spill Analysis of Sentinel-1A SAR Transition-1 April-May 2019.

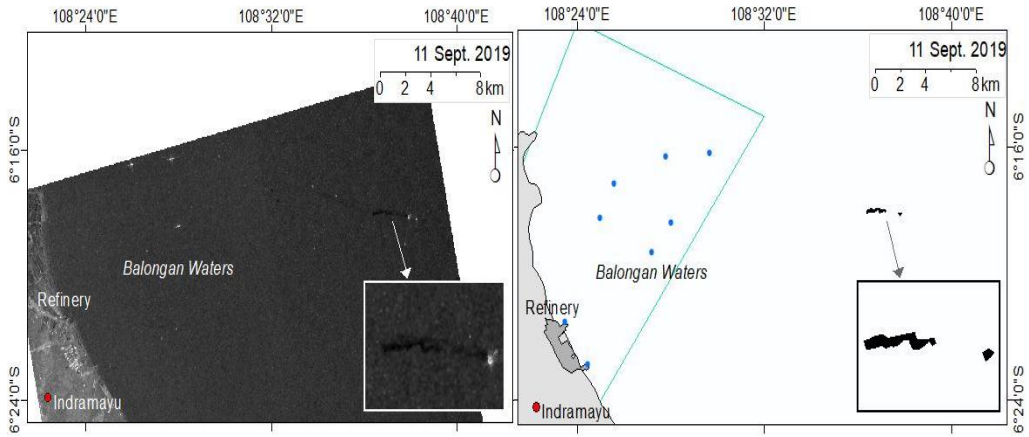


Fig. 3. Oil Spill Analysis of Sentinel-1A SAR East Monsoon September 2019.

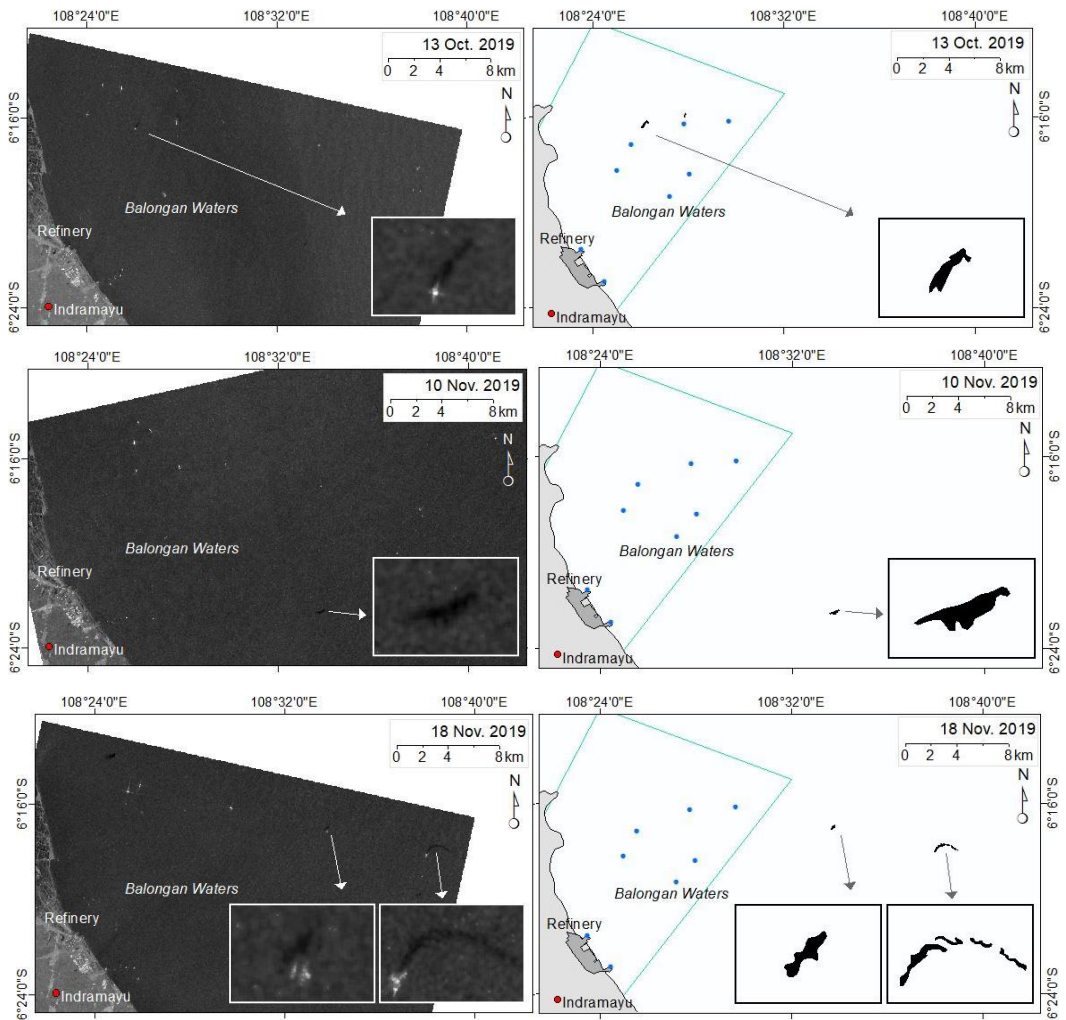
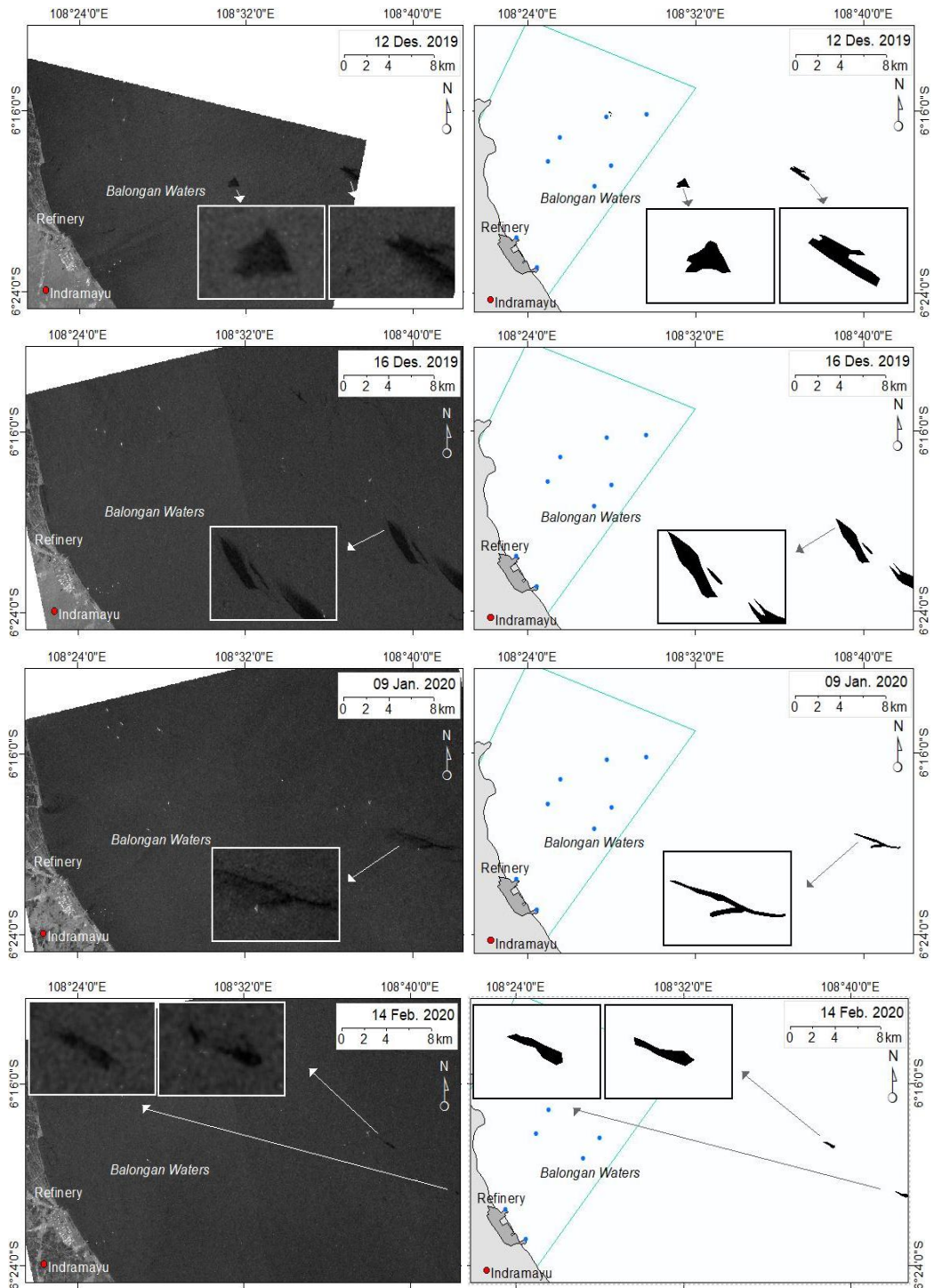


Fig. 4. Oil Spills Analysis of Sentinel-1A SAR During Transition-2 October – November 2019.



**Fig. 5.** Oil Spills Analysis of Sentinel-1A SAR During West Monsoon December 2019, January-February 2020.

The category of oil spill which are determined based on the spectral value at each oil spill plot profile, will indicate that the smaller the spectral value was indicator as the thicker the layer of oil spill in seawater. The thicker of the oil spill layer in seawater was assumed as the thicker oil spill



viscosity, which classified as a medium crude oil. Likewise, when the spectral value of the dark spot profile detected is higher spectral value then will be categorized as oil spill with a lower viscosity, which in this case include the category of diesel oil. Meanwhile, when the spectral value is in between of the two-plot profile value is classified as the light crude oil, refer to American Petroleum Institute (API) has the gravity value of 30 - 39.9. The medium crude oil class has API Gravity value of 22 - 29.9 and diesel classified to super-light crude oil with API more than 40 (Sauz *et al.*, 2018).

#### 4.2. Wind and Sea Surface Current Speed and Directions

The numerical wind data obtained from European Centre for Medium Range Weather Forecasts is specifically represent the study area at Balongan coastal water only. Predominant wind direction during the transition-1 of April and May 2019 is from the east with speed range of 2.10– 5.70 m.s<sup>-1</sup> (Fig. 6). Predominant wind direction during the east monsoon is southeast direction with speed range of 3.60-5.70 m.s<sup>-1</sup> (Fig. 7). Predominant wind direction during the transition-2 of October-November 2019 is southeast direction with speed range of 2.10-5.70 m.s<sup>-1</sup> (Fig. 8). Predominant wind direction during the west monsoon December 2019-February 2020 is from the west with wind speed range of 2.10-5.70 m.s<sup>-1</sup>.

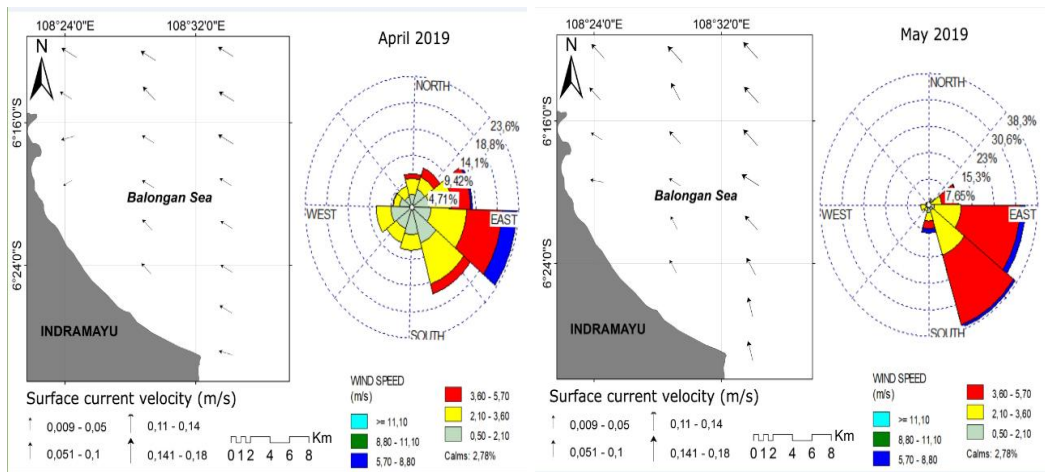


Fig. 6. Sea surface current and wind direction and speed of the transition-1 of April-May 2019.

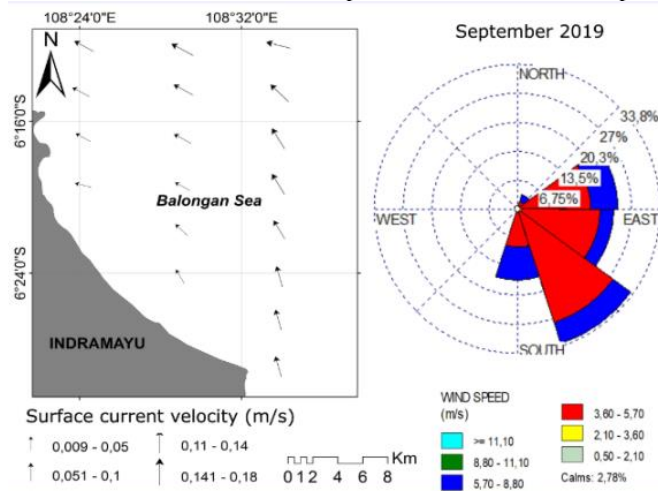
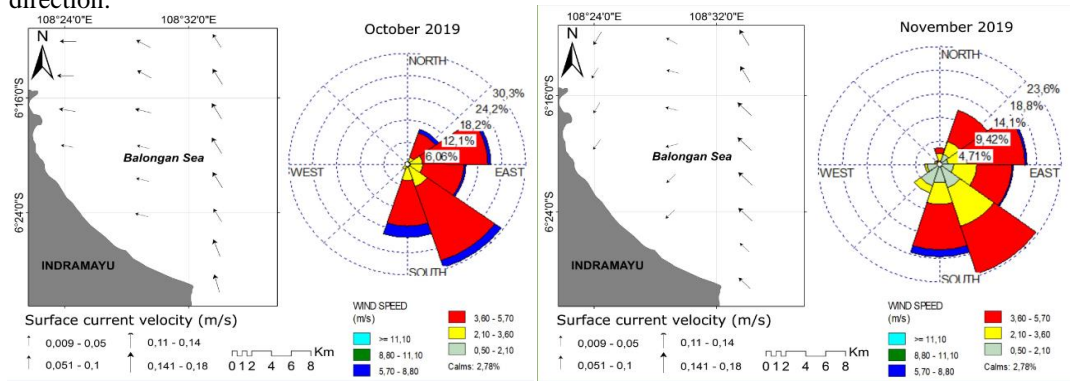
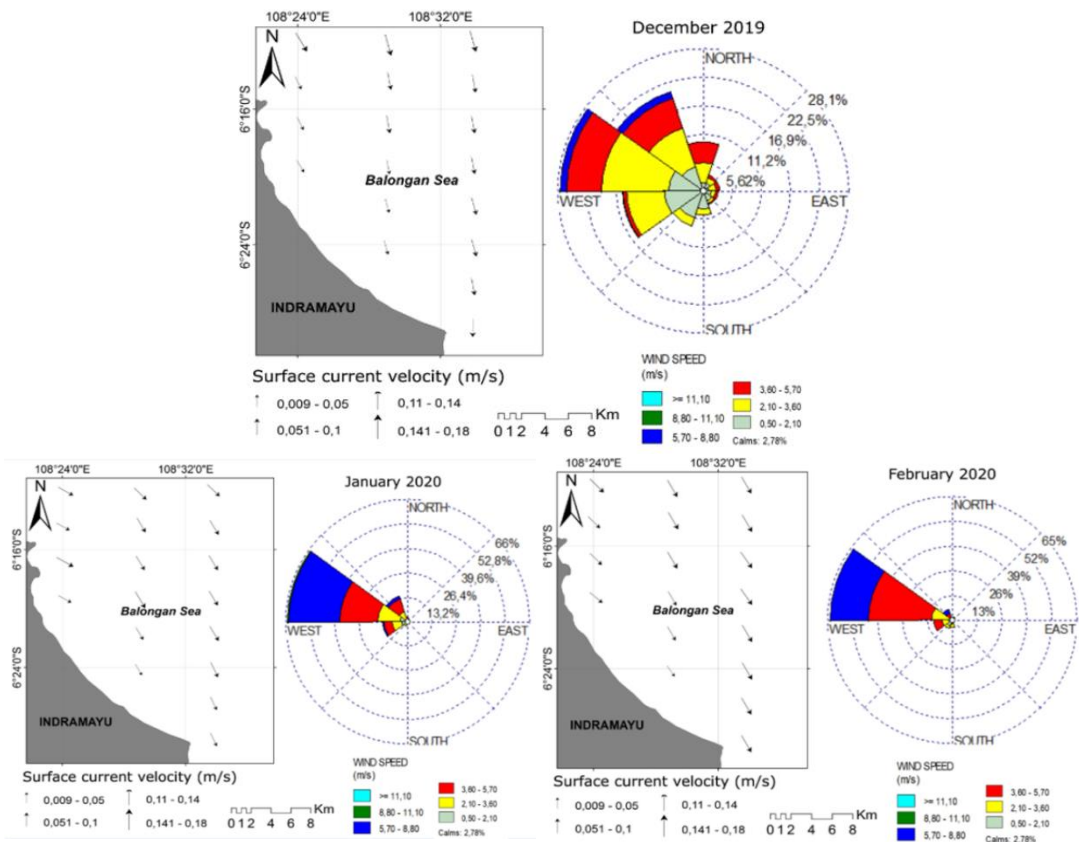


Fig. 7. Sea surface current and wind direction and speed in the east monsoon September 2019.

The result of spatial models for the sea surface current are presented in **Figures 6,7,8 and 9** was developed using data of the physical variables of the seawater such as the average seawater temperature, wind (**Table 4**). The sea surface current in the transition-1 occurred in May 2019 was found as the weakest with  $0.038 \text{ m}\cdot\text{s}^{-1}$  current speed and predominantly of northwest direction. The current is lightly increase during the east monsoon of September 2019 and weak again during the transition-2 of October and November 2019. The strongest sea surface current was happened during the west monsoon of February 2020 with current speed of  $0.369 \text{ m}\cdot\text{s}^{-1}$  with predominantly southwest direction.



**Fig. 8.** Sea surface current and wind direction and speed of the transition-2 October-November 2019.



**Fig. 9.** Sea surface current and wind direction and speed of the west monsoon December 2019 and January – February 2020.

Table 4.

**Data of sea surface current and wind direction and speed.**

Month	Average Current Speed (m.s <sup>-1</sup> )	Average Current Direction	Average Wind Speed (m.s <sup>-1</sup> )	Average Wind Direction
April 2019	0.045	Northwest	2.53	West
May 2019	0.038	Northwest	3.28	West
September 2019	0.191	Northwest	4.33	West
October 2019	0.214	Northwest	3.16	West
November 2019	0.139	West	2.51	Southwest
December 2019	0.251	Southeast	2.59	Southeast
January 2020	0.336	Southeast	4.42	East
February 2020	0.369	Southeast	4.19	East

**4.3. Oil Spill Spatial Distribution and Trajectory**

Result of each of 11 Sentinel-1A SAR data analysis confirmed with oil spill was used as reference to build the trajectory pattern from program running from day-0 to day-10 with input data of wind, sea surface current and tide. Also integrated with the loading and unloading schedule of ships at Balongan coastal water, the type of oil carried by the ships was obtained from PT PERTAMINA Balongan, and produce the trajectory pattern of oil spill using GNOME software. Specifically, the result of spatial distribution, wide area and the trajectory pattern of oil spills were represents type of medium crude oil, light crude oil and diesel oil spill which had indicated to follow the pattern of the sea surface current movement in Balongan coastal water, for four seasons are presented in **Figures 10, 11,12,13** and **Table 4**.

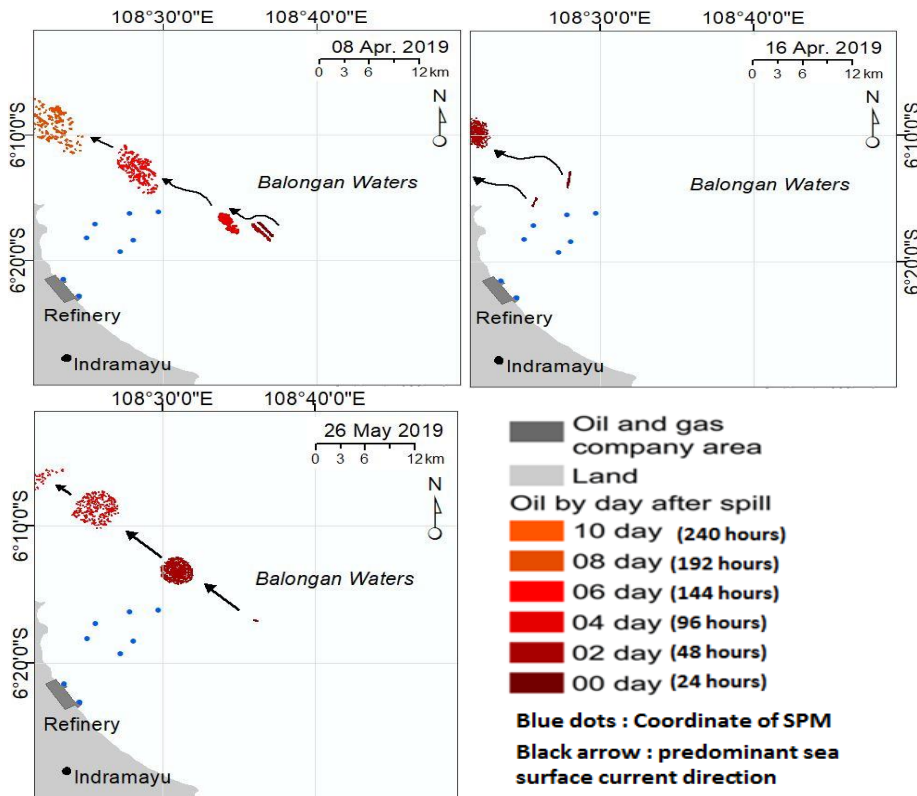


**Fig. 10.** The northwest oil spill trajectory direction at Balongan coastal water during the transition-1 from April-May 2019. Blue dots are SPM coordinates, red class of oil spill after 10 days trajectory modell.



During the transition-1 period of April-May 2019 (**Fig. 10**) predominant trajectory of oil spill is to the northwest direction from day-0 to day-10. Wide area at day-0 is range of 42.80-113.40 km<sup>2</sup> and dispersing out of the study area after 240 hours (**Table 5**). Following the east monsoon period (**Fig. 11**) which is only represented in data of September 11, 2019, the spatial trajectory of oil spill pattern to the northwest direction, and wide area of 23.25 km<sup>2</sup>. During the transition-2 in October – November 2019 (**Fig. 12**), oil spill trajectory still with the northwest direction pattern, with wide area of oil spill range 65.54-78.66 km<sup>2</sup>. In the west monsoon period of December 2019, January-February 2020 (**Fig. 13**) oil spill trajectory in contrary to the southeast direction pattern, with wide area range 27.08-107.90 km<sup>2</sup> (**Table 5**).

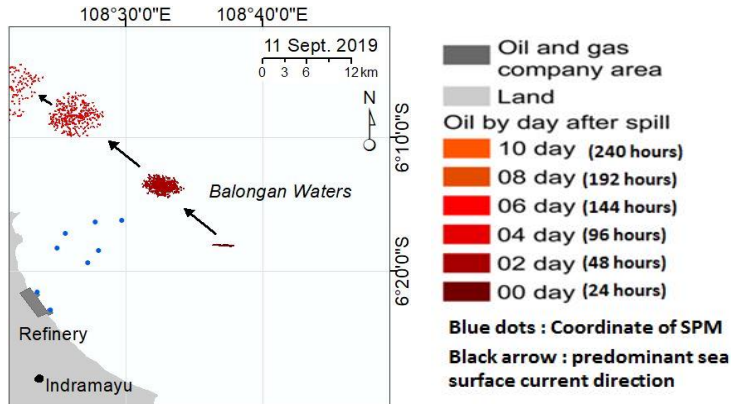


**Fig. 11.** The northwest oil spill trajectory direction at Balongan coastal water during the east monsoon in September 2019. Blue dots are SPM coordinates, red class of oil spill after 10 days trajectory modell.

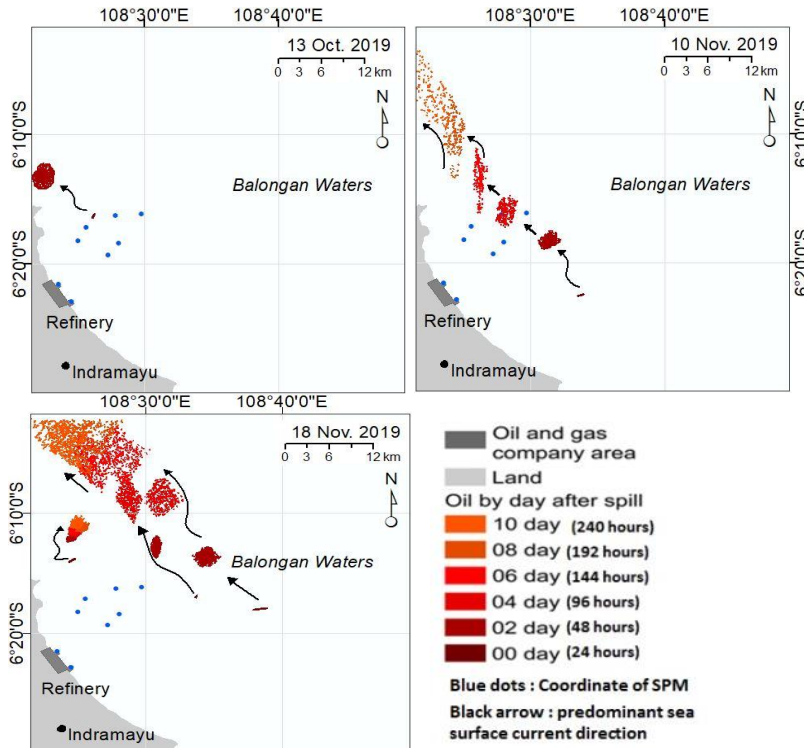


**Fig. 12.** Predominant northwest oil spill trajectory direction at Balongan coastal water during the transition-2 from October to November 2019. Blue dots are SPM coordinates, red class of oil spill after 10 days trajectory modell.

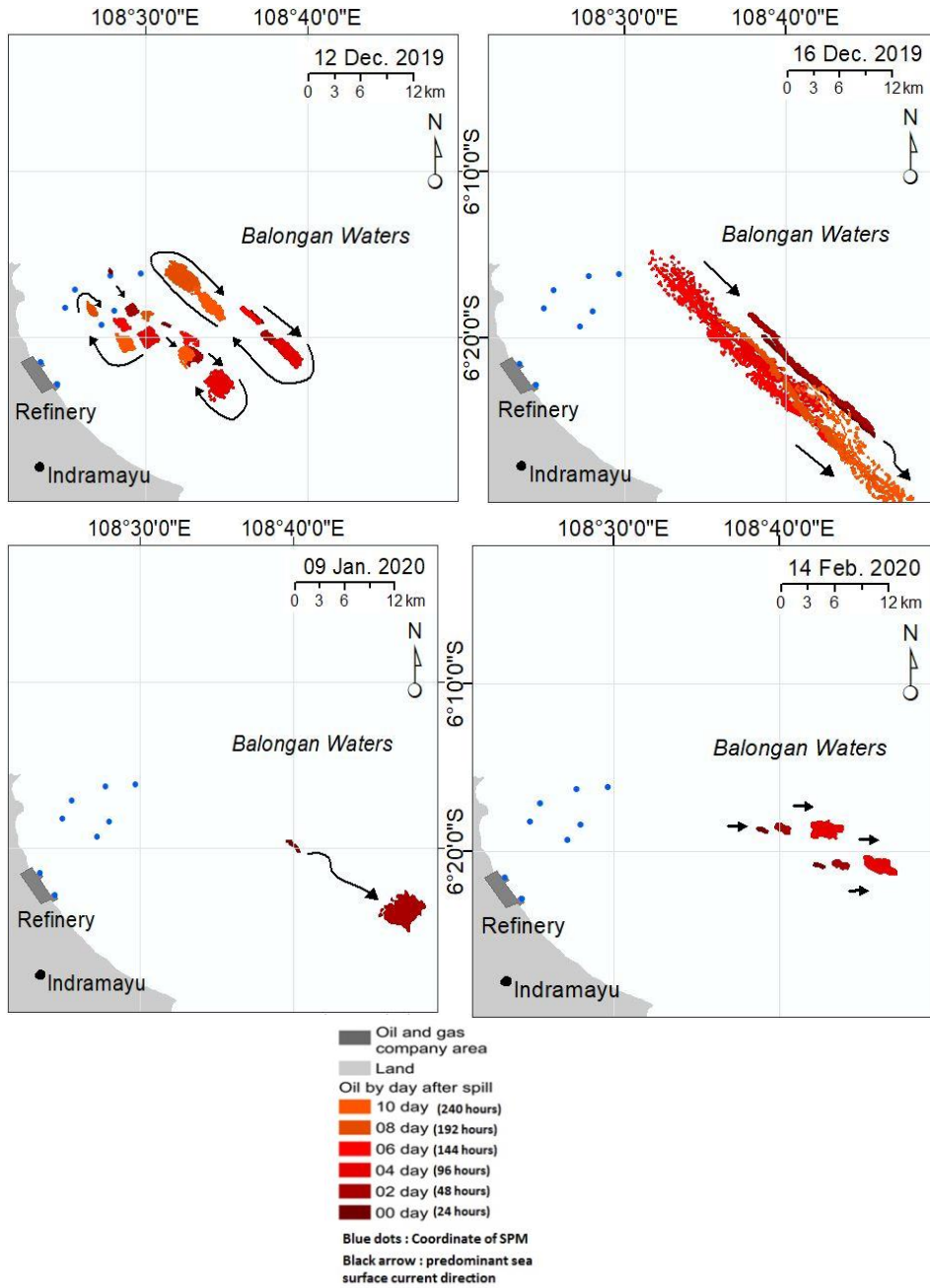


**Fig. 13.** Predominant southeast trajectory direction of oil spill at Balongan coastal water during the west monsoon from December 2019 to February 2020. Blue dots are SPM coordinates, red class of oil spill after 10 days trajectory modell.

#### 4.4. Oil Spill Volume After Dispersion and Evaporation

The numerical oil trajectory model using GNOME after the evaporation as in **Table 5**.

Table 5.

## The wide extent and volume of the oil spill using the GNOME model.

No	Date Detected/ Starting Model	Area Detected (km <sup>2</sup> )	Area After 120 hours (km <sup>2</sup> )	Area After 240 hours (km <sup>2</sup> )	Volume Detected (barrels)	Volume After 120 hours (barrel)	Evaporation after 120 hours (%)
1	08/04/2019	88.30	<b>57.07</b>	-	61.8	33.9	45.1
2	16/04/2019	113.40	-	-	79.3	58.7	26.0
3	26/05/2019	42.80	37.75	-	29.9	20.1	32.5
4	11/09/2019	23.25	25.40	-	11.6	5.0	<b>56.9</b>
5	13/10/2019	78.66	-	-	39.3	21.2	46.1
6	10/11/2019	78.13	37.01	19.98	39.0	20.4	47.7
7	18/11/2019	65.54	16.71	93.54	45.8	24.5	46.5
8	12/12/2019	91.52	12.10	79.90	<b>82.3</b>	<b>64.6</b>	21.5
9	16/12/2019	107.90	14.64	<b>144.85</b>	75.5	41.9	44.5
10	09/01/2020	56.70	-	-	28.3	14.2	49.9
11	14/02/2020	27.08	-	-	13.5	5.9	56.4

Note : the (-) indicate that oil spill had left from the extent of model area.

## 5. DISCUSSIONS

After four seasonal wind and sea surface current analysis, two predominant wind and sea surface current directions, are east and northeast direction during transition-1 and east monsoon and south to southeast direction during transition-2 and the west monsoon, this in accordance to the study of Alifidini et.al., (2021) as part of regional pattern of Java and Indonesian seas.

Analysis of 58 Sentinel-1A SAR data sets resulted to 11 data sets representing the real field oil spill events for four period from April 2019 to February 2020. Each data was used to build for further oil spill trajectory spatial modell from day-0 to day 10 (240 hours). The oil spill spatial trajectory modell carried out on diesel oil spill had indicated a longer distribution distance compared to the distribution distance of medium crude oil and light crude oil. During the east monsoon condition, in September 11, 2019 and during the transition-2 period of October 13, 2019, type of diesel oil spill of had spreaded to the northwest leaving Balongan coastal water before 240 hours period of the numerical model run. This has showed that the light density of diesel oil was very easy to flows in accordance to the sea surface currents and also easily evaporates. Similar to what happened in the west monsoon, diesel oil spill the during period of January 9 and February 14, 2020 was also very quickly left Balongan coastal water towards the southeast direction before the numerical model had been ranned for 120 hours period. During the east monsoon, the light crude oil spill for the period of April 8 and 16, and May 26, 2019, after the numerical modell ranned for 240 hours, had shown the oil spills spread out from Balongan coastal water to the northwest direction. During the west monsoon, the light crude oil spill had moved to the southeast direction in the period of October 18 and December 16, 2019. This was in accordance with the movement of the sea surface currents that flows to the northwest and southeast according to the monsoon. Likewise, the medium crude oil spill which has a higher oil density than diesel and light crude oil, had moved in the same direction as the direction of the sea surface current, but with slower movement and distribution than the other two types of oil spill.

Oil spill spatial trajectory analysis using GNOME method, revealed that the period of the oil spills detected were happened almost evenly distributed at every month, which the oil spill area extent found in the range of 23.25 – 113.40 km<sup>2</sup>. Lowest area of oil spill of 23.25 km<sup>2</sup> in September, 11.2019 was in accordance with smallest oil spill volume of 11.6 barrels (Table 5). The widest area of oil spill of 113.40 km<sup>2</sup> in April, 16.2019 was assumed related to the volume of oil spill detected of 79.3 barrels. Specific condition of the biggest volume of oil spill 82.3 barrels occured in December 12, 2019 and was assumed related to the rough wave at the SPM condition during loading and unloading process. Very interesting finding of the lowest evaporation rate of 21.5% in this month is in fact happened

during the west monsoon or the peak of the rainy season. While the highest evaporation rate of 56.9% found in the model in September, 11 2019 (Table 5) which is related to the condition of higher sea surface and atmospheric air temperature during the peak of the east monsoon or the dry season.

Specific finding also which oil spills in April 4, 2019 with 88.30 km<sup>2</sup> initial wide area in day-0 had experienced a significant decrease to 57.07 km<sup>2</sup> wide area after 120 hours trajectory model, and then dispersed finely to zero after the period of 240 hours trajectory model. In contrast, in data of December 16, 2019 that initial oil spill wide area of 107.90 km<sup>2</sup> in day-0 then decrease to 14.74 km<sup>2</sup> after 120 hours trajectory model, but then increase significantly to become 144.85 km<sup>2</sup> after 240 hours (Table 5), which is refer to the rough wave and sea surface current (Figure 9) during the west monsoon. After 120 hours of moving in the sea water, and the evaporation rate of oil spill range is between 26 – 56.9%. The numerical spatial model had shown a relatively high evaporation rate of oil spills after 240 hours period. Initial process of the oil spill enters the marine environment, the oil spill will undergo a spreading process. Which this initial process is the most important process during the initial and trajectory of oil spill into the marine environment. The entry of oil spill into the marine environment will be followed by various processes that will occur and effected by the physical conditions of the waters, one of which is sea surface currents. According to Zhang *et al.* (2019) that the spread and volume of oil spill on the sea will be primarily affected by the sea surface currents.

Naz *et al.* (2021) observed four oil spill events in the Indian Ocean including Chennai, Sharjah, Al Khiran and Mubarak Village analyzed using Sentinel-1 SAR data. The GNOME model was used for the production of the oil spill trajectory, while the oil spill weathering process was modeled using the Automated Data Inquiry for Oil Spill (ADIOS). The maximum oil spill movement (33 km) from the source point was observed at Al Khiran, while the rate of evaporation of crude oil was observed to be high. Balogun *et al.* (2021) developed an oil spill environmental vulnerability model to predict and map the trajectory of an oil spill in Kota Tinggi, Malaysia. Oil spill scenarios were being simulated using the GNOME. The results showed that the oil layer velocity at 40.8 m per minute was higher during the pre-monsoon period in the southwest and lower during the northeast monsoon (36.9 m per minute).

The high evaporation rate of oil spills had been generated in this research model was similar value to the evaporation of oil spills produced by Toz, (2017) in Samsun Bay Turkey and Afenyo *et al.*, (2016) in the Arctic Sea, and Ramirez *et al.*, (2019) in the Caribbean Sea, Colombia. This evaporation process had caused the volume of the oil spill to be reduced by an average of 43%. As in Table 5 showed that the volume of detected oil spills decreased by an average of 17.81 barrels after 10 hours. In the period during April 16 and October 13, 2019, the oil spill had moved outside the model limits after 120 hours as well as after 240 hours. This was because the occurrence of oil spills was generally located in the western part of the study area. Also when the model was ran for more than 120 hours during the east monsoon, it would be out of model limit area. Meanwhile, during the west monsoon, the average of oil spill area was spread evenly over the study area, mean that the volume of oil spill could still be analyzed within the model limits. The trajectory model showed that oil spills that occur during the period of the study in one year in the limit of the study area did not reach to the coast due to the effect of sea surface current and wind of northwest and southeast direction pattern. Oil spills direction pattern was mainly driven by sea surface currents moved parallel along to the coastline direction and away from the coastline, so that within the model limits during the study there were no oil spills that have been detected to reach and pollution to the coastline area. Difference with the current study in this research with the case that oil spill occurred on the sea surface caused by floating infrastructure of SPM. Another study by Heidaria *et al.* (2019), as comparison which had examined a more advanced modelling for assessing spatial and stochastic oil spill risk, which is a very specific case study of an oil spill from a sunken ship in Kattegat located between Denmark and Sweden in Northern Europe's inlet to the Baltic Sea. They use the VRAKA method which was used to estimate the probability of release in a quantitative oil spill risk assessment and 3D plumes using the GNOME. This research demonstrated the spatial and stochastic risk assessment of oil spills from shipwrecks, allowing a structured approach to incorporate the complex factors that influence the risk values.

## 6. CONCLUSIONS

Spatial modelling of wind and sea surface current, in general exhibit a predominant wind and sea surface current during transition-1 April-May until the east monsoon of September 2019 is the east direction. Predominant wind and sea surface current during transition-2 of October-November 2019 and during the west monsoon of December 2019-February 2020 is south and southeast direction, parallel to the coastline morphology.

Analysis of oil spills using 58 Sentinel-1A SAR data had confirmed 11 data on April 8 and 16, May 26 representing for the transition-1 period, only one oil spill event in September 11 to represents for the east monsoon. SAR data in October 13, and November 10 and 18, 2019 had confirmed the event of oil spill to represent for transition-2 period. SAR data in December 12 and 16, 2019, January 09, and February 14, 2020 to represents for the west monsoon with predominant to the southeast direction. The study had revealed that oil spills had moved mainly in accordance to sea surface current and seasonal wind direction based on the wind rose data. In the east monsoon, the wind and currents were generally dominated to the west and northwest from the east. Meanwhile, during the west monsoon, the wind and current directions from the west to the southeast and east.

The most important and critical finding based on integration of spatial Sentinel-1A SAR data, GNOME hydrodynamic- trajectory modelling revealed the oil spill trajectory, wide area, type, volume and evaporation rate of the oil spill. The smallest area of oil spill is 27.08 km<sup>2</sup> in the east monsoon of February 2020 and widest area of 113.40 during the transition-1 of April 2019 and widest area become 144.85 km<sup>2</sup> after 240 hours period during the west monsoon of December 16, 2019. Total detected oil spill volume of 773.28 barrels with an evaporation rate of 43% after 120 hours of numerical modelling, with average of 70.30 km<sup>2</sup> of oil spill area. The trajectory direction of the oil spill in the east monsoon was spread toward the northwest of Balongan coastal water, while during the west monsoon the spill moved toward the southeast. Smallest oil spill volume 11.6 barrel had been detected but with highest evaporation rate of 56.9% occurred in September 2019 of the east monsoon. Biggest volume of oil spill of 82.3 barrel occurred in December 2019 west monsoon with lowest evaporation rate of 21.5%.

## ACKNOWLEDGEMENT

The authors would like to thanks especially to the Institute for Research and Community Development – Diponegoro University for the funding support in contract no. 233-39/UN7.6.1/PP/2021 and other parties for their help and guide to the manuscript. Also to the Faculty of Fisheries and Marine of Universitas Diponegoro. University for the research funding No:19/UN7.5.10/PP/2019 APBN.FPIK Undip TA 2019.

## REFERENCES

- Afenyo, M., F. Khan, B. Veitch, dan M. Yang. (2016). Modeling Oil Weathering and Transport in Sea Ice. *Marine Pollution Bulletin*, 107(1): 206–215.
- Alifidini, I., Shimada, A., Wirasatriya. 2021. Seasonal Distribution and Variability of Surface Winds in the Indonesian Seas Using Scatterometer and Reanalysis Data. *International Journal of Climatology*. <https://doi.org/10.1002/joc.7101>
- Balogun, A. L., S. T. Yekeen., B. Pradha., K. B. W. Yusof. 2021. Oil spill trajectory modelling and environmental vulnerability mapping using GNOME model and GIS. *Environmental Pollution*. 268 : 115812.
- Cantorna, D., C. Dafonte., A. Iglesias., B. Arcay. 2019. Oil spill segmentation in SAR images using convolutional neural networks. A comparative analysis with clustering and logistic regression algorithms. *Applied Soft Computing Journal*. 84 : 105716.
- Chaturvedi, S. K., S. Banerjee., S. Lele. 2020. An assessment of oil spill detection using Sentinel 1 SAR-C images. *Journal of Ocean Engineering and Science*. 5 : 116–135.
- Fan, J., F. Zhang, D. Zhao, dan J. Wang. 2015. Oil Spill Monitoring Based on SAR Remote Sensing Imagery. *Aquatic Procedia*, 3: 112–118.

- Fitriyanto, B. R., M. Helmi, and Hadiyanto. 2019. Analyzing Spatiotemporal Types and Patterns of Urban Growth in Watersheds that Flow into Jakarta Bay, Indonesia. *Remote Sensing Applications: Society and Environment*, 14: 170 - 177.
- Fletcher, K., 2012. Sentinel-1: ESA's Radar Observatory Mission for GMES Operational Services. ESA Communications, SP-1322/1.
- Hartoko, Agus, Muhamad Helmi, Mujahid Sukarno, Hariyadi. 2016. Spatial Tsunami Wave Modelling for the South Java Coastal Area, Indonesia. *International Journal of Geomate*. Vol 11 (25) : 2455-2460.
- Hartoko Agus, Arief Febrianto, Aditya Pamungkas, Irvani Fachruddin, Muhammad Helmi, Hariyadi. 2019. The Myth and Legend of Sadai and Gaspar Strait Bangka Belitung (BANCA-BILLITON) and Oceanographic Conditions. *International Journal of Geomate*. 62 : 212-218. <https://doi.org/10.21660/2019.62.93965>.
- Heidari, P. A., L. Arneborg, J. F. Lindgren, A. Lindhe, L. Rosén, M. Raie, L. Axell, dan I. M. Hassellöv. 2019. A State of the Art Model for Spatial and Stochastic Oil Spill Risk Assessment: A Case Study of Oil Spill from a Shipwreck. *Environment International*, 126: 309–320.
- [Htpps://www.ecmwf.int](https://www.ecmwf.int)
- [Htpps://www.hycom.org](https://www.hycom.org)
- [Htpps://scihub.copernicus.eu](https://scihub.copernicus.eu)
- Josaphat, T. S. S and N. Imura. 2016. Development of Curcularly Polarized Synthetic Aperture Radar for Aircraft and Microsatellite. *IEEE International Geoscience and Remote Sensing Symposium (IGARSS)*. 5654 – 5657.
- Kingston, P. F. 2002. Long-term Environmental Impact of Oil Spills. *Spill Science & Technology Bulletin*, 7(1-2): 53-61.
- Lehr, W., R. Jones, M. Evans, D. Simecek-Beatty, dan R. Overstreet. 2002. Revisions of the ADIOS Oil Spill Model. *Environmental Modelling & Software*, 17(2): 189–197.
- Li, G., Y. Liu, P. Wu, & C. Chen. 2019. Marine Oil Slick Detection Based on Multi-Polarimetric Features Matching Method Using Polarimetric Synthetic Aperture Radar Data. *Sensors*, 19: 5176 p.
- Liu, X., J. Guo, M. Guo., X. Hua., C. Tang., C. Wang., Q. Xing. 2015. Modelling of oil spill trajectory for 2011 Penglai 19-3 coastal drilling field, China. *Applied Mathematical Modelling*. 39 : 5331–5340.
- Mera, David., Cotos, J.M., Varela-Pet, J & Garcia-Pineda, Oscar. 2012. Adaptive Thresholding Algorithm Based on SAR Images and Wind Data to Segment Oil Spills along The Northwest Coast of The Iberian Peninsula. *Marine Pollution Bulletin*, 64:2090 – 2096.
- Naz, S., M. F. Iqbal., I. Mahmood., M. Allam. 2021. Marine oil spill detection using Synthetic Aperture Radar over Indian Ocean. *Marine Pollution Bulletin*. 162 : 111921.
- Nordam T., CJ. Beegle-Krause., J. Skancke., R. Nepstad., M. Reed. 2019. Improving oil spill trajectory modelling in the Arctic. *Marine Pollution Bulletin*. 140 : 65–74.
- Qiao, f., G. Wang., L. Yina., K. Zeng., Y. Zhang., M. Zhang., B. Xiao., S. Jiang., H. Chen., G. Chen. 2019. Modelling oil trajectories and potentially contaminated areas from the Sanchi oil spill. *Science of the Total Environment*. 685 : 856–866.
- Rajendran, S., P. Vethamony., F. N. Sadooni., H. A. S. Al-Kuwari., J. A. Al-Khayat., H. Govil., S. Nasir. 2021. Sentinel-2 image transformation methods for mapping oil spill –A case study with Wakashio oil spill in the Indian Ocean, off Mauritius. *MethodsX*. 8 : 101327.
- Ramírez, J., A. Merlano, J. Lacayo, A. F. Osorio, dan A. Molina. 2017. A Model for the Weathering of Colombian Crude Oils in the Colombian Caribbean Sea. *Marine Pollution Bulletin*, 125(1-2): 367–377.
- Remyalekshmi, R dan A. V. Hedge. 2013. Numerical Modeling of Oil Spill Movement along North-West Coast of India Using GNOME. *International Journal of Ocean and Climate System*., 4(1): 75-86.
- Sauz, F. G. R., T. F. Reyes, C. Costa. 2018. Laser Induced Breakdown Spectroscopy (LIBS) for Express Identification of Crude Oils. *Revista Cubana De Física*, vol 35(1): 19-23.
- Sinurat, M.E.Br., A. Ismanto, and Hariyadi. 2016. Analysis of Crude Oil Spill Spatial Pattern Using Hydrodynamic Model at Balongan, Indramayu, Java Sea. *Jurnal Oseanografi UNDIP*, 5(2):218 - 226.
- Sun, S., C. Hu, L. Feng, G. A. Swayze, J. Holmes, G. Graettinger, I. MacDonald, O. Garcia, and I. Leifer. 2016. Oil Slick Morphology Derived from AVIRIS Measurements of the Deepwater Horizon Oil Spill: Implications for Spatial Resolution Requirements of Remote Sensors. *Marine Pollution Bulletin*, 103(1-2): 276–285.
- Susanti, Y., S. Syafrudin, and M. Helmi. 2019. Soil Erosion Modelling at Watershed Level in Indonesia: a Review. *E3S Web of Conferences, ICENIS 2019*, 125: 01008.
- Toz, A. C. 2017. Modelling Oil Spill around Bay of Samsun, Turkey, with the Use of Oilmap and Adios Software Systems. *Polish Maritime Research*, 24(3): 115–125.

- Wirasatriya, A., H. Kawamura, M. Helmi, D. N. Sugianto, T. Shimada, K. Hosoda, G. Handoyo, Y. D. G. Putra, dan M. Koch. 2020. Thermal Structure of Hot Events and Their Possible Role in Maintaining the Warm Isothermal Layer in the Western Pacific Warm Pool. *Ocean Dynamics*, 70: 771 - 786.
- Yang, Y., Z. Chen., Y. Li., X. Xiao., Q. Dan., T. Yang dan Z. Ren. 2013. Numerical Simulation of Oil Spill in The Gulf of Mexico Based on GNOME and ADIOS. *Journal Applied Mechanics and Materials* Vols. 295-298.
- Yu, X., W. Zhang, X. Liu, J. Lei, Z. Lin, Z. Yao, X. Yao, X. Jin, H. Yang, H. Huang. 2018. The Distribution of and Biodegradation Impact on Spilled Oil in Sediments from Dalian Bay, NE China. *Marine Pollution*, 135: 1007–1015.
- Zhang, B., E. J. Matchinski, B. Chen, X. Ye, L. Jing, dan K. Lee. 2019. Marine Oil Spills - Oil Pollution, Sources and Effects. *World Seas: An Environmental Evaluation*, 21: 391–406.



## ALGORITHMS IN MATLAB TO COMPUTE A LOCAL GEOID MODEL FOR GEOMATICS PURPOSES

Massimiliano PEPE<sup>1</sup>

DOI: 10.21163/GT\_2022.171.06

### ABSTRACT:

The aim of the paper is to show a methodology in order to build a local geoid model using the Compute-Remove-Restore technique; to achieve this aim, suitable algorithms in Matlab® environment were developed. The knowledge of a geoid model assumes an important role in the field of engineering, geosciences and geomatics since that it allows the definition of physical heights or the components of the deflection of the vertical on a specific area. The area taken into consideration for the research is the Campania region (Italy). By comparing the geoid undulation values of the model developed in this paper with those extracted from the benchmarks over this area derived from the national levelling network, it is possible to obtain centimetre accuracy.

**Key-words:** *Geoid, Compute-Remove-Restore, EGM, Physical geodesy.*

### 1. INTRODUCTION

Physical geodesy is the science of the figure of the Earth and its gravity field (Hofmann-Wellenhof & Moritz, 2006). A surface of particular interest for geomatics purposes is the geoid, i.e. an equipotential surface of the Earth gravity field (Sansò & Sideris, 2013). The geoid can be computed from knowledge of the gravitational field. The most commonly used technique for determining the regional geoid model is the "Remove-Compute-Restore" (RCR) technique which it is based on theory of the first-order approximation of either Molodensky's method for quasi-geoid determination or the classical geoid modelling by Helmert's second method of condensing the topography onto the geoid (Sjöberg, 2005). The RCR technique is the only practical geoid gravimetric modelling technique for combining terrestrial gravimetric data with an Earth Gravity Mode – EGM (Torge, 2001). Indeed, the recent global geopotential models, based on the CHAMP (Challenging Minisatellite Payload, a German BMBF-funded geophysical mini-satellite mission of GFZ-GeoForschungsZentrum) and GRACE (Gravity Recovery and Climate Experiment, a joint mission of National Aeronautics and Space Administration - NASA and the German Aerospace Center - DLR) space missions, have allowed to obtain high-performance local geoid models, as shown in Barzaghi et al., 2007 for the estimation of the gravimetric quasi-geoid named ITALGEO05.

RCR technique was applied with success in several country over the time. For example, Blázquez et al., 2003 show the good results of the regional model called ANDALUSGeoid2002 obtained using fast collocation method and the RCR Procedure. Lysaker et al., 2007 discussed of the quasi-geoid evaluation with improved levelled height data for Norway region. El-Ashquer et al, 2017 have developed an hybrid gravimetric geoid model HGM2016 by means of least-squares collocation method and remove-compute-restore process over Egypt. Kalu et al., 2021 wrote about the RCR technique in modelling a gravimetric geoid model for a large data deficient region in West Africa (Nigeria) using two sets of long and short wavelength data (a) EGM2008 (long) + Airborne

---

<sup>1</sup>Polytechnic of Bari, via E. Orabona 4, 70125 Bari, Italy, massimiliano.pepe@poliba.it

gravimetric observation (AGO) dataset (short) (b) EGM2008 (long) + Terrestrial gravimetric undulation (TGU) dataset (short).

The realization of a regional geoid model and, consequently, the knowledge of geoid undulation and vertical deviation components contributes positively in considerable geomatics applications. For example, Barzaghi et al., 2016 used the deflection of the vertical components obtained from a local model for the correction of External Orientation (EO) parameters (attitude angles) in Direct Georeferencing (DG) photogrammetry approach. In addition, the usefulness of the regional model in order to transform the ellipsoid height in orthometric in Global Navigation Satellite Systems (GNSS) measurements was applied in several geomatics works present in literature (Baiocchi et al., 2017; Parente & Pepe, 2018; Oluyori et al., 2019; Erol et al., 2020; Pepe et al., 2020; Costantino et al., 2021).

In this paper, a study for the computation of a local geoid model at a spatial resolution (2.5') is addressed, using the following methods: *i*) Remove-Compute-Restore technique; *ii*) constant and vertical shift of the EGM2008 geoid undulation model.

## 2. STUDY AREA

The study area taken into consideration concerns the Campania region, an administrative region of south Italy; most of it is in the south-western portion of the Italian peninsula (with the Tyrrhenian Sea to its west), but it also includes the small Phlegraean Islands and the island of Capri. The morphology of this territory is mainly hilly (51%); the remaining part of the territory is mountainous (34%) and flat (15%). It covers an area of 13670.95 km<sup>2</sup>. The area taken into consideration, reported in Fig. 1, is contained within the geographical coordinates:  $39^{\circ}\text{N} \leq \varphi \leq 42^{\circ}\text{N}$  and  $13^{\circ}\text{E} \leq \lambda \leq 16^{\circ}\text{E}$ .

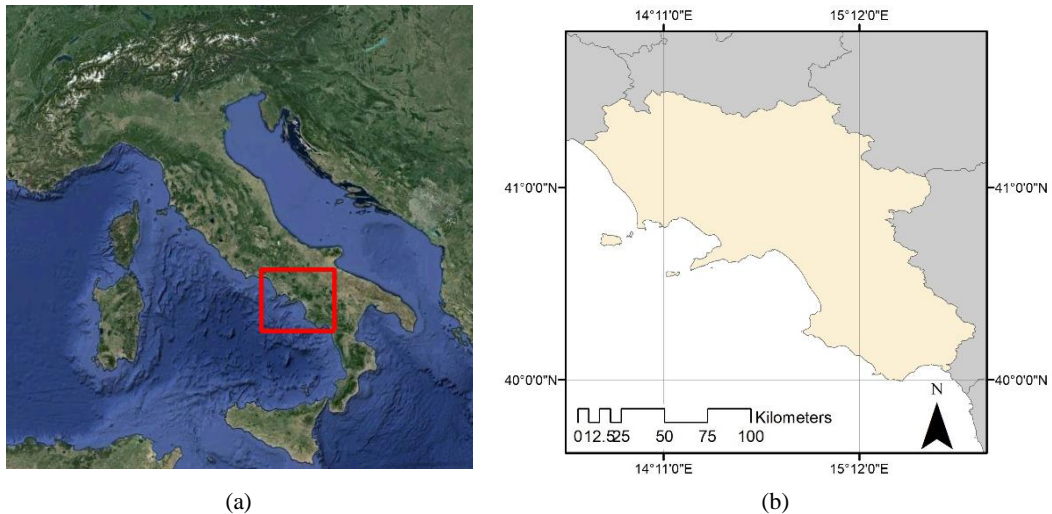


**Fig. 1.** Area of interest (AOI) to compute local geoid model; view on Google earth (a) and geographic framework (b).

## 3. DATA AND METHODS

### 3.1. Remove-Compute-Restore technique

The compute of any quantity of the gravity field is carried out by means of a frequency analysis of the quantity itself, i.e. the following three components are identified: *i*) low-frequency component, represented by global geopotential models (e.g. Earth Gravity Model - EGM2008); *ii*) medium-frequency component, which it can be calculated on the basis of local data and; *iii*) high-frequency

component, which can be linked to the topographic effect and is calculated on the basis of a digital terrain model (Corchete et al., 2005).

The "Remove-Compute-Restore" technique can be schematised into the following points:

- Remove: removal of the contribution of the global model (determined by a spherical harmonic model) and of an additional contribution called "Residual Terrain Correction" (RTC) representing the effect of the masses between the topography and a reference surface;
- Compute: calculation of co-geoid undulation residuals;
- Restore: addition, in terms of geoid undulation, of both that of the global model and that of the RTC effect, also called "indirect topographic effect".

These steps can be summarised as reported below (Srinivas et al., 2012):

$$N = N_{GM} + N_{ind} + N_{\Delta g} \tag{1}$$

where the geoid undulation values are derived from:

- $N_{GM}$  global geoid model;
- $N_{ind}$  the indirect effect;
- $N_{\Delta g}$  from the residues of gravity anomalies.

### 3.1.1. Contribution of global geoid model

The long-wavelength geoid component  $N_{GM}$  is obtained by the use of a global geopotential model; currently, the most widely used model is the EGM2008 (Pavlis et al., 2007; Pavlis et al. 2008; Pavlis et al., 2021) publicly released by the U.S. National Geospatial-Intelligence Agency (NGA) EGM Development Team which is derived from data from the GRACE satellite (Mayer-Gürr et al., 2016), topographic data (Saleh et al., 2002) and ground-based gravimetric observations.

The EGM2008 model was developed up to degree and order 2159, which results in a spatial resolution of the model of about 2.5' where the values of the vertical deviation and gravimetric anomalies are freely available at the NGA address.

Computationally, the current  $W$  potential expressed in terms of spherical polar coordinates, radius, longitude, latitude  $(r, \lambda, \psi)$ , is described by the coefficients  $C_{nm}$  and  $S_{nm}$  of degree  $n$  and order  $m$ , which are empirically determined and associated with the Legendre polynomial  $P_{nm}$  (Borre, 2008):

$$W(r, \lambda, \psi) = \frac{GM}{r} \left[ 1 + \sum_{n=2}^{n_{max}} \left(\frac{a}{r}\right)^n \sum_{m=0}^n (\bar{C}_{nm} \cos m\lambda + \bar{S}_{nm} \sin m\lambda) \bar{P}_{nm}(\sin \psi) \right] \tag{2}$$

where  $GM$  is the product of Newton's gravitational constant and Earth's total mass (including the atmosphere),  $a$  is the radius of the bounding sphere and  $r$  is the geocentric radius.

Recalling that the anomalous potential  $T$  is the difference between the one of the gravitational field  $W$  and the gravitational normal one  $U$ , it follows that in the hypothesis to know the anomalous potential  $T$ , it is possible to write with the formula of Bruns, the anomalous height  $\zeta$ :

$$\zeta = \frac{T}{\gamma} \tag{3}$$

Therefore, the previous equation becomes:

$$\zeta(r, \lambda, \psi) = \frac{GM}{\gamma(\varphi)r} \left[ \sum_{n=2}^{n_{max}} \left(\frac{a}{r}\right)^n \sum_{m=0}^n (\bar{C}_{nm} \cos m\lambda + \bar{S}_{nm} \sin m\lambda) \bar{P}_{nm}(\sin \psi) \right] \tag{4}$$

where the value of normal gravity  $\gamma(\varphi)$  is equal to:

$$\gamma(\varphi) = \frac{\gamma_e \cos^2 \varphi + (1 - f)\gamma_p \sin^2 \varphi}{\sqrt{\cos^2 \varphi + (1 - f)^2 \sin^2 \varphi}} \tag{5}$$

while at height  $h$ , the value of normal gravity  $\gamma(h)$  takes on the following expression:

$$\gamma(h) = \gamma(\varphi) \left[ 1 - 2(1 + f + m - 2f \sin^2 \varphi) \frac{h}{a} + 3 \left( \frac{h}{a} \right)^2 \right] \quad (6)$$

In addition, the geoid undulation  $N$  is related to the ellipsoid height  $h$  measured along the normal to the ellipsoid, the orthometric height  $H$ , the normal height  $H^*$  and the anomalous height  $\zeta$ , by equation (Heiskanen and Moritz, 1967):

$$N = H^* - H + \zeta \quad (7)$$

Furthermore, orthometric height is related to normal height through the relationship:

$$H = H^* - \frac{\Delta g_B}{\gamma(h)} H \quad (8)$$

where  $\Delta g_B$  represents the Bouguer anomaly.

Finally, it is possible to calculate the value of the gravity anomaly of the global geopotential model with the following relation (Heiskanen and Moritz, 1967; Kuroishi, 1993):

$$\Delta g_{GM} = \frac{GM}{r^2} \sum_{n=2}^{n_{max}} (n-1) \left( \frac{a}{r} \right)^n \sum_{m=0}^n \bar{P}_{nm}(\sin \varphi) (\bar{C}_{nm} \cos m\lambda + \bar{S}_{nm} \sin m\lambda) + \Delta g_0 \quad (9)$$

where  $\Delta g_0$  is the term of degree 0.

### 3.1.2. Contribution of the indirect effect

The removing or moving of masses changes the potential gravity and, consequently, the geoid; this change of the geoid is called indirect effect of gravity reduction. Therefore, the surface calculated with Stokes' formula does not refer to the geoid but to a slightly different surface, the co-geoid (Fig. 2), from which it is possible to extrapolate, using Bruns' theorem, the following formula:

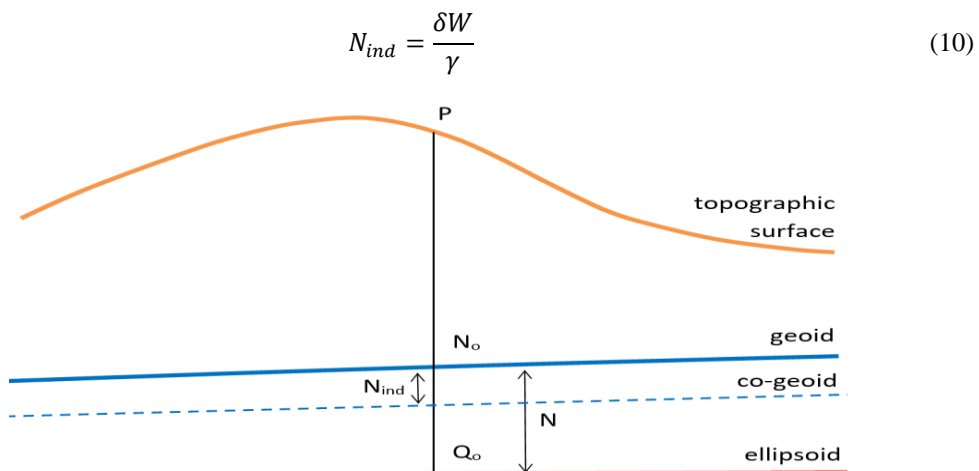


Fig. 2. Reference surfaces.

Under the assumption of a plane approximation, the term  $N_{ind}$  can be written using two terms (Schwarz et al., 1990):

$$N_{ind} = -\frac{\pi G \rho}{\gamma} h^2(x_P, y_P) - \frac{G \rho}{6\gamma} \iint_A \frac{h^3(x, y) - h^3(x_P, y_P)}{[(x_P - x)^2 + (y_P - y)^2]^{3/2}} dx dy \quad (11)$$

- $\rho$  density of topography assumed to be  $2,67g/cm^{-3}$ ;
- $(x_P, y_P)$  coordinates of the point;
- $(x, y)$  coordinates of integration points;

$h(x, y)$  elevation model, taking into account only the masses above the geoid, i.e. only the positive elevations;  
 $A$  study area.

The plane approximation of the expression of  $N_{ind}$  can be write as a convolution formula (Schwarz et al., 1990):

$$N_{ind} = -\frac{\pi G \rho}{\gamma} h^2 - \frac{G \rho}{6 \gamma} f * h^3 + \frac{G \rho}{6 \gamma} s h^3 \quad (12)$$

where:

$$f(x, y) = \frac{1}{(x^2 + y^2)^{3/2}} \quad (13)$$

$$s = \iint_A f(x, y) dx dy \quad (14)$$

### 3.1.3. Contribution of the residual gravity

The last term  $N_{\Delta g}$  of equation (1) represents the contribution of the gravity residual which, taking into account the Stokes equation, is (Hofmann and Moritz, 2006):

$$N_{\Delta g} = \frac{R}{4 \pi \gamma} \iint_A \Delta g(\psi, \alpha) S(\psi) dA \quad (15)$$

$\gamma$  normal gravity on the ellipsoid;  
 $R$  mean earth radius;  
 $S(\psi)$  Stokes function;  
 $\Delta g$  reduced anomalies according to the Helmert condensation method.

Under the assumption of spherical approximation, equation (15) can be expressed in convolution form using the one-dimensional (1-D) Fourier transform (Haagmans et al., 1993):

$$N_{\Delta g} = \frac{R \Delta \phi \Delta \lambda}{4 \pi \gamma} F_l^{-1} \left[ \sum_{\phi'=\phi_l}^{\phi_n} F_l(\Delta g \cos \phi) F_l(S) \right] \quad (16)$$

where  $F_l(S)$  represents the discrete Fourier transform (DFT) and  $F_l^{-1}$  its inverse transform (IDFT). Instead, in the hypothesis of plane approximation, the Stokes function becomes (Schwarz et al., 1990):

$$S(\psi) \approx 2/\psi \quad (17)$$

Therefore, the contribution of the gravity residue  $N_{\Delta g}$ , with appropriate substitutions and passing from polar coordinates  $(s, \alpha)$  to Cartesian coordinates  $(x, y)$ , takes on the following expression:

$$N_{\Delta g} = \frac{1}{2 \pi G} \iint_A \frac{\Delta g}{(x_p - x)^2 + (y_p - y)^2} \quad (18)$$

The equation (18) can be rewritten in terms of FFT (Fast Fourier Transform):

$$N_{\Delta g} = \frac{1}{2 \pi G} \Delta g(x, y) * l_p(x, y) \quad (19)$$

with  $l_p(x, y) = 1/\sqrt{x^2 + y^2}$ , which is called the "kernel of the plane approximation".

To determine the  $N_{\Delta g}$  term, it is necessary to calculate the value of the gravity anomalies, using the following relationship:

$$\Delta g = \Delta g_{free} + c_t + \delta g \quad (20)$$

$\Delta g_{free}$  free-air gravity anomaly;

$c_t$	terrain correction;
$\delta g$	indirect secondary effect on gravity.

The indirect secondary effect on gravity can be expressed as a function of  $N_{ind}$  (Heiskanen and Moritz, 1967; Kuroishi, 1993):

$$\delta g = 0.3086 N_{ind} \quad (21)$$

Therefore, the residual anomaly field must first be determined, removing the effect of the short wave associated with topography and bathymetry. This correction is called "Residual Terrain Correction" RTC (Forsberg, 1984) and can be described through the following relation (Corchete et al., 2005), where the superscript "pts" denotes that the points in the study area are randomly distributed:

$$\Delta g_{red}^{pts} = \Delta g_{free}^{pts} - 2\pi G\rho(h - h_{ref})^{pts} + c_t^{pts} - \Delta g_{GM}^{pts} \quad (22)$$

$G$	Newton's gravitational constant;
$\rho$	density;
$h$	point elevation;
$h_{ref}$	elevation of reference surfaces;
$c_t$	correction calculated for land and sea points;
$\Delta g_{GM}$	gravity anomaly calculated from the global geopotential model.

The reference surface  $h_{ref}$  can be obtained by applying a 2-D low-pass filter to the elevation model.

The density value that can be used in equation (22) for the RTC correction are:

$\rho_{ow} = 2,67 g cm^{-3}$  for points on the ground;

$\rho_{uw} = 1,64 g cm^{-3}$  for points below water.

The density value for the correction below water is given by the difference between the density of the soil and that of the water, which is equal to  $\rho_w = 1,03 g cm^{-3}$ .

For the computation of the Fourier transform, it is necessary that the data be arranged in the form of a grid; several methods and algorithms for performing this operation are available in the literature:

- Briggs method (Briggs, 1974);
- least squares collocation method (Moritz, 1980);
- Kriging method (Davis, 1986);
- spline algorithm (Smith & Wessel, 1990).

By arranging the values of the gravity anomalies in grid form, the effect of the RTC can be restored through the following relationship (Corchete, 2010):

$$\Delta g_{red}^{grid} = \Delta g_{free}^{grid} - 2\pi G\rho(h - h_{ref})^{grid} + c_t^{grid} - \Delta g_{GM}^{grid} \quad (23)$$

In equations (20) and (22), the term  $c_t$  takes into account the influence of the topography. In fact, especially in particularly steep terrain, the topography assumes a fundamental role in the calculation of the undulations. The correction  $c_t$  of the terrain to be applied, approximating  $z = h_p$ , i.e. in the so-called "linear approximation" (Heiskanen and Moritz, 1967), is:

$$c_t = G\rho \iint_A \int_{h_p}^h \frac{z - h_p}{[(x_p - x)^2 + (y_p - y)^2 + (z_p - z)^2]^{3/2}} \quad (24)$$

Equation (24), rewritten in the form of a convolution (Sideris, 1990), takes the following form:

$$c_t = \frac{1}{2} G\rho [f * h^2 - 2h(f * h) + h^2 s] \quad (25)$$

where

$$f(x, y) = \frac{1}{(x^2 + y^2)^{3/2}} \quad (26)$$

$$s = \iint_A \frac{1}{(x^2 + y^2)^{3/2}} dx dy \tag{27}$$

As an alternative to the FFT, terrain correction can be achieved with the prism method, which consists of dividing the terrain into many prisms; depending on the method of terrain condensation, two models are available: *i*) Prism model; *ii*) Mass line. The prism model associates the density of each prism with its average height, while in the mass line model the mass of the prism is mathematically concentrated along its barycentre axis, therefore the topography contained in the prism is represented by a line (**Fig. 3**).

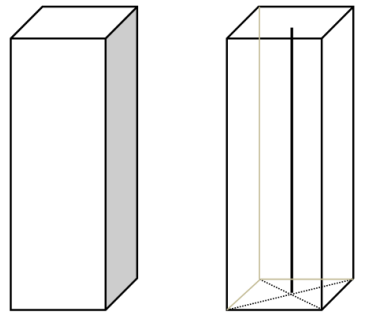


**Fig. 3.** Types of soil condensation: mass prism (left) and mass line (right).

In the first case, equation (25), after having reported the DTM in the form of a grid in *M* and *N* cell elements of size ( $\Delta x$ ;  $\Delta y$ ), can be rewritten in the following form (Yurt & Gokalp, 2006):

$$c_t = G\rho \sum_{n=0}^{N-1} \sum_{m=0}^{M-1} \left[ x \ln(y + r(x, y, z)) + y \ln(x + r(x, y, z)) \right] - z \arctan \frac{xy}{z r(x, y, x)} \Bigg|_{x_i - (x_n + \Delta x/2)}^{x_i - (x_n + \Delta x/2)} \Bigg|_{x_i - (x_n + \Delta x/2)}^{x_i - (x_n + \Delta x/2)} \tag{28}$$

while in the second case (Yang, 1999) becomes:

$$c_t = -G\rho\Delta x\Delta y \sum_{n=0}^{N-1} \sum_{m=0}^{M-1} \left[ \frac{1}{r(x_i - x, y_j - y, 0)} - \frac{1}{r(x_i - x, y_j - y, h_{ij} - h_{nm})} \right] \tag{29}$$

where:

- G* Newton's gravitational constant;
- $\rho$  density;
- $h_{ij}$  point elevation (*i, j*);
- r* radius of the coordinate sphere in the Cartesian system (*x, y, z*).

### 3.2. Adjustment of the gravimetric geoid model

The sum of the contributions  $N_i$  gives the undulation model according to a geophysical approach. If the *N* model of the geoid undulation were correct, the following relationship would occur:

$$h - H - N = 0 \tag{30}$$

Factors causing discrepancies are (Fotopoulos, 2003):

- random errors in the calculation of heights *h, H, N*;
- inconsistencies of the datum intrinsic to the different types of heights;
- errors and distortions (errors related to the measurement of the wavelength for the geoid measurement, systematic errors related to the GNSS measurement and to the limits of the levelling network);



- theoretical assumptions/approximations made in the treatment of the observed data (neglecting the topography of the sea or river, corrections due to the influence of the tides);
- instability of the reference monument station over time (geodynamic effects).

Therefore, it is necessary an "adjustment" of the geoid undulation model on the vertices deduced from the network where the orthometric height derived from a levelling (for example the fundamental network) and the ellipsoid height derived from GNSS (or Global Position System - GPS) measurement; the equation of the least squares system takes the following form:

$$(h^{GPS} - H^{lev}) - N^{gravim} = N^{GPS} - N^{gravim} = \delta N = l = AX \quad (31)$$

$h^{GPS}$	ellipsoid height of the reference point;
$H^{lev}$	orthometric height measured by levelling;
$N^{gravim}$	geoid undulation obtained by the gravimetric method;
$AX$	surface trend;
$\delta N$	residual.

Using a four-parameter model, it is possible to obtain the following formula (Isioye & Youngu, 2009):

$$AX = a_0 + a_1 \cos \varphi \cos \lambda + a_2 \cos \varphi \sin \lambda + a_3 \sin \varphi \quad (32)$$

where  $\varphi, \lambda$  are the geodetic latitude and longitude and the parameters  $a_0, a_1, a_2$  and  $a_3$  take into account the inconsistency between the GPS/levelling and the gravimetric geoid datum.

Subsequently, the residuals can be interpolated using the various interpolation techniques known in the literature, such as linear interpolation, kriging, etc.

## 4. RESULTS

### 4.1. Computation of the geoid on Campania region (Italy)

In the case study, the calculation of  $N_{GM}$  was performed using the EGM2008 geopotential model, freely available at the following website: <https://earth-info.nga.mil/php/download.php?file=egm-08interpolation>

Each raster file contains, in 2.5' steps, the geoid undulation values. Since the area under study is less extensive than that of a "tile" of the EGM2008 model, after downloading the raster file, it was necessary to implement an algorithm in Matlab® environment to extrapolate the undulation values and performing a clip on AOI. The contribute of geoid undulation model  $N_{GM}$  thus created (**Fig. 4**) showed a variability between 43m and 50m.

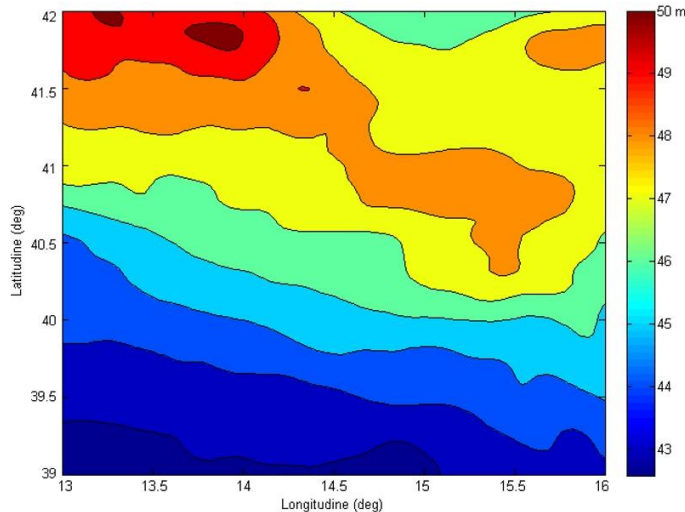


**Fig. 4.** Plot of the EGM2008 geoid model of the study area, contribute of  $N_{GM}$ .

Moreover, from the section shown in **Fig. 5** it is easy to notice how local variations over small areas are not detected by the geopotential model. For example, in the area under study, the island of Ischia, which has an extension of about 8' in longitude and 5' in latitude, the values at the nodes of which the grid is composed have an almost nil gradient, despite the morphology of the territory reaches altitudes up to almost 750m above sea level and has rather significant gravimetric anomalies.

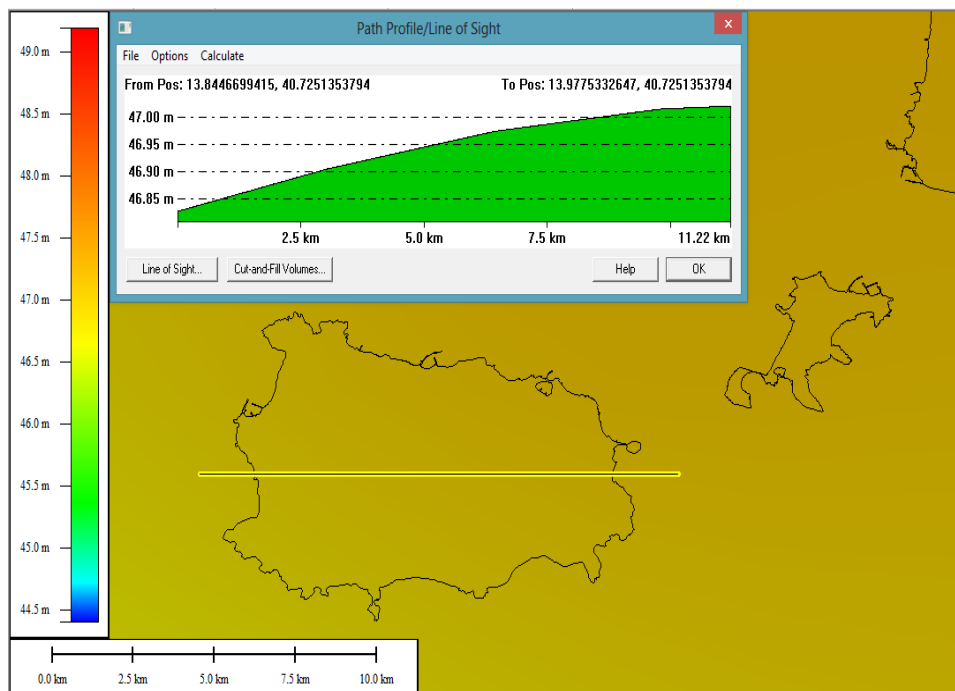


**Fig. 5.** Cross-section of the geoid model EGM2008 on the island of Ischia, an island close to the Italian peninsula (within Campania region).

The contribution of the indirect topographic effect  $N_{ind}$  was obtained, under the assumption of plane approximation, by applying the formula (12). In Matlab® environment, an algorithm for the calculation of  $N_{ind}$  has been implemented, where the convolution product between the functions in equation (14) was obtained using the Fourier transform, in particular the Fast Fourier Transformation. As regards the solution of the double integral reported in the formula (15), the Matlab® function implementing Simpson's quadrature method was used; this latter function was suitably modified in order to divide the area under study into a matrix of 200x200 elements and, on each of them, the double integral was calculated. To calculate the contribution of the indirect effect, the Shuttle Radar Topography Mission (SRTM) was used as Digital Terrain model (DTM); in this model, topographic and elevation data were collected in February 2000 by the Space Shuttle Endeavour, which used a sophisticated synthetic aperture radar-altimeter for this mission. The elementary measurement cell (pixel) corresponds to 3 square arc seconds, i.e. approximately 90m x 90m measured on the ground, with a declared accuracy of 20m in planimetry and 16m in altimetry (Werner, 2001). The elevation values of this model are freely downloaded from the Consortium for Spatial Information (CGIAR-CSI) website.

Since the contribution of the indirect effect is closely linked to the morphology of the territory, in the study area, which does not have any major reliefs, it was found to be of little relevance; more precisely, it varied from a few centimetres to about 1 metre. It should be noted that the previous values

are to be considered as absolute values, as the  $N_{ind}$  contribution always gives rise to negative values since the masses above the geoid have been removed.

$N_{\Delta g}$  can be calculated either by the collocation method or by the Stokes formula which, under the assumption of a plane approximation and expressed in the form of a convolution, assumes the following formula (Corchete et al., 2005):

$$N_{\Delta g} = \frac{1}{2\pi G} \Delta g(x, y) * l_p(x, y) + \frac{1}{\pi G} \Delta g(x, y) \sqrt{x^2 + y^2} \quad (33)$$

where a second term has been added to equation (20) to eliminate singular points. A Matlab® algorithm was implemented in order to extract the values of the residual anomalies,  $\Delta g$ , obtained from the relation (22). To achieve this aim, the values are gridded; therefore, the equation (22) can be written in the following way:

$$\Delta g_{red}^{grid} = \Delta g_{free}^{grid} - 2\pi G \rho (h - h_{ref})^{grid} + c_t^{grid} - \Delta g_{GM}^{grid} \quad (34)$$

Since all the terms in the previous relation are not gridded, as can be observed for  $\Delta g_{free}$ , the first operation performed was to transform them in grid form with a spatial resolution of 2.5', using "kriging" algorithm. The gravimetric values  $\Delta g_{free}$ , provided by the "Bureau Gravimétrique International" (BGI), are not distributed according to a regular grid but thicken where measurements were made for local surveys as shown in **Fig. 6**, where the gravity anomalies (free anomalies) are reported, both on land and sea.

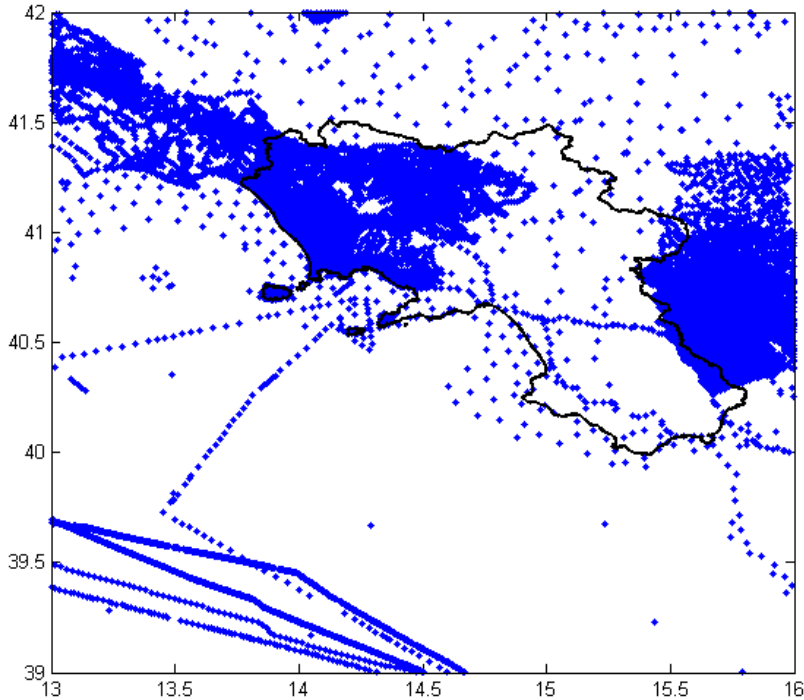


**Fig. 6.** Distribution of free-anomalies.

The term  $\Delta g_{GM}^{grid}$  represents the gravity anomaly, computed by the EGM2008 global geopotential model, whose grid of values with a 2.5' step can be obtained from the NGA website. The data are recorded in the 'big endian file' format and, thanks to a special script in Fortran, a text file of about 4.5GB was obtained containing three grids of values (N-S deflection of vertical component, E-O deflection of vertical component and gravity anomalies); subsequently, with a manual editing of the data, three separate files were created. The minimum, maximum and mean value of the local gravity anomalies and those related to the geopotential model are shown in **Table 1**.

**Table 1.**

**Statistical values of gravity anomalies.**

	<b>Min</b> (mgal)	<b>Max</b> (mgal)	<b>Medio</b> (mgal)
<b>Measured anomalies (<math>\Delta g_{free}</math>)</b>	-117	161	38
<b>Anomalies taken from EGM2008 (<math>\Delta g_{GM}</math>)</b>	21	203	43

The term  $2\pi G\rho (h - h_{ref})^{grad}$  represents the gravimetric contribution that masses of height  $h$ , obtained by integrating altimetric data from the SRTM height model with bathymetric data from ETOPO1 (Amante & Eakins, 2009), produce with respect to a reference surface  $h_{ref}$  obtained by applying a 2-D low-pass filter to the digital terrain model. By means of a "spatial query" in a Geographic Information Systems (GIS) environment, the land points were separated from the sea points. Indeed, spatial query make it possible to select elements in a vector layer using spatial relationships (intersect, contain, touch etc.) with elements in a second layer. As far as the terrain correction is concerned, the formula (22) valid for plane approximation was applied in the form of convolution. The trend of the contribution  $c_t^{grad}$  is of the order of some milligal. Therefore, once all the contributions of the residual anomalies  $\Delta g_{red}^{grad}$  (Eq. 24) were determined using FFT, it was possible to calculate the contribution of the residual effect  $N_3$ . In this way, the three contributions of the geoid undulation,  $N_1, N_2, N_3$ , were determined; the sum of these latter terms allows to obtain a geoid model on the basis of gravimetric measurements only, i.e. the so-called gravimetric geoid.

In the determination of the gravimetric geoid model, no reference has so far been made to levelled heights and thus to the national height reference network. Therefore, an adjustment of the geoid model on the vertices taken from the levelling network is necessary; these vertices contain the value of the geoid undulation since this value was obtained as the difference of the orthometric height, derived from the levelling vertices, and the ellipsoid height obtained from the GPS measurements. At present, the Italian Military Geographic Institute (IGMI) realized approximately 20,000 km of high-precision levelling lines. Analysing the levelling network on the Campania region, it is noted that on the islands, such as Ischia, it is completely absent; this translates into the lack of reference points for verifying the geoid undulation on these areas. However, it should be noted that in this area, there is a levelling network (Galvani et al., 2021) realized by National Institute of Geophysics and Volcanology (Italian: Istituto Nazionale di Geofisica e Vulcanologia, INGV).

In order to take into account the inconsistency between the GPS/levelling datum and the gravimetric geoid datum, 10 vertices of the IGM network with a uniform distribution in the test area were chosen. By adopting a four-parameter model and constructing a least squares system in Matlab®, the parameters  $a_0, a_1, a_2$  and  $a_3$  that characterise this inconsistency were determined. The residuals obtained from the difference between  $N_{gravimetrico}$  and  $N_{GPS/liv}$ , were subsequently interpolated by "kriging" method and added to the pre-adjustment  $N$  model, i.e. the gravimetric one.

In the following graph (**Fig. 7**) the abscissae indicate the vertices taken into consideration, while the ordinates indicate the geoid undulation values, expressed in metres. In **Fig. 7**, the red bar indicates the pre-adjustment undulation, the green bar the post-adjustment undulation and the blue bar the levelling reference undulation; by comparing them, it can be seen that the green bar is closer to the blue bar, denoting the improvement of the geoid model following the adjustment. It follows that the high resolution of the geoid is related to the levelling network, therefore, the higher the number of vertices with known double elevation, the higher the accuracy of the geoid model.

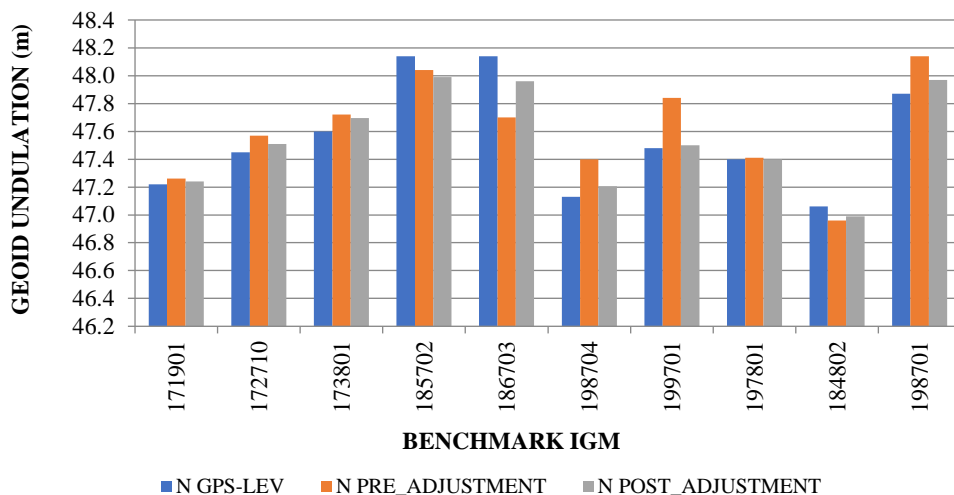


**Fig. 7.** Comparison of geoid undulations over ten benchmarks.

The new geoid undulation model, obtained in the GEOTRAV reference system relative to the test area, is shown in **Fig. 8**.

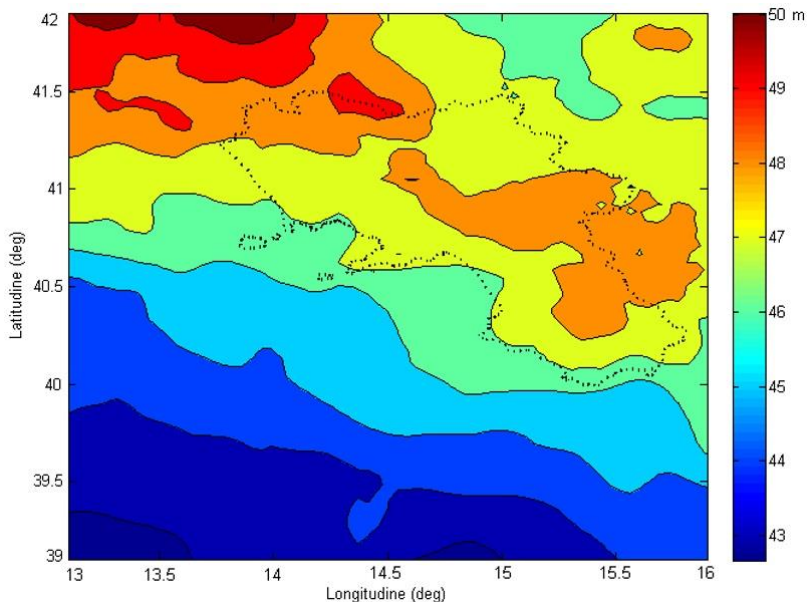


**Fig. 8.** Local geoid model on AOI.

## 4.2. 'Vertical shift' of the EGM2008 global geoid undulation model

The global model provides a good part of the geoid undulation values, net of the contribution due to the influence of topography and strong gravimetric influences.

For this reason, the undulation values of the geoid model EGM2008 were compared on the Campania region, where the contribution of topography is less relevant than in other areas (e.g. the Alps), with those obtained on the test area with the remove-restore technique with subsequent adjustment on the vertices by GPS/levelling (Pepe & Prezioso, 2016).

The differences in geoid undulation between the two models were assessed on the basis of those parameters that provide information on the characteristic of the distribution of a one-dimensional variable, namely the first-degree moment (or mean) and the standard deviation ( $\sigma$ ):

$$m_1(x) = \sum_{i=1}^n x_i f_i \quad (34)$$

$$\sigma = \sqrt{\sigma^2(x)} = \sqrt{\sum_{i=1}^n v_i^2 f_i} \quad (35)$$

where  $f_i$  is the relative frequency and with  $v_i$  the following quantity:

$$v_i = x_i - m_1(x) \quad (36)$$

In this case study, the differences of geoid undulation values showed mean and standard deviation values of  $m_1(x) = -0.21m$  and  $\sigma = 0.08m$  with minimum and maximum values, respectively  $min = -0.76m$  and  $max = +0.52m$ .

The analysis of the statistical data leads to the application of a constant translation equal to minus  $m_1(x)$ , to the EGM2008 model, obtaining a new local geoid model with minimum and maximum undulation difference values compared to the global one:  $min = -0.16m$ ,  $max = +0.22m$ .

## 5. CONCLUSIONS

The development of algorithms in Matlab® environment allowed, using the remove-compute-restore technique, to build a local geoid model. In this way, it was possible to obtain the values of the geoid undulation. The implementation of these algorithms in Matlab® is facilitated by the inclusion of numerous and increasingly powerful mathematical and algebraic functions in this environment.

In particular, the research that led to the building of a local geoid model allowed to highlight several aspects on the study area: *i)* high performance of the EGM2008 global model on the Campania region; *ii)* "smoothing" effect of the geoid undulation values of the EGM2008 model on the small islands; *iii)* improvements of the geoid model obtains by introducing into the adjustment the values of the IGM vertices determined with GPS technology and subsequently connected to the levelling network. In addition, the realization of new levelling lines would allow to obtain a higher accuracy of the geoid model and thus make it available at a higher spatial resolution.

Therefore, the geoid undulation, available in vector or raster format, can be used in several geomatics applications, such as the knowledge physical height by GNSS measurements. Indeed, GNSS-based applications are becoming increasingly common in various fields, such as topography, terrestrial or aerial photogrammetry and remote sensing.

Furthermore, once the geoid undulation model has been computed, it is possible to calculate with elevated accuracy the components of the deflection of the vertical (the meridional component  $\xi$  and the East-West component or first vertical  $\eta$ ) using the formulas of Vening Meisnez and useful in several geomatics applications.

## REFERENCES

- Amante, C. & B. W. Eakins. (2209). ETOPO1 1 Arc-Minute Global Relief Model: Procedures, *Data Sources and Analysis*, NOAA Technical Memorandum NESDIS NGDC-24, pp. 19.
- Baiocchi, V., Camuccio, P., Zagari, M., Ceglia, A., Del Gobbo, S., Purri, F., ... & Vatore, F. (2017). Development of a geographic database of a district area in open source environment. *GEAM-Geoingegneria ambientale e mineraria-geam-geoengineering environment and mining*, (151), 97-101.
- Barzaghi, R.; Borghi, A.; Carrion, D.; Sona, G. Refining the estimate of the italian quasi-geoid. *Boll. Geod. Sci. Affin.* 2007, 66, 145–160.
- Barzaghi, R., Carrion, D., Pepe, M., & Prezioso, G. (2016). Computing the deflection of the vertical for improving aerial surveys: a comparison between EGM2008 and ITALGEO05 estimates. *Sensors*, 16(8), 1168.
- Blázquez, E. B., Gil, A. J., Rodríguez-Caderot, G., De Lacy, M. C., & Ruiz, J. J. (2003). ANDALUSGeoid2002: The new gravimetric geoid model of Andalusia (Southern Spain). *Studia Geoph. et Geod.*, 47(3), 511-520.
- Borre K. (2008). Geoid Undulations Computed from EGM96, Aalborg University.
- Briggs, I.C. (1974). Machine contouring using minimum curvature, *Geophysics*, 39, 39–48.
- Corchete, V., Chourak, M. and Khattach, D. (2005), The high-resolution gravimetric geoid of Iberia: IGG2005. *Geophysical Journal International*, 162: 676–684. doi: 10.1111/j.1365-246X.2005. 02690.x
- Corchete V. (2010). The high-resolution gravimetric geoid of Italy: ITG2009, *Journal of African Earth Sciences*, 58, pp. 580-584.
- Costantino, D., Pepe, M., Dardanelli, G., & Baiocchi, V. (2020). Using optical Satellite and aerial imagery for automatic coastline mapping. *Geographia Technica*, 15(2), 171-190.
- Davis J.C. (1986). *Statistics and Data Analysis in Geology*, John Wiley e Sons Inc.
- El-Ashquer, M., Elsaka, B., & El-Fiky, G. (2017). An Improved Local Geoid Model for Egypt using Satellite Geopotential and Terrestrial Data. *Al-Azhar University Civil Eng. Research Magazine (CERM)*, 39(2).
- Erol, S., Özögel, E., Kuçak, R. A., & Erol, B. (2020). Utilizing Airborne LiDAR and UAV Photogrammetry Techniques in Local Geoid Model Determination and Validation. *ISPRS International Journal of Geo-Information*, 9(9), 528.
- Forsberg, R. (1984). *A study of terrain reductions, density anomalies and geophysical inversion methods in gravity field modelling*. Ohio State Univ Columbus Dept Of Geodetic Science and Surveying.
- Fotopoulos G. (2003). An analysis on the optimal combination of geoid, orthometric and ellipsoidal height data, PhD thesis, Department of Geomatics Engineering, University of Calgary, Alberta Canada.
- Galvani, A., Pezzo, G., Sepe, V., & Ventura, G. (2021). Shrinking of Ischia Island (Italy) from Long-Term Geodetic Data: Implications for the Deflation Mechanisms of Resurgent Calderas and Their Relationships with Seismicity. *Remote Sensing*, 13(22), 4648.
- Haagmans, R. (1993). Fast evaluation of convolution integrals on the sphere using 1D FFT and a comparison with existing methods of Stokes' integral. *Manuscr. Geod.*, 18, 227-241.
- Heiskanen W. A. & Moritz H. (1967). *Physical Geodesy*, W. H. Freeman e Co Ltd, San Francisco.
- Hofmann-Wellenhof, B., & Moritz, H. (2006). *Physical geodesy*. Springer Science & Business Media.
- Isioye O. A. & Youngu T. T. (2009). Global Geoid Modeling and height determination for enginnering applications.
- Kalu, I., Ndehedehe, C. E., Okwuashi, O., & Eyoh, A. E. (2021). Integration of satellite geodetic observations for regional geoid modeling using remove-compute-restore technique. *Earth Science Informatics*, 1-19.
- Kuroishi Y. (1993) Precise Gravimetric Determination of Geoid in the Vicinity of Japan. *Bulletin of the Geographical Survey Institute*, Vol. 41.
- Lysaker, D. I., Omang, O. C. D., Pettersen, B. R., & Solheim, D. (2007). Quasigeoid evaluation with improved levelled height data for Norway. *Journal of Geodesy*, 81(9), 617-627.
- Mayer-Gürr, T., Behzadpour, S., Ellmer, M., Klinger, B., Kvas, A., & Zehentner, N. (2016). ITSG-Grace2016-monthly and daily gravity field solutions from GRACE.
- Moritz H. (1980). *Advanced Physical Geodesy*, Herbert Wichmann Verlag Karlsruhe.
- Pavlis, N. K., Holmes, S. A., Kenyon, S. C., & Factor, J. K. (2012). The development and evaluation of the Earth Gravitational Model 2008 (EGM2008). *Journal of geophysical research: solid earth*, 117(B4).



- Oluyori, P. D., Ono, M. N., & Eteje, S. O. (2018). Computations of Geoid Undulation from Comparison of GNSS/Levelling with EGM 2008 for Geodetic Applications. *International Journal of Scientific and Research Publications*, 8(10), 235-241.
- Parente, C., & Pepe, M. (2018). Uncertainty in landslides volume estimation using DEMs generated by airborne laser scanner and photogrammetry data. *International Archives of the Photogrammetry, Remote Sensing and Spatial Information Sciences*, 42(3/W4), 397-404.
- Pavlis N.K., Factor J.K., Holmes S.A. (2007). Terrain-related gravimetric quantities computed for the next EGM, 1st Intern. Symposium of the International Gravity Field Service (IGFS), Turkey, Special Issue 18, pp. 318-323.
- Pavlis N. K., Holmes S.A., Kenyon S.C., Factor J.K. (2008). An Earth Gravitational Model to Degree 2160: EGM2008, General Assembly of the EGU, Vienna, April 13-18/2008.
- Pepe, M. & Prezioso, G. (2015). A matlab geodetic software for processing airborne LIDAR bathymetry data. *The International Archives of Photogrammetry, Remote Sensing and Spatial Information Sciences*, 40(5), 167.
- Pepe, M., Costantino, D., Alfio, V. S., Angelini, M. G., & Restuccia Garofalo, A. (2020). A CityGML Multiscale Approach for the Conservation and Management of Cultural Heritage: The Case Study of the Old Town of Taranto (Italy). *ISPRS International Journal of Geo-Information*, 9(7), 449.
- Saleh J., Pavlis N.K. (2002) Development and evaluation of the global digital terrain model DTM2002, 3rd Meeting of the International Gravity and Geoid Commission of the International Association of Geodesy, edited by I. Tziavos, pp. 207-222.
- Sansò, F. & Sideris, M. G. (2013). Geoid Determination: Theory and Methods, Springer Nature, Switzerland, <https://doi.org/10.1007/978-3-540-74700-0>.
- Schwarz K. P., Sideris M. G. & Forsberg R (1990). The use of FFT techniques in physical geodesy, *Geophysical Journal International*, 100, pp. 485-514.
- Sideris, M.G. (1990). Rigorous gravimetric terrain modelling using Molodensky's operator, *Manuscr. Geod.*, 15, 97-106.
- Sjöberg, L. E. (2005). A discussion on the approximations made in the practical implementation of the remove-compute-restore technique in regional geoid modelling. *Journal of Geodesy*, 78(11-12), 645-653.
- Smith W.H.F. & Wessel P. (1990). Gridding with continuous curvature splines in tension, *Geophysics*, 55(3), 293-305.
- Srinivas, N., Tiwari, V. M., Tarial, J. S., Prajapati, S., Meshram, A. E., Singh, B., & Nagarajan, B. (2012). Gravimetric geoid of a part of south India and its comparison with global geopotential models and GPS-levelling data. *Journal of earth system science*, 121(4), 1025-1032.
- Torge, W. (2001). Geodesy, Walter de Gruyter, Hawthorne.
- Werner, M. (2001). Shuttle radar topography mission (SRTM) mission overview. *Frequenz*, 55(3-4), 75-79.
- Yurt K. & Gokalp E. (2006). Spherical and Planar Approach in Determination of Local Geoid: Case Study in Trabzon/Turkey, XXIII FIG Congress, Germany, 13/8/2006.

## INTELLIGENT LOW-LEVEL WIND SHEAR ALERT PREDICTION SYSTEM BASED ON ANEMOMETER SENSOR NETWORK AND TEMPORAL CONVOLUTIONAL NETWORK (TCN)

Muhammad RYAN<sup>1</sup>, Adhi Harmoko SAPUTRO<sup>1</sup>, Ardhasena SOPAHELWAKAN<sup>2</sup>

DOI: 10.21163/GT\_2022.171.07

### ABSTRACT:

Wind shear is one of the dangerous meteorological phenomena for aviation. This phenomenon is significant, especially at the lower level. The duration of wind shear events varies greatly, ranging from short to long. The best way to avoid accidents caused by wind shear is by predicting the event and the duration. Recent studies use Machine Learning (ML) as a nonlinear geostatistical method to predict wind shear utilizing wind observing instruments data. The data is conditioned into temporal data which is fed to the ML model. However, the ML model used is not a temporal ML model for time-series data but a generic model for a common type of data. Many studies claimed temporal models are better than generic ones to tackle temporal data. In this study, we propose Temporal Convolutional Network (TCN) to predict incoming wind shear duration and occurrence using an anemometer sensor network i.e., Low-level Wind Shear Alert System (LLWAS). The wind shear occurrence is derived from wind shear duration prediction. The proposed model is compared with other temporal models, i.e., Long-Short Term Memory (LSTM) and Gated Recurrent Unit (GRU). Different schemes of total predictor were tested to find the best predictor scheme for wind shear prediction. To measure the performance of all models in all schemes, accuracy, False Alarm Ratio (FAR), Probability of Detection (POD), and Root Mean Squared Error (RMSE) metrics are used. The result is TCN dominating almost in all metrics used i.e., Accuracy, FAR, and RMSE for all schemes against LSTM and GRU. Scheme with 4 predictors proved to bring the best performance of all models for wind shear duration prediction. The result proves TCN is the best temporal model for wind shear forecasting using LLWAS. For better wind shear duration prediction, the best scheme choice is the 4-predictor scheme.

**Key-words:** *Wind shear, Aviation, Machine learning, Geostatistical, Temporal Convolutional Network.*

## 1. INTRODUCTION

Among the cause of aircraft accidents by meteorological phenomena, wind shear is the dominant factor (Huang, 2020). Its unpredictable nature makes an aircraft deviate from its track. By the direction, wind shear is distinguishable into 2 types, i.e., horizontal, and vertical wind shear. Harmful wind disturbances such as downbursts and microbursts are the kind of horizontal wind shear-type when they hit the ground (International Civil Aviation Organization, 2005).

Some instruments have already been developed to detect such phenomena as wind shear, especially horizontal wind shear i.e., Low-level Wind Shear Alert System (LLWAS) (International Civil Aviation Organization, 2005). The LLWAS consists of a network of anemometers distributed around the runway. Using the network any wind divergence that occurs in the runway area captured by LLWAS is an indicator of wind shear occurrence.

Other instruments i.e., Lidar Doppler and Terminal Doppler Weather Radar (TDWR) developed to detect wind shear is remote sensing-based tool (Chen et al., 2017; Chun et al., 2017; International

---

<sup>1</sup>University of Indonesia, Department of Physics, Indonesia, [muhammad.ryan03@ui.ac.id](mailto:muhammad.ryan03@ui.ac.id), [adhi@sci.ui.ac.id](mailto:adhi@sci.ui.ac.id).

<sup>2</sup>Agency for Meteorological, Climatological and Geophysics, Center for Applied Climate Services, Indonesia [ardhasena@gmail.com](mailto:ardhasena@gmail.com)

Civil Aviation Organization, 2005; Nechaj et al., 2019; Shun and Chan, 2008; Thobois et al., 2019). Those Remote sensing instruments can detect wind shear at any height unlike LLWAS, but they are susceptible to the weather condition. Lidar Doppler is good in fine weather but bad at rainy weather in contrast with TDWR. On the other hand, LLWAS can work well in any weather condition (International Civil Aviation Organization, 2005). Furthermore, LLWAS can detect wind shear faster because have a faster measurement cycle.

For the pilot to better avoid the wind shear area, information on the potential wind shear area must be obtained by the pilot before the wind shear occurs. Therefore, wind shear prediction is a must. Recent research regarding wind shear prediction is dominated by numerical and Geostatistical methods. Geostatistical method used for wind shear prediction dominated by Machine Learning (ML) (Bolgiani et al., 2020; Chan and Hon, 2016; Hou and Wang, 2019; Kwong et al., 2012; Lee et al., 2020; Liu et al., 2012; Wong et al., 2008; Yan et al., 2020). Previous studies suggest numerical methods tend to have longer lead time but need massive computation power and the ML method doesn't need extensive computing resources and produces faster prediction but a shorter lead time. Possessing a shorter lead time is not a problem if the system can produce a swift forecast nevertheless but not everyone has a sizeable computation power.

Prior research about wind shear prediction using ML, the source data used is from wind shear's instrument detection system. Mostly use Lidar Doppler as a data source for the ML model (Kwong et al., 2008; Liu et al., 2012; Wong et al., 2008). Other studies used an anemometer and LLWAS (Liu et al., 2012; Ryan et al., 2021). Lidar Doppler as a data source of the ML model will have the same cons which can't predict wind shear in rainy conditions (Gultepe et al., 2019). An anemometer can only forecast in a narrow area. On the other hand, LLWAS can do a forecast in any weather condition and cover the entire runway area (Ryan et al., 2021).

Wind shear occurs with varying duration. Wind shear happens in a matter of seconds, minutes, or hours (International Civil Aviation Organization, 2005). Prior studies using ML to predict wind shear only have a limited time frame prediction so it can't handle all possible wind shear.

This paper proposes a new approach to predict wind shear using a Temporal Convolutional Network (TCN) as an ML model and LLWAS in Soekarno-Hatta airport as the data source. TCN is used to forecast the duration of incoming wind shear. Ryan et al (2021) suggest TCN exceeds the generic ML model for wind shear prediction i.e. Multi-layer Perceptron (MLP). Nevertheless, the model has not been compared against another time-series model. This paper will compare TCN against Long-short Term Memory (LSTM) and Gated Recurrent Unit (GRU). Another difference is the model will do a regression task to predict the duration of incoming wind shear instead of a classification task. When the duration's prediction is below the threshold, it's treated as "no wind shear" conversely "wind shear occurrence". Using this approach, the model can predict multiple tasks without using multiple models which is an efficient approach compared with previous studies.

## 2. STUDY AREA

Soekarno-Hatta airport is in Tangerang, Indonesia at 6° 7' 32.0016" latitude South and 106° 39' 20.9880" longitude East. The airport has 2 runway zones and 12 LLWAS anemometers are surrounding them as shown in **Fig. 1**. The blue star icon in **Fig. 1** is an anemometer and 2 red lines are runway zones. A runway zone is an area that aircraft will approach or use for landing and takeoff necessities. Thus, runway zone not only includes the runway itself but along its way needed for landing and takeoff. LLWAS Wind shear warning data is derived from wind speed and direction data through a divergence analysis algorithm (Wilson, 1991). The analysis of the divergence area is conducted by involving a combination of 3 sensors from 12 existing sensors and comparing their wind measurement. Those 3 sensors represent the zone surrounded by them.

When a particular area has a divergence value that surpasses the threshold, LLWAS will treat the area as a wind shear zone. Since there are 2 runways in Soekarno-Hatta airport, LLWAS divides the runway area into 4 parts for each end of the existing runway.

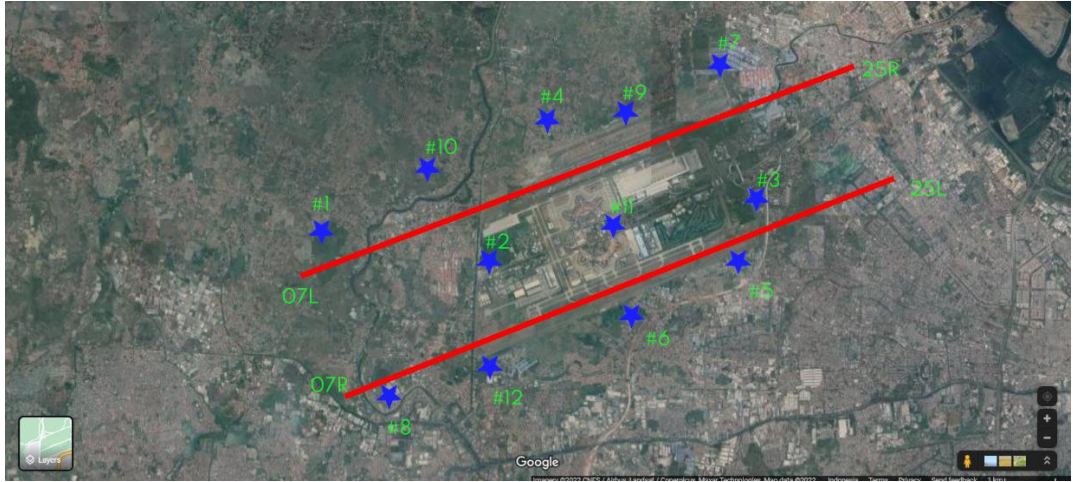


**Fig. 1.** LLWAS anemometer placement at Soekarno-Hatta airport.

The name of the runway area is presented in **Table 1**. Wind shear events detected by LLWAS can be in 1 area or more overlap with the other 3 areas. The Detection cycle of LLWAS is done every 10 seconds.

**Table 1.**  
All runway zone name in Soekarno-Hatta airport.

Runway zone name	Tip Coordinate	
	Latitude	Longitude
07L	6° 8' 2.3" S	106° 36' 10.1" E
25R	6° 5' 45.6" S	106° 42' 2.6" E
07R	6° 9' 19.3" S	106° 36' 37.4" E
25L	6° 6' 59.3" S	106° 42' 30.8" E

### 3. DATA AND METHODS

#### 3.1. Low-level Wind Shear Alert System (LLWAS) data

LLWAS data consist of wind speed and direction data and wind shear warning data. Wind speed and direction data become predictors meanwhile wind shear data is the predictand. The data period used for the experiment is from February 1 to April 18, 2020. The total dataset from the period is 2661128. Wind shear warning labeled data content made up only 0.042% and the rest is no wind shear warning data. Under-sampling was applied to manage this unbalance dataset. All "wind shear warning" labeled data is included in the dataset and "no wind shear warning" labeled data is chosen randomly from the whole dataset as much as wind shear warning data total. Data quality is also checked, any datum with typing error or empty discarded. After quality control and under-sampling, the total dataset used for each scheme is listed in **Table 2**.

**Table 2.**  
Total each label in the dataset for every experiment scheme.

Scheme	Wind Shear Occurrence	No Wind Shear
4 Predictors	915	955
6 Predictors	675	715
12 Predictors	352	392

### 3.2. Temporal Convolutional Network (TCN)

TCN is a one-dimensional Convolutional-based neural network model for temporal data (Lea et al., 2016). Besides the dimension, TCN has an additional property called dilation ( $d$ ) which depend on dilation rate ( $r$ ) as in (1). The dilation value will expand the more the TCN layer ( $l$ ) increase.

$$d = r^l \tag{1}$$

How dilation affects processing data in TCN is shown in **Fig. 2**. In most cases, dilation is set to 2 (Hewage et al., 2020; Yan et al., 2020). Dilation is a gap among data treated by a TCN filter in a layer.

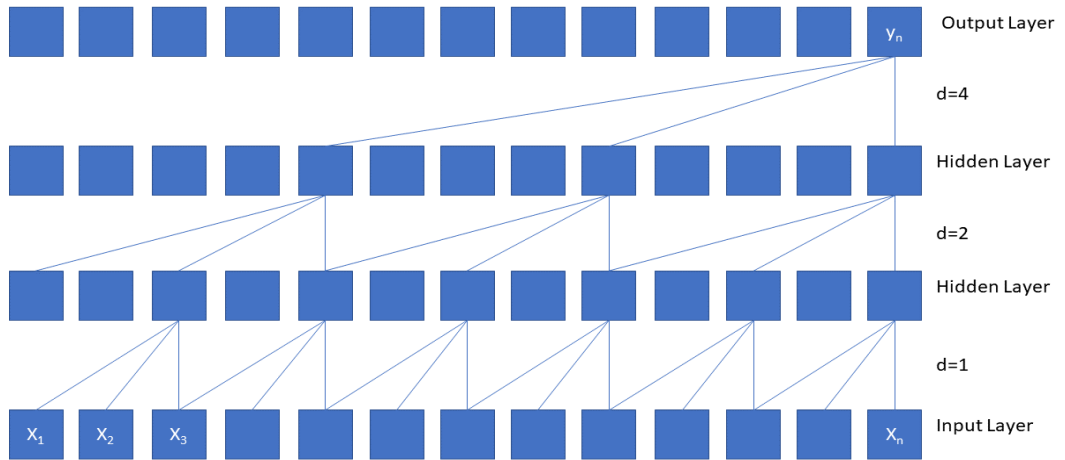


**Fig. 2.** TCN with dilation rate set as 2.

Another difference between TCN and ordinary Convolutional Neural Network (CNN) is the layer-to-layer processing data as shown in **Fig. 3**. There is no Max/Average Pooling after the activation function (Hewage et al., 2020; Yan et al., 2020). To avoid vanishing or exploding gradients due to deep layers, layer to layer processing data in TCN employ Residual Network (ResNet) (Tai et al., 2017). That is one extra process after filtering and activation function. Normally, TCN using Rectifier Linear Unit (ReLU) as an activation function (Abueidda et al., 2021; Hewage et al., 2020; Ryan et al., 2021).

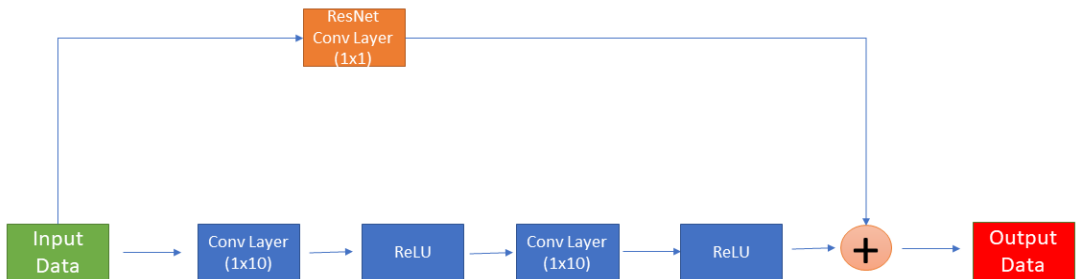


**Fig. 3.** Data processing block in TCN using ResNet for this study.

### 3.3. Long-Short Term Memory (LSTM)

LSTM is a popular Recurrent Neural Network (RNN) variant model that specializes in the time series model. An RNN has a loopback block computation that uses input data and output from the previous loop of the block. A vanilla RNN can't handle too long time series data because it can trigger a vanishing gradient (Fei and Tan, 2018). To patch this problem, a new variant of RNN with additional operation from base RNN was invented i.e., LSTM (Zhao et al., 2018). The extra operation in LSTM is represented in forget gate (f), input gate (i), memory gate (g) and output gate (o) as shown in **Fig. 4**.

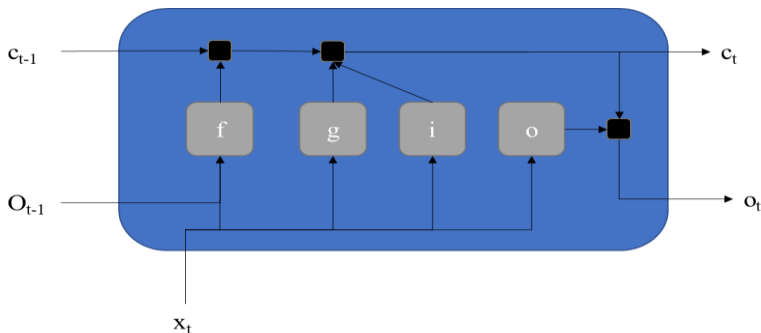


**Fig. 4.** LSTM architecture.

Forget gate is used to decide which part of the input to ignore, the input and memory gate determine which part to update, and the output gate computes the output LSTM block (Sadique and Sengupta, 2021). LSTM block will output 2 values i.e., cell state (c) and the real output (o) which will become for the next loop.

### 3.4. Gated Recurrent Unit (GRU)

GRU is another popular RNN besides LSTM. GRU has the same gate as LSTM except it doesn't have an output gate (Sadique and Sengupta, 2021). Similar to LSTM, GRU is immune to the vanishing gradient. Because of the lack of output gate, GRU has fewer trainable weights and biases. Thus, GRU is slightly more lightweight to run than LSTM.

### 3.5. Experiment Scheme

In this study, TCN will be used to do a regression task to forecast incoming wind shear duration. Wind speed and direction data from LLWAS transformed to west-east ( $U$ ) and south-north ( $V$ ) components. Furthermore,  $U$  and  $V$  data packed to become time-series data for every anemometer in LLWAS. The length of the time-series data tested in this study is 10 minutes. LLWAS has 10 seconds resolution data consequently time-series data length used is 60.

Wind shear duration ( $\omega_d$ ) data were obtained by using wind shear warning data. The number of consecutive warning times ( $\omega_c$ ) by LLWAS times resolution (2).

$$\omega_d = \omega_c \times 10 \quad (2)$$

The minimum consecutive is 1, so the minimum duration value is 10. This minimum value is set as the TCN threshold to predict the presence or absence of wind shear shortly. The data processing to produce a prediction for wind shear duration and wind shear event is summarised in **Fig. 5**. The model used for the processing is TCN, LSTM, and GRU alternately.

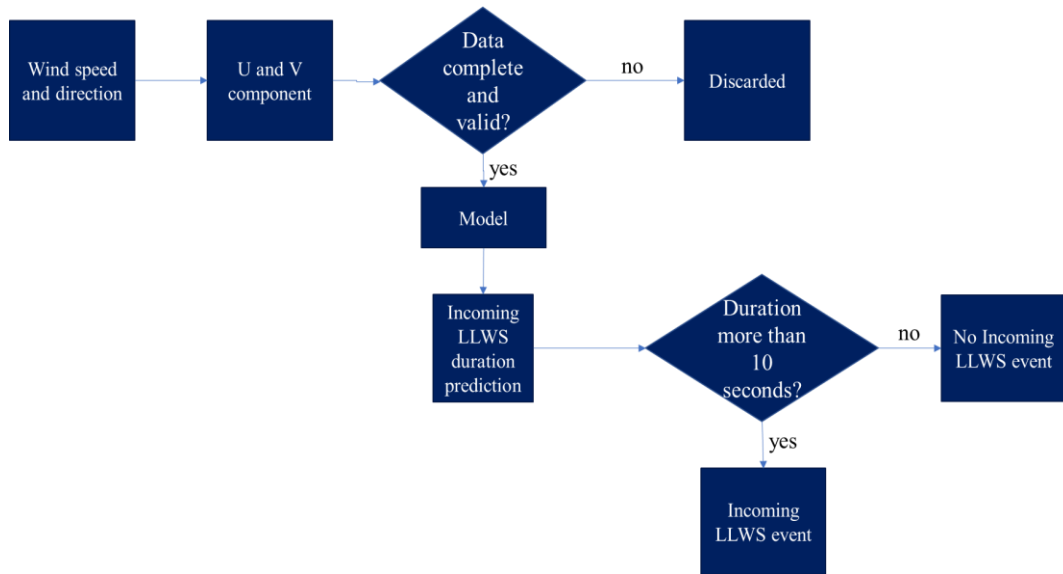


Fig. 5. Flowchart for data processing to produce wind shear prediction.

Four areas monitored by LLWAS also become forecast zone for TCN. In this study, 4, 6, and 12 anemometers were tested as the predictor to do a wind shear forecast for each area. Selected anemometers for every region in every scheme with 4 and 6 predictors are shown in **Table 3**. Twelve anemometers scheme predict every area using all anemometers. The selection is based on the nearest anemometers to the forecast area. The nearest sensor is the best data source to know the condition in a particular region (Gutierrez-Corea et al., 2016).

Table 3.

Predictor for every runway area in scheme 4 and 6 predictors.

Anemometer	Scheme							
	4 Predictors				6 Predictors			
	07L	25R	07R	25L	07L	25R	07R	25L
#1	✓				✓			
#2	✓		✓		✓		✓	
#3				✓		✓		✓
#4	✓	✓			✓	✓		
#5				✓		✓		✓
#6			✓	✓			✓	✓
#7		✓				✓		✓
#8			✓				✓	
#9		✓				✓		✓
#10	✓				✓		✓	
#11		✓		✓	✓	✓	✓	✓
#12			✓		✓		✓	

To benchmark the TCN's performance, LSTM and GRU will be the criterion model. All Hyperparameter configurations for those 3 models used for the experiment are listed in **Table 4**. These configurations were founded after trial and error which means to produce the best performance. LSTM and GRU will also have a similar threshold prediction as TCN and the same predictor set.



**Table 4.**  
Hyperparameter configuration used for experiment.

Hyperparameter	Model		
	TCN	GRU	LSTM
Layers	12	1 Stack	1 Stack
Filter Size	10	-	-
Neurons	15	15	15
Mini Batch Size	20	20	20
Epoch	100	100	100
Learning algorithm	Adam	Adam	Adam

### 3.6. Validation metric

Cross-validation 5-fold is used to measure all models' skills regardless of the scheme used. Thus, the dataset is split into 5 groups. Four groups will become the training dataset and the rest is the validation dataset. All groups alternately become validation datasets. Therefore there will be 5 times looping processes from training to validation. Models performance is measured using Root Mean Squared Error (RMSE) for wind shear duration and contingency table as shown in **Table 5**. Ground truth is obtained from cross-validation which is predictand of validation data. Furthermore, prediction value is a prediction obtained by using validation predictors data as an input model. Contingency table metric then derived to get accuracy (*acc*), Probability of Detection (POD) and False Alarm Ratio (FAR) given in (3-5) (Thobois et al., 2019). Since the performance was measured using cross-validation 5-fold, at the end of the experiment there will be 5 RMSE and contingency table derived metric values. The average of all metric values is calculated to summarize them.

**Table 5.**  
Contingency table product.

		Prediction Value	
		Right	Wrong
Ground Truth	Right	Hit (H)	Miss (M)
	Wrong	False Alarm (FA)	Correct Negative (CN)

$$acc = \frac{H+CN}{H+CN+M+FA} \quad (3)$$

$$POD = \frac{H}{H+M} \quad (4)$$

$$FAR = \frac{FA}{FA+CN} \quad (5)$$

$$RMSE = \sqrt{\sum_{i=1}^n \frac{(\bar{d}_r - d_r)^2}{n}} \quad (6)$$

where:

*acc* = accuracy

*POD* = Probability of Detection

*FAR* = False Alarm Ratio

*RMSE* = Root Mean Squared Error

#### 4. RESULTS

The output of this intelligent system is presented in a web display application as shown in **Fig. 6** and **7**. **Fig. 6** is a display condition when the model predicts wind shear duration below 10 seconds for all runway zones. Therefore, the model predicts that there is no incoming wind shear for all runway zones. **Fig. 7** shows the display when there is wind shear in several runway zones. The display shows the wind shear duration estimation when the model predicts incoming wind shear in that runway zone.

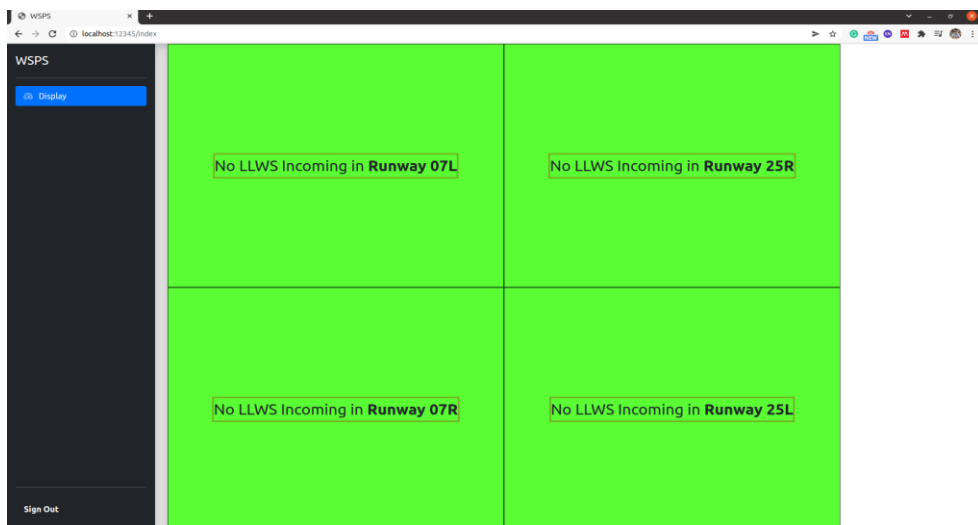


**Fig. 6.** Display condition when there is no wind shear incoming predicted.

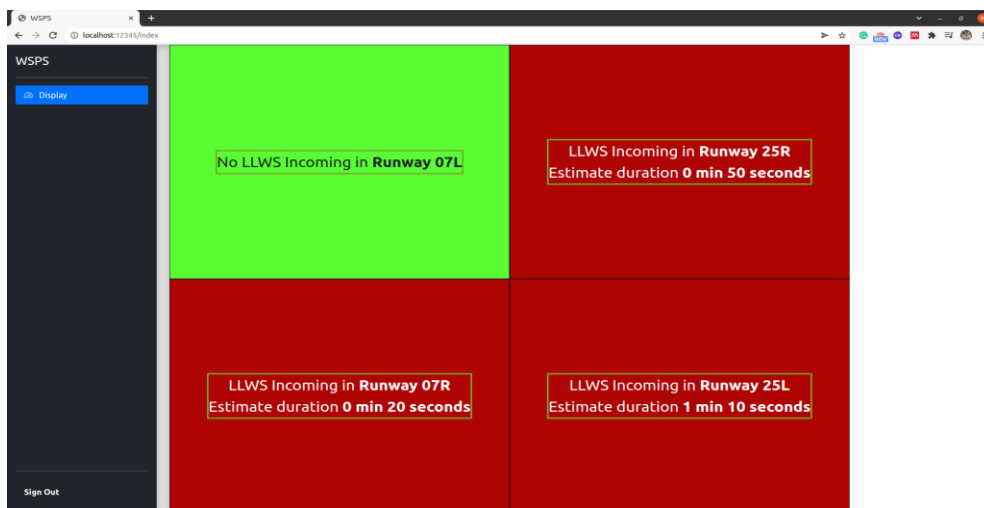


**Fig. 7.** Display condition when there is a wind shear predicted in several runway zones.

The TCN, LSTM, and GRU mean error convergence can be seen in **Fig. 8**. All models show the error decreased rapidly at the beginning phase of training and converged at some point. All models look converged after epoch 20. GRU looks converged a little late compared with TCN and LSTM. The validation error pattern for all models looks similar to training errors which means the training dataset has an alike pattern with training data. Overall, error in train and test data set for all models are very close which mean they can learn well.

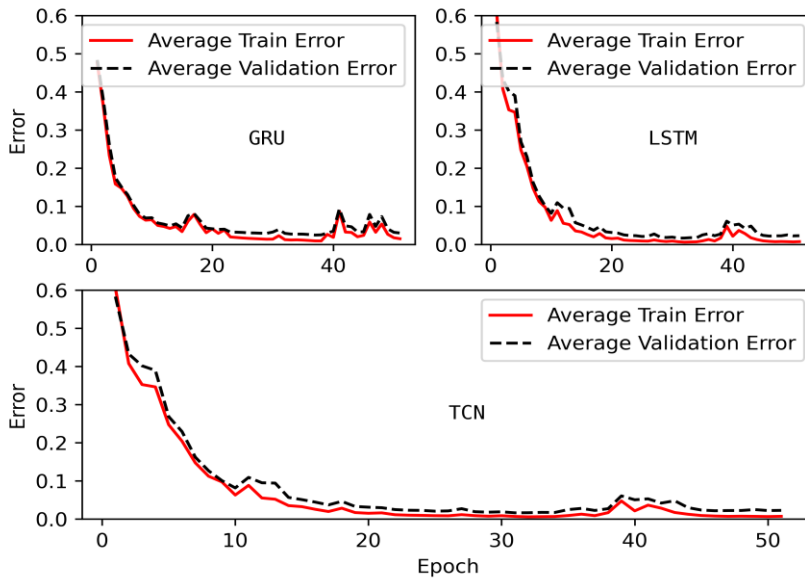


**Fig. 8.** Error convergence of all models.

All models' performance for all schemes is listed in **Table 6**. In the 4 predictors scheme, TCN has the best score in all metrics. Thus, TCN has the best performance for predicting wind shear duration and occurrence in the 4 predictors scheme. The second-best model is LSTM which all metrics show superiority over GRU.

**Table 6.**

**All models' performance.**

Model	Scheme	Average			
		Accuracy	FAR	POD	RMSE
GRU	4 predictors	0.857	0.202	0.933	22.874
	6 predictors	0.888	0.148	0.933	25.597
	12 predictors	0.860	0.201	0.962	78.718
LSTM	4 predictors	0.903	0.122	0.936	21.912
	6 predictors	0.899	0.139	0.944	36.549
	12 predictors	0.918	0.118	0.971	68.780
TCN	4 predictors	0.925	0.088	0.942	17.534
	6 predictors	0.920	0.104	0.948	20.611
	12 predictors	0.918	0.083	0.919	81.723

TCN still becomes the best model in the 6 predictors scheme. All metrics show TCN excellence over any other models in the scheme. TCN metrics in this scheme are not much different from TCN in the 4 predictors scheme. In this scheme, LSTM becomes the second-best model for predicting wind shear occurrence for having better average accuracy, FAR, and POD. Nevertheless, GRU exceeds LSTM regarding wind shear duration with a big margin in the average RMSE.

For the 12 predictors scheme, LSTM is the best performance model. LSTM and TCN have same average accuracy. LSTM average POD in this case is the biggest in all schemes against any model.

In contrast with other scheme, TCN here has the biggest average RMSE which means the worst for predicting wind shear duration.

The best model in average accuracy and RMSE is TCN in 4 predictors scheme. For FAR metric, the best model with the lowest average FAR is TCN using 12 predictors. That average FAR value is nearly same with TCN in the 4 predictors scheme which is the second-best model in average FAR metric. Their average FAR difference is subtle (only 0.005). In the average POD metric, the best model is LSTM using 12 predictors.

## 5. DISCUSSION

The metrics value in **Table 6** shows TCN superiority over criterion. From 4 metrics, TCN reign in 3 metrics as the best model. The superiority of TCN over other time-series models match fed with prior studies (Hewage et al., 2020; Yan et al., 2020; Zhu et al., 2020). Different from previous studies, this study proves TCN can outmatch classification tasks derived from regression values. TCN can detect incoming wind shear well in all schemes ( $POD > 0.9$ ) with minimum false alarm ( $FAR \geq 0.1$ ) against other models.

The TCN performance for predicting incoming wind shear looks not significantly affected by total predictors. This also applies to criterion models. There is no significant difference in the average accuracy, POD, and FAR for the same model with a different scheme. However, in predicting wind shear duration, the different scheme brings significantly different average RMSE value. TCN with 4 and 6 predictors do not have a significantly different average RMSE but have a great difference with 12 predictors. This also applies with GRU, which is the difference average RMSE value between 4 and 6 predictors scheme is 2.723 but against 12 predictors scheme, the difference is 55.784. This is different with LSTM where all schemes have a significant difference in average RMSE ( $>5$ ). However, the experiment shows the fact that the 12 predictors scheme has the biggest average RMSE for all models.

The increase in the number of predictors must be accompanied by an increase in the dataset. Nonetheless, the scheme with the largest total predictor in this experiment has the lowest total dataset. This causes the model can't learn well the general pattern of the dataset. For a regression model, the effect is an increase in RMSE value. Wind shear duration is a product of the regression model, that why the average RMSE value for 12 predictors is huge compared with another scheme. For wind shear duration prediction, the best scheme is the 4 predictors scheme which is has a biggest total dataset. This finding underlines the importance of the total dataset over the model used for wind shear duration prediction.

Overall, the experiment show TCN outperforms all criterion models slightly for this case. The criterion models have high performance because they are specializing in time series problems. Therefore, the difference in performance between TCN and criterion models is not significant. This finding is similar to (Gopali et al., 2022) and (Sadique and Sengupta, 2021) in a different case. Previous studies already confirm that convolutional network architecture is better than generic recurrent network architecture for sequence modeling across different tasks (Bai et al., 2018). Additional property for a convolutional network in TCN i.e., dilation makes the model can handle a long sequence data to perfect the model for sequence modeling.

## 6. CONCLUSIONS

This paper introduced a new way to predict wind shear using ML which can predict the wind shear occurrence and duration with just 1 model. The proposed model can reign over criterion models almost in all metrics. The proposed model can predict well if fed with enough training datasets. The proposed model's RMSE increases significantly as the total dataset decrease and the total predictor increase. Nevertheless, the proposed model can achieve high accuracy ( $>0.9$ ) in any scheme. Furthermore, the proposed model can converge fast enough against criterion models.

## REFERENCES

- Abueidda, D.W., Koric, S., Sobh, N.A., Sehitoglu, H., 2021. Deep learning for plasticity and thermo-viscoplasticity. *Int. J. Plast.* 136, 102852. <https://doi.org/10.1016/j.ijplas.2020.102852>
- Bai, S., Kolter, J.Z., Koltun, V., 2018. An Empirical Evaluation of Generic Convolutional and Recurrent Networks for Sequence Modeling.
- Bolgiani, P., Santos-Muñoz, D., Fernández-González, S., Sastre, M., Valero, F., Martín, M.L., 2020. Microburst Detection With the WRF Model: Effective Resolution and Forecasting Indices. *J. Geophys. Res. Atmos.* 125, e2020JD032883. <https://doi.org/10.1029/2020JD032883>
- Chan, P.W., Hon, K.K., 2016. Performance of super high resolution numerical weather prediction model in forecasting terrain-disrupted airflow at the Hong Kong International Airport: case studies. *Meteorol. Appl.* 23, 101–114. <https://doi.org/10.1002/met.1534>
- Chen, Y., An, J.L., Lin, J., Sun, Y. Le, Wang, X.Q., Wang, Z.F., Duan, J., 2017. Observation of nocturnal low-level wind shear and particulate matter in urban Beijing using a Doppler wind lidar. *Atmos. Ocean. Sci. Lett.* 10, 411–417. <https://doi.org/10.1080/16742834.2017.1368349>
- Chun, H.Y., Kim, J.H., Lee, D.B., Kim, S.H., Strahan, M., Pettegrew, B., Gill, P., Williams, P.D., Schumann, U., Tenenbaum, J., Lee, Y.G., Choi, H.W., Song, I.S., Park, Y.J., Sharman, R.D., 2017. Research collaborations for better predictions of aviation weather hazards. *Bull. Am. Meteorol. Soc.* 98, ES103–ES107. <https://doi.org/10.1175/BAMS-D-17-0010.1>
- Fei, H., Tan, F., 2018. Bidirectional Grid Long Short-Term Memory (BiGridLSTM): A method to address context-sensitivity and vanishing gradient. *Algorithms* 11. <https://doi.org/10.3390/a11110172>
- Gopali, S., Abri, F., Siami-Namini, S., Namin, A.S., 2022. A Comparison of TCN and LSTM Models in Detecting Anomalies in Time Series Data 2415–2420. <https://doi.org/10.1109/bigdata52589.2021.9671488>
- Gultepe, I., Sharman, R., Williams, P.D., Zhou, B., Ellrod, G., Minnis, P., Trier, S., Griffin, S., Yum, S.S., Gharabaghi, B., Feltz, W., Temimi, M., Pu, Z., Storer, L.N., Kneringer, P., Weston, M.J., Chuang, H. ya, Thobois, L., Dimri, A.P., Dietz, S.J., França, G.B., Almeida, M. V., Neto, F.L.A., 2019. A Review of High Impact Weather for Aviation Meteorology. *Pure Appl. Geophys.* 176, 1869–1921. <https://doi.org/10.1007/s00024-019-02168-6>
- Gutierrez-Corea, F.V., Manso-Callejo, M.A., Moreno-Regidor, M.P., Manrique-Sancho, M.T., 2016. Forecasting short-term solar irradiance based on artificial neural networks and data from neighboring meteorological stations. *Sol. Energy* 134, 119–131. <https://doi.org/10.1016/j.solener.2016.04.020>
- Hewage, P., Behera, A., Trovati, M., Pereira, E., Ghahremani, M., Palmieri, F., Liu, Y., 2020. Temporal convolutional neural (TCN) network for an effective weather forecasting using time-series data from the local weather station. *Soft Comput.* 24, 16453–16482. <https://doi.org/10.1007/s00500-020-04954-0>
- Hou, J., Wang, P., 2019. A Method of Shear Line Automatic Identification on High-precision Numerical Data. *Proc. World Congr. Intell. Control Autom.* 2018-July, 704–709. <https://doi.org/10.1109/WCICA.2018.8630549>
- Huang, C., 2020. Further improving general aviation flight safety: Analysis of aircraft accidents during takeoff. *Coll. Aviat. Rev.* 38, 88–105. <https://doi.org/10.22488/okstate.20.100206>
- International Civil Aviation Organization, 2005. Doc 9817 Manual on Low-level Wind Shear.
- Kwong, K.M., Liu, J.N.K., Chan, P.W., Lee, R., 2008. Using LIDAR Doppler velocity data and chaotic oscillatory-based neural network for the forecast of meso-scale wind field, in: 2008 IEEE Congress on Evolutionary Computation, CEC 2008. pp. 2012–2019. <https://doi.org/10.1109/CEC.2008.4631064>
- Kwong, K.M., Wong, M.H.Y., Liu, J.N.K., Chan, P.W., 2012. An artificial neural network with chaotic oscillator for wind shear alerting. *J. Atmos. Ocean. Technol.* 29, 1518–1531. <https://doi.org/10.1175/2011JTECHA1501.1>
- Lea, C., Ren, M.D.F., Reiter, A., Hager, G.D., 2016. for Action Segmentation and Detection 156–165.
- Lee, Y.G., Ryoo, S.B., Han, K., Choi, H.W., Kim, C., 2020. Inter-comparison of ensemble forecasts for low level wind shear against local analyses data over Jeju area. *Atmosphere (Basel)*. 11, 198. <https://doi.org/10.3390/atmos11020198>

- Liu, J.N.K., Kwong, K.M., Chan, P.W., 2012. Chaotic oscillatory-based neural network for wind shear and turbulence forecast with LiDAR data. *IEEE Trans. Syst. Man Cybern. Part C Appl. Rev.* 42, 1412–1423. <https://doi.org/10.1109/TSMCC.2012.2188284>
- Nechaj, P., Gaál, L., Bartok, J., Vorobyeva, O., Gera, M., Kelemen, M., Polishchuk, V., 2019. Monitoring of low-level wind shear by ground-based 3D lidar for increased flight safety, protection of human lives and health. *Int. J. Environ. Res. Public Health* 16, 4584. <https://doi.org/10.3390/ijerph16224584>
- Ryan, M., Saputro, A.H., Sopaheluwakan, A., 2021. Enhancing Low-level Wind Shear Alert System (LLWAS) to Predict Low-level Wind Shear (LLWS) Phenomenon Using Temporal Convolutional Network, in: 2021 8th International Conference on Electrical Engineering, Computer Science and Informatics (EECSI). Institute of Advanced Engineering and Science (IAES), pp. 5–9. <https://doi.org/10.23919/eeesi53397.2021.9624225>
- Sadique, F., Sengupta, S., 2021. Modeling and Analyzing Attacker Behavior in IoT Botnet using Temporal Convolution Network (TCN) 2021, 1–22.
- Shun, C.M., Chan, P.W., 2008. Applications of an infrared Doppler lidar in detection of wind shear. *J. Atmos. Ocean. Technol.* 25, 637–655. <https://doi.org/10.1175/2007JTECHA1057.1>
- Tai, Y., Yang, J., Liu, X., 2017. Image super-resolution via deep recursive residual network. *Proc. - 30th IEEE Conf. Comput. Vis. Pattern Recognition, CVPR 2017 2017-Janua*, 2790–2798. <https://doi.org/10.1109/CVPR.2017.298>
- Thobois, L., Cariou, J.P., Gultepe, I., 2019. Review of Lidar-Based Applications for Aviation Weather. *Pure Appl. Geophys.* 176, 1959–1976. <https://doi.org/10.1007/s00024-018-2058-8>
- Wilson, F.W., 1991. Wind Shear Alert System.
- Wong, M.H.Y., Lee, R.S.T., James, N.K.L., 2008. Wind Shear Forecasting by Chaotic Oscillatory-based Neural Networks (CONN) With Lee Oscillator (Retrograde Signalling) Model, in: *Neural Networks*. pp. 2041–2048.
- Yan, J., Mu, L., Wang, L., Ranjan, R., Zomaya, A.Y., 2020. Temporal Convolutional Networks for the Advance Prediction of ENSO. *Sci. Rep.* 10, 1–15. <https://doi.org/10.1038/s41598-020-65070-5>
- Zhao, Z., Rao, R., Tu, S., Shi, J., 2018. Time-weighted lstm model with redefined labeling for stock trend prediction. *Proc. - Int. Conf. Tools with Artif. Intell. ICTAI 2017-November*, 1210–1217. <https://doi.org/10.1109/ICTAI.2017.00184>
- Zhu, R., Liao, W., Wang, Y., 2020. Short-term prediction for wind power based on temporal convolutional network. *Energy Reports* 6, 424–429. <https://doi.org/10.1016/j.egy.2020.11.219>

## NIGHTTIME LIGHT EMISSIONS EXPLAIN THE DECLINE IN NO<sub>2</sub> DURING A COVID-19-INDUCED TOTAL LOCKDOWN IN FRANCE

Kamill Dániel KOVÁCS <sup>1</sup> 

DOI: 10.21163/GT\_2022.171.08

### ABSTRACT:

Referring to a total lockdown due to COVID-19 in Metropolitan France, this study investigates the geospatial correlation between nighttime light emission and the relative change of NO<sub>2</sub> air pollution (dNO<sub>2</sub> %). To address the research problem, near-surface NO<sub>2</sub> data and nighttime light data were implemented. Stable night lights were obtained for a long period on average (2014-2019) using Day-Night Band (DNB) data from the Visible Infrared Imaging Radiometer Suite (VIIRS). The relative change in tropospheric NO<sub>2</sub> was calculated using Sentinel-5P satellite data from the Tropospheric Monitoring Instrument (TROPOMI). The dNO<sub>2</sub> calculation was performed considering an equivalent reference period (April 2019) to the major lockdown period in France (April 2020). The correlation between the variables DNB nighttime lights and dNO<sub>2</sub> was tested with a statistical T-test. The findings revealed an intense phenomenon of decreasing NO<sub>2</sub> air pollution in France (decreases by -25% to -50%). Decreases < -50% were mainly recorded in the greater Paris metropolitan area, in Alsace, and other locations. The results showed a strong and statistically significant inverse geospatial correlation between the two variables under anti-COVID-19 control measures. The higher was the emission of nighttime lights, the higher was the degree of tropospheric NO<sub>2</sub> decrease in the regions of France (R<sup>2</sup>=0.72). It is concluded that employing remote sensing techniques, DNB nighttime light is a reliable indicator to estimate the degree of air decontamination. DNB as an independent variable is recommended for future research on changes in the concentration of other pollutant gases.

**Key-words:** *Satellite data, NO<sub>2</sub>, Decontamination, Visible to near-infrared, Constraint, France*

### 1. INTRODUCTION AND LITERATURE REVIEW

Is there a connection between emitted nighttime lights and the drop in NO<sub>2</sub> air pollution caused by the measures taken against COVID-19?

The outbreak of the novel SARS-CoV-2 coronavirus caused a great impact on global society. It was estimated that the pandemic may have slowed the global economy by 3% to 6% in 2020 (Jackson et al., 2021) having negative repercussions on whole societies.

From March, countries' governments imposed total or partial confinements leading to curfews (WHO, 2020a, 2020b). Moreover, transportation limitations were implemented in several countries. Consequently, the anti-COVID-19 measures have slowed the anthropogenic activities, resulting in a decrease in air pollution (Cameletti, 2020; Dutheil et al., 2020; Kumari & Toshniwal, 2020; Muhammad et al., 2020; Rugani & Caro, 2020; Zaib et al., 2021; Zambrano-Monserrate et al., 2020). In France, the first total lockdown lasted between March 17, 2020 and May 11, 2020 (Gouvernement Français, n.d.). Many impacts of human activities on the environment can be remotely monitored using satellite data. Nighttime light emissions represent an indicator of population density, urbanization, and economic development of regions (Levin & Zhang, 2017; Small & Elvidge, 2013). Furthermore, these emissions have an impact on human health and ecosystems (light pollution) (Gaston et al., 2013; Koo et al., 2016).

The use of night light data for economic growth studies is well known (Beyer et al., 2018; Ghosh et al., 2017; Ivan et al., 2020; Prakash et al., 2019). Besides, there are recent studies that addressed the phenomenon of dimming night lights during COVID-19 lockdowns (Bustamante-Calabria et al.,

---

<sup>1</sup> Université de Lorraine, Laboratoire LOTERR-EA7304, Île du Saulcy, 57045 Metz, France, [kamill-daniel.kovacs@univ-lorraine.fr](mailto:kamill-daniel.kovacs@univ-lorraine.fr)



2021; Elvidge et al., 2020; Ghosh et al., 2020; S. Zheng et al., 2021). Low-light imaging satellite sensors were also implemented to detect dimming and recovery of night lights after natural disasters (Román et al., 2019; Zhao et al., 2018; Y. Zheng et al., 2019) or other social problems (e.g. wars) (Li et al., 2018), humanitarian crises (Zhang et al., 2020), or economic collapse (Elvidge et al., 2016). NO<sub>2</sub> data from both satellite sensors and on-site measurements were used in previous studies that addressed air pollution decrease during the pandemic (Chan et al., 2021; Ikhlassé et al., 2021; Tian et al., 2021).

This study's purpose is to examine the geospatial relationship between night light emission and the decline in NO<sub>2</sub> air pollution over Metropolitan France during the first total confinement (April 2020). Sentinel-5P satellite data with high spatial resolution were used to calculate the change in tropospheric NO<sub>2</sub> concentration. Night lights were obtained using low-light satellite imagery data collected by the National Aeronautics and Space Administration and National Oceanic and Atmospheric Administration's (NASA/NOAA) Visible Infrared Imaging Radiometer Suite (VIIRS) Day-Night Band (DNB).

The novelty that this study brings to the literature is to determine the geospatial connection between the intensity of nighttime anthropogenic activity and the air decontamination observed under mobility control measures. The research hypothesis was raised that the greater the night light emission in a certain territory, the greater the decline in NO<sub>2</sub> air pollution during the first month of total lockdown.

## 2. DATA USED

Night light radiance data were retrieved from Suomi National Polar-orbiting Partnership's (SNPP) Visible Infrared Imaging Radiometer Suite (VIIRS) that is compatible with the DNB sensor, providing global daily measurements of night lights in the visible and near-infrared (NIR) bands of the electromagnetic spectrum. VIIRS DNB is ultra-sensitive even in low light conditions, which allows generating high-quality by-products in terms of resolution and sensor calibration. Through these enhancements, VIIRS DNB products allow monitoring nighttime events and light emission sources associated with human activities.

VIIRS DNB data product contains the nocturnal radiance obtained in the upper part of the atmosphere. The VNP46A1 sensor contains 26 datasets, including sensor luminosity, azimuth and zenith angles, cloud mask, shortwave infrared radiance, brightness temperature, moon phase angle, moonlight fraction, and other quality indicators. With millions of times intensification of the signal, the DNB band detects electrical lighting on Earth's surface (Miller et al., 2013). The data is pre-processed to remove cloud cover, solar and lunar pollution, forest fires, and auroras (Elvidge et al., 2017). In this study, nighttime light data of monthly averaged composites of radiance were used from VIIRS's DNB. The data were accessed using Google Earth Engine (GEE) platform with lines of code.

The collection called in GEE was `ee.ImageCollection("NOAA/VIIRS/DNB/MONTHLY_V1/VCMSLFCFG")` (Earth Engine Data Catalog, n.d.-c). The VIIRS Cloud Mask Stray Light Corrected Nighttime DNB Composites (VCMSLFCFG) were retrieved (Elvidge et al., 2021). This data is available from 2014-01-01. The used VIIRS DNB has 463.83 m spatial resolution.

Near-surface NO<sub>2</sub> data were obtained from the Tropospheric Monitoring Instrument (TROPOMI) sensor onboard the Sentinel-5P satellite. TROPOMI detects atmospheric NO<sub>2</sub> density as concentrations via optical depth techniques in three vertical columns: total, stratospheric, and tropospheric. Tropospheric NO<sub>2</sub> data was accessed using GEE, by calling the `ee.ImageCollection("COPERNICUS/SSP/OFFL/L3_NO2")` collection. The 'Offline' (OFFL) product was used instead of the 'Near-real time' (NRTI) product because it is considered slightly more accurate (Earth Engine Data Catalog, n.d.-a; Verhoelst et al., 2021). The band `"tropospheric_NO2_column_number_density"` was used, which provides NO<sub>2</sub> data from the tropospheric vertical column. The vertical column means the ratio between the density of the inclined NO<sub>2</sub> column and the factor of the total air mass. This data is available from 2018-06-28. In addition to the raster data, tropospheric NO<sub>2</sub> time series data were obtained from TROPOMI and Aura Ozone Monitoring Instrument (OMI/Aura) (Krotkov et al., 2019).

### 3. TECHNIQUES

#### 3.1. Obtaining DNB nighttime lights and tropospheric NO<sub>2</sub> data, and calculating the relative NO<sub>2</sub> change

VIIRS DNB data was obtained using the GEE platform through javascript code (Kovács, 2021). The DNB images used represented monthly average radiances. Because this data is compiled monthly, there are areas where it is difficult to get good data coverage due to cloud cover or poleward solar illumination. Considering these technical aspects of the DNB data, an image representing annual average nightlight radiances between 2014-2019 was created over the territory of Metropolitan France. The 'cf\_cvg' band was selected not assuming zero (0 indicates no observation of lights). Cloud cover was determined using VIIRS Cloud Mask (VCM). Based upon quality indicators, DNB data was subjected to a filtering process excluding the data affected by the "parasitic" light (rays, fires, ships, solar lighting, cloud cover, and temporary lights). Finally, the resulting DNB image was exported from GEE for subsequent analysis.

Tropospheric NO<sub>2</sub> data was also retrieved through the GEE platform by accessing Sentinel-5P's collection. Daily averaged images were created for April 2019 (lockdown-free reference period) and April 2020 (lockdown period) over Metropolitan France. The conversion of Level 2 (L2) data to Level 3 (L3) gridded data was performed using the *harperconvert* tool and *bin\_spatial* operation. Then, the original NO<sub>2</sub> data was filtered to remove pixels with QC (quality control) values less than 75% for the NO<sub>2</sub> tropospheric density band (Earth Engine Data Catalog, n.d.-b). In the last step, the resulting two rasters representing NO<sub>2</sub> concentrations over France were exported from GEE for the subsequent analysis.

Accordingly, the NO<sub>2</sub> relative change (%) between the confinement-free period (RP) and the period under lockdown restriction measures (LP) was determined as follows (1):

$$Ch_{\%} = \left( \frac{X_a}{X_b} - 1 \right) * 100 \quad (1)$$

where  $Ch_{\%}$  is the relative change (%) between RP and LP,  $X_a$  is the raster image representing the NO<sub>2</sub> concentrations during LP, and  $X_b$  is the raster image representing the NO<sub>2</sub> concentrations in the equivalent calendar period RP.

#### 3.2. Time series of average NO<sub>2</sub> evolution

To check the temporal evolution of NO<sub>2</sub> in 68 cities of France, time-series data analysis was performed using Savitzky–Golay filter. The Savitzky–Golay filtering method is based on the calculation of a local polynomial regression (of degree  $k$ ) with at least  $k+1$  equispaced points (Savitzky & Golay, 1964). The obtained result is a function similar to the input data but smoothed avoiding the presence of noise. An optimal window length of 101 with polynomial order 2 was chosen for the filter. The filter was made with Python using *scipy.signal* library: "from *scipy.signal* import *savgol\_filter*". The Savitzky–Golay filter is defined as follows (Savitzky & Golay, 1964) (2):

$$Y_j = \sum_{i=\frac{1-m}{2}}^{\frac{m-1}{2}} C_i y_{j+i}, \quad \frac{m+1}{2} \leq j \leq n - \frac{m-1}{2} \quad (2)$$

where  $\{x_j, y_j\}, j = 1, \dots, n$ , are the set of points,  $x_j$  is the independent variable, and  $y_j$  is the observed value. The points are treated with a set of  $m$  convolution coefficients:  $C_i$ .

### 3.3. Establishing and testing the correlation between geospatial variables

The spatial correlation analysis between the geospatial variables DNB nighttime lights and relative NO<sub>2</sub> change (dNO<sub>2</sub>) was performed by implementing zonal statistical computations for a given administrative-territorial units' level, which were the regions of Metropolitan France. For this purpose, the 'Zonal Statistics' tool of QGIS was used. For the regional units, in the case of the variable dNO<sub>2</sub>, the average relative change value was assumed and in the case of the variable DNB night lights, the value of the most represented majority was considered. The majority statistic is a measure that returns the most represented and prevalent pixel value in a given spatial feature. Further, the correlation (R) and determination (R<sup>2</sup>) coefficients were computed. T-test was used to verify the statistical significance of the correlation coefficient between the variables DNB and dNO<sub>2</sub>. The T-test determines if the correlation between two variables differs significantly from zero. In a T-test for correlation, the statistically significant difference from 0 indicates that both variables are interdependent. Based on the null hypothesis (H0) of the test, it is assumed that there is no difference from 0 ( $\rho = 0$ ), while the alternative hypothesis for that (H1) states that the correlation between the two variables is statistically different from 0 ( $\rho \neq 0$ ). The t-test value was calculated as follows (Kanji, 2006) (3):

$$t_{r_{xy}} = \frac{r_{xy}\sqrt{n-2}}{\sqrt{1-r_{xy}^2}} \quad (3)$$

with Student T distribution and  $n - 2$  degrees of freedom (df).  $r_{xy}$  is the correlation coefficient between DNB and dNO<sub>2</sub>,  $r_{xy}^2$  is the coefficient of determination, and  $n$  is the total number of even observations. H0 is maintained if the T-test result is  $t_{r_{xy}} \leq CV$  (critical value from the Student t Distribution Table, based on df). Otherwise, H0 is rejected by opting for H1 if the test's output is  $t_{r_{xy}} > CV$ . This analysis assumed  $\alpha = 0.05$  level of statistical significance. Concerning the p-value, H0 is maintained if  $p > 0.05$ , and H1 is true if  $p < 0.05$ .

## 4. RESULTS

Remote sensing results on DNB nighttime lights observed over a long period (2014-2019) revealed the main areas of high anthropogenic impact in Metropolitan France (Fig. 1). Generally, the highest radiance values correspond to densely populated cities and their conurbations. The DNB values, beyond indicating the presence of human settlements, reflected several socio-economic aspects of the territory such as unequal population density, emptying areas, monopoly of the capital-city in the hierarchy of settlements, more developed areas with greater economic potential, and terrain orography. The visualization of stable nighttime lights (2014-2019) provided a different perspective of the territory of Metropolitan France. Unlike daytime remote sensing, this type of satellite data provides a valuable picture of the spatial distribution of multiple sources of nighttime illumination. The nighttime light data revealed social-economic patterns relating to urban environments and anthropogenic activity. Mostly, in the case of France, these relate to electrification and transportation in the national territory. The Greater Paris metropolitan area in the Île-de-France region stood out above the rest of the country. Other spots corresponding to large cities and their conurbations (Lyon, Marseille, Nice, Toulouse, Nantes, Lille, Bordeaux) were also highlighted. Apart from the capital city, zones with high DNB radiance emission were identified along the Mediterranean coast, in the Saône-Rhône valley, in Alsace, and near the Belgian border at the north.

Results of the TROPOMI sensor's high spatial resolution data showed a significant overall decline in tropospheric NO<sub>2</sub> concentrations during the full-month total lockdown of April 2020 in Metropolitan France compared with the previous reference period (

**Fig. 2a, b).** Particularly, northern regions experienced a sharper and more general decrease than the other areas of France (i.e. Île-de-France, Hauts-de-France, Grand Est, Bourgogne-Franche-Comte,

Centre-Val de Loire, Pays de la Loire, Bretagne, Normandie). Auvergne-Rhône-Alpes region also experienced a salient reduction in air pollution.

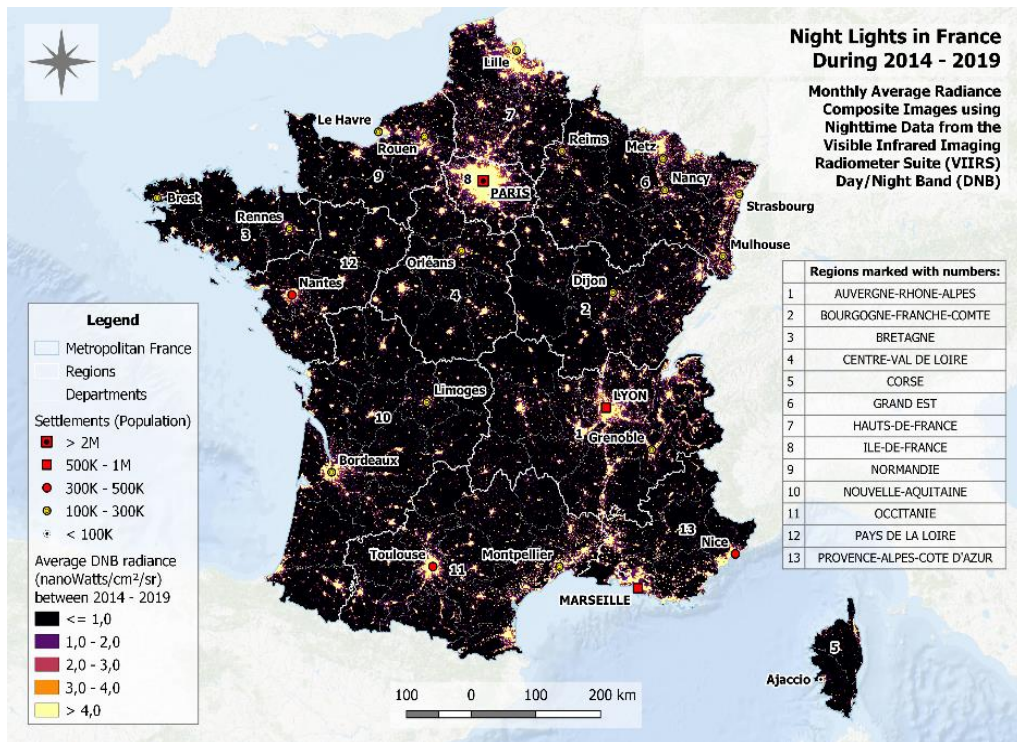


**Fig. 1.** Stable nighttime lights in France during 2014-2019.

The decrease in NO<sub>2</sub> levels was less pronounced in the southern, south-western regions, (i.e. Nouvelle-Aquitaine, Occitanie, Provence-Alpes-Côte d'Azur, Corse), but was still evident in some densely populated areas. Based on these results, it can be stated in general that the NO<sub>2</sub> decline phenomenon was more noticeable in all major cities of the country (

**Fig. 2a, b).**

Based on the relative changes detected in NO<sub>2</sub> concentrations (dNO<sub>2</sub> %) over the entire Metropolitan France, results showed that there were extensive areas experiencing decreases ranging from -25% to -50% (**Fig. 3**). It was determined that the greatest drop in air pollution occurred predominantly in the northern parts (in Île-de-France, Grand Est, and Centre-Val de Loire regions) where NO<sub>2</sub> was decreased by  $\leq -50\%$  in several areas, especially around the city of Paris and in the Alsace region. However, the central and southern areas of the country also experienced reductions ranging from -25% to -50% and even below -50%. This was especially perceptible around large cities (Marseille, Nice, Lyon, Limoges, Toulouse, Montpellier) and localities in mountainous valleys (the Pyrenees, Alps, Massif Central, Corsica).

Consequently, during total confinement, NO<sub>2</sub> pollution levels decreased significantly in northern France across a west-east line, as well as in the Saône, Rhône, and Isère valley regions across a north-south axis (**Fig. 3**). Besides, significant decreases occurred locally in the south-southwest zones too. Overall, on average, Île-de-France has experienced the most decline (-39.03%), followed by Grand Est (-33.69%) and Centre-Val de Loire (-31.71%) regions. By regional average, the smallest decrease in NO<sub>2</sub> was recorded in the case of Corsica Island (Corse), where a slight increase was detected compared with the reference period (4.07%). This was followed by Nouvelle-Aquitaine (-11.04%) and Provence-Alpes-Côte d'Azur (-12.02%) regions.

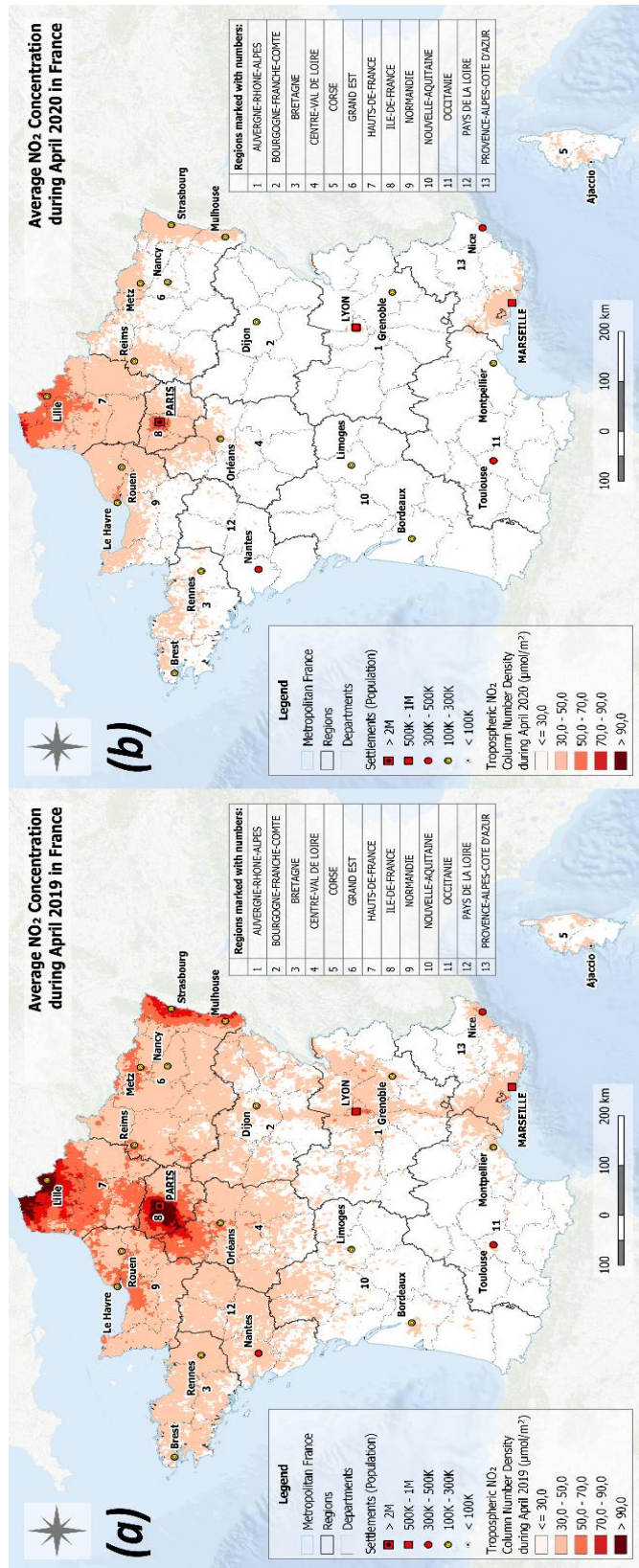
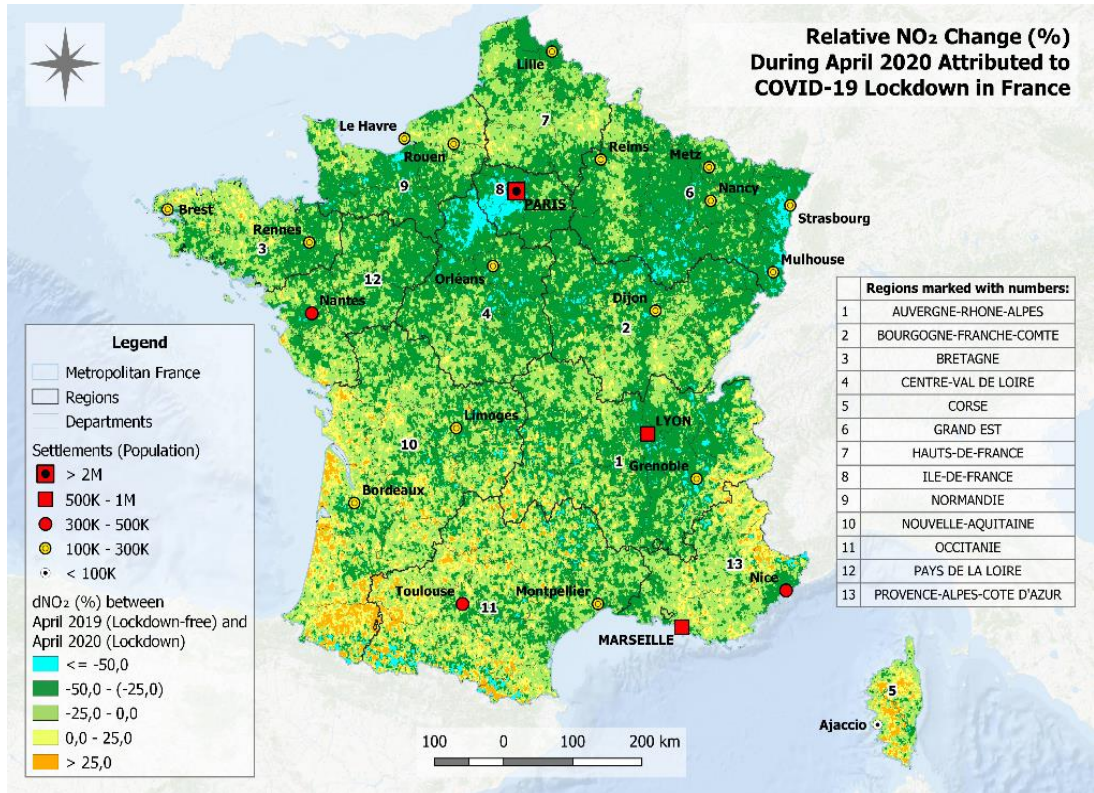


Fig. 2. Average NO<sub>2</sub> concentration during (a) April 2019 and (b) April 2020 in Metropolitan France





**Fig. 3.** Relative NO<sub>2</sub> change (dNO<sub>2</sub> %) during April 2020 attributed to COVID-19-induced total confinement in Metropolitan France.

The regression and correlation analysis with the T-test demonstrated that there was a statistically significant inverse relationship between the intensity of DNB night lights and decreases in NO<sub>2</sub> concentrations during total confinement in Metropolitan France (**Fig. 4**).

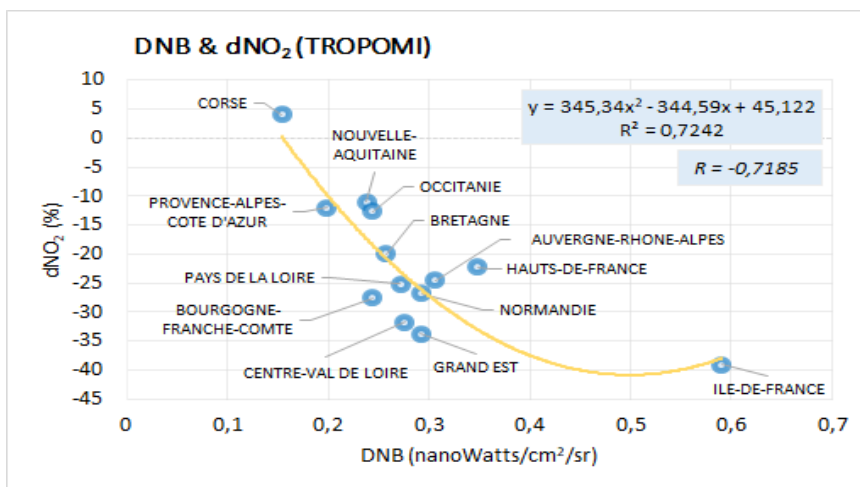


**Fig. 4.** Scatter diagram of the relationship between DNB and the relative change in NO<sub>2</sub> concentrations in the troposphere during April 2020 (COVID-19 lockdown) in French regions.

The correlation coefficient between DNB night lights and dNO<sub>2</sub> was  $R = -0.72$ . The coefficient of determination between the two variables using a quadratic function curve was  $R^2 = 0.72$ . Based on the T-test for correlation, it was found that:  $T(11) = -2.922 > CV = 2.201$ ,  $\alpha = 0.05$ ;  $p = 0.014$ . According to these findings tested with statistical methods, as the intensity of night lights was higher, the greater was the decrease in NO<sub>2</sub> pollution in France due to anti-COVID-19 measures. Tropospheric NO<sub>2</sub> time series data in 68 cities evidenced that two peaks of high NO<sub>2</sub> concentration occurred each year, one in autumn and the other during winter-spring. Lower NO<sub>2</sub> levels tended to occur during summer. The Savitzky-Golay filter indicated that during the total lockdown in 2020, the second peak was much smaller than in 2018, 2019, or 2021. Past observations indicated that after the first peak follows a second one. However, time-series data showed that during total lockdown the second peak was diminished (**Fig. 5**). This result indicated that during April 2020 the previous “normal” behavior of the NO<sub>2</sub> was modified due to the anti-COVID-19 measures.

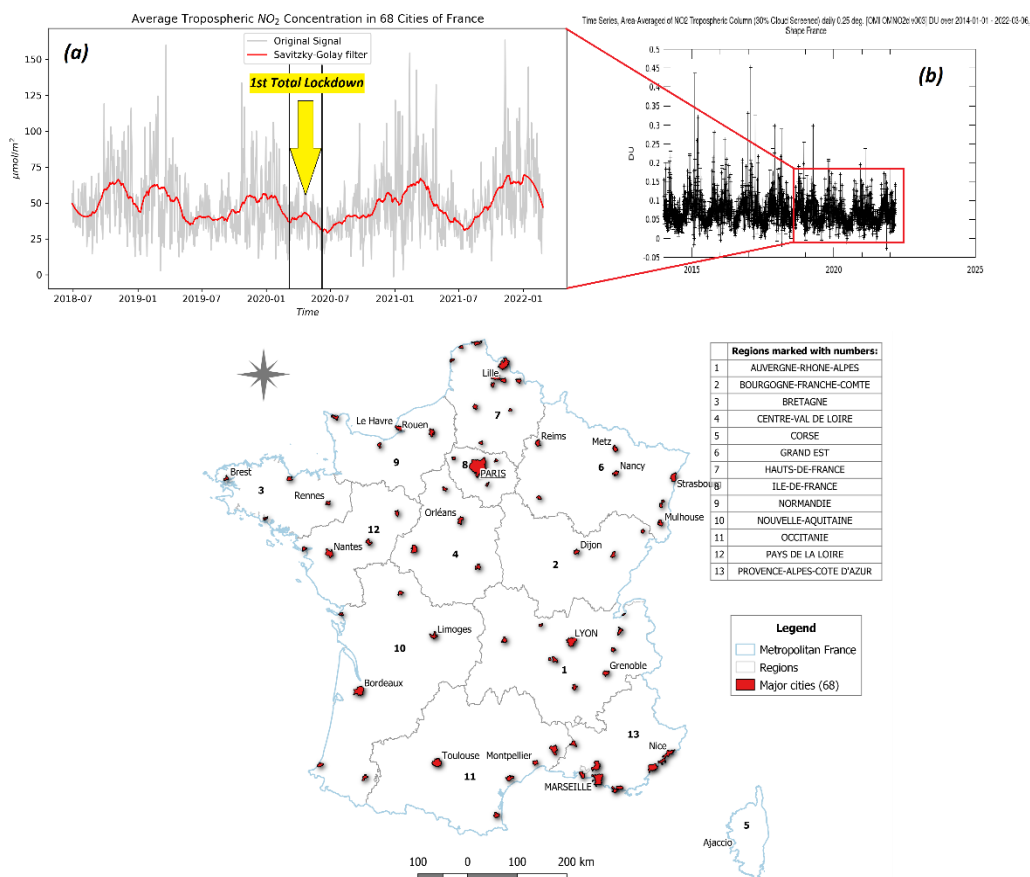


**Fig. 5.** Time series evolution of the tropospheric NO<sub>2</sub> concentration in 68 cities of Metropolitan France measured by (a) the TROPOMI and (b) OMI.

### 5. DISCUSSION

The results of this study indicate that there was a strong geospatial correlation between the past emission of nighttime lights and the relative change in near-surface NO<sub>2</sub> concentration. Using TROPOMI data, the analysis revealed that during total confinement there was a strong NO<sub>2</sub> air pollution reduction phenomenon over most of the territory of Metropolitan France. Taking a reference period prior to COVID-19 confinement, it was found that NO<sub>2</sub> levels dropped by -25% to -50% over



large areas of the country, and an even greater drop of -50% was recorded in the vicinity of Paris (Île-de-France), in areas of the Grand Est (Alsace) and the localities of the Pyrenees and Alps valleys. Generally, a reduction of -25% - (-50%) was detected in all major cities (**Fig. 3**). The study also found a statistically significant connection between DNB night lights (independent variable) and the degree of NO<sub>2</sub> decrease in the context of anti-COVID-19 measures (dependent variable).

In accordance with the research's hypothesis, the study showed that the higher the intensity of nighttime light emissions in a given territory, the greater the NO<sub>2</sub> decontamination of the air (**Fig. 4**). This clearly indicates the relationship between the impact of anthropogenic activities estimated by remote sensing observations and their effect on the change of atmospheric pollution (Levin & Zhang, 2017; Small & Elvidge, 2013). This suggests that nighttime lights are also an indicator of atmospheric pollution and the potential degree of decontamination, in addition to their consequences on ecosystems and the health of living beings (Gaston et al., 2013; Koo et al., 2016). The stable correlation between DNB night lights and dNO<sub>2</sub> showed that air pollution is also a social-environmental problem that can be studied with satellite sensor's nighttime lights imaging data (Zhao et al., 2018; Y. Zheng et al., 2019, Zhang et al., 2020, Li et al., 2018).

As an alternative to previous research, in terms of mobility control measures, this study provides new insight into the relationship between nighttime light emission before the COVID-19 crisis and air pollution reduction during COVID-19 also detected with remote sensing techniques (Chan et al., 2021; Ikhlassé et al., 2021; Tian et al., 2021). Observations on the magnitude of the NO<sub>2</sub> decrease due to COVID-19 control measures were in agreement with recent research on this phenomenon in different countries (Cameletti, 2020; Dutheil et al., 2020; Kumari & Toshniwal, 2020; Muhammad et al., 2020; Rugani & Caro, 2020; Zaib et al., 2021; Zambrano-Monserrate et al., 2020). Recent investigations addressed the phenomenon of nighttime light's dimming during confinements (Bustamante-Calabria et al., 2021; Christopher D. Elvidge et al., 2020; Ghosh et al., 2020; S. Zheng et al., 2021), however, these studies focused on specific urban areas where particularly there was an effect on nighttime illumination, therefore dimming was not a general and widespread phenomenon in many areas.

The methodological choices of the study were constrained by the current low temporal resolution of Sentinel-5P data accessible since mid-2018. The equivalent reference period for the confinement was therefore exclusively April 2019. Despite this condition of the data, the relative change in NO<sub>2</sub> concentrations could be determined between a period under confinement measures and another equivalent confinement-free period. To strengthen this limitation of the TROPOMI Sentinel-5P data, a time series analysis of the tropospheric NO<sub>2</sub> was performed based on satellite data (**Fig. 5**). In addition, it is beyond the scope of this study to address the relationship between the emission of nighttime lights and the change in the concentration of other types of pollutant gases due to containment actions. In this direction, future research is needed to analyze air quality (AQ) as a whole.

## 6. CONCLUSIONS

Since the effect of total and partial confinements have so far demonstrated the importance of human involvement in the change of air pollution, it becomes important to understand the contribution of anthropogenic processes to these dynamics. Analyzing a period of COVID-19 confinement, this study investigated the connection between the emission of nighttime lights and the relative change of near-surface NO<sub>2</sub> concentration. The investigation focused on Metropolitan France. The results of the analysis revealed a broad phenomenon of decreasing NO<sub>2</sub> concentrations in the country. In addition, the geospatial correlation analysis showed that the higher the observed DNB nighttime light emission, the higher the NO<sub>2</sub> reduction during the April 2020 confinement in the administrative-territorial units of France. This demonstrates that utilizing remote sensing techniques, DNB nighttime lights can explain the change in NO<sub>2</sub> air pollution over large territories.

In the context of other lockdowns or similar regulatory measures, future research on the remotely sensed nighttime lights and air pollution change should be aimed at improving our understanding of the behavior of other gases or particulate matter (PM).

## REFERENCES

- Beyer, R. C. M., Chhabra, E., Galdo, V., & Rama, M. (2018). Measuring Districts' Monthly Economic Activity from Outer Space. *Policy Research Working Paper*, 8523. <https://doi.org/10.1596/1813-9450-8523>
- Bustamante-Calabria, M., de Miguel, A. S., Martín-Ruiz, S., Ortiz, J. L., Vílchez, J. M., Pelegrina, A., García, A., Zamorano, J., Bennie, J., & Gaston, K. J. (2021). Effects of the covid-19 lockdown on urban light emissions: Ground and satellite comparison. *Remote Sensing*, 13(2), 1–22. <https://doi.org/10.3390/rs13020258>
- Cameletti, M. (2020). The Effect of Corona Virus Lockdown on Air Pollution: Evidence from the City of Brescia in Lombardia Region (Italy). *Atmospheric Environment*, 239, 117794. <https://doi.org/10.1016/j.atmosenv.2020.117794>
- Chan, K. L., Khorsandi, E., Liu, S., Baier, F., & Valks, P. (2021). Estimation of surface NO<sub>2</sub> concentrations over Germany from TROPOMI satellite observations using a machine learning method. *Remote Sensing*, 13(5), 1–24. <https://doi.org/10.3390/rs13050969>
- Dutheil, F., Baker, J. S., & Navel, V. (2020). COVID-19 as a factor influencing air pollution? In *Environmental Pollution* (Vol. 263). Elsevier Ltd. <https://doi.org/10.1016/j.envpol.2020.114466>
- Earth Engine Data Catalog. (n.d.-a). *Sentinel-5P NRTI NO<sub>2</sub>: Near Real-Time Nitrogen Dioxide*. Retrieved June 20, 2021, from [https://developers.google.com/earth-engine/datasets/catalog/COPERNICUS\\_S5P\\_NRTI\\_L3\\_NO2](https://developers.google.com/earth-engine/datasets/catalog/COPERNICUS_S5P_NRTI_L3_NO2)
- Earth Engine Data Catalog. (n.d.-b). *Sentinel-5P OFFL NO<sub>2</sub>: Offline Nitrogen Dioxide*. Retrieved June 20, 2021, from [https://developers.google.com/earth-engine/datasets/catalog/COPERNICUS\\_S5P\\_OFFL\\_L3\\_NO2](https://developers.google.com/earth-engine/datasets/catalog/COPERNICUS_S5P_OFFL_L3_NO2)
- Earth Engine Data Catalog. (n.d.-c). *VIIRS Nighttime Day/Night Band Composites Version 1*. Retrieved June 20, 2021, from [https://developers.google.com/earth-engine/datasets/catalog/NOAA\\_VIIRS\\_DNB\\_MONTHLY\\_V1\\_VCMCFG#description](https://developers.google.com/earth-engine/datasets/catalog/NOAA_VIIRS_DNB_MONTHLY_V1_VCMCFG#description)
- Elvidge, C. D., Hsu, F. C., Baugh, K. E., & Ghosh, T. (2016). Lighting tracks transition in Eastern Europe. In G. Gutman & V. Radeloff (Eds.), *Land-Cover and Land-Use Changes in Eastern Europe after the Collapse of the Soviet Union in 1991* (pp. 35–56). Springer International Publishing. [https://doi.org/10.1007/978-3-319-42638-9\\_3](https://doi.org/10.1007/978-3-319-42638-9_3)
- Elvidge, Christopher D., Baugh, K., Zhizhin, M., Hsu, F. C., & Ghosh, T. (2017). VIIRS night-time lights. *International Journal of Remote Sensing*, 38(21), 5860–5879. <https://doi.org/10.1080/01431161.2017.1342050>
- Elvidge, Christopher D., Ghosh, T., Hsu, F. C., Zhizhin, M., & Bazilian, M. (2020). The dimming of lights in China during the COVID-19 pandemic. *Remote Sensing*, 12(17), 2851. <https://doi.org/10.3390/RS12172851>
- Elvidge, Christopher D., Zhizhin, M., Ghosh, T., Hsu, F. C., & Taneja, J. (2021). Annual time series of global viirs nighttime lights derived from monthly averages: 2012 to 2019. *Remote Sensing*, 13(5), 1–14. <https://doi.org/10.3390/rs13050922>
- Gaston, K. J., Bennie, J., Davies, T. W., & Hopkins, J. (2013). The ecological impacts of nighttime light pollution: A mechanistic appraisal. *Biological Reviews*, 88(4), 912–927. <https://doi.org/10.1111/brv.12036>
- Ghosh, T., Elvidge, C. D., Baugh, K., Chi Hsu, F., & Zhizhin, M. (2017). Using VIIRS nighttime image in estimating gross state domestic product for India and its comparison with estimations from the DMSP-OLS radiance-calibrated image. *Proceedings of the 38th Asian Conference on Remote Sensing-Space Applications: Touching Human Lives, ACRS 2017*. <https://www.ngdc.noaa.gov/eog/>. Accessed on March 10, 2022.
- Ghosh, T., Elvidge, C. D., Hsu, F. C., Zhizhin, M., & Bazilian, M. (2020). The dimming of lights in India during the COVID-19 pandemic. *Remote Sensing*, 12(20), 1–17. <https://doi.org/10.3390/rs12203289>
- Gouvernement Français. (n.d.). *Tableau de bord COVID-19*. Retrieved July 27, 2021, from <https://www.gouvernement.fr/info-coronavirus/carte-et-donnees>
- Ikhlasse, H., Benjamin, D., Vincent, C., & Hicham, M. (2021). Environmental impacts of pre/during and post-lockdown periods on prominent air pollutants in France. *Environment, Development and Sustainability*, 1–22. <https://doi.org/10.1007/s10668-021-01241-2>

- Ivan, K., Holobâca, I. H., Benedek, J., & Török, I. (2020). VIIRS nighttime light data for income estimation at local level. *Remote Sensing*, 12(18), 2950. <https://doi.org/10.3390/RS12182950>
- Jackson, J. K., Weiss, M. A., Schwarzenberg, A. B., & Nelson, R. M. (2021). *Global Economic Effects of COVID-19*. <https://fas.org/sgp/crs/row/R46270.pdf>. Accessed on March 10, 2022.
- Kanji, G. K. (2006). t-test of a correlation coefficient. In *100 Statistical Tests* (3rd ed., p. 39). The Cromwell Press Ltd. [https://www.researchgate.net/profile/Paul-Louangrath/post/Ranking\\_or\\_scoring\\_variables\\_using\\_conditional\\_probability/attachment/59d63c45c49f478072ea7c1a/AS%3A273748962283533%401442278246675/download/100+Statistical+Tests.pdf](https://www.researchgate.net/profile/Paul-Louangrath/post/Ranking_or_scoring_variables_using_conditional_probability/attachment/59d63c45c49f478072ea7c1a/AS%3A273748962283533%401442278246675/download/100+Statistical+Tests.pdf). Accessed on March 10, 2022.
- Koo, Y. S., Song, J. Y., Joo, E. Y., Lee, H. J., Lee, E., Lee, S. K., & Jung, K. Y. (2016). Outdoor artificial light at night, obesity, and sleep health: Cross-sectional analysis in the KoGES study. *Chronobiology International*, 33(3), 301–314. <https://doi.org/10.3109/07420528.2016.1143480>
- Kovács, K. D. (2021). *Obtaining VIIRS DNB Data - Earth Engine Code Editor*. Google Earth Engine Code Editor. <https://code.earthengine.google.com/2467b33932381bcc99de28373a5df76a?noload=true>. Accessed on March 10, 2022.
- Krotkov, N. A., Lamsal, L. N., Marchenko, S. V., Celarier, E. A., Bucsela, E. J., Swartz, W. H., Joiner, J., & Team, and the O. core. (2019). *OMI/Aura NO2 Cloud-Screened Total and Tropospheric Column L3 Global Gridded 0.25 degree x 0.25 degree V3*. NASA Goddard Space Flight Center, Goddard Earth Sciences Data and Information Services Center (GES DISC). <https://doi.org/10.5067/Aura/OMI/DATA3007>. Accessed on March 10, 2022.
- Kumari, P., & Toshniwal, D. (2020). Impact of lockdown on air quality over major cities across the globe during COVID-19 pandemic. *Urban Climate*, 34, 100719. <https://doi.org/10.1016/j.uclim.2020.100719>
- Levin, N., & Zhang, Q. (2017). A global analysis of factors controlling VIIRS nighttime light levels from densely populated areas. *Remote Sensing of Environment*, 190, 366–382. <https://doi.org/10.1016/j.rse.2017.01.006>
- Li, X., Liu, S., Jendryke, M., Li, D., & Wu, C. (2018). Night-time light dynamics during the Iraqi Civil War. *Remote Sensing*, 10(6), 858. <https://doi.org/10.3390/rs10060858>
- Miller, S. D., Straka, W., Mills, S. P., Elvidge, C. D., Lee, T. F., Solbrig, J., Walther, A., Heidinger, A. K., & Weiss, S. C. (2013). Illuminating the capabilities of the Suomi National Polar-orbiting Partnership (NPP) Visible Infrared Imaging Radiometer Suite (VIIRS) Day/Night Band. *Remote Sensing*, 5(12), 6717–6766. <https://doi.org/10.3390/rs5126717>
- Muhammad, S., Long, X., & Salman, M. (2020). COVID-19 pandemic and environmental pollution: A blessing in disguise? *Science of the Total Environment*, 728. <https://doi.org/10.1016/j.scitotenv.2020.138820>
- Prakash, A., Shukla, A. K., & Bhowmick, C. (2019). Night-time Luminosity: Does it Brighten Understanding of Economic Activity in India? *Reserve Bank of India Occasional Papers*, 40. [https://www.researchgate.net/publication/334811462\\_Night-time\\_Luminosity\\_Does\\_it\\_Brighten\\_Understanding\\_of\\_Economic\\_Activity\\_in\\_India](https://www.researchgate.net/publication/334811462_Night-time_Luminosity_Does_it_Brighten_Understanding_of_Economic_Activity_in_India)
- Román, M. O., Stokes, E. C., Shrestha, R., Wang, Z., Schultz, L., Sepúlveda Carlo, E. A., Sun, Q., Bell, J., Molthan, A., Kalb, V., Ji, C., Seto, K. C., McClain, S. N., & Enenkel, M. (2019). Satellite-based assessment of electricity restoration efforts in Puerto Rico after Hurricane Maria. *PLoS ONE*, 14(6), e0218883. <https://doi.org/10.1371/journal.pone.0218883>
- Rugani, B., & Caro, D. (2020). Impact of COVID-19 outbreak measures of lockdown on the Italian Carbon Footprint. *Science of the Total Environment*, 737, 139806. <https://doi.org/10.1016/j.scitotenv.2020.139806>
- Savitzky, A., & Golay, M. J. E. (1964). Smoothing and Differentiation of Data by Simplified Least Squares Procedures. *Analytical Chemistry*, 36(8), 1627–1639. <https://doi.org/10.1021/AC60214A047>
- Small, C., & Elvidge, C. D. (2013). Night on Earth: Mapping decadal changes of anthropogenic night light in Asia. *International Journal of Applied Earth Observation and Geoinformation*, 22(1), 40–52. <https://doi.org/10.1016/j.jag.2012.02.009>
- Tian, X., An, C., Chen, Z., & Tian, Z. (2021). Assessing the impact of COVID-19 pandemic on urban transportation and air quality in Canada. *Science of the Total Environment*, 765, 144270. <https://doi.org/10.1016/j.scitotenv.2020.144270>

- Verhoelst, T., Compernelle, S., Pinardi, G., Lambert, J. C., Eskes, H. J., Eichmann, K. U., Fjæraa, A. M., Granville, J., Niemeijer, S., Cede, A., Tiefengraber, M., Hendrick, F., Pazmiño, A., Bais, A., Bazureau, A., Folkert Boersma, K., Bogner, K., Dehn, A., Donner, S., ... Zehner, C. (2021). Ground-based validation of the Copernicus Sentinel-5P TROPOMI NO<sub>2</sub> measurements with the NDACC ZSL-DOAS, MAX-DOAS and Pandonia global networks. *Atmospheric Measurement Techniques*, *14*(1), 481–510. <https://doi.org/10.5194/amt-14-481-2021>
- WHO. (2020a). *Updated WHO advice for international traffic in relation to the outbreak of the novel coronavirus 2019-nCoV*. <https://www.who.int/news-room/articles-detail/updated-who-advice-for-international-traffic-in-relation-to-the-outbreak-of-the-novel-coronavirus-2019-ncov>. Accessed on July 27, 2021.
- WHO. (2020b). *Updated WHO recommendations for international traffic in relation to COVID-19 outbreak*. <https://www.who.int/news-room/articles-detail/updated-who-recommendations-for-international-traffic-in-relation-to-covid-19-outbreak>. Accessed on July 27, 2021.
- Zaib, S., Lu, J., Shahid, M. Z., Ahmar, S., & Shahid, I. (2021). Impact of SARS-CoV-2 on Ambient Air Quality in Northwest China (NWC). *Atmosphere*, *12*(4), 518. <https://doi.org/10.3390/atmos12040518>
- Zambrano-Monserrate, M. A., Ruano, M. A., & Sanchez-Alcalde, L. (2020). Indirect effects of COVID-19 on the environment. *Science of the Total Environment*, *728*, 138813. <https://doi.org/10.1016/j.scitotenv.2020.138813>
- Zhang, L., Li, X., & Chen, F. (2020). Spatiotemporal Analysis of Venezuela's Nighttime Light during the Socioeconomic Crisis. *IEEE Journal of Selected Topics in Applied Earth Observations and Remote Sensing*, *13*, 2396–2408. <https://doi.org/10.1109/JSTARS.2020.2995695>
- Zhao, X., Yu, B., Liu, Y., Yao, S., Lian, T., Chen, L., Yang, C., Chen, Z., & Wu, J. (2018). NPP-VIIRS DNB daily data in natural disaster assessment: Evidence from selected case studies. *Remote Sensing*, *10*(10), 1526. <https://doi.org/10.3390/rs10101526>
- Zheng, S., Fu, Y., Sun, Y., Zhang, C., Wang, Y., & Lichtfouse, E. (2021). High resolution mapping of nighttime light and air pollutants during the COVID-19 lockdown in Wuhan. *Environmental Chemistry Letters*, *1*, 1. <https://doi.org/10.1007/s10311-021-01222-x>
- Zheng, Y., Shao, G., Tang, L., He, Y., Wang, X., Wang, Y., & Wang, H. (2019). Rapid assessment of a typhoon disaster based on NPP-VIIRS DNB daily data: The case of an urban agglomeration along western Taiwan Straits, China. *Remote Sensing*, *11*(14), 1709. <https://doi.org/10.3390/rs11141709>

## APPLICATION OF 3S TECHNOLOGY IN DISASTER RISK RESEARCH IN THE NORTHERN MOUNTAINOUS REGION OF VIETNAM

Dieu Trinh NGUYEN<sup>1</sup> , Quoc Lap KIEU<sup>2\*</sup> 

DOI: 10.21163/GT\_2022.171.09

### ABSTRACT:

The article presents an overview of 3S technology application studies and prospects for 3S technology application in disaster risk management in the northern mountainous region of Vietnam. The study uses the document review method and builds an experimental research model by GIS spatial analysis method, data mining method from satellite images, combined with positioning equipment. 3S technology shows great promise in disaster management, assessment and warning in mountainous areas, especially the online warning model based on artificial intelligence and smart applications on mobile phones. This is a research direction with high practicality, accuracy and applicability. Experimental research model applying 3S technology to build landslide risk map in Lai Chau province has identified 753.62 km<sup>2</sup> (accounting for 8.31%) with very high landslide risk and 1633.29 km<sup>2</sup> (accounting for 18.01%) have a high risk of landslides. In areas with high and very high risk of landslides, the study tested the installation of online landslide warning devices, which help prevent and mitigate damage caused by landslides.

**Key-words:** 3S technology, disaster risk, landslides, mountainous region, Vietnam

### 1. INTRODUCTION

The mountainous area in the North of Vietnam has diverse natural conditions, high mountainous terrain, complex climate, and rich mineral resources. However, this is an area where natural disasters often occur, causing great damage to people and properties. According to statistics in 20 years (2001-2021) in the northern mountainous provinces of Vietnam, there have been 318 flash floods, 3537 landslides, 128 hail storms, 604 storms, making 1486 people dead, 3512 injured, 17129 houses destroyed, property and crop damage estimated at over \$4.3 billion (Statistical Office of Vietnam, 2022). The northern mountainous region of Vietnam is home to mainly ethnic minorities, with very limited skills in responding to natural disasters. Local authorities have not yet taken practical measures to forecast and warn of natural disaster risks. Natural disaster risks often occur quickly, with great consequences, and are often concentrated in remote, isolated and ethnic minority areas. Research and application of new technologies for disaster risk management in mountainous areas of Vietnam are still limited.

3S technology is a geospatial technology, combining 3 components: Remote Sensing (RS), Geographic Information System (GIS) and Global Positioning System (GPS). RS technology provides satellite image data to analyze the factors of climate, topography, geomorphology, soil, flow, vegetation these are the factors that form disaster risk. GIS supports spatial analysis, the establishment of warning maps, and disaster risk forecasting. GPS allows locating sensor devices, serving online forecasting and warning on mobile devices. Nowadays, the application of 3S technology in disaster risk management research is very popular. 3S technology is often applied in spatial analysis, establishment of disaster risk zoning maps, analysis of factors that arise and types of disaster risk, management and prediction of disaster risks (Albano et al., 2018).

---

<sup>1</sup>Graduate University of Science and Technology, Vietnam Academy of Science and Technology, Hanoi 100000, Vietnam, [nguyendieutrinh70@gmail.com](mailto:nguyendieutrinh70@gmail.com)

<sup>2,\*</sup>Thai Nguyen University of Sciences, Thai Nguyen 250000, Vietnam, [lapkq@tnus.edu.vn](mailto:lapkq@tnus.edu.vn)

Current trending disaster risk susceptibility assessment focuses on the use of machine learning, spatial statistics, and multi-criteria decision-making algorithms. The directions for studying the susceptibility to disaster risks are provided by machine learning models such as logistic regression laws (Ali et al., 2020), decision trees (Khosravi et al., 2019; Zhao et al., 2019), artificial neural networks (Chapi et al., 2017; Choubin et al., 2017; Costache et al., 2019; Bui, 2020), support vectors (Tehrany et al., 2014), neural fuzzy inference systems (Wang et al., 2019). Bilateral statistical models, including studies involving: frequency ratio (Shafapour et al., 2019), weight of evidence (Rahmati et al., 2016), statistical index, the coefficient of certainty (Costache et al., 2019) and the entropy index (Azareh et al., 2019). For multi-criteria decision making, commonly used analytical hierarchical techniques (Souissi et al., 2019), multi-criteria optimization (Dano et al., 2019) and sorting techniques are commonly used. order of preference according to the similarity to the ideal solution (Kim et al., 2020). Method of applying K-Star model to determine and calculate disaster risk potential index (Der et al., 2019; Uddin et al., 2021).

The application of 3S technology brings many advantages in spatial analysis, creating disaster risk warning partition maps (Cao, 2016; Albano, 2018; Der Sarkissian et al., 2019; Popa, 2019; Yi, 2021). Studies regarding based on remote sensing and GIS mainly use the FFPI model to create disaster risk warning maps (Gregory, 2010; Ballesteros et al., 2017; Costache et al., 2019). Studies used the data of slopes, soil types, soil utilization types and vegetation cover to build a potential map, which provided excellent support for disaster risk forecasting activities (Bajabaa, 2014; Roxana, 2018). Proposed the physically based, space-time distributed hydrological model and the geomorphological instantaneous unit hydrograph has been derived from the geomorphological characteristics of a catchment and used in simulation of the surface runoff hydrographs for ten rainfall events in the Ajay Catchment in eastern India (Estupina-Borrell et al., 2006; Kumar et al., 2007). Growing knowledge of disaster risk mechanisms shows that the morphometric variables of a catchment control its hydrological response (Moussa, 2003). Based on this understanding, the geomorphological unit hydrograph has become one of the most popular methods for estimating hydrological processes when data are inadequate (Du et al., 2009; Diakakis, 2011).

Research into the application of opensource software, webGIS, and artificial intelligence in disaster risk management is also becoming more and more popular. The case studies were promoting spatial thinking through local disaster risk management planning (Berse et al., 2011, Kieu, 2021), application of WebGIS technology in disaster risk management support (Kawasaki et al., 2012), disaster risk reduction in agriculture through Big data processing (Reznik et al., 2017), potential disaster risk zonation and flood shelter suitability mapping for disaster risk mitigation using artificial intelligence (Uddin et al., 2021).

In recent years 3S technology has been applied in disaster risk management research in Vietnam. However, the research is in the initial application form, the database and research methods are still limited. This study will present an overview of the application of 3S technology in Vietnam and new prospects for the application of 3S technology in disaster risk management in the northern mountainous region of Vietnam. Experimental study to establish landslide map and landslide warning model in Lai Chau province as an illustrative example. This is the first study on the application of 3S technology in landslide warning in Lai Chau province, especially the online warning model. The research results have shown the prospect of applying 3S technology in research and management of different types of disaster risks in Vietnam.

## **2. STUDY AREA**

The northern mountainous region of Vietnam has a total area of 100,965 km<sup>2</sup>, with a population of about 14.62 million, which are mainly ethnic minorities (Statistical Office of Vietnam, 2022). Administratively, this region includes 15 provinces (Ha Giang, Cao Bang, Lao Cai, Bac Kan, Lang Son, Tuyen Quang, Yen Bai, Thai Nguyen, Phu Tho, Bac Giang, Lai Chau, Dien Bien, Son La, Hoa Binh and Quang Ninh). This is an area with diverse and complex natural conditions, into two sub-regions Northwest and Northeast. The Northwest is an area consisting mainly of medium and high mountains. This is the place with the highest, divided and most dangerous terrain in Vietnam.

The average slope is 23.7 degrees, many areas have slopes above 30 degrees. The common terrain types here are high mountains, deep valleys or canyons, limestone plateaus with an average altitude of 800-1000m. The highest and most massive mountain range is Hoang Lien Son range with many peaks over 2500m, the highest peak is Fansipan 3143m high. The Northeast mountainous region consists mainly of medium and low mountains. The massif upstream of Chay river has many peaks above and below 2000m, which is the highest area of the region. From this massif to the sea are bow-shaped mountain ranges that gradually lower towards the East Sea.

The river and stream system in the northern mountainous region of Vietnam is quite dense, with an average density of about 1.45km/km<sup>2</sup>, with the Red river, Da river and Chay river being the main hydrological systems. The tropical monsoon climate of the high mountains has cold winters, the average annual temperature ranges from 18-25°C, the average annual rainfall is 1800 mm (Vietnam's Ministry of Natural Resources and Environment, 2020). Due to the high mountainous terrain and distinct seasonality, the climate is clearly differentiated, with many areas having extreme climates, with extreme cold in winter and heavy rainfall in summer. Forest coverage in the area reaches 46.28%, unevenly distributed, mainly planted forest area. The area of natural forests and protection forests accounts for only 5.1% of the natural area. Meanwhile, the area of bare land and bare hills tends to increase. Data from satellite image analysis in December 2020 shows that bare land and bare hills account for 23.7% of the area's natural area (Kieu, 2021). Soil in the mountainous area is quite rich, with nearly 30 main soil groups, of which the most are red-yellow ferralit soils, black soils, red humus soils, alite humus in the mountains, coarse humus in the mountains, and soil. Yellow-red soil is changed by rice cultivation, strongly eroded soil inert with gravel, alluvial soil, and sloping soil (Vietnam's Ministry of Natural Resources and Environment, 2020).

The northern mountainous region of Vietnam is an area that frequently experiences natural disaster risks and suffers heavy losses due to major types of natural disasters such as flash floods, landslides, cold weather, hoarfrost, drought, storm, ice, snow, etc. The provinces most affected are Lai Chau province, Yen Bai province, Lao Cai province and Son La province. This is the main distribution area of ethnic minorities, and disaster risk prevention skills are still limited. Agricultural farming activities are backward, mainly cultivating crops (maize, cassava, upland rice, medicinal plants,...) in the uplands, growing wet rice in the valleys, farming by terraced fields, and exploiting forest products. Economic activities depend on nature, which makes the risk of natural disasters and damage from disaster risks tend to increase (Vietnam's Disaster Prevention and Control Office, 2021).

### **3. DATA AND METHODS**

#### **3.1. Study data**

To analyze the prospects of 3S technology application in disaster risk management and forecasting, the study has reviewed many different data sources. The author has reviewed more than 300 studies related to the application of geospatial technology in disaster risk management, including 50 basic studies on 3S technology application in analysis, assessment and management natural disaster risks in mountainous areas. In Vietnam, all relevant studies are collected, including reporting data, statistics on the current state of disaster risk in mountainous areas in the last 20 years, research data on types of natural disaster risks; and especially studies with application of satellite images, GIS and GPS in disaster risk management are collected and analyzed.

In an empirical research model, an applied case study of landslides in Lai Chau province, the study used survey data, statistical data, data observations, satellite images, paper maps and data from landslide-related studies in Lai Chau province. Topographic data is inherited, extracted from the topographic map of Lai Chau province, scale 1:200,000. Slope data, terrain segmentations are built on digital elevation model (DEM) and satellite image data. The petrographic map is built according to the principle of morphological origin, combining data from geological maps.



Soil type data was surveyed by the author and inherited from the analysis results of 100 soil profiles, representing 18 soil types covering the entire study area. Data on land use status based on Sentinel-2B satellite image, Landsat 8 ETM image (Earthexplorer.usgs.gov, 2022) and field inspection data. Rainfall data are collected from the rainfall database of the National Institute of Meteorology, Hydrology and Climate Change over a period of over 60 years (1960-2021), combining rainfall monitoring data of 35 IMETOS monitoring stations located in the study area. The data on the current state of landslides (location, extent, extent of influence, time) for 20 years (2001-2021) are used from statistical documents, combined with survey and interview methods. people in the study area.

### 3.2. Study methods

Review of related studies to analyze the prospects of 3S technology in disaster risk management in the northern mountainous region of Vietnam. The main method is to collect, analyze and synthesize documents; The study evaluates the overview based on the analysis of previous research results. Using the method of collecting and processing statistical data, using remote sensing image data to collect data related to natural features, current state of landslides, factors affecting landslides in the experimental area. The field survey method conducts a survey of sample study sites to verify statistical data and verify analysis results. At the same time, through the survey process, to locate and identify the locations of natural disasters in the study area.

In the experimental research model, the hierarchical analysis method is applied, combined with the spatial analysis method in GIS to build a landslide hazard map. The method of hierarchical analysis (Saaty, 1987) is applied to calculate the consistency index, determine the randomness index, the weight of each factor causing landslides in the experimental area. Employing Multi-Criteria Analysis technique (Triantaphyllou, 2000), this study focused on the determination of factors that formed landslides in the research area and simultaneously combined the goal with statistical data for comparisons, ultimately leading to the hierarchy of the capability to cause landslides of information layers. With the application of GIS in determining weights, the spatial integration of factors and weights in order to build a map of landslides potentials in the study area.

The sensitivity level reflecting landslide risk is calculated according to the formula (1):

$$LSI = \sum_{j=1}^n W_j . X_{ij} \quad (1)$$

where: *LSI* is landslide susceptibility index

*W<sub>j</sub>* is the weight of factor (*j*)

*X<sub>ij</sub>* is landslide factor (*j*) in layer (*i*)

*n* is the number of factors causing landslides.

In the experimental model, 6 factors that cause landslides including slope, daily rainfall, soil type, current land use status, geological background and topographic dissection.

GIS enables spatial analysis, management, integration and superposition of information layers. Three algorithms used in GIS spatial analysis include spatial superposition algorithm (Fischer, 2019), attribute classification algorithm (Jia, 2017; Shirowzhan et al., 2019) and algorithmic spatial interpolation (Comber, 2019). The hierarchical analysis model will support GIS, synthesize information, assign the most appropriate weights to the selected elements. After the factors have been hierarchical and weighted, integrating them will give us the landslide susceptibility index. Using the overlay tool in QGIS for the edited maps, new maps are formed and weighted to create a landslide susceptibility index map. After being divided according to appropriate influence levels, a landslide hazard map will be formed in the study area.

## 4. RESULTS AND DISCUSSIONS

### 4.1. Research overview on 3S technology application in disaster risk management in the northern mountainous region of Vietnam

3S technology with outstanding advantages compared to traditional methods in disaster risk management research, especially in establishing zoning maps, assessing and warning levels of disaster risk. The use of 3S technology with comparison with statistics brings positive, quantitative and highly accurate results. This result contributes to support for managers in the prevention and mitigation of impacts caused by disaster risks. Therefore, right from the 1990s, 3S technology (mainly Remote Sensing and GIS) has been applied in studies on disaster risk management in mountainous areas of Vietnam. Initial studies mainly used remote sensing images to collect background data (topography, slopes, vegetation, rivers) for the study of disaster risk factors (La, 2009). GIS technology supports the establishment of zoning maps and disaster warnings. GPS technology supports field investigations and data collection (Tran, 2020).

The beginning of the twenty-first century is the period of strong development of geoinformatics technology, the application of 3S technology in researches and projects related to disaster risk management in mountainous areas. variable. Applied studies do not stop at analyzing and describing the current status from spatial data. The combination of tools in the 3S component has allowed users to integrate the functions of data collection, spatial analysis, zoning, assessment and precise location of disasters. The Vietnamese government has paid attention and invested in projects and research topics at all levels on the investigation and monitoring of disaster risks using 3S technology. For example, research and application of 3S technology to warn of natural disasters, including landslides in Hoa Binh province (Nguyen, 2003); research on establishing landslide susceptibility maps in Northwestern border provinces using remote sensing and GIS technology (Nguyen et al., 2008).

During the period 2011-2015, the Asian Development Bank supported Vietnam to implement the project "Application of remote sensing technology in flood forecasting, warning and monitoring". The project has applied 3S technology in flood management, monitoring and forecasting in river basins, applied in Phu Tho province. The monitoring system is established through remote sensing activities, the information is transmitted to and sent to the local command board for flood and storm control via text message (SMS). On the basis of the information received, the local government has a plan to relocate people, to reduce the impact of natural disasters. In 2016, the project "Investigation, assessment and zoning for landslide hazard warning in mountainous areas of Vietnam" in 10 northern mountainous provinces using 3S technology. The total investigation area of nearly 60,000 km<sup>2</sup> has identified nearly 9,000 landslide points of different sizes and levels of danger; nearly 3,000 questionable slip points were discovered from analyzing the terrain on digital stereoscopic models and interpreting aircraft images. The main product of the project is the current map of landslides and rocks at the scale of 1:50,000; Spatial and Web-GIS database structure of landslides (Vietnam's Ministry of Natural Resources and Environment, 2018).

In addition to the projects, there have been many studies and applications of 3S technology in monitoring, monitoring, prevention and mitigation of natural disasters. For example, research and application of 3S technology to warn of landslides in Son La province (Nguyen, 2003); research to establish disaster risk maps for northern mountainous provinces by remote sensing technology (Du, 2009); research and application of geoinformatics technology to warn of landslides in Hoa Binh and Son La hydropower reservoirs (Nguyen, 2015); application of radar remote sensing images (Sentinel, Alos PALSAR) established flood map for downstream Tra Khuc river basin (Nguyen et al., 2017); applying geoinformatics technology to build an early warning system for flash floods in mountainous areas, testing it in Thuan Chau district, Son La province (Lai, 2018); application of 3S in constructing a flash flood warning model in northern mountainous regions of Vietnam: a case study at Trinh Tuong commune, Bat Xat district, Lao Cai province (Kieu and Tran, 2021), and flash flood hazard mapping using satellite images and GIS integration method: a case study of Lai Chau province, Vietnam (Kieu, 2021).

In recent years, 3S technology has been widely applied, as an indispensable method in management, monitoring, warning and assessment of damage caused by natural disasters in Vietnam. Some key projects are currently working towards application, for example the project of applying remote sensing technology and GIS to assess some elements of environmental resources for warning, prevention and mitigation of natural disasters, piloted in Quang Ninh province (Vietnam's Ministry of Natural Resources and Environment, 2020); Research on building a warning model and zoning flash flood risk on the basis of integrating artificial intelligence, data and geoinformatics technology, experimentally applied to Lao Cai province (Vietnam's Ministry of Science and Technology, 2020); Application of remote sensing, GIS, GPS technology in surveying and mapping for flash floods and landslides in the Northwest region of Vietnam (National Science and Technology Fund, 2021).

The literature review shows that the research and application of 3S technology in disaster risk management in mountainous areas of Vietnam is quite developed. However, researches still have some limitations: The first limitation is most of the studies are stopping at using 3S technology as a research tool, in which remote sensing provides data, GIS for spatial analysis, GPS for positioning; The ability to combine to build synthetic models is limited. The second limitation is lack of applications capable of online connectivity, dynamic data mining, opensource software applications, webGIS, big data and artificial intelligence. This is a huge limitation, because disaster risks often occur very quickly, requiring online data in disaster monitoring alerts. The third limitation is Vietnam does not have uniform standards on disaster risk data. The data has not been synchronized, making it difficult to use and inherit research data. Another difficulty is the cost of applying 3S technology in research is often very large, especially the cost of data collection. In the economic conditions of Vietnam, especially the mountainous provinces will face many difficulties when building research projects with high technology applications.

#### **4.2. Prospects of 3S technology application in disaster risk management in the northern mountainous region of Vietnam**

Natural disaster risks in the northern mountainous region of Vietnam tend to increase due to human impacts and the effects of climate change. Applying 3S technology can build disaster risk prediction and warning models. The analytical data from the 3S model is a decision support tool for disaster risk management and monitoring. With the strong development of science and technology, especially geospatial technology, the prospect of 3S technology application in disaster risk management in the northern mountainous region of Vietnam is reflected in the following fields:

(1) *The prospect for disaster risk database construction:* Database in disaster risk management is very important. Currently, with the strong development of remote sensing technology, the data is very diverse, the resolution and accuracy are getting higher and higher. Spatial positioning data from GPS devices are increasingly complete, with high coverage and precise spatial positioning capabilities. Besides, with the explosion of opensource GIS software, allowing users to access, collect and process data from many different sources (Reznik et al., 2017). This is a great prospect in building a 3S database system for forecasting, warning, zoning and disaster risk management in the northern mountainous region of Vietnam.

(2) *The prospect for disaster risk spatial analysis:* Disaster risk management, the first goal must be to manage the disaster risk space. In which, it is necessary to partition, decentralize, identify locations, locations and spaces that are frequent or likely to occur. Today's GIS software has very good spatial analysis capabilities. Input data ensures accuracy, specialized software is capable of analyzing data, accurately determining the space of disaster. The northern mountainous region of Vietnam often occurs types of natural disaster risks such as flash floods, pipe floods, and landslides. These are types of natural disasters caused by natural factors such as topography, slope, soil thickness, vegetation cover characteristics, rainfall, combined with human factors such as farming methods, measures to plant and protect forests, to build civil works.

Currently, GIS software (ArcView, ArcGIS, QGIS, SuperMap, ...) is capable of analyzing the superposition of agent elements, partitioning, assessing the extent and spatial forecasting of the probability of disaster risk.

(4) *The prospect for disaster risk forecasting:* Disaster risk forecasting depends on forecasting the factors that occur that type of disaster. In mountainous areas, except for fixed factors (geology, topography), most types of disaster risks can be predicted in advance on the basis of sudden factors such as rainfall, decline vegetation cover, displacement of rock masses, the appearance of underground runoff. Currently, data from satellite images, aircraft images and navigation devices allow for relatively accurate forecasting and calculation of fluctuating factors causing various types of disasters. Typically, flash floods in the northern mountainous areas of Vietnam are mainly caused by heavy rains, combined with topographic factors on steep areas, and loss of vegetation (Lai et al., 2018). Based on satellite images, it is possible to forecast rainfall and calculate the possibility of flash floods in a certain area.

(5) *The prospect for online disaster risk warning:* Currently, with the support of devices capable of providing online data, connecting to online software on mobile devices allows setting up online disaster warning systems. The cost for the online disaster risk warning system is not too large, it is completely possible to set up the system at high-risk points. This is a great prospect of 3S technology applied in disaster risk warning in the northern mountainous region of Vietnam.

#### **4.3. Experimental research model: A case study of landslide zoning and warning in Lai Chau province of Vietnam**

To clearly see the prospect of 3S technology application in disaster risk management in the northern mountainous region of Vietnam, the report presents simulation results of 3S technology application model in landslide zoning and warning in Lai Chau province as an illustrative example.

Lai Chau is a typical mountainous province of Vietnam, has 9068.78 square kilometers, 8 administrative units including Lai Chau city and 8 districts of Muong Te, Sin Ho, Nam Nhun, Tam Duong, Phong Tho, Tan Uyen, and Than Uyen. The province has more than 400 thousand of people of 20 ethnic groups living together, in which Thai ethnic people cover the majority of population in Lai Chau with 131.822 people, accounting for 34% of the total population. The other ethnic groups consist of Mong people 86.467 people (22.30%), Kinh ethnic group 54.027 people (13.94%), Dao ethnic people 51.995 people (13.41%), Ha Nhi ethnic people 14.658 people (3.78%) and other ethnic minorities. Local people mainly plant corn, cassava, upland rice, herbs, and etc on hills and wetland rice in valleys, while they also do exploitations in forests (Statistical Office of Lai Chau Province, 2022). These forms of agricultural cultivation are completely free and much dependent on natural conditions, leading to an incline in terms of landslide potential and subsequently increasing damage. According to statistical data, in the term from 2001 - 2021, the locality has 219 landslide points. Through investigations and surveys, landslide forming factors in the research location are relatively typical with the characteristics of basins, partitioned terrains, high slopes, and flows that tend to aggregate. Moreover, in recent times the forest vegetation cover of Lai Chau tends to decrease; combined with the unsustainable form of agricultural cultivation of the people, the impact of climate change, erratic heavy rain, ... increases the intensity and impact of landslide.

From actual data, combined with research results on landslides of related studies in mountainous areas of Vietnam (Nguyen et al., 2008; La, 2009; Nguyen, 2015), the empirical research model has identified 6 factors forming landslide in Lai Chau province, including slope, daily rainfall, soil type, current land use status, geological background and topographic dissection. 3S data serving landslide warning zoning was built on the basis of data analysis of 6 factors that cause landslides in Lai Chau province. Each element is classified, the density of points/square kilometer is calculated, and the weights for each element are calculated in **Table 1**.

**Table 1.**  
**Classification and weighted values of landslide-generating factors in Lai Chau province.**

Factor	Subclass	Density of points/km <sup>2</sup>	Weight	Factor	Subclass	Density of points/km <sup>2</sup>	Weight
<b>Slopes (Degree)</b>	Below 10	0.025	0.015	<b>Current land use situation</b>	Natural forest	0.002	0
	10-20	0.075	0.058		Plantation forest	0.069	0.025
	20-30	0.120	0.215		Poor forest	0.135	0.852
	30-40	1.135	0.258		Shrubs	0.981	1.325
	Above 40	0.105	0.095		Agricultural land	1.126	0.296
<b>Rainfall/day (mm)</b>	Below 25	0.102	0.015		Residential land, specialized land	0.687	0.558
	25-50	0.150	0.025		Rocky mountains	0.054	0.032
	50-75	0.128	0.060		Water surface	0.005	0
	75-100	0.098	0.122		Disjointed rock group	0.012	1.252
	100-125	0.042	0.217		Carbonate rock group	0.028	0.527
	125-150	0.072	0.348	Metamorphic rock group	0.056	0.321	
	150-175	0.085	0.879	Sedimentary rock group	0.126	0.213	
	Above 175	0.068	1.759	Eruption rock group	0.098	0.122	
	Mountain limestone	0.015	0.242	Intrusive rock group	0.056	0.098	
	Alisol	0.124	0.156	Quaternary rock group	0.037	0.052	
<b>Soil type</b>	Mountain humus	0.028	0.269	<b>Deep cleavage (m)</b>	Below 100	0.12	0.035
	Dark soil	0.098	0.196		100-200	0.212	0.521
	Oxisols	0.159	0.127		200-300	0.145	0.265
	Ferralsols	0.214	0.568		300-400	0.085	0.132
	Strongly erosive soils	0.037	0.055		400-500	0.039	0.086
	Aggregating sloped soils	0.026	0.012		Above 500	0.012	0.012

Overlapping 6 types of maps, corresponding to landslide-forming factors in Lai Chau province according to formula (1), obtain a landslide risk map of Lai Chau province with 5 levels as follows: very low ( $LSI \leq 0.1$ ), low ( $LSI = 0.1-0.2$ ), medium ( $LSI=0.2-0.3$ ), high ( $LSI=0.3-0.4$ ), very high ( $LSI \geq 0.4$ ) (**Fig. 1**).

The results of spatial analysis show that Lai Chau province areas with very high risk of landslides is 753.62 km<sup>2</sup> (accounting for 8.31% of the area), distributed in areas with sloping terrain and loose soil layers, the vegetation cover is low, the largest area is in Phong Tho, Muong Te, and Nam Nhun districts. The area assessed as having a high risk of landslide is 1633.29 km<sup>2</sup> (accounting for 18.01% of the area), scatteredly distributed, the most is Muong Te district with 786.51 km<sup>2</sup>. The area assessed to have a medium risk of landslides is 3097.9 km<sup>2</sup>, accounting for 34.16% of the province's natural area.

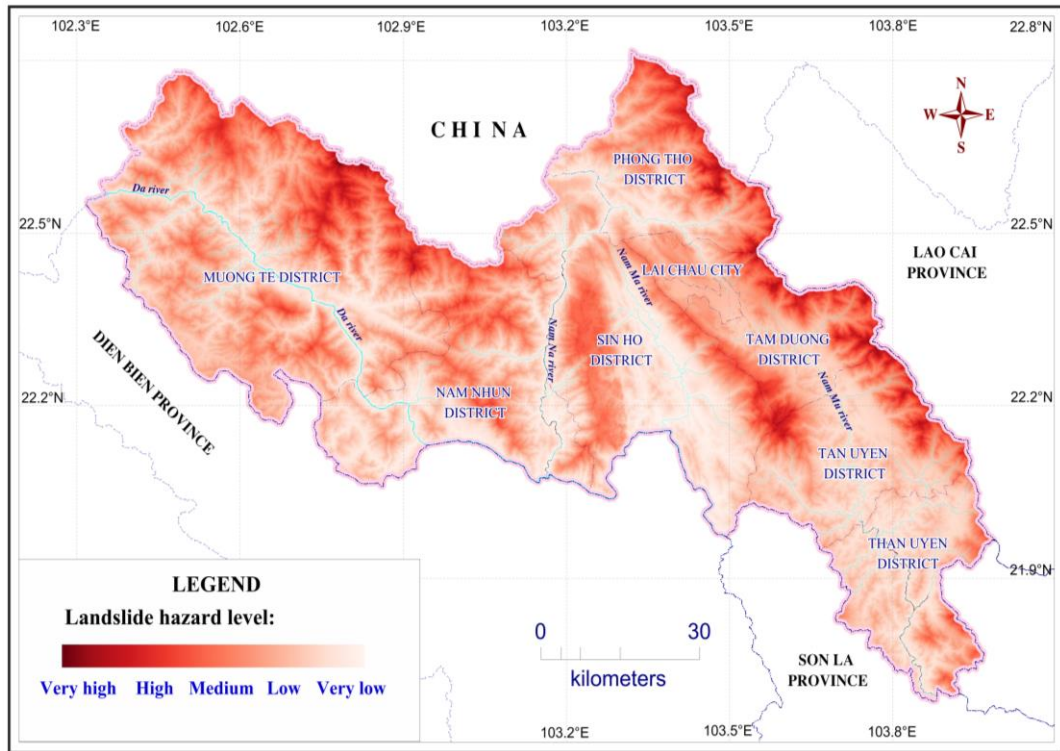


Fig. 1. Mapping of landslide risk in Lai Chau province.

Areas with small slopes, vegetation is planted or natural forest, low terrain fragmentation, often basins with geological strata of sedimentary rocks are assessed as low risk of landslides and very low risk of landslides. In Lai Chau province, the area with low landslide risk accounts for about 25% of the area, and the area with very low risk of landslides accounts for 14.56% of the area (Table 2).

Classification of landslide levels in Lai Chau province.

Table 2.

Hierarchy	Intensity	LSI score	Area (km <sup>2</sup> )	Proportion (%)
Level 1	Very low	$\leq 0.1$	1320.41	14.56
Level 2	Low	0.1 – 0.2	2263.57	24.96
Level 3	Medium	0.2 – 0.3	3097.90	34.16
Level 4	High	0.3 – 0.4	1633.29	18.01
Level 5	Very high	$\geq 0.4$	753.62	8.31

The results of landslide classification in Table 2 are consistent with the results of field surveys and reports related to landslides in mountainous areas (Vietnam's Disaster Prevention and Control Office, 2021). The landslide sites all coincided with areas assessed as high and very high risk of landslides. Areas with high and very high risk of landslides are studied in detail, combining the results of the current survey to define landslide warning zones. On warning points, set up analysis equipment and online landslide warning. Online locators and analyzers (mainly daily rainfall data) collect landslide-causing data to generate online landslide warning information.

#### **4.4. Some solutions to develop the application of 3S technology in disaster risk management in the northern mountainous region of Vietnam**

Based on the above analysis, the study proposes a few solutions to develop the application of 3S technology in disaster risk management in the northern mountainous region of Vietnam, the solutions are as follows:

Firstly, it is necessary to study, evaluate and categorize types of natural disaster risks. The mountainous area in the North of Vietnam has a large area and complicated types of natural disasters. To apply 3S technology for disaster risk management, it is necessary to make preliminary assessment and classification of disaster risk types. This is also a limitation when previous studies have not been able to solve it (Vietnam's Ministry of Natural Resources and Environment, 2020). Develop a theoretical basis, a scientific basis and an application model suitable for each type of disaster risk is one of the important solutions that should be prioritized.

Second, it is necessary to build a synchronous, comprehensive and modern 3S database. Building a database is an important solution and should be given top priority. Currently, the biggest difficulty when applying 3S technology in Vietnam in general and in mountainous areas in particular is the lack of database. The satellite image data in Vietnam is still not active, the current satellite images have low image resolution, especially the level of updating and synchronizing the image database is still limited. GPS data also depends on handheld devices, the accuracy is not high. GIS data is not synchronized, depending on traditional data sources; digital data sources are limited.

Third, it is necessary to build infrastructure and human resources in the field of 3S technology. In which, it is necessary to develop infrastructure and human resources for mountainous areas in stages. First, priority should be given to developing a system of satellite base stations, combining automatic warning systems, and building disaster risk management webGIS in high-risk areas. The staff and specialists have very limited qualifications and understanding of 3S technology. Therefore, it is necessary to strengthen human resources by organizing conferences, seminars, publishing documents and in-depth training. Can establish mechanisms to network and promote public awareness; Exchange and train professional staff through technical transfer training courses.

Fourth, it is necessary to develop an online application model system to warn and manage disaster risks. Natural disasters often happen very quickly, so it is necessary to have an online warning system. In which, it is necessary to exploit the system of sensors, online satellite images, webGIS system associated with application software on mobile devices. Online application models have the ability to quickly analyze and provide accurate information to help managers and people have early plans in disaster risk prevention.

#### **5. CONCLUSIONS**

3S technology is very promising in disaster risk management in the northern mountainous region of Vietnam. Application of 3S technology can build databases, perform spatial analysis algorithms, build forecasting models and warn of disaster risks. The analytical data from the 3S model is a decision support tool for disaster risk management and monitoring for mountainous areas. Experimental research model applying 3S technology in building landslide warning zoning map in Lai Chau province is a proof of the potential application of 3S technology in disaster risk management. In the future, to develop 3S technology, it is necessary to build a synchronous database, develop human resources, and at the same time need to build online application model systems.

**Acknowledgements:** The author gratefully acknowledge Vietnam's Ministry of Natural Resources and Environment, Thai Nguyen University's project, code: DH2021-TN06-02 provided data and other necessary facilities for this study.



## REFERENCES

- Albano, R., & Sole, A., 2018. Geospatial Methods and Tools for Natural Risk Management and Communications. *ISPRS International Journal of Geo-Information*. 7(12), 470.
- Ali SA, Parvin F, Pham QB, Vojtek M, Vojteková J, Costache R, Linh NTT, Nguyen HQ, Ahmad A, Ghorbani MA., 2020. Comparative GIS-based assessment of multi-user flood susceptibility Criteria combining decision-making approaches, naive Bayesian trees, two-variable statistics and logistic regression: A case of the Topľa basin, Slovakia. *Ecol. India*. 117.
- Asadzadeh S., Souza C.R., 2016. A review on spectral processing methods for remote sensing. *International Journal of Applied Earth Observation and Geoinformation*. 47, 69-90.
- Azareh A, Rahmati O, Rafiei-Sardooi E, Sankey J.B, Lee S, Shahabi H, Ahmad B.B., 2019. Modelling gully-erosion susceptibility in a semi-arid region, Iran: Investigation of applicability of certainty factor and maximum entropy models. *Sci. Total Environ*. 655, 684–696.
- Babajaa, S., Masoud, M., Ai-Amri, N., 2014. Flash flood hazard mapping based on quantitative hydrology, geomorphology and GIS techniques (case study of Wadi AI Lith, Saudi Arabia). *Arabian J. Geosci*, 7(6), 2469-2481.
- Ballesteros, C., Jiménez, J. A, Viavattene, C., 2017. A multi-component flood risk assessment in the Maresme coast (NW Mediterranean). *Natural Hazards*. 90(1), 265–292.
- Berse, K. B., Bendimerad, F., & Asami, Y., 2011. Beyond geo-spatial technologies: promoting spatial thinking through local disaster risk management planning. *Procedia - Social and Behavioral Sciences*. 21, 73–82.
- Bui. D.T, Hoang N.D, Martínez-Álvarez F, Ngo. P.T.T, Hoa. P.V, Pham. T.D, Samui. P, Costache R., 2020. A novel deep learning neural network approach for predicting flash flood susceptibility: A case study at a high frequency tropical storm area. *Sci. Total Environ*. 701, 134413
- Cao, C., Xu, P., Wang, Y., Chen, J., Zheng, L., Niu, C., 2016. Flash Flood Hazard Susceptibility Mapping Using Frequency Ratio and Statistical Index Methods in Coalmine Subsidence Areas. *Sustainability*. 8, 948-961.
- Chapi K, Singh VP, Shirzadi A, Shahabi H, Bui DT, Pham BT, Khosravi K., 2017. A new hybrid artificial intelligence approach to flood susceptibility assessment. *Environment Model Lightly*. 95, 229–245.
- Choubin B, Moradi E, Golshan M, Adamowski J, Sajedi-Hosseini F, Mosavi A., 2019. An Ensemble prediction of flood susceptibility using tree analysis, classification and multivariable regression, and support vector machines. *Science Total environment*. 651, 2087–2096.
- Comber A., Zeng W., 2019. Spatial interpolation using areal features: A review of methods and opportunities using new forms of data with coded illustrations. *Geography Compass*.
- Costache R, 2019. Flood Susceptibility Assessment by Using Bivariate Statistics and Machine Learning Models-A Useful Tool for Flood Risk Management. *Water Resour Manag*. 33, 3239–3256.
- Costache R, Bui. D.T., 2019. Spatial prediction of flood potential using new ensembles of bivariate statistics and artificial intelligence: A case study at the Putna river catchment of Romania. *Sci. Total Environ*. 691, 1098–1118.
- Costache, R., Pham, Q. B., Sharifi, E., Linh, N. T. T., Abba, S. I., Vojtek, M., Khoi, D. N., 2019. Flash-Flood Susceptibility Assessment Using Multi-Criteria Decision Making and Machine Learning Supported by Remote Sensing and GIS Techniques. *Remote Sensing*. 12(1), 106-120.
- Dano U.L, Balogun A.L, Matori A.N, Wan Yusouf K, Abubakar I.R, Said Mohamed M.A, Aina Y.A, Pradhan B., 2019. Flood susceptibility mapping using a distributed network procedure GIS-based analysis: A case study by Perlis, Malaysia Country.
- Der Sarkissian, R., Zaninetti, J.-M., & Abdallah, C., 2019. The use of geospatial information as support for Disaster Risk Reduction; contextualization to Baalbek-Hermel Governorate/Lebanon. *Applied Geography*. 111, 102075.
- Diakakis, M., 2011. A method for flood hazard mapping based on basin morphometry: Application in two catchments in Greece. *Nat. Hazards* 56(3), 803-814.
- Du, J.K., Xi, H., Hu, Y.J., Xu, Y.P., Xu, C.Y., 2009. Development and testing of a new storm runoff routing approach based on time variant spatially distributed travel time method. *J. Hydrol*. 369(1-2), 44-54.
- Elkhrachy, I., 2015. Flash flood hazard mapping using satellite images and GIS tools: A case study of Najran City, Kingdom of Saudi Arabia (KSA). *Egypt. J. Remote Sens. Space Sci*. 18, 261-278.

- Estupina-Borrell, V., Dartus, D., Ababou, R., 2006. Flash flood modeling with the MARINE hydrological distributed model. *Hydrology Earth Syst. Sci. Discuss.* 3(6), 3397-3438.
- Goodchild M.F., Haining R.P., 2003. GIS and spatial data analysis: Converging perspectives. *Papers in Regional Science.* 83(1), 363-385.
- IPCC, 2012. Managing the Risks of Extreme Events and Disasters to Advance Climate Change Adaptation; IPCC: New York, USA.
- Jia P, Cheng X, Xue H, Wang Y., 2017. Applications of geographic information systems (GIS) data and methods in obesity-related research. *Obesity Reviews.* 18(4), 400-411.
- Kawasaki, A., Berman, M. L., & Guan, W., 2012. The growing role of web-based geospatial technology in disaster response and support. *Disasters.* 37(2), 201–221.
- Kieu Q.L., Do T.V.H., Van H.T., 2020. Constructing a spatial analysis model in assessing the sensitivity of landscape erosion in mountainous regions of Vietnam. *SN Applied Sciences.* 2 (2020): 43-56.
- Kieu Q.L, Tran D.V., 2021. Application of geospatial technologies in constructing a flash flood warning model in northern mountainous regions of Vietnam: a case study at Trinh Tuong commune, Bat Xat district, Lao Cai province. *Bulletin of Geography. Physical Geography Series.* 20: 31-43.
- Kieu Q.L., 2021. Flash Flood hazard mapping using satellite images and GIS integration method: a case study of Lai Chau province, Vietnam. *Geographia Technica.* 16(2): 105-115.
- Kim. T.H, Kim. B, Han. K.Y., 2019. Application of Fuzzy TOPSIS to Flood Hazard Mapping for Levee Failure. *Water* 11, 592-612.
- Khosravi, K., Pham, B.T., Chapi, K., Shirzadi, A., Shahabi, H., Revhaug, I., Prakash, I., Bui, D.T., 2019. A comparative assessment of decision trees algorithms for flash flood susceptibility modeling at Haraz watershed, northern Iran. *Sci. Total Environ.* 627, 744-755.
- Kumar, R., Chatterjee, C., Singh, R.D., Lohani, A.K., Kumar, S., 2007. Runoff estimation for an ungauged catchment using geomorphological instantaneous unit hydrograph (GIUH) models. *Hydrol. Process.* 21(14), 1829-1840.
- La T.H, 2009. Research and develop flash flood risk zoning maps to serve the prevention of flash floods for Yen Bai province. *Journal of Meteorology and Hydrology.* 211 (2), 11-15.
- Lai T.A, Nguyen N.T, Pham X.C, Le N.N, 2018. Building an early warning system for flash floods in mountainous areas, testing it in Thuan Chau district, Son La province. *Journal of Science and Technology of Vietnam.* 60 (8), 28-35.
- Manfré, L. A., Hirata, E., Silva, J. B., Shinohara, E. J., Giannotti, M. A., Larocca, A. P. C., & Quintanilha, J. A., 2012. An Analysis of Geospatial Technologies for Risk and Natural Disaster Management. *ISPRS International Journal of Geo-Information.* 1(2), 166–185.
- Miyazaki, H., Nagai, M., & Shibasaki, R., 2015. Reviews of Geospatial Information Technology and Collaborative Data Delivery for Disaster Risk Management. *ISPRS International Journal of Geo-Information.* 4(4), 1936–1964.
- Moussa, R., 2003. On morphometric properties of basins, scale effects and hydrological response. *Hydrol. Process.* 17(1), 33-58.
- Nguyen N.T, 2003. Research and forecast of natural disasters in Hoa Binh province, Special scientific project report, code QG 0017. VNU, Vietnam.
- Nguyen T.D, Tran A.T, Saro Lee, 2008. Application of GIS technology to establish landslide susceptibility maps of northwestern border provinces of Vietnam. *Journal of Earth Sciences.* 30 (2), 12-20.
- Nguyen V.H, 2015. Study on landslide warning in Hoa Binh and Son La hydroelectric reservoirs by analysis of geographic information systems. *Journal of Earth Sciences.* 37(3), 193-203.
- Nguyen T.L, Nguyen T.H, Vu D.D, Nguyen T.H, 2017. Research on establishing inundation maps from Radar remote sensing images applied to downstream Tra Khuc and Ve river basins, Quang Ngai province. *Journal of Irrigation Science and Technology.* 39, 21-28.
- Oliveira, E. A., Pires, R. S., Oliveira, R. S., Furtado, V., Herrmann, H. J., Andrade, J. S., 2019. A universal approach for drainage basins. *Scientific Reports.* 9(1).
- Park, S.J., Lee, C.W., Lee, S., Lee, M.J., 2018. Landslide susceptibility mapping and comparison using decision tree models: A Case Study of Jumunji in Area, Korea. *Remote Sens.* 10, 1545-1560.
- Popa, M. C., Diaconu, D. C., 2019. Flood and Flash Flood Hazard Mapping Using the Frequency Ratio, Multilayer Perceptron and Their Hybrid Ensemble. *Proceedings.* 48(1), 6-21.

- Pu, R., Gong, P., Tian, Y., Miao, X., Carruthers, R. I., Anderson, G. L., 2008. Using classification and NDVI differencing methods for monitoring sparse vegetation coverage: a case study of saltcedar in Nevada, USA. *International Journal of Remote Sensing*. 29(14), 3987–4011.
- Rahmati O, Pourghasemi H.R, Zeinivand H., 2016. Flood susceptibility mapping using frequency ratio and weights-of-evidence models in the Golastan Province, Iran. *Geocarto Int.* 31, 42–70.
- Reznik, T., Lukas, V., Charvat, K., Charvát, K., Kepka, M., 2017. Disaster Risk Reduction in Agriculture through Geospatial (Big) Data Processing. *ISPRS International Journal of Geo-Information*. 6(8), 238.
- Roux, H., Labat, D., Garambois, P.A., Maubourguet, M.M., Chorda, J., Dartus, D., 2011. A physically-based parsimonious hydrological model for flash floods in Mediterranean catchments. *Nat. Hazards Earth Syst. Sci.* 11(9), 2567–2582.
- Saaty, T.L., 1987. The analytic hierarchy process - What it is and how it is used. *Mathl Modelling*. (3), 161–176.
- Shafapour Tehrani M, Kumar L, Neamah Jebur M, Shabani F., 2019. Evaluating the application of the statistical index method in flood susceptibility mapping and its comparison with frequency ratio and logistic regression methods. *Geomat Nat Hazards Risk*. 10, 79–101.
- Shirowzhan S., Sepasgozar S., 2019. Spatial Analysis Using Temporal Point Clouds in Advanced GIS: Methods for Ground Elevation Extraction in Slant Areas and Building Classifications. *ISPRS International Journal of Geo-Information*. 8(3), 110–120.
- Souissi D, Zouhri L, Hammami S, Msaddek M.H, Zghibi A, Dlala M., 2019. GIS-based MCDM-AHP modeling for flood susceptibility mapping of arid areas, southeastern Tunisia. *Geocarto Int.* 1–25.
- Statistical Office of Lai Chau Province, 2022. Statistics of natural disasters for the period 2001 - 2021. *Statistical Publishing House*, 248–269.
- Tehrani, M.S., Pradhan, B., Jebur, M.N., 2015. Flood susceptibility analysis and its verification using a novel ensemble support vector machine and frequency ratio method. *Stoch. Environ. Res. Risk Assess*, 29, 1149–1165.
- Thomas L, Saaty, 2008. Decision making with the analytic hierarchy process. *Int. J. Services Sciences*, 1(1), 167–175.
- Tran Viet Khanh, 2020. Studying the current situation and establishing flash flood zoning maps for some mountainous areas of Vietnam. *Journal of Science and Technology of Thai Nguyen University*. 225 (11), 38–47.
- Triantaphyllou, E., 2000. *Multi-Criteria Decision Making Methods: A Comparative Study*; Kluwer Academic Publishers: Dordrecht, The Netherlands.
- Uddin, K., & Matin, M. A., 2021. Potential flood hazard zonation and flood shelter suitability mapping for disaster risk mitigation in Bangladesh using geospatial technology. *Progress in Disaster Science*. 11, 100185.
- Vietnam's Disaster Prevention and Control Office, 2021. Report on flash floods and landslides in mountainous areas in the period 2001–2021.
- Vietnam's Ministry of Natural Resources and Environment, 2020. Project "Investigation, assessment and zoning for landslide hazard warning in mountainous areas of Vietnam", Hanoi, Vietnam.
- Wang Y, Hong H, Chen W, Li S, Panahi M, Khosravi K, Shirzadi A, Shahabi H, Panahi S, Costache R., 2019. Flood susceptibility mapping in Dingnan County (China) uses an adaptive neural fuzzy inference system with biogeography-based optimization and an imperial competition algorithm. *J. Environment. Manag.* 247, 712–729.
- Wessel B., Huber M., Wohlfart C., Marschalk U., Kosmann D., 2018. Accuracy assessment of the global TanDEM-X Digital Elevation Model with GPS data. *ISPRS Journal of Photogrammetry and Remote Sensing*. 139, 171–182.
- Yi W., Yang, M., 2021. Flood susceptibility mapping by integrating frequency ratio and index of entropy with multilayer perceptron and classification and regression tree. *Journal of Environmental Management*. 289 (1), 235–251.
- Zhao G, Pang B, Xu Z, Yue J, Tu T., 2019. Mapping flood susceptibility in mountainous areas on a national scale in China. *Sci. Total Environ.* 615, 1133–1142.

## PHYSICAL DRIVERS OF THE 2013 MARINE HEATWAVE IN THE SEAS OF THE SOUTHERN JAVA-NUSA TENGGARA

*Tria MAULIDA*<sup>1,4</sup> , *Anindya WIRASATRIYA*<sup>2,3</sup> , *Dwi Haryo ISMUNARTI*<sup>2</sup>  
and *Ardiansyah Desmont PURYAJATI*<sup>2</sup> 

DOI: 10.21163/GT\_2022.171.10

### ABSTRACT:

Marine heatwave (MHW) is an extreme phenomenon of warm sea surface temperature anomaly that has a destructive impact on the marine ecosystem and organisms. This phenomenon increases every year in duration, frequency, and area due to the global warming. Almost all of the world's oceans have experienced MHW, including in the seas of the southern Java-Nusa Tenggara. The lack of detailed research in this area motivated us to analyze MHW drivers. MHW was identified with the 99th percentile method and duration of  $\geq 5$  days as a threshold by using blended product of SST data. In 2013, an MHW event was identified in the seas of the southern Java-Nusa Tenggara. This MHW lasts for 37 days, from 8 June to 14 July. The maximum (mean) intensity of sea surface temperature anomaly reaches  $2.60^{\circ}\text{C}$  ( $1.83^{\circ}\text{C}$ ) above climatology with an average area of  $36.53 \times 10^4 \text{ km}^2$ . Locally, we found that probably the positive downward shortwave radiation affected this anomaly. Furthermore, a remote process of the propagation of downwelling Kelvin wave during negative Indian Ocean Dipole may also affect this anomaly. The strong westerly wind along the equatorial Indian ocean forms downwelling Kelvin wave that propagates to the southern Java-Nusa Tenggara increasing SST in this area.

**Key-words:** *Marine heatwave, Extreme Sea surface temperature, Downwelling Kelvin wave, Remote Sensing, South Java-Nusa Tenggara*

### 1. INTRODUCTION

Global warming has increased the temperature of the earth's surface. This has also contributed to rising sea surface temperatures (SSTs) as the oceans have absorbed more than 93% of heat excess from greenhouse gas emissions since the 1970s (Rhein et al. 2013). It is noted that the global average SST has increased since the early 20th century and 1950. The average SST in the Indian, Atlantic and Pacific Oceans increased by  $0.65^{\circ}\text{C}$ ,  $0.41^{\circ}\text{C}$ , and  $0.31^{\circ}\text{C}$  during the period 1950–2009. This SST increase results in more frequent extreme events and a greater risk to marine ecosystems (Hoegh-Guldberg et al. 2014). One category of extreme event that has attracted more attention from researchers is the Marine Heatwave (MHW).

MHW is a warm SST anomalous event that occurs for five days or more with an SST warmer than the 90th percentile based on a historical baseline period of 30 years (Hobday et al. 2016). MHW can also be defined by the relative threshold of the 99th percentile (Collins et al. 2019). Oliver et al. (2018) stated that the frequency, duration, and days of global MHW during 1925–2016 had increased

---

<sup>1</sup>Faculty of Fisheries and Marine Sciences, Diponegoro University, 50275, Semarang, Indonesia, [triamaulida2008@gmail.com](mailto:triamaulida2008@gmail.com)

<sup>2</sup>Department of Oceanography, Faculty of Fisheries and Marine Sciences, Diponegoro University, 50275, Semarang, Indonesia, [aninosti@yahoo.co.id](mailto:aninosti@yahoo.co.id), [dwiহার্যইসমুনর্তি@lecturer.undip.ac.id](mailto:dwiহার্যইসমুনর্তি@lecturer.undip.ac.id), [a.desmont213@gmail.com](mailto:a.desmont213@gmail.com)

<sup>3</sup>Center for Coastal Rehabilitation and Disaster Mitigation Studies, Diponegoro University, 50275, Semarang, Indonesia

<sup>4</sup>Indonesian Agency for Meteorology Climatology and Geophysics, 10610, Jakarta, Indonesia

by 34%, 17%, and 54%, respectively. This trend of increasing MHW can undoubtedly continue to increase across the oceans as long as global warming continues.

Previous research has shown that many MHW events have occurred in oceans. Some of them are Western Australia 2010/2011 MHW (Pearce et al. 2011), the Atlantic Northwest 2012 MHW (Mills et al. 2013), the Northeast Pacific "The Blob" 2015 MHW (Bond et al. 2015), the Tasman Sea 2015 MHW (Oliver et al. 2017), and the North Pacific 2019 MHW (Amaya et al. 2020). The Indonesian Ocean was not spared from the MHW incident. Benthuyesen et al. (2018) and Iskandar et al. (2021) showed the presence of MHW in the Indo-Australian Basin (9°S to 18°S, 110°E to 122°E) in 2016, and Ismail (2021) identified MHW in coastal and offshore areas of West Sumatra.

MHW in several oceans has a driver mechanism that varies significantly from region to region and is different in each case. MHW can generally occur due to atmospheric-ocean interactions, atmospheric conditions, ocean conditions, modulation of climate variability (MJO, ENSO, IOD, PDO), and remote teleconnection (Holbrook et al. 2020). For example, Pearce and Feng (2013) mention that the West Australia 2011 MHW occurred simultaneously as a strong La Niña, which increased the Leeuwin current and the presence of high-value air-to-ocean heat fluxes. The North Australian 2016 MHW, which included the Indo-Australian Basin, was due to a strong El Niño, which weakened monsoon activity resulting in a positive anomaly of heat flux entering the ocean (Benthuyesen et al. 2018). The Northwest Atlantic 2015/2016 MHW occurred due to a combination of atmospheric-ocean processes, namely the position of the jet stream and ocean advection that played a role in heating the SST (Perez et al. 2021). The South Java MHW in 1998 and 2016 occurred due to the strong El Niño and weakening monsoons (Iskandar et al. 2021).

Research related to the mechanism that causes MHW has been proliferating throughout the world, but unfortunately, research related to this is still very lacking in the territory of Indonesia. Meanwhile, MHW can cause significant damage to marine organisms and ecosystems, such as the Northwest Atlantic 2012 MHW. This MHW disrupted fishery production, species shift, and low ocean productivity, so it impacted the socioeconomic (Mills et al. 2013). Another massive impact of MHW is causing coral bleaching, such as in the Bay of Bengal (Krishnan et al. 2011) to resistant corals in Western Australia (Le Nohaïc et al. 2017). Therefore, we are interested in conducting an analysis related to the causes of MHW in Indonesia's territory, namely the seas of the southern Java-Nusa Tenggara (Fig. 1).

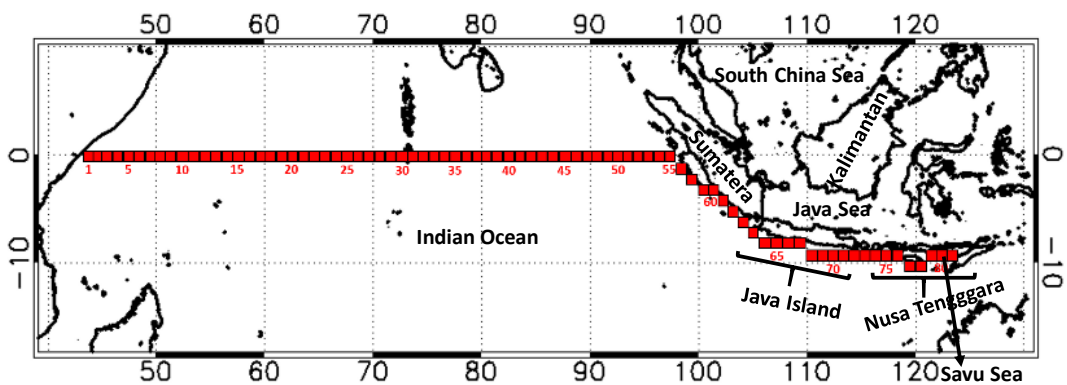


**Fig. 1.** Kelvin wave trajectory identified from the Indian Ocean to the coasts of Sumatra, Java, and Nusa Tenggara. The red box showed 81 sample areas with  $0.1^\circ \times 0.1^\circ$  bin sizes.

This location was chosen because the southern seas of Java-Nusa Tenggara are included in the State Fisheries Management Area of the Republic of Indonesia 573, which has excellent fishery potential. So that the analysis of the physical mechanisms of MHW and the extent to which local and remote factors play a role will improve our understanding of the development of MHW in this area.

Thus, this study can be a consideration in mitigating the impact to marine ecosystems if MHW retakes place.

## 2. DATA AND METHODS

Sea surface temperature data use daily Optimum Interpolation Sea Surface Temperature from Remote Sensing System (REMSS OISST) from June 2002-June 2021 with a resolution of 0.09° (<ftp://ftp.remss.com/sst/daily/>). This data uses microwave and infrared sensors. The microwave sensors used include the Global Precipitation Measurement (GPM) Microwave Imager (GMI), Tropical Rainfall Measuring Mission (TRMM) Microwave Imager (TMI), NASA Advanced Microwave Scanning Radiometer-EOS (AMSRE), Advanced Microwave Scanning Radiometer 2 (AMSR2), and WindSat. As for infrared sensors such as Moderate Resolution Imaging Spectroradiometer (MODIS) and Visible Infrared Imaging Radiometer Suite (VIIRS).

Sea level anomaly (SLA) data was obtained from <https://resources.marine.copernicus.eu/products>. This data is calculated by the optimal interpolation method and combines many data from various satellites such as Jason-3, Sentinel-3A, HY-2A, Saral/AltiKa, Cryosat-2, Jason-2, Jason-1, T/P, ENVISAT, GFO, ERS1/2. Monthly SLA data (SEALEVEL\_GLO\_PHY\_L4\_REP\_OBSERVATIONS\_008\_047) with a resolution of 0.25° x 0.25° were used for the analysis and Hovmöller plots of the 2013 MHW.

The surface wind vector data used is the second version of the Cross-Calibrated Multi-Platform (CCMP) level 3 data. The second version of this data combines the wind speed RSS Radiometer version 7, QuikSCAT and the ASCAT wind vector scatterometer, tethered buoy wind data, and the ERA-Interim model. The compilation of this data was processed using the Variational Analysis Method (VAM). This method produces wind data with a high resolution of 0.25° with a data period of 6 hours, which can be downloaded via <ftp://ftp.remss.com/ccmp>.

The latent heat flux, sensible heat flux, and shortwave radiation data used are model data from ERA-5, a reanalysis product from the European Center for Medium-Range Weather Forecasts (ECMWF). These data were collected from January-December 2013 with 0.25° × 0.25° resolution available at <https://cds.climate.copernicus.eu/cdsapp#!/dataset/reanalysis-era5-single-levels?tab=form>. The coverage area used is 6°S to 18°S, 104°E to 128°E. Based on the ECMWF convention, these three data values are positive downwards. Positive downward means a positive value indicating the presence of heat or radiation entering the ocean. Conversely, a negative value indicates heat or radiation coming out of the ocean.

MHW identification was carried out by following Hobday et al. (2016), using a duration threshold of 5 days. However, we did not use the 90th percentile in this study but used the 99th percentile (Frölicher et al. 2018; Collins et al. 2019). The 99th percentile was chosen because this method identifies more extreme MHWs, so relatively weak MHWs and those that may not have an ecological impact can be eliminated. Besides that, this threshold value has never been applied in our research area.

Using Hobday et al. (2016), climatological averages ( $T_m$ ) and threshold values ( $T_{99}$ ) were calculated for each day of the year using the daily temperature data for each year. The equation for climatological averages ( $T_m$ ) is expressed as follows:

$$T_m(j) = \sum_{y=y_s}^{y_e} \sum_{d=j-5}^{j+5} \frac{T(y,d)}{11(y_e-y_s+1)} \tag{1}$$

where  $j$  is day of year,  $y_s$  and  $y_e$  are the start and end of the climatological base period, respectively, and  $T$  is the daily SST on day  $d$  and year  $y$ .  $T_m$  unit is °C.

As for the threshold, it is calculated based on

$$T_{99}(j) = P_{99}(X) \tag{2}$$

where  $T_{99}$  is the seasonally varying temperature value at the 99th percentile,  $P_{99}$  is the 99th percentile and  $P_{99}(X)$  where  $X = \{T(y, d) | y_s \leq y \leq y_e, j - 5 \leq d \leq j + 5\}$ .

The period for calculating climatological value was limited only from 19 years data since REMSS OISST data is only available from June 2002. We chose REMSS OISST due to its high spatial resolution (i.e.,  $0.09^\circ\text{C}$ ) since our study area is limited only in the seas of the southern Java-Nusa Tenggara. Furthermore, Schlegel et al. (2019) stated that the detection of MHW can use time-series data less than 30 years, whereas the result of the short period analysis of 10 years does not have a duration or intensity of MHW that is sufficiently different from the events detected in the standard 30-year time series data as suggested by Hobday et al. (2016).

After the MHW was identified, we calculated the MHW metrics. The MHW metrics consist of duration (time between the start and end of the MHW event), maximum intensity (highest SST anomaly during MHW), average intensity (mean SST anomaly during MHW), and area size (areas where MHW was detected). To determine the parameters of duration ( $D$ ), we must set the date on which MHW starts ( $t_s$ ), where  $t_s$  is the time,  $t$ , where  $T(t) > T_{99}(j)$  and  $T(t - 1) < T_{99}(j)$  and MHW ends ( $t_e$ ), where  $t_e$  is the time,  $t$ , where  $t_e > t_s$  dan  $T(t) < T_{99}(j)$  and  $T(t - 1) > T_{99}(j)$ , so the duration can be calculated using the formula

$$D = t_e - t_s \quad (3)$$

As for maximum intensity ( $i_{max}$ ) and average intensity ( $i_{mean}$ ), we use these equations:

$$i_{max} = \max(T(t) - T_m(j)) \quad (4)$$

$$i_{mean} = \overline{T(t) - T_m(j)} \quad (5)$$

For the analysis of the MHW trigger mechanism, Holbrook et al. (2020) mention that various mechanisms can trigger the occurrence of MHW. Locally, atmosphere-ocean interactions such as heat flux exchange can lead to an increase in SST. So, we will be analyzed the mechanism from local influences with parameters of wind speed, latent heat flux, sensible heat flux, and shortwave radiation. Besides that, we also analyze the SLA and zonal wind anomalies to determine the effect of Kelvin waves. To further investigate how Kelvin waves occur and their effect on SST, we construct a Hovmöller plot. The plot consists three parameters: SST, zonal wind anomalies, and SLA according to the Kelvin wave trajectory from the Indian Ocean to the coasts of Sumatra, Java and Nusa Tenggara as shown in **Fig. 1**. Analysis was also carried out in temporal variation using a coverage area of  $8^\circ\text{S}$  to  $9^\circ\text{S}$ ,  $112^\circ\text{E}$  to  $115^\circ\text{E}$  (black box in **Fig. 2**).

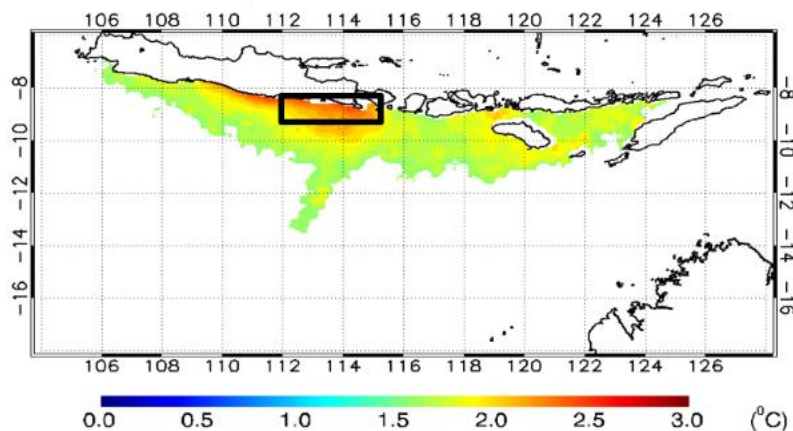


**Fig. 2.** MHW amplitude map for 8 June to 14 July. The colour bar shows the SST anomaly from the MHW threshold (smoothed daily climatology +  $1.6^\circ\text{C}$ ).



### 3. RESULTS AND DISCUSSION

#### 3.1. Characteristic of 2013 MHW

Applying the method of Hobday et al. (2016) and Collins et al. (2019), we found a threshold value of SST anomaly to identify MHW is  $1.6^{\circ}\text{C}$ . From this threshold value, 20 MHW events were identified during June 2002-June 2021. One of the longest cases was MHW in 2013 that occurred from 8 June to 14 July. We chose 2013 MHW as our case study because this MHW has a duration of more than one month. Based on the MHW metric parameters, the 2013 MHW had a duration of 37 days, a maximum intensity of  $2.60^{\circ}\text{C}$ , the average intensity of  $1.93^{\circ}\text{C}$ , and an area of  $36.53 \times 10^4 \text{ km}^2$ .

**Fig. 2** shows the 2013 MHW amplitude map. The 2013 MHW occurs in the southern coast of Java to Nusa Tenggara. The highest SST anomaly value occurs in the southern coast of Java, precisely in the southern coast of East Java, with an anomaly value of  $2.75^{\circ}\text{C}$ . In general, the value of the SST anomaly is higher in the coastal seas i.e., about  $2.5^{\circ}\text{C}$  than off the coast, where the value decreases to  $1.6^{\circ}\text{C}$ . Ismail (2021) also showed that the 1998 and 2016 MHWs that occurred in the west coast of Sumatra had a more severe category, than the offshore area, which was only detected in the moderate to strong category. High SST values in the coastal seas can occur due to various factors. Coastal areas where land, sea, and air meet have complex SST variation mechanisms (Wirasatriya et al. 2019a).

Next, we made the temporal variation of SST with the threshold value and the climatological mean (**Fig. 3**). Temporal variation of SST was averaged from the area with the highest anomaly value, i.e.,  $8^{\circ}\text{S}$  to  $9^{\circ}\text{S}$ ,  $112^{\circ}\text{E}$  to  $115^{\circ}\text{E}$  (black box in **Fig. 2**). Red shading indicates the period of identified MHW. **Fig. 3a** shows the variation of SST during 2013 and we identified one MHW incident which is categorized as an extreme event. The temporal variation of SST during the 2013 MHW event (**Fig. 3b**) shows that the SST value exceeds the 99th percentile threshold from 8 June with an SST value of  $29.19^{\circ}\text{C}$ . The SST value in this incident ranges from  $29.37$  to  $27.55^{\circ}\text{C}$ . On 10 July, the SST value starts to decline, approaches the threshold value, and finally ends on 14 July with an SST value of  $27.55^{\circ}\text{C}$ .

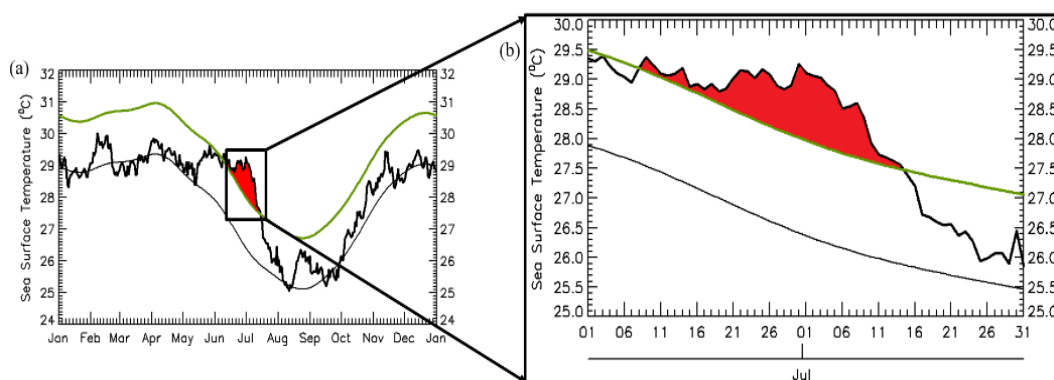


**Fig. 3.** Temporal variation of SST (thick black line), SST climatology (thin black line) and 99th percentile climatology (green line) during (a) 2013 and (b) 2013 MHW events at  $8^{\circ}\text{S}$  to  $9^{\circ}\text{S}$ ,  $112^{\circ}\text{E}$  to  $115^{\circ}\text{E}$  (black box in **Fig. 2**). The red shaded indicates the occurrence of MHW.

In addition, we also compared the SST anomaly with the area during MHW 2013 (**Fig. 4**). At the beginning of its occurrence, MHW has an area of  $5.19 \times 10^4 \text{ km}^2$  with an SST anomaly of  $1.61^{\circ}\text{C}$ . The area of MHW increases along with the increasing value of the SST anomaly. However, at the highest SST anomaly, which occurs on 14 July ( $2.75^{\circ}\text{C}$ ), the previous maximum area occurs on 28 June at  $25.66 \times 10^4 \text{ km}^2$ . Meanwhile, at the end of the MHW period, the area is getting smaller and ends up with  $7.52 \times 10^4 \text{ km}^2$ .

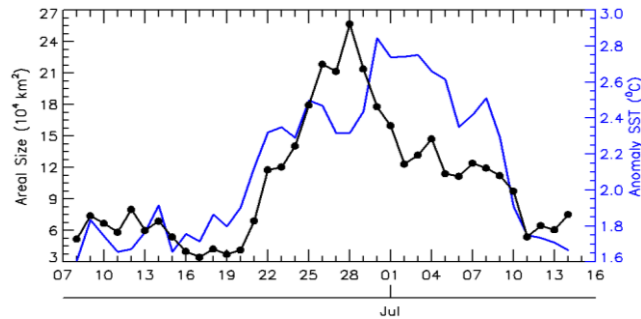


**Fig. 4.** Temporal variation of MHW area (black line) with SST anomaly (blue line) during MHW 2013.

### 3.2. Mechanisms of 2013 MHW

During 2013 MHW, the wind blows from the east-southeast direction (**Fig. 5a**). The wind speed in the southern coast of Java-Nusa Tenggara ranges from 2 to 6 m/s. This is lower than the offshore wind speed which is ranging from 6 to 8 m/s. Theoretically, the wind speed variation can affect the latent heat flux. For example, Wirasatriya et al. (2019b) stated that the increase in wind speed in the Sulawesi Sea and the Maluku Sea increases the latent heat flux released from the ocean. In the present study the latent heat flux distribution during 2013 MHW is shown in **Fig. 5b**.

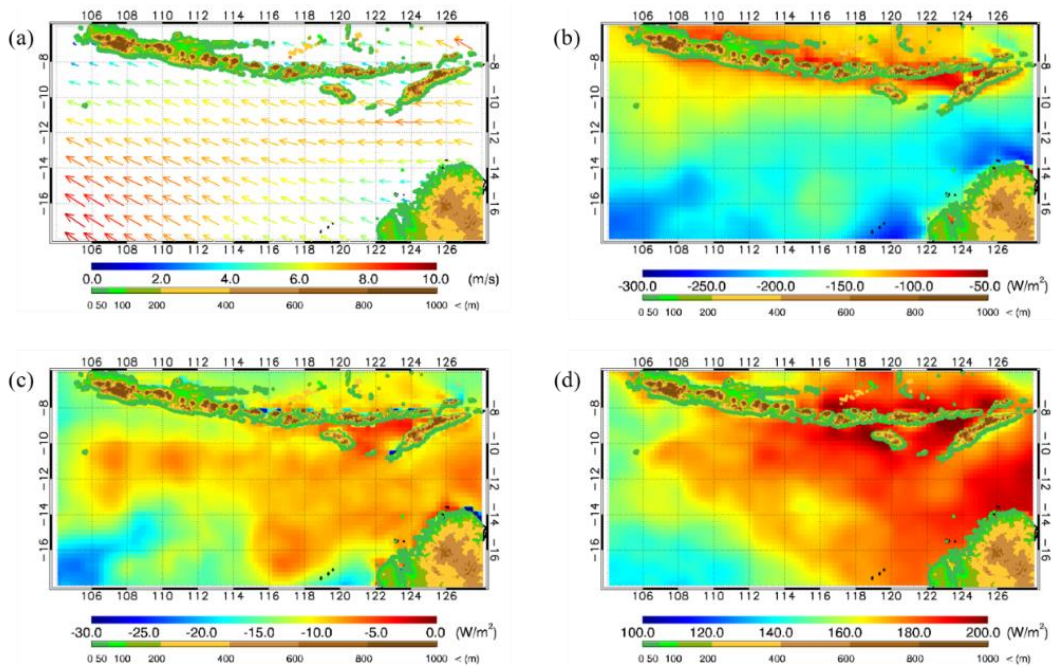


**Fig. 5.** Spatial distribution of (a) surface wind, (b) latent heat flux, (c) sensible heat flux, and (d) shortwave radiation during 2013 MHW.

Negative values of latent heat flux dominate the entire MHW area. This negative value indicates that the oceans are losing heat due to the heat escaping. The southern coast of Java-Nusa Tenggara, which has lower wind speeds, tends to release a lower latent heat flux (i.e., -50 to -150 W/m<sup>2</sup>) than the offshore area. Meanwhile, offshore area with higher wind speed releases more significant heat flux, i.e., -150 to -200 W/m<sup>2</sup>.

The distribution of negative values is also visible for the sensible heat flux distribution (**Fig. 5c**). There is no difference between coastal and offshore in the sensible heat flux. This flux value ranges from 0 to  $-15 \text{ W/m}^2$ . The lowest sensible heat flux is detected in the Savu Sea which ranges from 0 to  $-5 \text{ W/m}^2$ . The lowest value indicates that the air temperature in the Savu Sea is lower than in other ocean areas. This results in less heat loss compared to other areas. However, compared with the MHW amplitude map (**Fig. 2**), the less heat loss in the Savu Sea does not have a significant effect because the SST anomaly value is only around  $1.7^\circ\text{C}$ .

In contrast to the latent and sensible heat flux, the shortwave radiation shows a positive distribution of values (**Fig. 5d**). The value of shortwave radiation on the coast of the island to the offshore is relatively the same as the value of  $170\text{-}200 \text{ W/m}^2$ . Areas with  $>200 \text{ W/m}^2$  generally occur in the south of West Nusa Tenggara and the Savu Sea. Meanwhile, in other areas with less than  $200 \text{ W/m}^2$ , including the southern region of East Java has the highest SST anomaly value. This positive value indicates that there is a radiation entering the sea which can heating the SST. In the case of South Atlantic, 2013/2014 MHW occurred because of the increase of shortwave radiation intensity due to the reduced cloud cover and reduced heat loss from the ocean (Rodrigues et al. 2019).

Since the analysis of heat flux and wind speed could not explain well the mechanism of MHW 2013, we analyzed the possible contribution of remote modulation such as Kelvin wave propagation. Tracking Kelvin waves eastward along the equator and then along the coasts of Sumatra and Java can be done effectively using altimetry satellites (Drushka et al. 2010). Kelvin wave propagation can be observed using SLA data. We can determine whether the Kelvin wave is downwelling or upwelling from the SLA data.

The Hovmöller SST diagram (**Fig. 6a**) shows several SST anomalies that exceed the threshold value of the 99<sup>th</sup> percentile as in June-July and August. However, the most extensive and most widespread anomaly occurred from 8 June to 14 July. The SST anomaly value was detected from bin 64-81, i.e., the Southern coast of Java-Nusa Tenggara area. As for the Hovmöller diagram of the zonal wind anomaly during 2013 (**Fig. 6b**), bin 64-81 (south of Java-Nusa Tenggara) has a negative value, indicating an easterly wind occurrence. From this anomaly, it is known that the easterly wind is stronger than the climatological value.

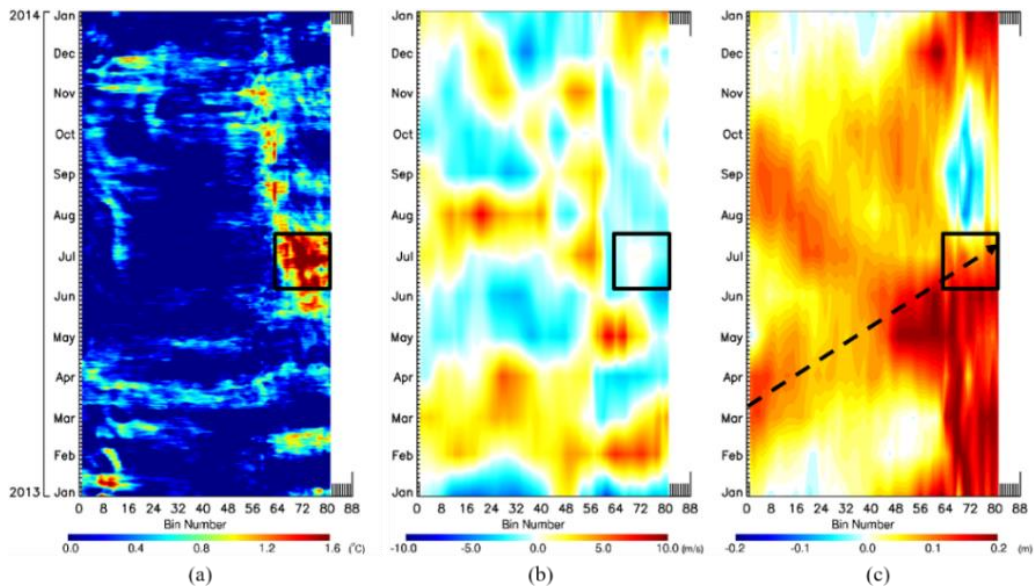


**Fig. 6.** Hovmöller diagram (a) SST, (b) zonal wind anomaly, and (c) SLA in 2013. Bin 1-55 shows the Indian Ocean region, bin 56-62 the coastal area of Sumatra, and bin 63-81 the coastal area of Java -Nusa Tenggara. The dashed black arrow in fig. c shows the direction of the downwelling Kelvin wave propagation. The black box indicates the 2013 MHW period.

Easterly wind anomaly generally causes upwelling Kelvin wave that cools SST (Drushka et al. 2010). However, in the southern region of Java to Nusa Tenggara, the MHW has a hot SST anomaly. We suspect that the SST warm anomaly is caused by a long-distance process, namely the downwelling Kelvin wave propagation. From April to October (Fig. 7, red line), a negative Indian Ocean Dipole (IOD) value is detected. A negative IOD causes an increase in westerly winds blowing along the equator of the Indian Ocean so that it can trigger a downwelling Kelvin wave (Fig. 8b). Although the IOD value had started to return to normal at the MHW incident, the propagation of the downwelling Kelvin wave is still going on and affects the southern Java-Nusa Tenggara region. This may cause an increase of the SST anomaly in the area.

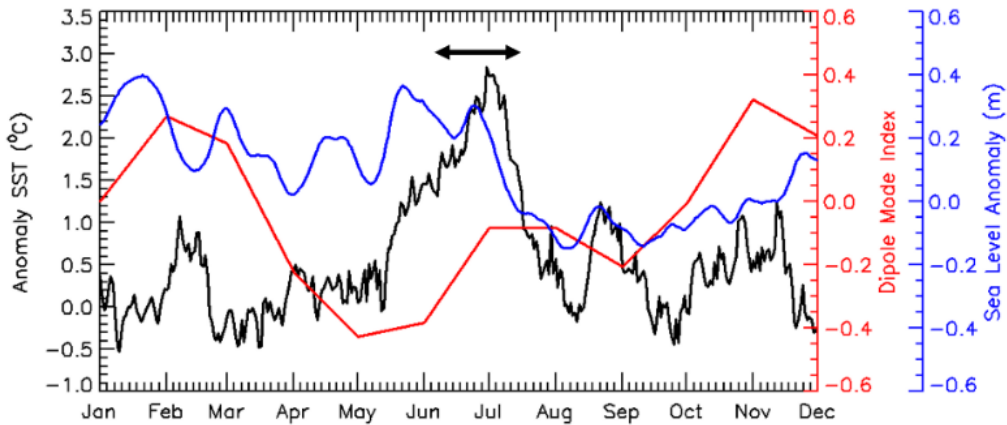


**Fig. 7.** Temporal variation between SST anomalies (black line) at  $8^{\circ}\text{S}$  to  $9^{\circ}\text{S}$ ,  $112^{\circ}\text{E}$  to  $115^{\circ}\text{E}$  (black box in Fig. 2) with Dipole Mode Index (DMI) (red line) and SLA (blue line) during 2013. The black arrow shows the 2013 MHW period.

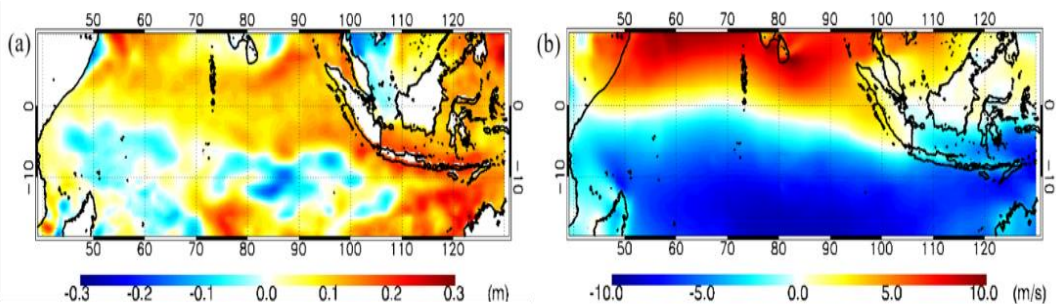


**Fig. 8.** Amplitude map of (a) SLA and (b) zonal wind during 2013 MHW.

The indication of the downwelling Kelvin wave is depicted on the Hovmöller SLA diagram (Fig. 6c). Positive SLA values are identified from bin 1 to 88 during March-August. The highest positive value  $>0.2$  m occurred in April-June at bin 48-70, i.e., from the central Indian Ocean region to the southern coast of Java. Meanwhile, for the coastal areas of Java-Nusa Tenggara (bin 64-81), the positive SLA value is consistently seen from January to the end of August.

In addition, the SLA time series (Fig. 7, blue line) shows consistent positive values during the 2013 MHW period. The highest SLA values reach up to 0.3 m on 24-25 June, and as MHW end, the SLA values decrease to -0.03 m. From the SLA map during 2013 MHW (Fig. 8a), positive SLA values are distributed throughout the MHW area, both inshore and offshore areas. The value of SLA on the coast ranges from 0.2 to 0.3 m, higher than the SLA in the offshore, which has a value of 0.1-0.2 m.



The positive SLA value up to 0.3 m indicates the downwelling Kelvin wave and is the dominant mechanism in causing 2013 MHW. Based on Kutsuwada and McPhaden (2002), downwelling Kelvin wave can suppress the thermocline by several meters, raising sea level elevation by several centimeters and increasing the SST above the thermocline. As happened in Northern Australia, the propagation of sea Kelvin waves triggered by La Niña causes the warm SST anomaly (Benthuisen et al. 2014). In addition, the Kelvin wave also affected the phenomenon of warm SST on the coast of Angola-Namibia in 1995, known as the Benguela Niño. These Kelvin waves are triggered by Atlantic tropical wind anomalies (Gammelsrød et al. 1998). On the other hand, a negative SLA value indicates the upwelling Kelvin wave because the upwelling Kelvin wave propagation induces a negative SLA anomaly along the southern coast of Sumatra-Java (Li et al. 2018).

From these results, we found that the propagation of the downwelling Kelvin wave is one of the driving mechanisms that caused the 2013 MHW in Southern Java-Nusa Tenggara besides the shortwave radiation. However, it should be noted that this is case study research so that the mechanism obtained only applies to the case of the 2013 MHW event and cannot be generalized for the other MHW cases. Each MHW event will have a different mechanism variation in each case, depending on the location and time of the incident. Holbrook et al. (2020) stated that the mechanisms that affect MHW vary greatly, influenced by local scales, large-scale modulation of climate variability or teleconnection mechanisms such as planetary wave propagation in the atmosphere or ocean. So, the mechanism of one MHW case cannot be generalized as the cause of another MHW case. As an example, the results of the driving mechanism for the 2013 MHW are different from the mechanism for 1998 and 2016 MHWs in Southern Java. Based on Iskandar et al. (2021), 1998 and 2016 MHW in South Java occurred in the austral winter months, lasted during the austral spring, disappeared in the early austral winter, and lived with intense El Niño events. During this El Niño period, the Australian monsoon weakens. These two things are most likely the cause of the 1998 and 2016 MHWs in South Java.

#### 4. CONCLUSIONS

We have found MHW events in the seas of the southern Java-Nusa Tenggara in 2013, which occurs from 8 June to 14 July with an extreme category. The metric parameters of this MHW have duration, maximum intensity, average intensity, and area with values of 37 days, 2.60°C, 1.83°C, and  $36.53 \times 10^4 \text{ km}^2$ , respectively. The highest anomaly value occurs on the southern coast of East Java at 2.75°C. The SST warm anomaly occurs due to the downwelling Kelvin wave because of the westerly wind blowing along the equatorial Indian Ocean during the negative IOD. Downwelling Kelvin wave is identified from the positive value of SLA that occurred during the MHW incident. In addition, shortwave radiation may also play a role in increasing SST in Southern Java-Nusa Tenggara due to heat entering the ocean. Related mechanisms about MHW are an interesting subject for future studies, so further understanding of these MHW mechanisms is needed by adding large-scale climate variability analyses such as IOD, ENSO, and MJO.

#### ACKNOWLEDGEMENTS

The authors would like to thank you for the support from PUSDIKLAT BMKG and Diponegoro University. CCMP Version-2.0 vector wind analyses and REMSS OISST data are produced by Remote Sensing Systems available at [www.remss.com](http://www.remss.com). Sea level anomaly is provided by CMEMS available at <https://resources.marine.copernicus.eu/products>.

Latent heat flux, sensible heat flux, and shortwave radiation are provided by ERA5 available at <https://cds.climate.copernicus.eu/cdsapp#!/dataset/reanalysis-era5-single-levels?tab=form>.

## REFERENCES

- Amaya, D.J., Miller, A.J., Xie, S.P. and Kosaka, Y. (2020). Physical drivers of the summer 2019 North Pacific marine heatwave. *Nature Communications*, 11(1), pp.1–9. Available from: <http://dx.doi.org/10.1038/s41467-020-15820-w>.
- Benthuisen, J., Feng, M. and Zhong, L. (2014). Spatial patterns of warming off Western Australia during the 2011 Ningaloo Niño: Quantifying impacts of remote and local forcing. *Continental Shelf Research*, 91, pp.232–246. Available from: <http://dx.doi.org/10.1016/j.csr.2014.09.014>.
- Benthuisen, J.A., Oliver, E.C.J., Feng, M. and Marshall, A.G. (2018). Extreme Marine Warming Across Tropical Australia During Austral Summer 2015–2016. *Journal of Geophysical Research: Oceans*, 123(2), pp.1301–1326.
- Bond, N.A., Cronin, M.F., Freeland, H. and Mantua, N. (2015). Causes and impacts of the 2014 warm anomaly in the NE Pacific. *Geophysical Research Letters*, 42(9), pp.3414–3420.
- Collins, M., Sutherland, M., Bouwer, L., Cheong, S.-M., Frölicher, T., Jacot Des Combes, H., Koll Roxy, M., Losada, I., McInnes, K., Ratter, B., Rivera-Arriaga, E., Susanto, R. D., Swingedouw, D., and Tibig, L. (2019), Extremes, Abrupt Changes and Managing Risks, In: Pörtner, H.-O., Roberts, D. C., Masson-Delmotte, V., Zhai, P., Tignor, M., Poloczanska, E., Mintenbeck, K., Alegria, A., Nicolai, M., Okem, A., Petzold, J., Rama, B., and Weyer, N. M. (eds.) *IPCC Special Report on the Ocean and Cryosphere in a Changing Climate*, in press.
- Drushka, K., Sprintall, J., Gille, S.T. and Brodjonegoro, I. (2010). Vertical structure of Kelvin waves in the Indonesian throughflow exit passages. *Journal of Physical Oceanography*, 40(9), pp.1965–1987.
- Frölicher, T.L., Fischer, E.M. and Gruber, N. (2018). Marine heatwaves under global warming. *Nature*, 560(7718), pp.360–364.
- Gammelsrød, T., Bartholomae, C.H., Boyer, D.C., Filipe, V.L.L. and O’Toole, M.J. (1998). Intrusion of warm surface water along the Angolan-Namibian coast in February-March 1995: The 1995 Benguela Niño. *South African Journal of Marine Science*, 7615(19), pp.41–56.
- Hobday, A.J., Alexander, L. V., Perkins, S.E., Smale, D.A., Straub, S.C., Oliver, E.C.J., Benthuisen, J.A., Burrows, M.T., Donat, M.G., Feng, M., Holbrook, N.J., Moore, P.J., Scannell, H.A., Sen Gupta, A. and Wernberg, T. (2016). A hierarchical approach to defining marine heatwaves. *Progress in Oceanography*, 141, pp.227–238.
- Hobday, A. J., Oliver, E. C., Sen Gupta, A., Benthuisen, J. A., Burrows, M. T., Donat, M. G., Holbrook, N. J., Moore, P. J., Thomsen, M. S., Wernberg, T., and Smale, D. A. (2018). Categorizing and naming marine heatwaves. *Oceanography*, 31(2), 162-173.
- Hoegh-Guldberg, O., Cai, R., Poloczanska, E. S., Brewer, P. G., Sundby, S., Hilmi, K., Fabry, V. J., and Jung, S. (2014), The Ocean, In: Barros, V. R., Field, C. B., Dokken, D. J., Mastrandrea, M. D., Mach, K. J., Bilir, T. E., Chatterjee, M., Ebi, K. L., Estrada, Y. O., Genova, R. C., Girma, B., Kissel, E. S., Levy, A. N., MacCracken, S., Mastrandrea, P. R., and White, L. L. (eds.) *Climate Change 2014: Impact, Adaptation, and Vulnerability. Part B: Regional Aspects. Contribution of Working Group II to the Fifth Assessment Report of the Intergovernmental Panel on Climate Change*, Cambridge University Press, Cambridge, United Kingdom and New York, 1655-1731.
- Holbrook, N.J., Sen Gupta, A., Oliver, E.C.J., Hobday, A.J., Benthuisen, J.A., Scannell, H.A., Smale, D.A. and Wernberg, T. (2020). Keeping pace with marine heatwaves. *Nature Reviews Earth and Environment*, 1(9), pp.482–493. Available from: <http://dx.doi.org/10.1038/s43017-020-0068-4>.
- Iskandar, M.R., Ismail, M.F.A., Arifin, T. and Chandra, H. (2021). Marine heatwaves of sea surface temperature off south Java. *Heliyon*, 7(12).
- Ismail, M.F.A. (2021). Characteristics of Marine Heatwaves off West Sumatra Derived from High-Resolution Satellite Data. *Journal of Human University Natural Sciences*, 48(6), pp.130–136.
- Krishnan, A.P., Roy, S.D., George, G., Srivastava, R.C., Anand, A., Kaliyamoorthy, M., Vikas, N. and Soundararajan, R. (2011). Elevated sea surface temperature during May 2010 induces mass bleaching of corals in the Andaman Published by: Current Science Association Stable URL: <http://www.jstor.org/stable/24069723> Elevated sea surface temperature duri. *Current Science*, 100(1), pp.111–117.

- Kutsuwada, K. and McPhaden, M. (2002). Intraseasonal variations in the upper equatorial Pacific ocean prior to and during the 1997-98 El Niño. *Journal of Physical Oceanography*, 32(4), pp.1133–1149.
- Li, S., Wei, Z., Susanto, R.D., Zhu, Y., Setiawan, A., Xu, T., Fan, B., Agustadi, T., Trenggono, M. and Fang, G. (2018). Observations of intraseasonal variability in the Sunda Strait throughflow. *Journal of Oceanography*, 74(5), pp.541–547. Available from: <https://doi.org/10.1007/s10872-018-0476-y>.
- Le Nohaïc, M., Ross, C.L., Cornwall, C.E., Comeau, S., Lowe, R., McCulloch, M.T. and Schoepf, V. (2017). Marine heatwave causes unprecedented regional mass bleaching of thermally resistant corals in northwestern Australia. *Scientific Reports*, 7(1), pp.1–11.
- Mills, K. E., Pershing, A. J., Brown, C. J., Chen, Y., Chiang, F.-S., Holland, D. S., Lehuta, S., Nye, J. A., Sun, J. C., Thomas, A. C., and Wahle, R. A. (2013). Fisheries management in a changing climate: Lessons from the 2012 ocean heat wave in the Northwest Atlantic. *Oceanography*, 26(2), 191-195.
- Oliver, E.C.J., Donat, M.G., Burrows, M.T., Moore, P.J., Smale, D.A., Alexander, L. V., Benthuisen, J.A., Feng, M., Sen Gupta, A., Hobday, A.J., Holbrook, N.J., Perkins-Kirkpatrick, S.E., Scannell, H.A., Straub, S.C. and Wernberg, T. (2018). Longer and more frequent marine heatwaves over the past century. *Nature Communications*, 9(1), pp.1–12. Available from: <http://dx.doi.org/10.1038/s41467-018-03732-9>.
- Oliver, E.C.J., Benthuisen, J.A., Bindoff, N.L., Hobday, A.J., Holbrook, N.J., Mundy, C.N. and Perkins-Kirkpatrick, S.E. (2017). The unprecedented 2015/16 Tasman Sea marine heatwave. *Nature Communications*, 8(May), pp.1–12. Available from: <http://dx.doi.org/10.1038/ncomms16101>.
- Pearce, a, Lenanton, R., Jackson, G., Moore, J., Feng, M. and Gaughan, D. (2011). *The “marine heat wave” off Western Australia during the summer of 2010/11. Fisheries Research Report No. 222. Department of Fisheries, Western Australia.*
- Perez, E., Ryan, S., Andres, M., Gawarkiewicz, G., Ummenhofer, C.C., Bane, J. and Haines, S. (2021). Understanding physical drivers of the 2015/16 marine heatwaves in the Northwest Atlantic. *Scientific Reports*, 11(1), pp.1–11. Available from: <https://doi.org/10.1038/s41598-021-97012-0>.
- Rhein, M., Rintoul, S. R., Aoki, S., Campos, E., Chambers, D., Feely, R. A., Gulev, S., Johnson, G. C., Josey, S. A., Kostianoy, A., Mauritzen, C., Roemmich, D., Talley, L. D., and Wang, F. (2013), Observation: Ocean, In: Stocker, T. F., Qin, D., Plattner, G.-K., Tignor, M., Allen, S. K., Boschung, J., Nauels, A., Xia, Y., Bex, V., and Midgley, P. M. (eds.) *Climate change 2013: The Physical Science Basis Contribution of Working Group I to the Fifth Assessment Report of the Intergovernmental Panel on Climate Change*, Cambridge University Press, Cambridge, United Kingdom and New York.
- Rodrigues, R.R., Taschetto, A.S., Sen Gupta, A. and Foltz, G.R. (2019). Common cause for severe droughts in South America and marine heatwaves in the South Atlantic. *Nature Geoscience*, 12(8), pp.620–626.
- Schlegel, R.W., Oliver, E.C.J., Hobday, A.J. and Smit, A.J. (2019). Detecting Marine Heatwaves With Sub-Optimal Data. *Frontiers in Marine Science*, 6(November), pp.1–14.
- Wirasatriya, A., Kawamura, H., Koch, M. and Helmi, M. (2019a). Satellite-borne detection of high diurnal amplitude of sea surface temperature in the seas west of the Tsugaru Strait, Japan, during Yamase wind season. *Journal of Oceanography*, 75(1), pp.23–36.
- Wirasatriya, A., Sugianto, D.N., Helmi, M., Setiawan, R.Y. and Koch, M. (2019b). Distinct Characteristics of SST Variabilities in the Sulawesi Sea and the Northern Part of the Maluku Sea during the Southeast Monsoon. *IEEE Journal of Selected Topics in Applied Earth Observations and Remote Sensing*, 12(6), pp.1763–1770.



## SPATIAL VARIATION OF NO<sub>2</sub> LEVELS DURING THE COVID-19 PANDEMIC IN THE BALI TOURISM AREA

I Nyoman SUNARTA<sup>1</sup>  and Moh SAIFULLOH<sup>2</sup> 

DOI: 10.21163/GT\_2022.171.11

### ABSTRACT:

NO<sub>2</sub> levels that exceed quality standards will negatively impact the environment and human health. The purpose of this study was to determine changes in the content of NO<sub>2</sub> temporally. The method used is descriptive quantitative, with data analysis using Geographic Information Systems (GIS) and remote sensing data extraction using Google Earth Engine (GEE). The remote sensing data used is Sentinel 5p - TROPOMI whose sensors have the ability to detect air pollution. The results of this study indicate the occurrence of different variations during the Covid-19 Pandemic in the Bali Tourism Area, decreasing or increasing NO<sub>2</sub> levels. The decrease in NO<sub>2</sub> levels in the air is due to reduced human activities outside the home due to the implementation of the Indonesian Government's policies in the form of Large-Scale Restrictions, Work From Home (WFH), and the religious traditions of Hindus in Bali (*Nyepi* Day on March 25, 2020). NO<sub>2</sub> levels increase again after a long holiday in Indonesia on November-December 2020, due to the large number of tourists visiting Bali Province. The arrival of these tourists increases human activities around the tourism area, such as opening hotels, restaurants, and means of land, sea, and air transportation. Tourism areas tend to have high building density and population. Thus, making green open space low. Whereas green open space is very useful in absorbing air pollution, it is recommended to add green open space or revegetation in every hotel building to maintain good air quality.

**Key-words:** Covid-19, Tourism, NO<sub>2</sub>, Google Earth Engine, Bali.

### 1. INTRODUCTION

Bali is known as a world tourist destination with an increasing number of tourists. From 2007 to 2019, the number of tourists increased by an average of 11.86%. The number of tourists in 2020 experienced a very drastic decline, namely by 82.96% (BPS Province of Bali, 2020). The decline in the number of tourists was due to the Covid-19 virus outbreak which paralyzed the Bali tourism sector, even the tourism sector throughout the world. The impact of Covid-19 has caused most tourism infrastructure businesses to close since early April 2020 and the layoff of employees in the tourism sector has increased (Nurudin et al., 2020).

The World Health Organization (WHO) has announced that Covid-19 is a world pandemic resulting in a lockdown for several countries including Italy, China, the UK, and other countries. Indonesia does not implement Lockdown but rather a Large-Scale Social restriction (PSBB) and Work From Home (WFH). The implementation of PSBB is carried out in the Covid-19 red zone areas, one of which is Jakarta. The implementation of WFH is implemented in all regions in Indonesia, one of which is the Province of Bali. The implementation of these two policies reduces human activities outside the home so that it is hoped that it will be able to suppress cases of Covid-19 transmission. The Covid-19 outbreak in addition to having a detrimental impact also has a positive impact, namely reducing air pollution. This is due to the decreasing number of human activities in tourism and other activities. One of the activities that cause air pollution is a motorized vehicle which is an accommodation in human activities. As much as 70% of air pollution is caused by transportation activities (Arifin and Sukoco, 2009). Budiyanto (2011) states that motor vehicle fumes make a major contribution to air quality pollution.

---

<sup>1</sup> Faculty of Tourism, Udayana University, Indonesia, [nyoman\\_sunarta@unud.ac.id](mailto:nyoman_sunarta@unud.ac.id)

<sup>2</sup> Spatial Data Infrastructure Dev. Center, Udayana University, Indonesia, [moh9saifulloh@gmail.com](mailto:moh9saifulloh@gmail.com)

Gorglulu (2018) stated that air pollution contains corrosive exhaust gases, namely NO<sub>x</sub>. NO<sub>x</sub> gas contains 2 gases, namely nitrogen monoxide (NO) and nitrogen dioxide (NO<sub>2</sub>). The transportation sector accounts for pollutant NO<sub>2</sub> by 69% in urban areas, followed by industry and households (Mukono A, 2006). The level of NO<sub>2</sub> in the air if it is too high above the Air Pollution Standard Index (ISPU) 100 will have a negative impact on human health (Prayudi et al, 2010).

Actually, given the current digital advance, the NO<sub>2</sub> data can be obtained via satellite, known also as the remote sensing data. The satellite that plays a role in monitoring air quality is Sentinel 5-P. Sentinel 5-P has a mission to monitor air quality, climate, and the ozone layer on a global scale from 2017 to 2023, thereby providing better data to support research on NO<sub>2</sub> (Berger et al, 2012). As the first imaging spectrometer to provide global data at the moderate spatial resolution, TROPOMI has significant advantages over previous sensors in resolution (7 x 3.5 km) and the number of observations with low cloud cover (Guanter et al, 2015). The use of remote sensing data, derived from Sentinel-5P since the Covid-19 incident, for air quality monitoring, is often carried out by researchers around the world. The NO<sub>2</sub> species originating from Sentinel-5P, has not been widely studied in Indonesia, especially Bali Province during the Covid-19 pandemic, so that is the reason for researchers to explore monthly NO<sub>2</sub> satellite data during 2020.

## 2. STUDY AREA

The research was conducted in Bali Province (**Fig.1**) from January to December 2020. The province of Bali consists of 8 regencies (Badung, Tabanan, Jembarana, Buleleng, Karangasem, Bangli, Gianyar, Klungkung) and 1 City (Denpasar). The province of Bali is geographically located between 360000 mE and 910000 mN to 220000 mE and 9020000 mN. Each district and city has a tourist attraction and tourism infrastructure, but tourism sector activities are more dominant in the coastal part of Bali due to the natural potential, namely beach panoramas.

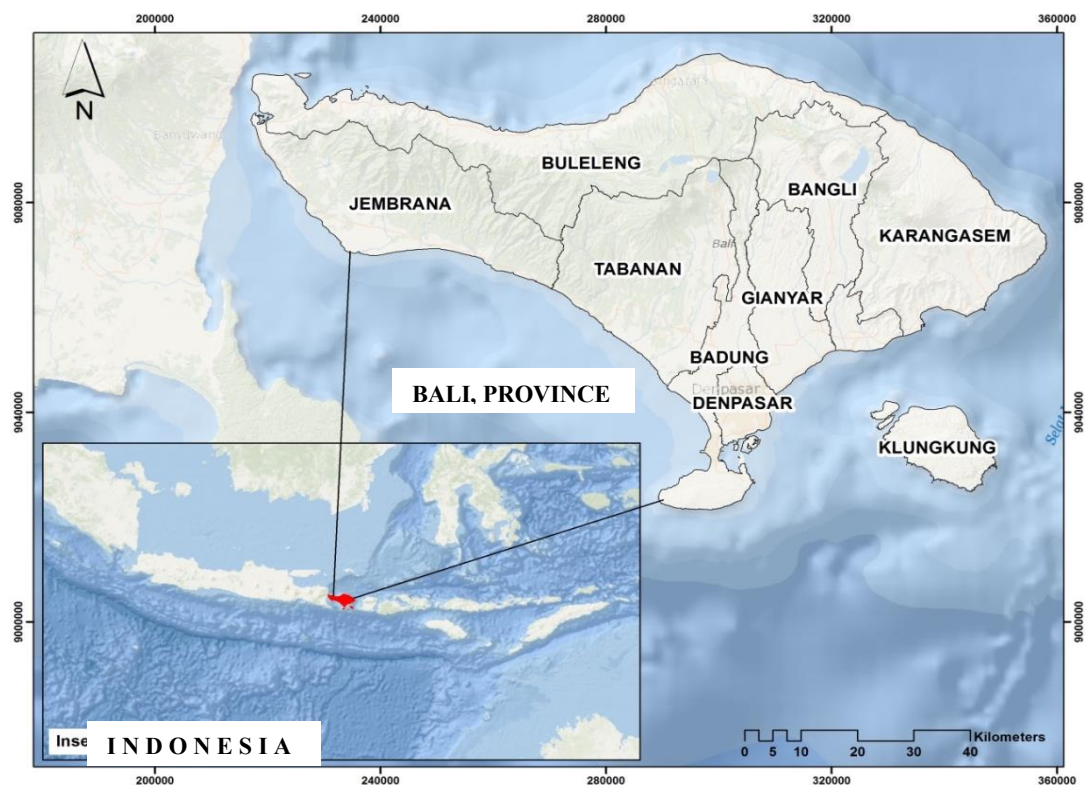


**Fig. 1.** Research Locations in Bali Province-Indonesia (Located on the World Geodetic System Projection (WGS) 1984 - Universal Transverse Mercator (UTM) 50 South Zone.

### 3. DATA AND METHODS

#### 3.1. Remote Sensing Data

The main tool that will be used in this research is Google Earth Engine (GEE). Google Earth GEE is a platform cloud-based spatial data computing developed by Google, which offers a worldwide analysis of environmental data. GEE is used to analyze satellite data to produce the distribution of pollutant concentrations. GIS software (ArcGIS 10.6) is used to process spatial data and map layout.

The processed data is TROPospheric Monitoring Instrument (TROPOMI) data brought by the Copernicus Sentinel-5 Precursor satellite. The instrument, the single payload of the Sentinel-5P spacecraft, uses passive remote sensing techniques to achieve its goal by measuring, at the Top Of Atmosphere (TOA), the solar radiation reflected and emitted from the earth. The instrument operates in a push sweep (non-scan) configuration, with a sweep width of ~2600 km at the earth's surface. The primary objective of the Copernicus Sentinel-5P mission is to perform atmospheric measurements with high spatio-temporal resolution, which will be used for air quality, ozone, UV radiation, and climate monitoring & forecasting. The satellite was successfully launched on October 13, 2017, from the Plesetsk cosmodrome in Russia. The TROPOMI instrument combines the power of SCIAMACHY, OMI, and advanced technology to provide observations with performances that today's instruments cannot meet in space. The performance of current orbital instruments is surpassed in terms of sensitivity, spectral resolution, spatial resolution, and temporal resolution (European Space Agency, 2014). The Nitrogen Dioxide data was released on 10 July 2018 and is accessible on the GEE platform. NO<sub>2</sub> in GEE has a spatial resolution of 0.01° or 1.11 km per pixel. In this study, Sentinel-5P satellite data was used to monitor changes in NO<sub>2</sub> pollutants during the Covid-19 pandemic in Bali Province. The variable of this research is the level of NO<sub>2</sub> extracted from the Sentinel 5-P Satellite Remote Sensing Data by cloud computing through the GEE platform. Utilization of Sentinel 5-P satellite data for air quality monitoring has been carried out by (Zheng et al, 2019; Lorente et al, 2019; Mahato et al, 2020; Otmami et al, 2020; Shikwambana et al, 2020; Goldberg et al, 2020; Sanningrahi et al, 2021) in several countries, including China, India, Paris, and Africa. NO<sub>2</sub> monitoring has also been previously studied by (Rushayati et al, 2020) in the Greater Jakarta Region of Indonesia.

#### 3.2 Data Analysis

Sentinel 5P TROPOMI satellite data is available in high temporal resolution (daily). Therefore, it is necessary to filter by data acquisition date. The date range chosen is January 2020 to December 2020. The time range was chosen to determine changes in NO<sub>2</sub> gas concentration before WFH was implemented when WFH was implemented, and after New Normal was implemented during the Covid-19 Pandemic in Bali Province. The result of this filtering process is a twelve-month temporal composite image for each pollutant gas NO<sub>2</sub>. Each data is then clipped to get the area according to the focus area of the study, namely the Province of Bali. This process is carried out on the GEE platform. The resulting data is then exported for later download so that it can be opened in GIS software (ArcGIS 10.4). Furthermore, the results of data extraction for each pixel are compared both spatially and temporally from January 2020 to December 2020. To get the trend of changes in NO<sub>2</sub> levels for each district, an overlay is carried out on the district boundaries in Bali Province.

### 4. RESULTS AND DISCUSSIONS

#### 4.1. Data Analysis on GEE

Data analysis in GEE uses the programming language JavaScript. Data analysis was carried out by importing Sentinel-5P NRTI NO<sub>2</sub> data: Near Real-Time Nitrogen Dioxide. Next, filter date and average NO<sub>2</sub> data for each month during 2020 and carried out masking is image based on research boundaries so that levels are obtained for the Province of Bali. **Fig. 2** is a visualization of the dashboard GEE. The utilization of GEE for data analysis makes it easy for users including a fast process, does not require high computer specifications, and saves computer memory because the data

analysis process is carried out with cloud computing by utilizing Google servers. It displays a dashboard GEE on the analysis of NO<sub>2</sub> levels during 2020.

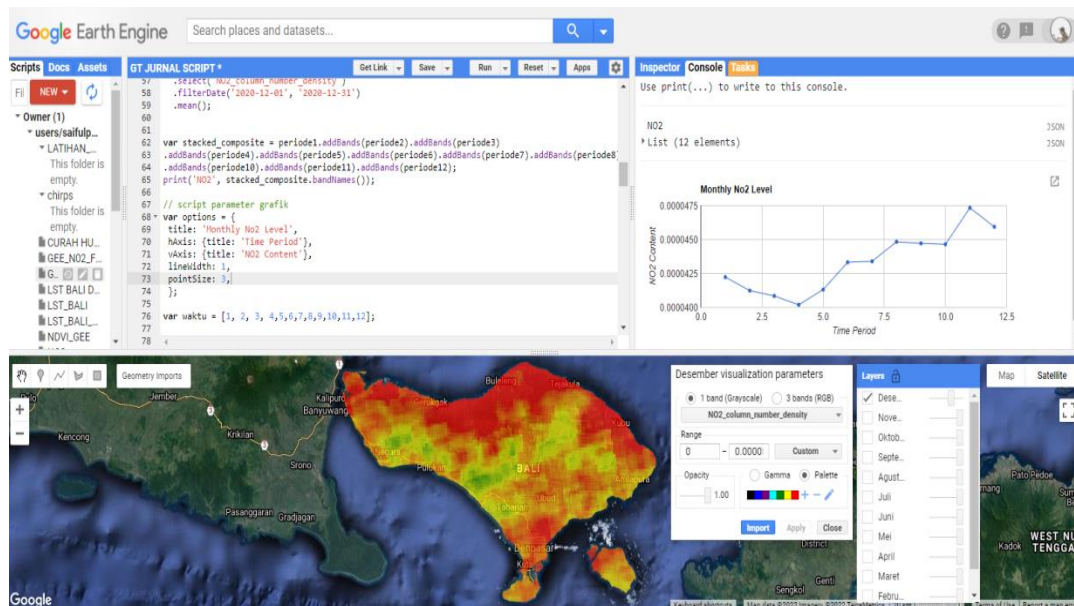


**Fig. 2.** Google Earth Engine Dashboard: Data Analysis by cloud computing platform.

### 4.2. Spatial Distribution of NO<sub>2</sub> Levels

The results of NO<sub>2</sub> data extraction show different levels of levels during 2020 due to the Covid-19 pandemic (Fig. 3). In January and February, the Government has not implemented the WFH policy, because the Covid-19 outbreak has not yet entered Indonesian territory. The condition of NO<sub>2</sub> levels was still relatively high but continued to decline until April 2020. The decrease in NO<sub>2</sub> levels was due to the WFH policy during March-June 2020. The Decrease in NO<sub>2</sub> lowest levels occurred in March and April 2020. Such conditions because on March 11, 2020, WHO has announced that Covid-19 is a world pandemic so that tourism activities and other activities are limited. March 25, 2020, is *Nyepi* Day for Hindus in Bali, so there is no human activity outside the house for 24 hours. In July, the Bali Provincial Government announced the Policy New Normal and the opening of several tourist attractions, causing human activities to begin to increase. The increase in NO<sub>2</sub> levels also occurred in Java (Zulkarnain, 2020), (Anggraini, 2020) in line with the implementation of the New Normal and the easing of Large-Scale Social Restrictions (PSBB). The graph of NO<sub>2</sub> levels starting from July to peaking in November continues to experience an increase in NO<sub>2</sub> levels.

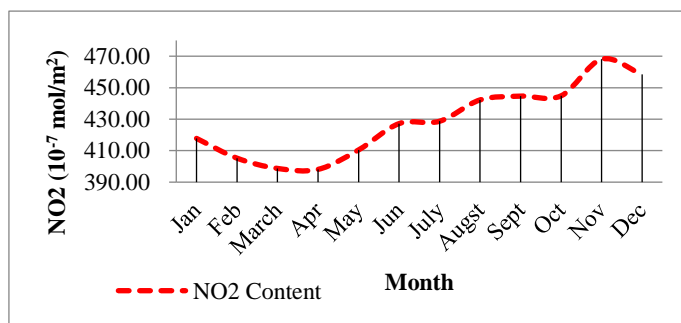


**Fig. 3.** Graph of Variability of NO<sub>2</sub> Levels During 2020: extraction from Sentinel 5P remote sensing data.



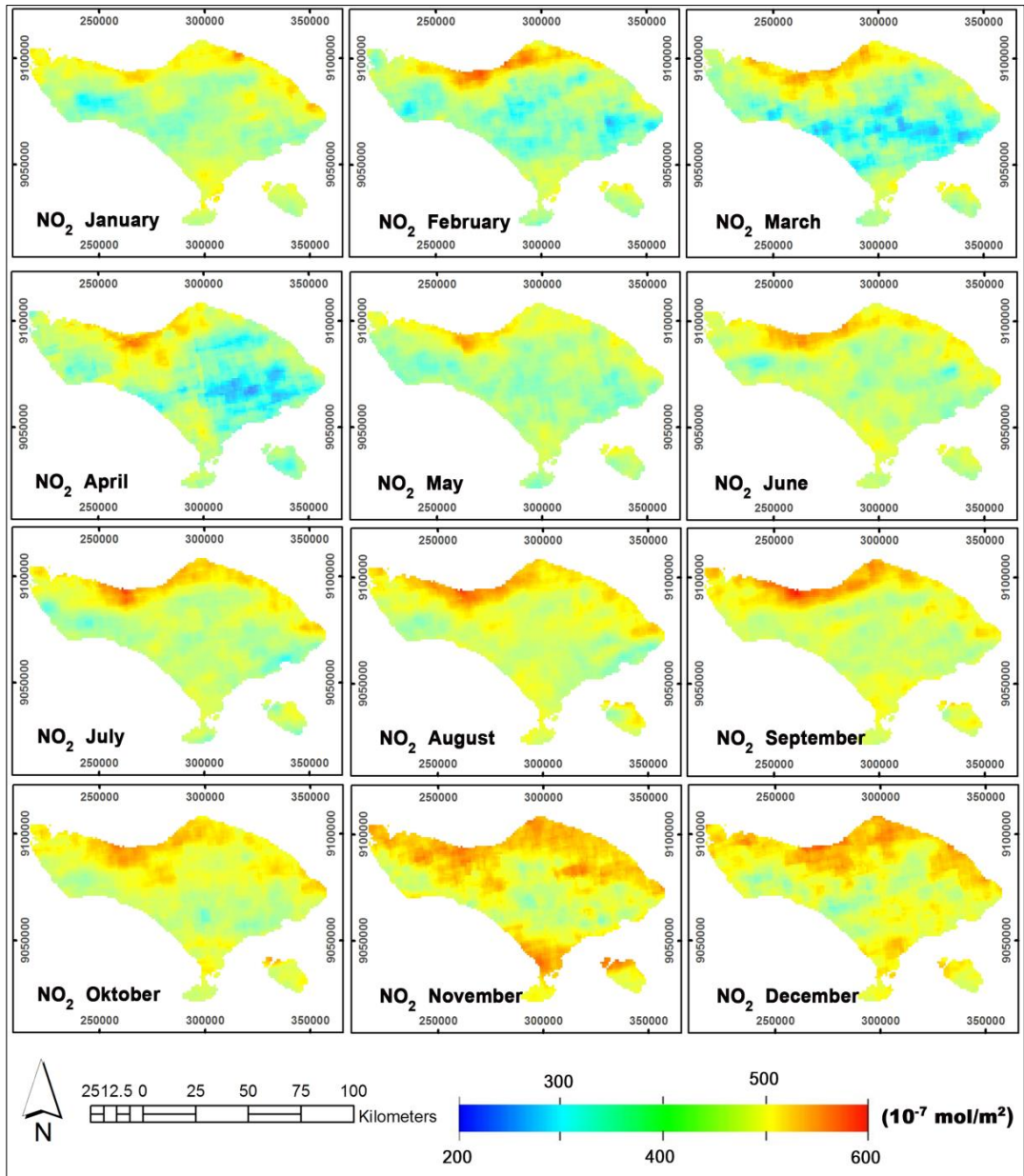


**Fig. 4.** Spatial Distribution of Monthly NO<sub>2</sub> Levels, During 2020.

**Fig. 4** shows the spatial-temporal changes in NO<sub>2</sub> levels before the Work From Home (WFH) policy was implemented (January and February 2020), when WFH was applied (March-June 2020), after the WFH or New Normal policy (July-December 2020).

Prior to WFH, spatially on the map showed the dominance of light blue, green, yellow, and orange. When applied WFH spatially on a map showing variations of the new color dark blue and orange color with shrinking lead to a decline in levels of NO<sub>2</sub>. Once set policy, the New Normal dark blue color on the map began to disappear and be replaced by orange, indicating increased levels of NO<sub>2</sub>. Spatially kadaNO<sub>2</sub> highest are located throughout the coastal province of Bali, which is the center of tourism activities and other activities in the province of Bali.

### 4.3 NO<sub>2</sub> Level Per District

**Table 1** shows the changes in NO<sub>2</sub> for each district in the province of Bali. The average levels of NO<sub>2</sub> were 425.32 10<sup>-7</sup> mol/m<sup>2</sup> were found to be evenly distributed throughout the County and City in the province of Bali. Levels of NO<sub>2</sub> low of 344.74 10<sup>-7</sup> mol/m<sup>2</sup> contained in April in Gianyar Regency. The highest levels of NO<sub>2</sub> reaches 512.62 10<sup>-7</sup> mol/m<sup>2</sup> contained in November in the city of Denpasar. **Fig. 5** shows changes in NO<sub>2</sub> levels in each District in Bali Province in 2020. The pattern of increase and decrease in the graph is relatively the same for each Regency, except for Buleleng Regency which shows NO<sub>2</sub> levels higher than January-December 2020. This is presumably due to the existence of tourism activities in the coastal part of the Buleleng Regency and the influence of land transportation on the Mengwitani-Singaraja route.

**Table 1.**

**NO<sub>2</sub> Levels of Each Regency in Bali Province in 2020.**

Average Nitrogen Dioxide Level (10 <sup>-7</sup> mol/m <sup>2</sup> ) in 2020												
Regency	Jan	Feb	Mar	Apr	May	Jun	Jul	Aug	Sep	Okt	Nov	Dec
Badung	416.56	394.10	378.12	395.29	399.95	420.25	419.88	435.41	434.60	428.03	459.86	454.34
Bangli	418.27	399.70	379.30	355.52	409.08	419.49	424.17	437.67	434.92	442.12	481.74	443.69
Buleleng	441.91	453.57	455.92	449.02	441.24	454.01	462.80	476.92	478.10	477.10	494.04	494.68
Denpasar	455.52	435.91	433.22	412.18	427.60	439.23	425.33	433.30	450.90	447.83	512.62	475.33
Gianyar	414.51	393.30	361.79	344.74	402.92	415.38	416.67	421.26	432.64	425.30	441.41	451.93
Jembrana	392.41	390.31	396.93	406.58	392.20	417.53	409.79	425.17	439.70	433.31	459.94	439.47
Karangasem	424.30	383.72	374.16	365.74	403.55	421.46	424.27	435.59	434.10	441.39	461.92	463.73
Klungkung	415.33	406.58	398.79	373.71	407.46	414.25	412.35	427.65	437.81	431.14	465.25	454.12
Tabanan	393.71	372.59	365.80	398.85	393.87	415.58	416.81	432.29	423.67	432.08	441.13	427.28

Source : Sentinel 5P remote sensing data.

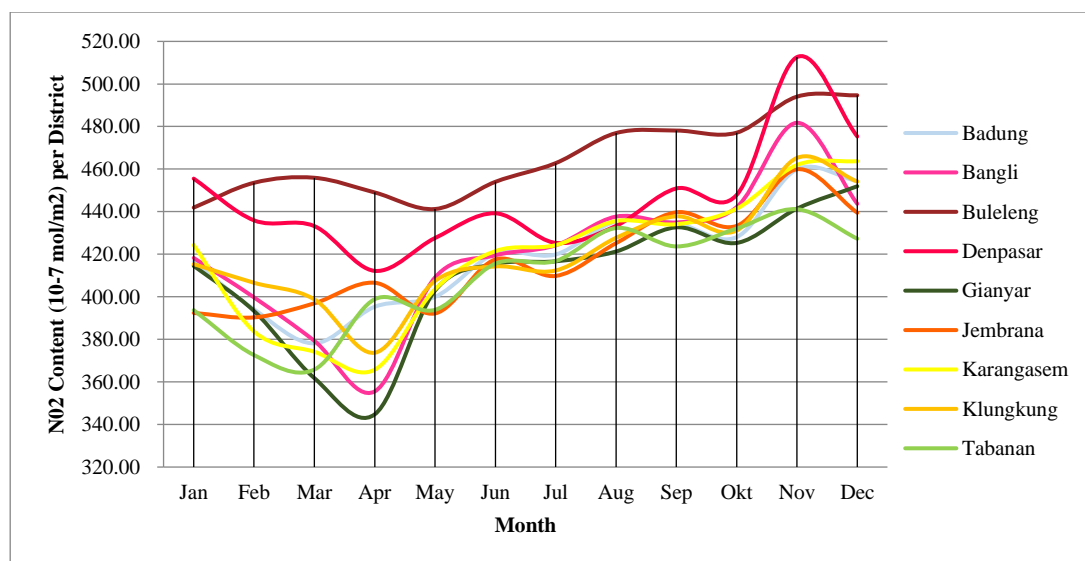


**Fig. 5.** Graph of Changes in NO<sub>2</sub> Levels for Each District in Bali Province in 2020.

## 5. DISCUSSION

Google Earth Engine is an a-based cloud platform that can be used for regional, national and global environmental data analysis. The utilization of GEE for global-scale remote sensing data analysis has been carried out by Tamiminia, 2020 while utilization on a regional scale is one of them for the identification of land cover (Novianti, 2020) and land cover changes (Wang, 2020). Earth Engine consists of catalog data used for computationally based analysis with a fast and integrated process. Earth Engine also offers an Integrated Development Environment (IDE) online for the visualization of complex spatial data using Javascript API (Gorelick, 2017). The use of GEE in this study was implemented in the calculation of the 2020 Monthly NO<sub>2</sub> levels in the Province of Bali. The results of this study indicate that the highest variability of NO<sub>2</sub> levels is in the Tourism Area.

Territorial tourism destinations include tourism areas (KP) and special tourist attraction areas (KDTWK) It has been regulated in Regional Regulation No. 3 of 2020. Pujaastawa (2016) states that tourism areas are strategic tourism areas that are the ones that are geographically located in one or more village administrative areas that have the potential for tourist attraction, accessibility, tourism facilities, and social and cultural activities of the community that support each other. The Special Tourist Attraction Area (KDTWK) is a strategic tourism area located in the geography of one or more administrative areas of 4 villages that have the potential for tourist attraction, accessibility, and limited tourism facilities as well as community social and cultural activities that support each other, but its development very limited to be more directed to the preservation of culture and the environment.

On average, tourism areas in Bali Province are spatially located along the coast of Bali Province. The tourism area in Bali Province has relatively high human activities. Because in this area there are tourist destinations, dense settlements and tourism facilities (hotels, restaurants, mini markets, etc.). The area is the center of the economy and the center of human activities in Bali Province so that the pollutants in the form of NO<sub>2</sub> levels as a result of these activities are high before the WFH policy is implemented and after the WFH/New Normal policy is implemented. However, the levels of NO<sub>2</sub> decreased with the ongoing implementation of the WFH due to the decline of human activities in the area of Bali Provincial Tourism.

**Fig. 6** shows the relationship between tourism areas and NO<sub>2</sub> levels. A high level of NO<sub>2</sub> is shown with a dark orange color. **Fig. 6** is the average level of NO<sub>2</sub> in the Sentinel 5-P image acquisition from January 1 to November 30, 2020. The data was chosen because it shows NO<sub>2</sub> levels a drastic increase compared to the previous month during 2020. Spatially, almost all tourism areas have high levels of NO<sub>2</sub> in November 2020. Accessibility such as Seririt-Singaraja Roads, Singaraja-Gilimanuk in the northern coastal area of Bali Province as well as, Gatot Subroto Roads, By Pass Ngurah Rai Roads, and Imam Bonjol Roads, Denpasar City are contributors to high levels of NO<sub>2</sub> because of the use of various land transportation. Arifin (2009) and Budianto (2011) stated that air pollution (NO<sub>2</sub>), the biggest cause is due to motorized vehicle activity on the highway. Febriani (2021) also suggested a reduction in the use of modes of transport and industrial activity during Large-Scale Social Restriction (PSBB) and WFH can degrade air quality NO<sub>2</sub>.

The high level of NO<sub>2</sub> in Bali Province spatially occurs in the center of the tourism industry. The center of the tourism industry is dominated by built-up land so it has low vegetation cover. The low area of green open space and low vegetated land cover are the causes of high levels of NO<sub>2</sub> (Rusyayati, 2020). So it is necessary to add green space, which functions as an absorber of harmful NO<sub>2</sub> levels in the air (Purwanto, 2021).

NO<sub>2</sub> levels during the Covid-19 pandemic show different variations in values. This study found that human activities have an effect on these variations. The *Nyepi* Day for Hindus in Bali, as well as the government's policy to limit activities outside the home, have caused NO<sub>2</sub> levels to decrease, and air quality to improve. This condition only occurred during March 2020. Other studies also stated that due to restrictions on human activities outside the home, NO<sub>2</sub> levels decreased (Copat et al., 2020; Berman & Ebisu, 2020; Chu et al., 2021; Paital et al., 2021). The weakness of this study is related to the short duration of time, so it cannot distinguish variations in NO<sub>2</sub> before the COVID-19 pandemic (before 2020) and when Covid-19 occurs (starting in 2020).



Because other studies stated that there was an increase in NO<sub>2</sub> concentrations before the Covid-19 pandemic, including in urban area of Klang Valley, Malaysia and Bangkok Metropolitan Thailand (Nadzir et al., 2020; Wetchayont et al., 2021).

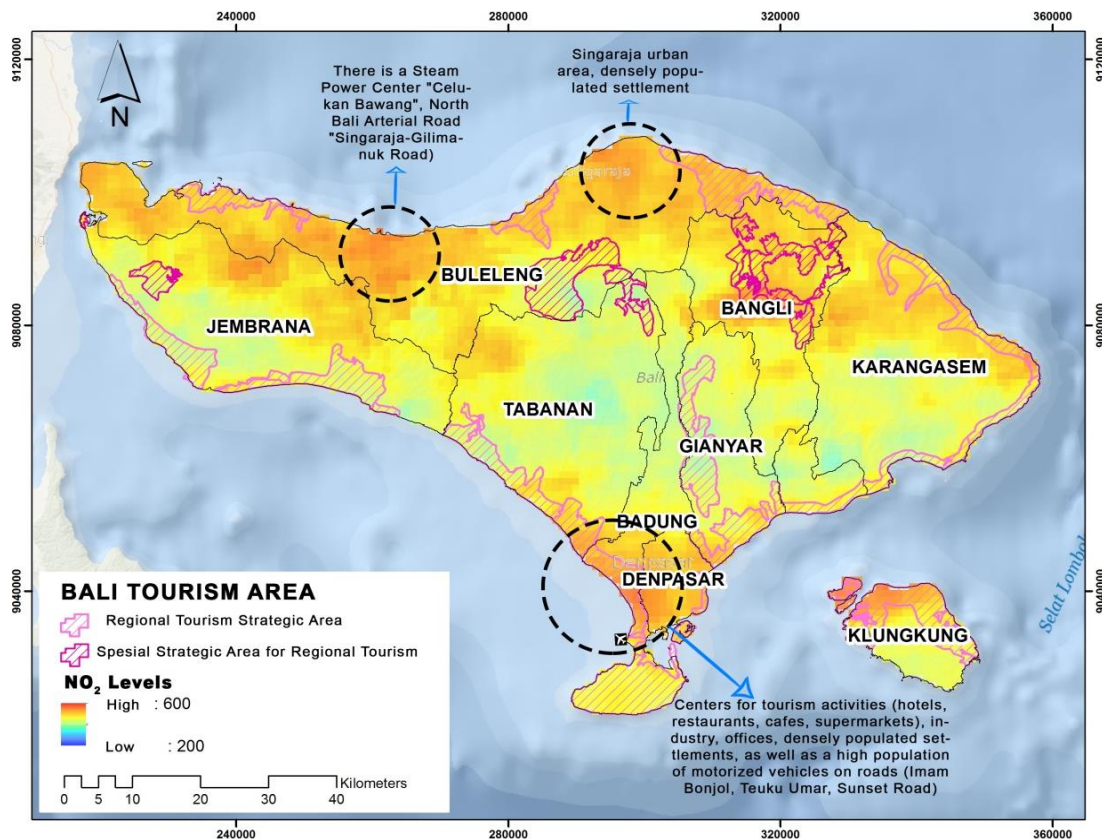


**Fig. 6.** Map Overlay: Tourism Areas with NO<sub>2</sub> Levels During 2020.  
Source: Tourist Area Map from Bali Province Spatial Plan 2009-2029.

## 6. CONCLUSIONS

Air pollution is known as an environmental problem associated with urban areas around the world. Air pollution is also an indicator of environmental quality that has an impact on public health and affects air quality in the region. Modern era, in line with the development of the physical development of cities and industrial centers, as well as the development of transportation, the air quality also undergoes changes due to air pollution. NO<sub>2</sub> emissions are affected by population density because the main source of NO, which is produced by humans is from combustion and most of the combustion is caused by vehicles, energy production, and waste disposal. The Covid-19 outbreak that has hit the world has caused enormous losses to the tourism sector in Bali Province. But on the other hand, it provides benefits for environmental recovery, which is shown by decreasing NO<sub>2</sub> levels in the air. The decrease in NO<sub>2</sub> levels in the air is due to reduced human activities outside the home due to the implementation of the Indonesian Government's policies in the form of Large-Scale Restrictions, Work From Home (WFH), and the religious traditions of Hindus in Bali (Silent/ Nyepi Day). Nyepi Day makes people in Bali, lock themselves and meditate at home for 24 hours, without any activity on March 25, 2020. Even though the Covid-19 pandemic is still ongoing, it turns out that NO<sub>2</sub> levels are back up after a long holiday in Indonesia on November-December 2020, due to the large number of tourists visiting Bali Province.

The arrival of these tourists increases human activities around the tourism area, such as opening hotels, restaurants, and means of land, sea, and air transportation. Tourism areas tend to have high building density and population. Thus, making green open space low. Whereas green open space is very useful in absorbing air pollution, it is recommended to add green open space or revegetation in every hotel building to maintain good air quality.

## REFERENCES

- Anggraini, T. S., Artaningh, F., Sihotang, E., Sakti, A., & Agustan, A. (2020). Variations in Nitrogen Dioxide Emissions during Large-Scale Social Restrictions in West Java Province from Sentinel-5p Data Processing. *Indonesian Journal of Remote Sensing*, 2(2), 19-24. Retrieved from <http://jurnal.mapin.or.id/index.php/jpji/article/view/34>
- Arifin, Z.M.T., & Sukoco. (2009). *Vehicle Pollution Control*. Bandung: Alfabeta
- Berger, M ; Moreno, J ; Johannessen, J.A ; Levelt, P F ; Hanssen, R F. 2012. ESA's sentinel missions in support of Earth system science. *Remote Sens. Environ.* 120, 84-90. 37.
- Berman, J. D., & Ebisu, K. (2020). Changes in US air pollution during the COVID-19 pandemic. *Science of the total environment*, 739, 139864.
- Chu, B., Zhang, S., Liu, J., Ma, Q., & He, H. (2021). Significant concurrent decrease in PM<sub>2.5</sub> and NO<sub>2</sub> concentrations in China during COVID-19 epidemic. *Journal of Environmental Sciences*, 99, 346-353.
- Copat, C., Cristaldi, A., Fiore, M., Grasso, A., Zuccarello, P., Santo Signorelli, S., ... & Ferrante, M. (2020). The role of air pollution (PM and NO<sub>2</sub>) in COVID-19 spread and lethality: a systematic review. *Environmental research*, 191, 110129.
- Febriani, RA (2021) The Effect of the Number of Transportation Modes and Industrial Closures on Air Quality at PSBB During the Covid-19 Pandemic In DKI Jakarta Province. Undergraduate Thesis, Diponegoro University.
- Goldberg, D.L., Anenberg, S.C., Griffin, D., McLinden, C.A., Lu, Z., Streets, D.G., 2020. Disentangling the impact of the COVID-19 lockdowns on urban NO<sub>2</sub> from natural variability. *Geophys. Res. Lett.* 47 (17), e2020GL089269.
- Gorelick N, Hancher M, Dixon M, lyushchenko S, Thau D, Moore R. (2017). Google Earth Engine: Planetary-scale geospatial analysis for everyone. 202, 18-27. <https://doi.org/10.1016/j.rse.2017.06.031>
- Guanter, L ; Aben, I ; Tol, P ; Krijger, J.M ; Hollstein, A ; Köhler, P ; Damm, A.; Joiner, J.; Frankenberg, C.; Landgraf, J. (2015). Potential of the TROPospheric Monitoring Instrument (TROPOMI) onboard the Sentinel-5 Precursor for the monitoring of terrestrial chlorophyll fluorescence. *Atmos. Meas. Tech.* 8, 1337-1352.
- Lorente, A., Boersma, K.F., Eskes, H.J., Veeffkind, J.P., van Geffen, J.H.G.M., de Zeeuw, M.B., Denier van der Gon, H.A.C., Beirle, S., Krol, M.C., (2019). Quantification of nitrogen oxides emissions from build-up of pollution over Paris with TROPOMI. *Sci. Rep.* 9, 20033. <https://doi.org/10.1038/s41598-019-56428-5>.
- Mahato, S., Pal, S., Ghosh, K.G., (2020). Effect of lockdown amid COVID-19 pandemic on air quality of the megacity Delhi, India. *Sci. Total Environ.* 730, 139086. <https://doi.org/10.1016/j.scitotenv.2020.139086>.
- Mukono, H.J. (2006). *Air Pollution and Its Effect on Respiratory Tract Disorders*. Surabaya: Airlangga University Press.
- Nadzir, M. S. M., Ooi, M. C. G., Alhasa, K. M., Bakar, M. A. A., Mohtar, A. A. A., Nor, M. F. F. M., ... & Nor, M. Z. M. (2020). The impact of movement control order (MCO) during pandemic COVID-19 on local air quality in an urban area of Klang valley, Malaysia. *Aerosol and Air Quality Research*, 20(6), 1237-1248.
- Novianti TC. (2021). Land Cover Classification Using Google Earth Engine. *Jurnal Geografi dan Pembelajaran Geografi*. Vol 6, No 1. DOI: <http://dx.doi.org/10.31851/swarnabhumi.v6i1.5105>.
- Nuruddin, Wirawan PE, Pujjastuti S, Astuti, NNS. (2019). Hotel Survival Strategy in Bali During the Covid-19 Pandemic *Journal of Bali Studies (Journal of Bali Studies)*, [S.l.], v. 10, n. 2, p. 579-602, oct. 2020. ISSN 2580-0698. doi: <https://doi.org/10.24843/JKB.2020.v10.i02.p11>.

- Otmani, A., Benchrif, A., Tahri, M., Bounakhla, M., Chakir, E.M., El Bouch, M., Krombi, M., (2020). Impact of covid-19 lockdown on PM10, SO<sub>2</sub> and NO<sub>2</sub> concentrations in salé city (Morocco). *Sci. Total Environ.* 735, 139541. <https://doi.org/10.1016/j.scitotenv.2020.139541>.
- Paital, B., & Agrawal, P. K. (2021). Air pollution by NO<sub>2</sub> and PM<sub>2.5</sub> explains COVID-19 infection severity by overexpression of angiotensin-converting enzyme 2 in respiratory cells: a review. *Environmental Chemistry Letters*, 19(1), 25-42.
- Prayudi, T. dan J. P. Susanto. 2001. Dust Quality in Air as Impact of Flat Metal Casting Industry. *Journal of Environmental Technology*, Vol. 2, No. 2, Mei 2001: 168-174.
- Pujaastawa IBG. (2016). Development Model and Regional Tourism Problems in Bali. National Seminar and Workshop on Bali's Regional Tourism Policy in the Framework of Towards Equitable and Sustainable Tourism. Udayana University Culture and Tourism Research Center
- Purwanto Utomo, H., & Ratnawati, R. (2021). Vegetation Effectiveness for Reducing Carbon Monoxide (CO) and Nitrogen Dioxide (NO<sub>2</sub>) levels. *Time: UNIPA Engineering Journal*, 19(01), 38-43. <https://doi.org/10.36456/waktu.v19i01.3638>
- Putria DPD, Santosa B. (2021). Correlation Analysis of Nitrogen Dioxide Gas Variations on the Increase in Positive Cases Confirmed by Covid-19 Case Study of East Java Province. *Geomatics Engineering Scientific Journal. IMAGI (2021) Vol. 1*
- Regional Regulation of Bali Province Number 3 of 2020 concerning Amendments to Regional Regulation Number 16 of 2009 concerning Spatial Planning of the Province of Bali for 2009-2029
- Rusyayati SB, Hermawan R, Setiawan Y, Wijayanto AK, Prasetyo LB, Permatasari PA. (2020). The effect of the pattern of utilization of green open space on the dynamics of changes in air quality due to the Covid-19 Pandemic in the Greater Jakarta Area. *Journal of Natural Resources and Environmental Management*. 10, 559-567. <http://dx.doi.org/10.29244/jpsl.10.4.559-567>
- Sanningrahi S., Kumar P., Molter A., Zhang Q., Basu B., Basu AS., Pilla F., (2021). Examining the status of improved air quality in world cities due to COVID-19 led temporary reduction in anthropogenic emissions. *Environmental Research*. 196, 1-22. <https://doi.org/10.1016/j.envres.2021.110927>
- Shikwambana, L., Mhangara, P., Mbatha, N., (2020). Trend analysis and first time observations of sulphur dioxide and nitrogen dioxide in South Africa using TROPOMI/Sentinel-5 P data. *Int. J. Appl. Earth Obs. Geoinf.* 91, 102130. <https://doi.org/10.1016/j.jag.2020.102130>.
- Tamiminia, H., Salehi, B., Mahdianpari, M., Quackenbush, L., Adeli, S., Brisco, B., (2020). Google Earth Engine for geo-big data applications: A meta-analysis and systematic review. *ISPRS Journal of Photogrammetry and Remote Sensing*, 164, 152-170. <https://doi.org/10.1016/j.isprsjprs.2020.04.001>
- The European Space Agency. (2014). User Guide Sentinel 5 P. <https://sentinels.copernicus.eu/web/sentinel/user-guides/sentinel-5p-tropomi>. Diakses pada 1 April 2021.
- Wang, L., Diao, C., Xian, G., Yin, D., Lu, Y., Zou, S., Erickson, T. A. 2020., A summary of the special issue on remote sensing of land change science with Google earth engine. *Remote Sensing of Environment*, 248. <https://doi.org/10.1016/j.rse.2020.112002>
- Wetchayont, P., Hayasaka, T., & Khatri, P. (2021). Air quality improvement during COVID-19 lockdown in Bangkok metropolitan, Thailand: Effect of the long-range transport of air pollutants. *Aerosol and Air Quality Research*, 21, 200662-200662.
- Zheng, Z., Yang, Z., Wu, Z., Marinello, F., (2019). Spatial variation of NO<sub>2</sub> and its impact factors in China: an application of sentinel-5P products. *MDPI Remote Sensing*. 11, 1-24. <https://doi.org/10.3390/rs11161939>.
- Zulkarnain R. Ramadani KD. (2020). Kualitas Udara dan Potensi Transmisi COVID-19 di Pulau Jawa. Conference: Seminar Nasional Official Statistics 2020.

## COMPARING CHOROPLETH AND GRADUATED SYMBOLS: HOW DIFFERENT MAP TYPES AFFECT PUBLIC UNDERSTANDING IN COVID-19 MAP READING IN BADUNG REGENCY, BALI, INDONESIA

Tri Tanami SUKRAIN<sup>1</sup> , I Made Adi YASA<sup>2</sup>  and Putu Perdana Kusuma WIGUNA<sup>3</sup> 

DOI: 10.21163/GT\_2022.171.12

### ABSTRACT:

Information on COVID-19 is vital in protecting the entire community. As the diffusion pattern changes rapidly over time, originally simple data must be presented differently to provide more representative and quickly readable information. Relevant data are now offered in maps to support the public dissemination of COVID-19 information, with Choropleth and Graduated Symbols being the most common map types. This research was the first to analyze community's map reading skills, particularly in interpreting or understanding Indonesia's COVID-19 case distribution portrayed on the map. To test both map types, an online questionnaire was sent to respondents selected by random sampling from people living in Badung Regency. Then, they were given 11 tasks, namely to identify, find extreme values, differentiate, retrieve values, compare, interpret, categorize, group, sort, associate, and locate information contents on both maps. Then, chi-squared, Cramer's V, and Mann-Whitney U tests were conducted to statistically analyze three aspects: accuracy, time, and level of difficulty. The results showed that the choropleth map was easier to read than the graduated symbols. Furthermore, the null hypothesis (H0) was rejected, which means there is a correlation between map type and community's ability to read and understand maps.

**Key-words:** COVID-19, Map Reading, Map Type, Statistics.

### 1. INTRODUCTION

In 2020, the world was hit by the novel coronavirus disease COVID-19. It was first discovered in December 2019 in Wuhan, the capital of China's Hubei Province, and has since spread throughout the world (Wu, Chen & Chan, 2020; Zhou et al., 2020). The World Health Organization (WHO) declared the 2019–2020 outbreak a Public Health Emergency of International Concern (PHEIC) on January 30, 2020, and a pandemic on March 11, 2020 (El Hakim, Tourab & Zouiten, 2020; Leite et al., 2021).

In the last two years, the COVID-19 pandemic has shaken the global population tremendously. With almost every country in the world reporting infection cases (Casella et al., 2020), governments have mainly focused on introducing various efforts to curb the spread and inform the community about how and to what extent the disease diffused. This effort includes presenting useful, relevant data to facilitate case updates and instill public understanding. Currently, COVID-19 distributions are mostly described in the form of statistical data, which can be correctly understood when visualized appropriately and according to the purpose of the data usage.

Thematic maps are a commonly used visualization method to convey statistical data (Sudaryatno, El-Yasha & Afifah, 2019, Korycka-Skorupa & Gołebowska, 2020).

---

<sup>1</sup>Department of Business, Politeknik Negeri Bali, Indonesia, [tritanami@pnb.ac.id](mailto:tritanami@pnb.ac.id)

<sup>2</sup>Department of Electrical Engineering, Politeknik Negeri Bali, Indonesia, [imdadiyasa@pnb.ac.id](mailto:imdadiyasa@pnb.ac.id)

<sup>3</sup>Faculty of Agriculture, Udayana University, Bali, Indonesia, [wiguna@unud.ac.id](mailto:wiguna@unud.ac.id)

Geographic Information System (GIS) and cartography are two different fields of study that share the map concept. GIS refers to a set of technologies that include the interface of hardware, software, data, procedures, and networks. GIS is used to store, display and represent, interpret, and analyze geospatial data. In other words, GIS is a group of information systems that store and represent data that are associated with specific places in the real world. (Cantwell & Milem, 2010; Prah & Štrubelj, 2018). GIS can show many different kinds of data in one map, such as streets, buildings, and vegetation. This enables people to see, analyze, and understand patterns and relationships more easily. During recent years, maps have become very popular and frequently produced cartographical outputs. Cartography deals with the method expression and communication of these facts and phenomena with symbols and graphs on a map (Voženílek, & Bělka, 2016; Kraak & Fabrikant, 2017).

Nowadays, most GIS software incorporates advanced representation and labeling possibilities, and thanks to the database, there are multiple symbolization possibilities. Database is a collection of related information that permits the entry, storage, input, output, and organization of data. A database management system (DBMS) serves as an interface between users and their databases (Magyari-Sáska, 2020). Spatial database systems are concerned with the representation and manipulation of data that have a geometrical or topological interpretation of the physical world (Fekihal, Jaluta & Osman, 2012; Susanto & Meiryani, 2019). Spatial databases connect users to the GIS database. Then the database was visualized into a map.

Data visualization with thematic maps has its advantage, i.e., the map displays data by adding geographical symbols to represent statistical values while showing their location and spatial distribution (He, Tang & Huang, 2011; Pánek, 2020). However, its effectiveness statistically depends on how frequently the target populations read maps. Also, it should be noted that GIS data representation needs to be adjusted to the circumstances of the map users (Havelková & Hanus, 2019; Słomska-Przech, Panecki & Pokojski, 2021).

The application of GIS is applied in various fields of study, one of which is in the health sector. There have been studies regarding the application of geospatial analysis in COVID-19, especially the studies that were focused on understanding the distribution patterns of the pandemic. The widespread use of GIS for COVID-19 response has demonstrated the power of geospatial technology in a spatial, territorial, locational and landscape perspective. The online dashboard, maps and near-live tracking of cases and COVID-19 related fatalities were the first of its kind and aided the scientific community and practitioners in comprehending the magnitude of the pandemic, distribution of vulnerability until the smallest neighborhood and act as a critical source of information during this pandemic (Dong, Du, & Gardner, L., 2020, Franco-Pardo, 2020, Ahasan, & Hossain, 2021, Permatasari, et al., 2021, Ahasan, et al., 2022).

As one of the countries severely hit by the pandemic, Indonesia draws on the ability and advantage of thematic maps to help produce chiefly choropleth and graduated symbol maps to visualize infection cases at the provincial and regency levels. **Fig. 1** shows the graduated symbol and choropleth maps of COVID-19 distribution in Indonesia derived from covid19.go.id (COVID-19 Handling Task Force, 2021a; COVID-19 Handling Task Force, 2021b).

The graduated symbol map contains red circles proportional to provincial cases—with nationwide cases as the comparison, while the choropleth map divides the provinces into four risk categories: high (colored red), moderate (orange), low (yellow), and no cases (green). Both show that Bali is among the provinces at risk and with a relatively high number of reported cases. Therefore, to contain the spread and prevent new COVID-19 outbreaks, it is imperative that the right map be disseminated to visualize and educate the public about the spatial distribution of COVID-19 and identify the highly impacted areas in Bali.

In the province, a high cumulative COVID-19 case can be found in Badung Regency. Most of its area is tourist destinations; therefore, to observe and anticipate potential COVID-19 spread, the regency requires comprehensive information to be presented in an easy-to-understand map. This study aimed to analyze the public understanding of the COVID-19 distribution data in Badung Regency using two subtypes of thematic maps, namely graduated symbol map and choropleth map.

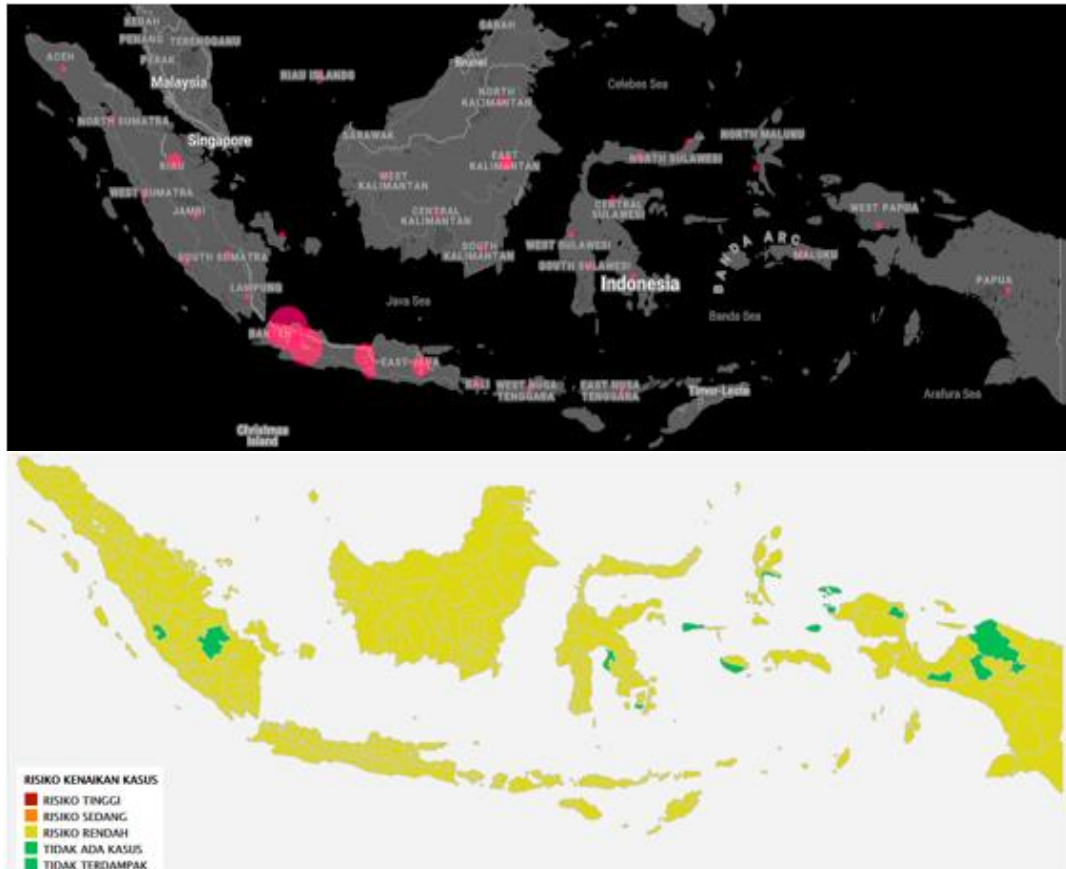


**Fig. 1.** The graduate symbol (top) and choropleth map (bottom) visualizing COVID-19 case distribution in Indonesia.

## 2. STUDY AREA

The study area is Badung Regency, Bali Province, Indonesia, which lies from  $8^{\circ}14'20''$  to  $8^{\circ}50'52''$  S and from  $115^{\circ}55'03''$  to  $115^{\circ}26'51''$  E. Badung has an area of 418.52 km<sup>2</sup> consisting of six districts: Kuta Selatan, Kuta, Kuta Utara, Mengwi, Petang, and Abiansemal, and 62 villages (Krisnandika, Wijaya & Ambarawati et al., 2019, BPS-Statistics of Badung Regency, 2019). **Fig. 2** shows the research location.

## 3. DATA AND METHODS

This study used COVID-19 distribution data in 62 villages of the six districts in the Badung Regency. It aimed to analyze the community's ability to read or understand statistical data presented in thematic maps, i.e., graduated symbol and choropleth maps. The map reading test refers to the use of comparison matrices and different tasks—expressed in questions or commands—formulated and tested by Słomska-Przech and Galebiowska (2021). Participants were asked to compare which map was easier to understand by firstly completing eleven tasks: to identify, to find extreme values, to distinguish, to retrieve values, to compare, to interpret, to categorize, to group, to sort, to associate, and to locate. Then, the responses to these tasks were analyzed from three aspects: accuracy, time, and difficulty level. Accuracy measures how accurately the public answers each question or responds to each command. Time measures the speed with which the public responds, while the level of difficulty indicates how the public assesses the difficulty of the tasks given for each map. **Fig. 3** shows the maps sent to participants for the map reading test.



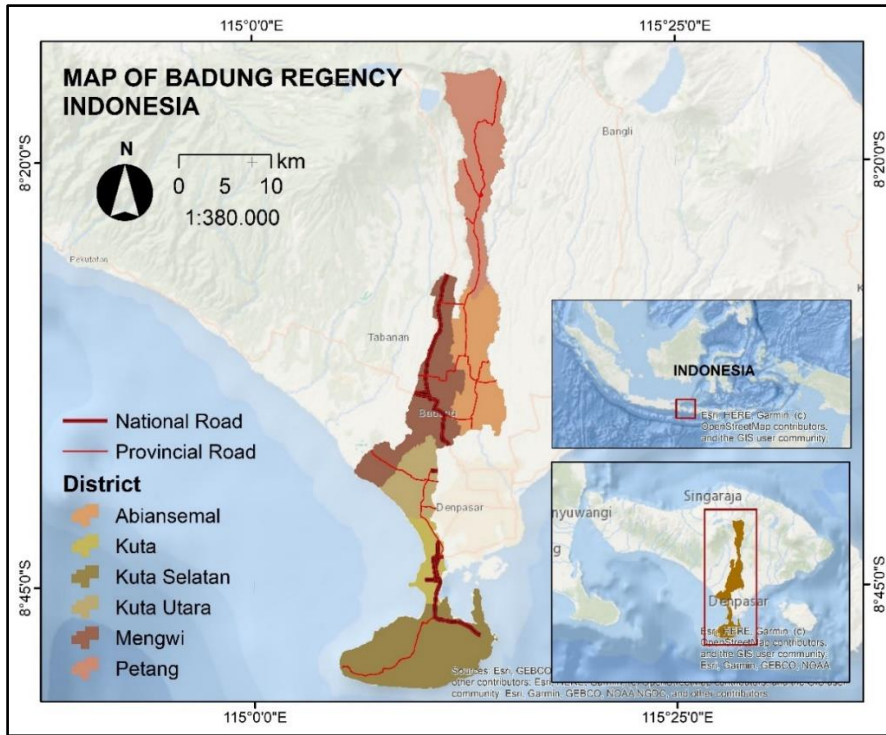


Fig. 2. Research location.

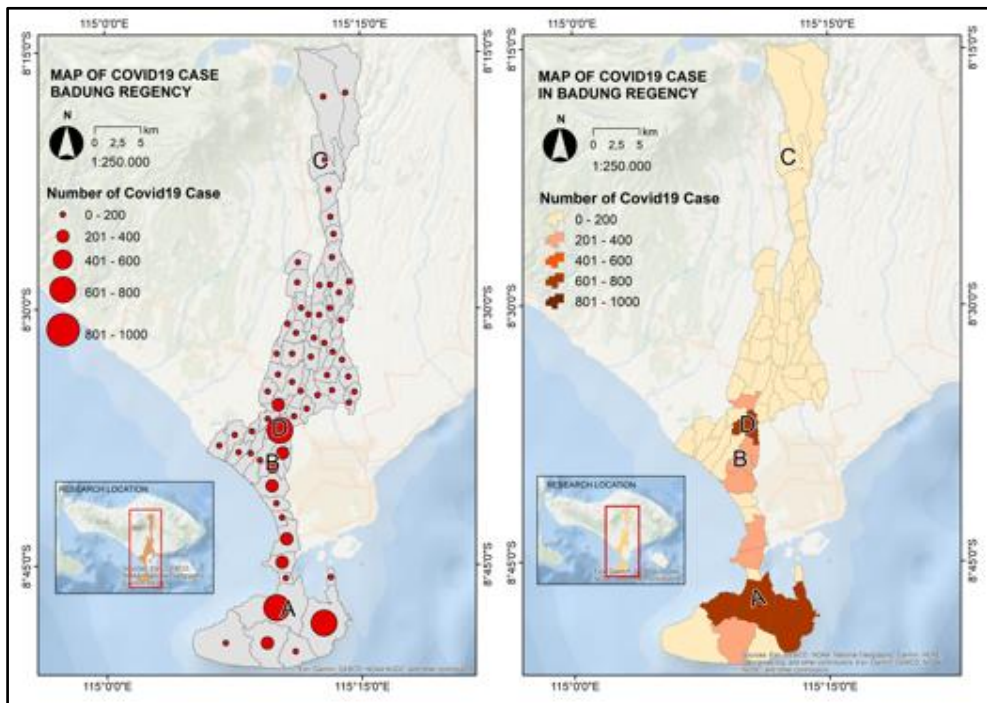


Fig. 3. COVID-19 case distribution maps for the map reading test: graduated symbols map (left) and choropleth map (right).



The test involved 120 participants or respondents selected by random sampling from the people living in Badung Regency. They were divided into two groups: 60 were asked to read the choropleth map and 60 others read the graduated symbols map. The respondents were 18–35 years old, comprising 77.5% female (93 respondents) and 22.5% male (27). Regarding their map reading frequency, 24.2% (29) stated that they never used or read maps, 23.3% (28) read maps once a week, and the remainder 52.5% (63) read or used maps more than once a week, be it Google Maps, Google Earth, or other applications with map features. The age range was selected based on the assumption that the respondents in this demography were more active in searching for information related to COVID-19 and more accustomed to using information and communication technology, including maps.

The research was the first to analyze the best map for understanding COVID-19 pandemic distribution in Indonesia. It employed an experimental research design that tested three aspects of map reading using descriptive statistical analysis: accuracy, time, and difficulty level. In addition, it also analyzed the correlation between two variables, namely map type and the public's ability to read maps using Chi-squared, Cramer's V, and Mann-Whitney U tests, which were selected for analysis because of the nature of data (Ahammed & Smith, 2019). In light of this, the formulated hypothesis was as follows:

*Ho: There is no correlation between map type and the public's ability to understand the map*

*H1: There is a correlation between map type and the public's ability to understand the map*

Pearson's chi-square test was used to test the significance of a categorical variable relationship. However, it cannot measure how closely related or correlated the two categorical variables are. To measure the closeness of the relationship between categorical variables, which can use the Phi coefficient, the coefficient of congruence and the Cramer's V correlation. According to Field (2009) and Okeke (2019) the three tests can both describe the relationship between two variables if the data matrix is 2x2. However, when the variable has more than two categories or different matrix dimensions, Cramer's V produces the best value. Therefore, in the case of this study, the Cramer's V correlation test is used because the matrix formed in this case is 2x2 for accuracy and 2x3 for difficult.

The use of the chi square test table is also equipped with the results of the Fisher's exact test which can also test the significance of the relationship between two variables. The condition for using the Pearson chi-square test is that when there are cells or squares, with an expected frequency value of less than 5, then the Pearson chi-square statistical sampling distribution will get inaccurate results. The analysis in this study resulted in 0% expected frequency value of less than 5 so, the chi square test was appropriate to be used in this analysis (McHugh, 2013; Kim, 2017).

While the Mann Whitney U Test is a non-parametric test used to determine the difference in the median of 2 independent groups if the dependent variable data scale is ordinal or interval/ratio but not normally distributed. Based on this definition, the Mann Whitney U Test requires data to be on an ordinal, interval or ratio scale (Hazra & Gogtay, 2016; Siddiqui, et al., 2016). In the cases tested, for testing accuracy and difficult, the Chi-Square method is used because the data used is on an ordinal category. Meanwhile, Time uses two types of data, namely ordinal and ratio. That is ordinal for map type and ratio for time. Time data were gathered from 2 groups, in which the variables are independent of each other, meaning that the data comes from different groups or are not paired so that the Mann Whitney U Test method is used.

The test instrument sent online to the respondents contained eleven (11) tasks with corresponding questions or commands. The respondents were asked to pinpoint the label A, B, C, or D or their combinations on the map (T2, T3, T7, T8), to choose a sentence that correctly described the marked area on the map (T1, T5, T6, T10, T11), to sort the data according to the instructions (T9), and to determine the amount of data (T4). Questions were inputted and set in a census-based mobile phone application; hence, the online data collection process. The tasks and their respective questions or commands are presented in **Table 1**. **Fig. 4** shows the research flowchart.

Table 1.

## Tasks, questions or commands, and answer options for the Map Reading test.

Code	Task	Question/Command	Answer Options
T1	To identify	Choose the sentence that correctly describes the area with 201 to 400 COVID-19 patients.	A. In the northern part of the research area B. In the southern part of the research area C. At the center of the research area D. In the northern and southern parts of the research area
T2	To find extreme values	Choose a location with the highest reach of COVID-19 cases.	A. A-B B. A-C C. A-D D. B-D
T3	To distinguish	Choose an area whose COVID-19 patients are in the range of 201–400 and 601–800.	A. A-B B. A-C C. A-D D. B-A
T4	To retrieve values	What is the range of the number of COVID-19 patients in region D?	A. 201–400 B. 401–600 C. 601–800 D. 801–1000
T5	To compare	Identify the area(s) showing the lowest and highest reach of COVID-19 cases.	A. Located at the south and center of the map B. Located at the edge of the map C. Located at the north, south, and center of the map D. Located at the north and edge of the map
T6	To interpret	Choose the right sentence.	A. Region B has the highest number of COVID-19 cases B. Regions B and D have the same range of COVID-19 cases C. All areas bordering Region C have the same range of COVID-19 cases D. Region A has the same range of COVID-19 cases as the neighboring area on the west
T7	To categorize	Which region is marked with the lowest COVID-19 case?	A. D B. C C. B D. A
T8	To group	Group the regions that have the same range of COVID-19 cases.	A. A-B B. A-C C. A-D D. B-D
T9	To sort	Sort the regions in order of the lowest to highest COVID-19 cases.	A. A-B-C B. C-B-A C. D-C-B D. B-C-D
T10	To associate	Choose a sentence that describes the correlation between two areas.	A. Regions A and B have the same range of COVID-19 cases B. Regions A and B are located on the south side of the map C. Regions B and C have the same range of COVID-19 cases D. Regions A and D have the same range of COVID-19 cases
T11	To locate	Choose the sentence that describes the location with the highest number of COVID-19 cases.	A. Located at the south of the area B. Located at the edge of the area C. Located at the center and south of the area D. Located at the north of the area

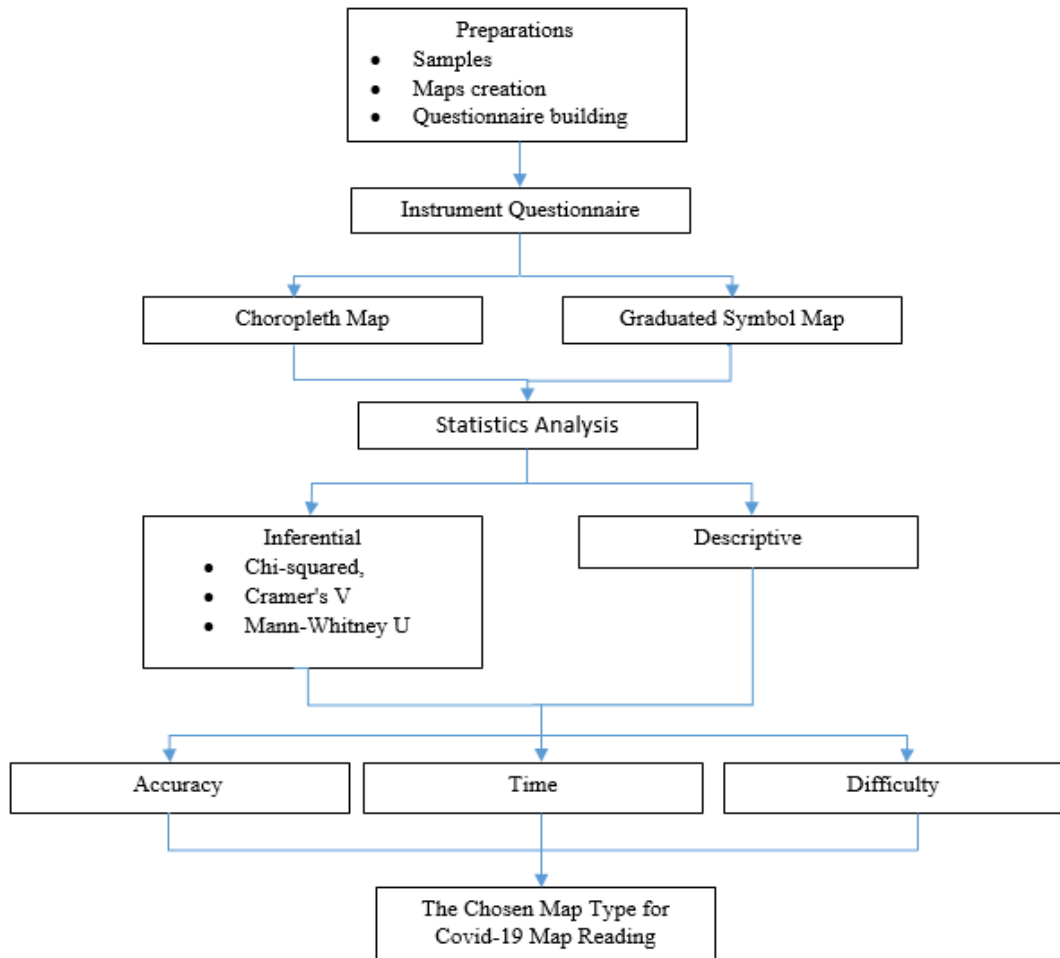
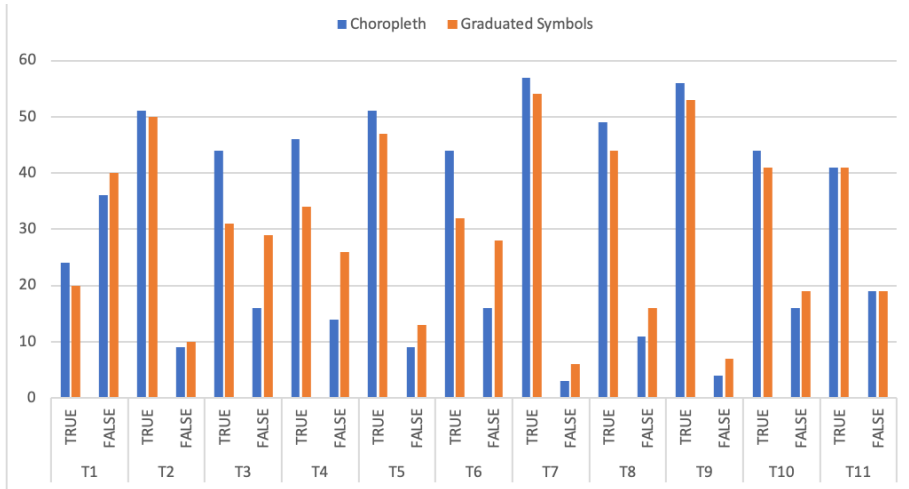


Fig. 4. The research flowchart.

#### 4. RESULTS

This section presents the descriptive analysis results for three map reading aspects (accuracy, time, and difficulty level) and the correlation analysis between map type and the public's ability to read maps. **Figures 4, 5, and 6** show the accuracy of answers for each task, the difficulty of understanding the two COVID-19 maps based on the given task, and the speed of map reading. The average accuracy of answers for the 11 tasks was 68%. The best results were shown by the group of respondents who read the choropleth map, with 73% correct answers. For comparison, 63% correct answers were obtained from the graduated symbols map group. Regarding difficulty level, 54% of the respondents stated that it was easy to read the choropleth map type, whereas 11% found it difficult. As for the graduated symbols map, it was easy to read according to 25% of the respondents but difficult for the other 12%. Based on this information, it can be inferred that the shares of respondents perceiving the two maps as difficult to read were only slightly different. In addition, the average time to read the maps and answer each question or command was 31.97 seconds. The choropleth map group took 28.15 seconds, while the graduated symbols map group required a longer time to complete the task, averagely 35.78 seconds. Lastly, inferential statistics were employed to analyze the correlation between map type and the community's map reading ability. The sections below describe the correlation analysis with every aspect of map reading.



**Fig. 4.** Accuracy of answers in the COVID-19 map reading test for choropleth and graduated symbols maps per task (presented in frequency).

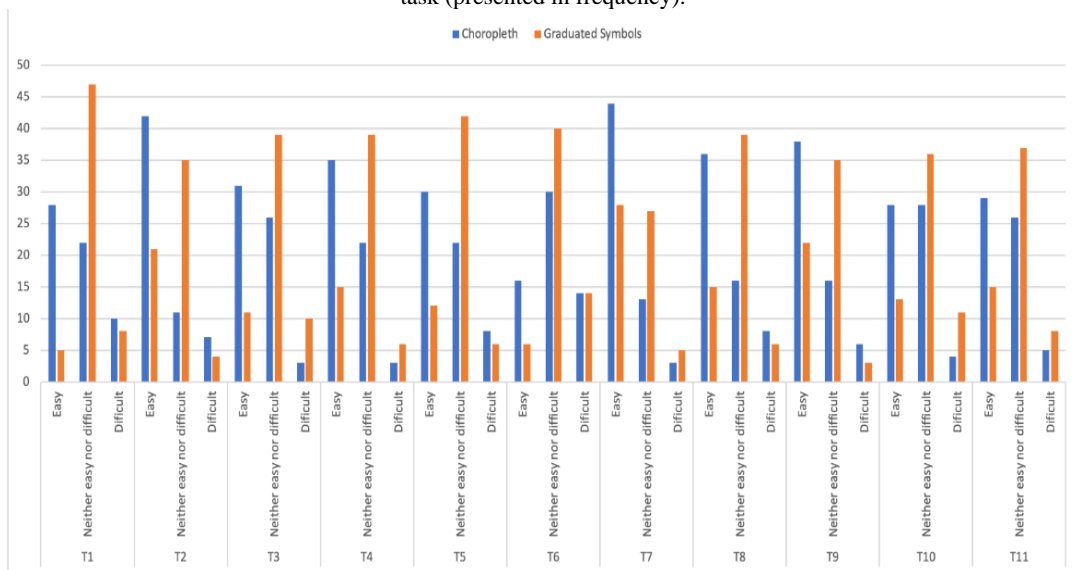


**Fig. 5.** Difficulty levels of the COVID-19 map reading for choropleth and graduated symbols maps per task (presented in frequency).

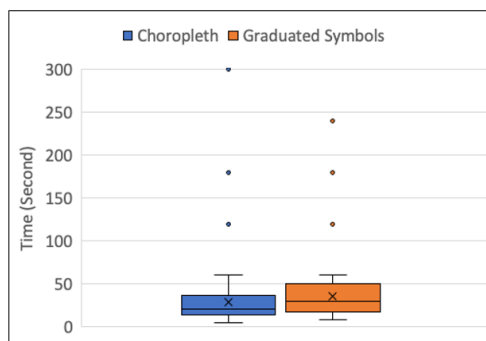


**Fig. 6.** Answer time boxplot for choropleth and graduated symbols maps.

The boxplot shows that the time data distribution on the graduated symbols map is more spread out than Choropleth, with the standard deviation obtained is 24.4 for GS and 22.1 for Choropleth. This proves that the data is not normally distributed so that the measurement of the center value is measured using the median with the Choropleth median is 30 seconds and Graduated Symbols is 21 seconds. **Table 2** shows the descriptive analysis for answer time.

**Table 2.**

<b>The descriptive analysis for Answer Time.</b>		
	<b>Choropleth</b>	<b>Graduated Symbols</b>
<b>count</b>	660	660
<b>mean</b>	28,15	35,781818
<b>std</b>	22,142323	24,40256
<b>min</b>	5	8
<b>25%</b>	14	17,75
<b>50%</b>	21	30
<b>75%</b>	36	50
<b>max</b>	300	240

#### 4.1. Correlation between Map Type and Accuracy of the Answer

The chi-squared and Cramer's V tests were used to determine the correlation between map type and the community's ability to read maps based on the first aspect, i.e., accuracy. In this case, the proposed hypothesis was as follows:

- *Ho: There is no correlation between map type and the accuracy of the answer as an aspect of the public's ability to understand the map*
- *H1: There is a correlation between map type and the accuracy of the answer as an aspect of the public's ability to understand the map*

**Tables 3 and 4** show the chi-square and Cramer's V test results, respectively. The first correlation analysis produced a Pearson chi-square of 13.808 and a significance value (p-value) of 0.0000. To test the null hypothesis, the chi-square value (count) was compared with the chi-square table, and it was found that the former was higher than the latter ( $13.808 > 3.841459$ ), which means that  $H_0$  is rejected. Then, the p-value was deemed significant because it was smaller than 0.05 ( $p\text{-value} = 0.000 < 0.05$ ), which means that  $H_0$  is rejected. Because the two analyses rejected the  $H_0$ , it can be concluded that there is a correlation between map type and the accuracy of the answer as an aspect or subset of the community's ability to understand the map. Furthermore, the Cramer's V test produced a value of 0.102 and a p-value of  $0.0000 > 0.05$ . It means that there is a correlation between map type and the accuracy of the answer, confirming the chi-squared test results.

**Table 3.**

<b>Chi-Squared test results for the Answer Accuracy.</b>					
	<b>Value</b>	<b>df</b>	<b>Asymptotic Significance (2-sided)</b>	<b>Exact Sig. (2- sided)</b>	<b>Exact Sig. (1- sided)</b>
<b>Pearson Chi-Square</b>	13.808 <sup>a</sup>	1	.000		
<b>Continuity Correction<sup>b</sup></b>	13.373	1	.000		
<b>Likelihood Ratio</b>	13.846	1	.000		
<b>Fisher's Exact Test</b>				.000	.000
<b>Linear-by-Linear Association</b>	13.797	1	.000		
<b>N of Valid Cases</b>	1.320				

a. 0 cells (0.0%) have an expected count of less than 5. The minimum expected count is 211.50;

b. Computed only for a 2x2 table.

Table 4.

Cramer's V test results for the Answer Accuracy.			
		Value	Approximate Significance
Nominal by Nominal	Phi	.102	.000
	Cramer's V	.102	.000
N of Valid Cases		1320	

Table 5 shows the inferential statistical test results per task. It shows that only T3, T4, and T6 are significant. These results indicate a correlation between map type and accuracy for T3 To distinguish, T4 To retrieve values, and T6 To interpret. For T3, the chi-square count > chi-square table ( $6.009 > 3.841459$ ), and the p-value was  $0.014 < 0.05$ ; both rejected the  $H_0$ . In conclusion, there is a correlation between map type and the accuracy of the public in distinguishing a particular map object. For T4, the chi-square count > chi-square table ( $5.4 > 3.841459$ ), and the p-value was  $0.02 < 0.05$ ; both rejected the  $H_0$ . Thus, there is a correlation between map type and the accuracy of the public in retrieving values of a specific map object. Similarly, for T6, the chi-square count > chi-square table ( $5.167 > 3.841459$ ), and the p-value was  $0.023 < 0.05$ , rejecting the  $H_0$ . These results indicate a correlation between map type and the accuracy of the public in interpreting a particular situation portrayed on the map.

Table 5.

Inferential statistics for the Answer Accuracy.				
Task	Chi-squared	p	Cramer's V	p
T1 To identify	0.574	0.449	0.069	0.449
T2 To find extreme values	0.063	0.803	0.023	0.803
T3 To distinguish	6.009	0.014	0.224	0.014
T4 To retrieve values	5.4	0.02	0.212	0.02
T5 To compare	0.891	0.345	0.086	0.345
T6 To interpret	5.167	0.023	0.208	0.023
T7 To categorize	1.081	0.298	0.095	0.298
T8 To group	1.195	0.274	0.1	0.274
T9 To sort	0.901	0.343	0.087	0.343
T10 To associate	0.363	0.547	0.055	0.547
T11 To locate	0	1	0	1
ACCURACY	13.808	0.000	0.102	0.000

#### 4.2. Correlation between Map Type and Answer Time

In addition to the accuracy of the answer, the correlation between map type and the public's ability to read maps was also tested using the second aspect, i.e., time. Therefore, the following hypothesis was formulated:

- *H<sub>0</sub>: There is no correlation between map type and answer time as an aspect of the public's ability to understand the map*
- *H<sub>1</sub>: There is a correlation between map type and answer time as an aspect of the public's ability to understand the map*

Table 6 shows the Mann-Whitney U test results for the answer time. The results included a significance value (p-value) of  $0.000 < 0.05$ , thus rejecting the  $H_0$ . In other words, there is a correlation between map type and the answer time as an aspect or subset of the community's map reading ability.

**Table 6.**  
**Mann-Whitney U test results for the Answer Time.**

Test Statistics	Time
<b>Mann-Whitney U</b>	168566.500
<b>Wilcoxon W</b>	386696.500
<b>Z</b>	-7.118
<b>Asymo. Sig. (2-tailed)</b>	.000

**Table 7** shows the inferential statistical test results for the answer time per task. In general, the figures in this table indicate a correlation between map type and answer time. However, five tasks are insignificant because their p-values were higher than 0.05, i.e., T2 To find extreme values was 0.59, T3 To distinguish 0.945, T1 To identify 1.000, T9 To sort 0.069, and T10 To associate 0.18. These p-values indicate a failure to reject the null hypothesis ( $H_0$ ). In other words, there is no correlation between map type and the time the public requires to understand maps, especially to find extreme values, to distinguish and categorize a particular object, to sort map objects based on a situation, and to associate or correlate two areas. In contrast, the  $H_0$  is rejected for T1, T4, T5, T6, T8, and T11, whose p-value was smaller than 0.05. Consequently, there is a correlation between map type and the time the public takes to understand the map, specifically to identify, retrieve values, compare, interpret, group, and locate objects on the map.

**Table 7.**  
**Inferential statistics for the Answer Time.**

Task	Mann-Whitney U	<i>p</i>
<b>T1 To identify</b>	1073.5	0.000
<b>T2 To find extreme values</b>	1440	0.59
<b>T3 To distinguish</b>	1787	0.945
<b>T4 To retrieve values</b>	1050.5	0.000
<b>T5 To compare</b>	1388	0.03
<b>T6 To interpret</b>	1283	0.006
<b>T7 To categorize</b>	1800	1.000
<b>T8 To group</b>	935.5	0.000
<b>T9 To sort</b>	1454.5	0.069
<b>T10 To associate</b>	1348.5	0.18
<b>T11 To locate</b>	1004.5	0.000
<b>TIME</b>	168566	0.000

### 4.3. Correlation between Map Type and Difficulty of the Map-Reading Tasks

The third aspect tested to determine the correlation between map type and the public's ability to read maps is difficulty level. Similar to accuracy and answer time, this correlation was assessed using inferential statistics (the chi-squared and Cramer's V) to test the hypothesis below:

- *H<sub>0</sub>: There is no correlation between map type and difficulty of the task as an aspect of the public's ability to understand the map*
- *H<sub>1</sub>: There is a correlation between map type and difficulty of the task as an aspect of the public's ability to understand the map*



**Tables 8 and 9** show the chi-squared and Cramer's V test results for the difficulty level, respectively. To test the null hypothesis, the calculated chi-square value (count) was compared with the chi-square table, and the level of significance was set at 0.05. The results can be described as follows:

- *Chi-square count (125.282) > chi-square table (5.9915), then  $H_0$  is rejected*
- *P-value = 0.000 < 0.05, then  $H_0$  is rejected.*

The two analyses rejected the null hypothesis ( $H_0$ ). In other words, there is a correlation between map type and the difficulty level of the map-reading task as an aspect or subset of the public's ability to understand the map. Furthermore, the Cramer's V test yielded a value of 0.308 and a p-value of  $0.000 < 0.05$ . It can be concluded that there is a correlation between map type and the difficulty level of the map-reading tasks, confirming the chi-squared test results.

**Table 8.**

<b>Chi-Squared test results for the Task Difficulty.</b>			
	<b>Value</b>	<b>df</b>	<b>Asymptotic Significance (2-sided)</b>
<b>Pearson Chi-Square</b>	125.282 <sup>a</sup>	2	.000
<b>Likelihood Ratio</b>	127.788	2	.000
<b>Linear-by-Linear Association</b>	73.031	1	.000
<b>N of Valid Cases</b>	1.320		

a. 0 cells (0.0%) have an expected count of less than 5. The minimum expected count is 76

**Table 9.**

<b>Cramer's V test results for the Task Difficulty.</b>			
		<b>Value</b>	<b>Approximate Significance</b>
<b>Nominal by Nominal</b>	<b>Phi</b>	.308	.000
	<b>Cramer's V</b>	.308	.000
<b>N of Valid Cases</b>		1320	

**Table 10** summarizes the inferential statistical test results per task.

**Table 10.**

<b>Inferential statistics for the Task Difficulty.</b>				
<b>Task</b>	<b>Chi-squared</b>	<b>p</b>	<b>Cramer's V</b>	<b>p</b>
<b>T1 To identify</b>	25.31	0.000	0.459	0.000
<b>T2 To find extreme values</b>	20.34	0.000	0.412	0.000
<b>T3 To distinguish</b>	15.893	0.000	0.364	0.000
<b>T4 To retrieve values</b>	13.738	0.001	0.338	0.001
<b>T5 To compare</b>	14.25	0.001	0.345	0.001
<b>T6 To interpret</b>	5.974	0.05	0.223	0.05
<b>T7 To categorize</b>	8.956	0.011	0.273	0.011
<b>T8 To group</b>	18.551	0.000	0.393	0.000
<b>T9 To sort</b>	12.345	0.002	0.321	0.002
<b>T10 To associate</b>	9.754	0.008	0.285	0.008
<b>T11 To locate</b>	7.067	0.029	0.243	0.029
<b>DIFFICULTY</b>	125.282	0.000	0.308	0.000

It shows that almost all of the tasks are significant, except for T6 To interpret. Its chi-square was 5.974, whereas that of the other ten tasks was higher than 5.9915. Therefore, the chi-square value of T6 was smaller than 5.9915, indicating a failure to reject  $H_0$ . Moreover, the p-value derived from both chi-squared and Cramer's V tests was equal to 0.05, confirming the chi-squared test results for T6. Overall, there is no correlation between map type and the difficulty of interpreting a particular object portrayed on the map.

#### 4.4. Spatial Distribution

Spatial distribution of map reading results is very important for the education and public health sectors in order to effectively solve problems in the area and find ways to prevent the spread of the epidemic. **Fig. 7** shows the different result between choropleth map reading (top) and graduated symbol map reading (bottom). Both are presented in choropleth map.

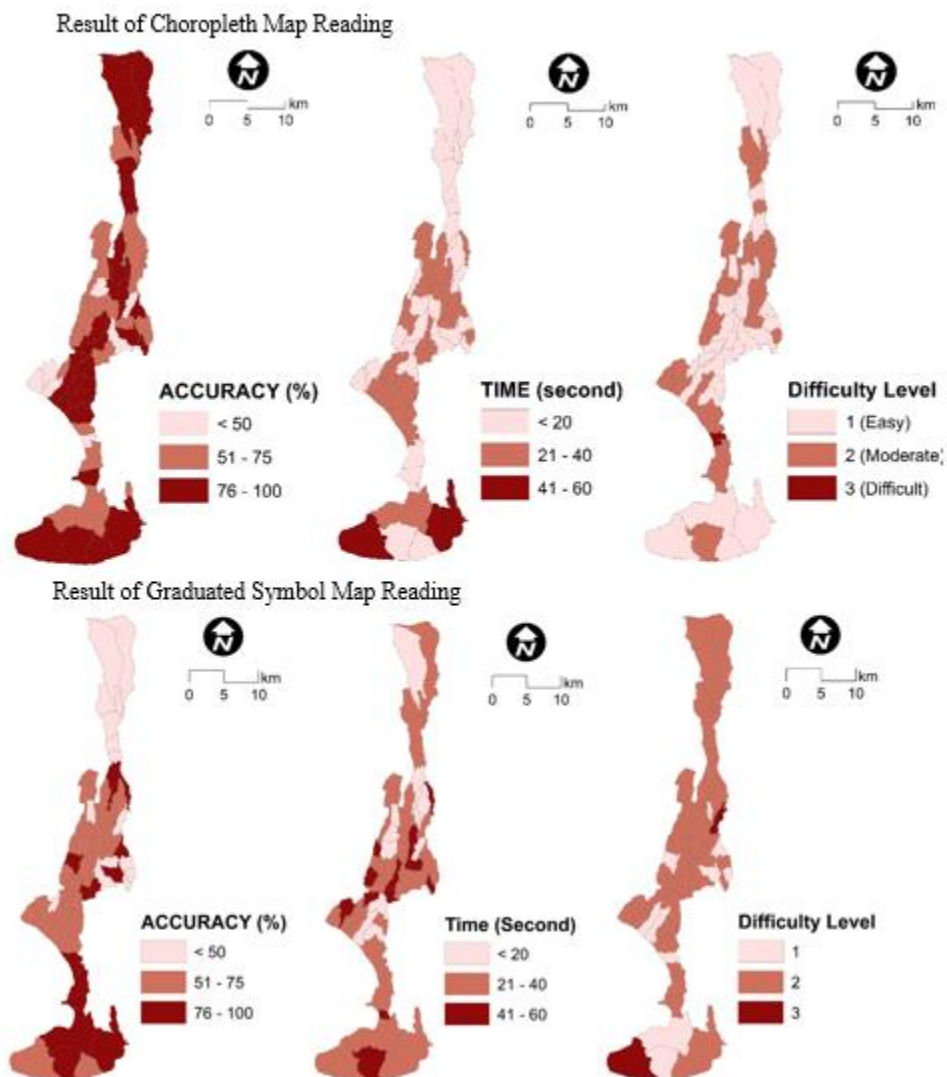


**Fig. 7.** Distribution of Map Reading Results Presented in Choropleth Map. Top: Result of Choropleth Map Reading. Bottom: Result of Graduated Symbol Map Reading.

The results show that, spatially, people have better accuracy, time and difficulty levels when reading choropleth maps. Respondents in the southern region of Badung Regency answered with an accuracy of more than or equal to 76%. This result can be related to the condition of the southern area which is a tourism location, so that people are more accustomed to reading maps or using maps. Very few areas had less than 50% accuracy and spent more than 40 seconds when reading the Choropleth map. Respondents also chose the choropleth map as a map that is easier to read, indicated by a lower level of difficulty than the graduated symbol map.

Meanwhile, reading a graduated symbol map shows results that are not as good as reading a choropleth map. In general, this can be caused by people who are not used to reading graduated symbol maps. This can be seen from the distributions of respondents who answered with poor accuracy, spent more time and experienced higher level of difficulty.

## **5. DISCUSSION**

The correlation analysis between map type and the accuracy of the answer showed different results for all map-reading tasks. The descriptive analysis revealed that the public is able to find location points on both the choropleth and graduated symbols maps (T11). This statement is true for the public's ability to find extreme values (T2), compare (T5), categorize (T7), group (T8), sort (T9), and associate (T10). Although there are only slight differences in the ability to read both maps, the map reading accuracy is better for the choropleth map. In contrast, significant differences are observed in the ability to distinguish (T3), retrieve values (T4), and interpret (T6) data on the map. In this case, the public exhibits a better ability to complete these tasks on the choropleth map. This statement is confirmed by the statistical results, i.e., chi-square values, p-values, and Cramer's V values, which indicate a strong correlation between map type and the accuracy of the answer provided to distinguish, retrieve values, and interpret map objects. Overall, the choropleth map is considered capable of presenting the best results in terms of accuracy.

Based on the second aspect, the average time the public requires to complete each task on the choropleth map is 28.15 seconds. However, it takes a longer time for the public to finish the same question or command on the graduated symbols map, i.e., 35.78 seconds. Statistically, they can quickly identify (T1), retrieve values (T4), compare (T5), interpret (T6), group (T8), and locate (T11) information on the map.

As for the third aspect, more respondents (54%) find that it is easy to read the choropleth map, whereas fewer (25%) perceive the graduated symbols map as easy to read. These findings are supported by the statistical analysis results, which indicate that almost all tasks are significant, except for T6 To interpret. However, T6 does not give a statistically significant effect on the overall measurements for the difficulty of the map-reading tasks because its p-value is very low. The choropleth map is considered easier to read in terms of identifying (T1), finding extreme values (T2), differentiating (T3), retrieving values (T4), comparing (T5), categorizing (T7), grouping (T8), sorting (T9), associating (T10), and locating (T11) its information content.

In general, the public answers accurately, takes a shorter answer time, and finds it easy to retrieve values (T4) from both maps. They provide the correct answers and experience little to no difficulty in distinguishing (T3) and interpreting (T6). Further, they require a relatively quick time and experience little to no difficulty in identifying (T1), comparing (T5), grouping (T8), and locating (T11) the information contents of both maps. Lastly, they do not experience a significant challenge in finding extreme values (T2), categorizing (T7), sorting (T9), and associating (T10) particular objects portrayed on the map.

The results of this study indicate that the choropleth map shows the best results for each data analyzed (accuracy, time, and level of difficulty). Based on the statistically significant tasks, it can be summarized in the order of the highest to the lowest: related to the difficulty of the map-reading tasks (10 out of 11 tasks), the answer time (6 out of 11), and the accuracy of the answers (3 out of 11).

A research from Słomska-Przech and Galebiowska (2021) shows that when it comes to the overall results, the best metrics of performance (answer accuracy and time) for all tasks were obtained

when working with the choropleth map. It means that choropleth map was used in many tasks and field of study, not only in Indonesia but also abroad. Similar task and methodology were also used by Słomska-Przech, Panecki & Pokojski, (2021) who compared the usability of heat maps with different levels of generalization. The objective (the correctness of the answer, response times) and subjective (response time self-assessment, task difficulty, preferences) metrics were measured. The tasks for map reading were used widely and were able to measure the benefits of the map by giving tasks to the map reader. It is worth comparing the effectiveness of numbers on maps with other methods of data presentation—for example, heat maps, isopleths, etc (Korycka-Skorupa & Golebiowska, 2020).

## 6. CONCLUSIONS

The average accuracy or correctness of the answer for the choropleth and graduated symbols maps is 73% and 63%, respectively. For the first aspect (i.e., difficulty level), 54% of the respondents claim that it is easier to read the choropleth map, whereas 25% perceive the graduated symbols map as easy to read. The average time required to read and answer each question or command on the choropleth map is 28.15 seconds, which is faster than completing the same task on the graduated symbols map (35.78 seconds). In other words, it takes more time to answer questions or respond to commands using the graduated symbols map.

Based on the analysis results for the three aspects (accuracy, time, and level of difficulty), it appears that the choropleth map is easier to understand. Each has been analyzed for their correlations with map type as the subsets of the map-reading ability. The hypothesis tests revealed that there is a correlation between map type and the public's ability to understand the map based on accuracy, task difficulty, and answer time.

This study shows that the choropleth map becomes an effective and preferred map for understanding information about COVID-19. The choropleth map is considered the easiest solution to map spatial phenomena related to COVID-19. This condition may have positive and negative sides. On the one hand, choropleth maps are a powerful way of presenting spatial data. On the other hand, the creation of choropleth map must be done carefully to avoid mistakes. The use of the map depends on the purpose and the problem to be solved. Therefore, mappers cannot restrict the use to one type of map and may not ignore other types of maps. Research related to cartography, must pay attention to every type of map.

## REFERENCES

- Ahammed, F. & Smith, E. (2019). Prediction of Students' Performances Using Course Analytics Data: A Case of Water Engineering Course at the University of South Australia. *Education Sciences*, 9(3), 245, 1–15. doi:10.3390/educsci9030245.
- Ahasan, R., & Hossain, M. M. (2021). Leveraging GIS and spatial analysis for informed decision-making in COVID-19 pandemic. *Health Policy and Technology*, 10(1), 7-9. <https://doi.org/10.1016/j.hlpt.2020.11.009>.
- Ahasan R, Alam MS, Chakraborty T and Hossain MM. (2022). Applications of GIS and geospatial analyses in COVID-19 research: A systematic review [version 2; peer review: 1 approved, 1 approved with reservations]. *F1000Research*, 9:1379. <https://doi.org/10.12688/f1000research.27544.2>.
- BPS-Statistics Agency of Badung Regency. (2019). *Badung in Numbers*. Mangupura: Central Bureau of Statistics of Badung Regency
- Cantwell, B. & Milem, J.F. (2010). Locating Space and Place in the College Access Debate: New Tools for Mapping and Understanding Educational Inequity and Stratification, Editor(s): Penelope Peterson, Eva Baker, Barry McGaw. *International Encyclopedia of Education (Third Edition)*, Elsevier. <https://doi.org/10.1016/B978-0-08-044894-7.00120-2>.

- Cascella, M., Rajnik, M., Aleem, A., Dulebohn, S. C., & Di Napoli, R. (2021). *Features, Evaluation, and Treatment of Coronavirus (COVID-19)*. In StatPearls. StatPearls Publishing.
- COVID-19 Handling Task Force. (2021a, October 24). *Peta Sebaran COVID-19 (Covid-19 Distribution Map)*. <https://covid19.go.id/peta-sebaran-covid19>.
- COVID-19 Handling Task Force. (2021b, October 24). *Peta Zonasi Risiko (Risk Zonation Map)*. <https://covid19.go.id/peta-risiko>.
- Dong, E., Du, H. & Gardner, L. (2020). An interactive web-based dashboard to track COVID-19 in real time. *Lancet Infect Dis.* 20(5), 533–534. doi: 10.1016/S1473-3099(20)30120-1
- Elhakim, M., Tourab, S.B. & Zouiten, A. (2020). COVID-19 Pandemic in Djibouti: Epidemiology and the Response Strategy Followed to Contain the Virus During the First Two Months, 17 March to 16 May 2020. *PLoS ONE.* 15(12), 1–12. <https://doi.org/10.1371/journal.pone.0243698>.
- Field, A. (2009) *Discovering Statistics Using SPSS*. 3rd Edition, Sage Publications Ltd., London.
- Franch-Pardo, I., Napoletano, B.M., Rosete-Verges, F. & Billa, L. (2020). Spatial analysis and GIS in the study of COVID-19. A review. *Science of the Total Environment*, 739. <https://doi.org/10.1016/j.scitotenv.2020.140033>.
- Fekihal, M., Jaluta, I. & Osman, I. (2012). Multidimensional Index Structure for Spatial Database Management Systems. *Journal of Computing Press*, 4(2), <https://sites.google.com/site/journalofcomputing>.
- Havelková, L. & Hanus, M. (2019). Map skills in education: a systematic review of terminology, methodology, and influencing factors. *Review of International Geographical Education Online (RIGEO)*, 9(2), 361–401. <http://www.rigeo.org/vol9no2/Number2Summer/RIGEO-V9-N2-6.pdf>.
- Hazra, A., & Gogtay, N. (2016). Biostatistics Series Module 3: Comparing Groups: Numerical Variables. *Indian Journal of Dermatology*, 61(3), 251–260. <https://doi.org/10.4103/0019-5154.182416>.
- He, M., Tang, X. & Huang, Y. (2011). To visualize spatial data using thematic maps combined with infographics. *Proceedings - 2011 19th International Conference on Geoinformatics, Geoinformatics 2011*. 1–5. 10.1109/GeoInformatics.2011.5980880.
- Kim H. Y. (2017). Statistical Notes For Clinical Researchers: Chi-Squared Test and Fisher's Exact Test. *Restorative Dentistry & Endodontics*, 42(2), 152–155. <https://doi.org/10.5395/rde.2017.42.2.152>
- Korycka-Skorupa, J. & Gołebiewska, I.M. (2020). Numbers on Thematic Maps: Helpful Simplicity or Too Raw to Be Useful for Map Reading?. *ISPRS International Journal of Geo-Information*, 9(7), 1–24. <https://doi.org/10.3390/ijgi9070415>.
- Kraak, M.-J. & Fabrikant, S.I. (2017) Of maps, cartography and the geography of the International Cartographic Association. *International Journal of Cartography*, 3(1), 9–31. DOI: 10.1080/23729333.2017.1288535
- Krisnandika, A.A.K., & Wijaya, I.M.A.S., & Ambarawati, I.G.A.A., & Adi, A.A.A.M., & Tamura, Eisaku, T. & Hongo, C. (2019). Rice Productivity Growth during Nine Years in Badung Regency, Bali Province. *International Journal of Agriculture System*, 7(2), 106–115. doi:10.20956/ijas.v7i2.1808.
- Leite, J.A., Gresh, L., Vicari, A., Gabastou, J.M., Perez, E., Aldighieri S, et al. (2021). COVID-19 laboratory preparedness and response in the Americas Region: Lessons learned. *PLoS ONE*, 16(6), 1–10. <https://doi.org/10.1371/journal.pone.0253334>.
- Magyari-Sáska, Z. (2020). Precipitation Used As Key Factor in Tapered Line Based River Representation. *Geographia Technica*, 15(2), 212–221. doi:10.21163/GT\_2020.152.20.
- McHugh M. L. (2013). The Chi-Square Test of Independence. *Biochemia Medica*, 23(2), 143–149. <https://doi.org/10.11613/bm.2013.018>
- Okeke, C. (2019). Alternative Methods of Solving Biasedness in Chi - Square Contingency Table. *Academic Journal of Applied Mathematical Sciences*. 1-6. doi:10.32861/ajams.51.1.6.
- Pánek, J. (2020). Spatial Visualisation, in Pászto, V., Jürgens, C., Tominc, P. & Burian, J. (Eds.). *Spationomy: Spatial Exploration of Economic Data and Methods of Interdisciplinary Analytics*. 207–219. *Springer International Publishing*, Cambridge. [https://doi.org/10.1007/978-3-030-26626-4\\_9](https://doi.org/10.1007/978-3-030-26626-4_9)
- Permatasari, A.L., Suherningtyas, I., Febriarta, E. & Wiguna, P.P.K. (2021). Analysis of Vulnerability to Covid-19 Transmission based on Building Function at Padukuhan Mancasan Kleben, Pandowoharjo, Sleman, Yogyakarta, Indonesia. *Forum Geografi*, 35(2). doi: 10.23917/forgeo.v35i2.13755

- Prah, K. & Štrubelj, G. (2018). Comparison of using different kinds of traffic data in best route analysis based on GIS. *FME Transactions*, 46, 668-673. doi:10.5937/fmet1804668P
- Słomska-Przech, K. & Galebiowska, I.M. (2021). Do Different Map Types Support Map Reading Equally? Comparing Choropleth, Graduated Symbols, Isoline Maps for Map Use Tasks. *International Journal of Geo-Information*. <https://doi.org/10.3390/ijgi10020069>.
- Siddiqui, K., Siddiqui, A., Bajwa, A., Elahi, M., Syed, M. & Fahim, S. (2016). Heuristics of Applying Statistical Tests Using Appropriate Measurement Scales. *Sci.Int.*, 28(5),4433-4438. <https://ssrn.com/abstract=2967694>.
- Słomska-Przech, K., Panecki, T. & Pokojski, W. (2021). Heat Maps: Perfect Maps for Quick Reading? Comparing Usability of Heat Maps with Different Levels of Generalization. *ISPRS International Journal of Geo-Information*, 10(8), 1–24. <https://doi.org/10.3390/ijgi10080562>.
- Sudaryatno, El-Yasha, S.R. & Afifah, Z.N. (2019). Thematic Geovisualization of the Data Profile of Kaligesing, Purworejo, Central Java. *Forum Geografi*, 33(2), 153–161. DOI: 10.23917/forgeo.v33i2.8876.
- Susanto, A. & Meiryani. (2019). Database Management System. *International Journal of Scientific & Technology Research*, 8(6), 309-312. <https://www.ijstr.org/paper-references.php?ref=IJSTR-0619-20463>
- Voženílek, V. & Bělka, L. (2016). THE CARTOGRAPHIC CONCEPT OF THE IMAGE MAP. *ISPRS - International Archives of the Photogrammetry, Remote Sensing and Spatial Information Sciences*. XLI-B4. 605-610. doi:10.5194/isprsarchives-XLI-B4-605-2016.
- Wu, Y-C., Chen, C-S. & Chan, Y-J. (2020). The outbreak of COVID-19: An overview. *Journal of the Chinese Medical Association*, 83(3), 217–220. doi: 10.1097/JCMA.0000000000000270.
- Zhou, F., Yu, T., Du, R., Fan, G., Liu, Y., Liu, Z., Xiang, J., Wang, Y., Song, B., Gu, X., Guan, L., Wei, Y., Li, H., Wu, X., Xu, J., Tu, S., Zhang, y., Chen, H. & Cao, B. (2020). Clinical Course and Risk Factors for Mortality of Adult Inpatients with COVID-19 in Wuhan, China: A Retrospective Cohort Study. *Lancet*, 395(10229), 1054–1062. [https://doi.org/10.1016/S0140-6736\(20\)30566-3](https://doi.org/10.1016/S0140-6736(20)30566-3).

## 3D MODELLING OF BUILDINGS AND URBAN AREAS USING GRASSHOPPER AND RHINOCEROS

*Domenica COSTANTINO<sup>1</sup>*, *Arianna GRIMALDI<sup>1</sup>*, *Massimiliano PEPE<sup>1</sup>*

DOI: 10.21163/GT\_2022.171.13

### ABSTRACT:

3D modelling of buildings using modern tools and techniques is an important objective for the management and planning of urban areas. Rhinoceros with Grasshopper is a powerful 3D modeller in the field of architecture, engineering and construction. In this paper, 3D modelling of several case studies based on the joint use of Rhinoceros and Grasshopper are shown. In particular, different levels of geometric complexity and detail are investigated. In order to achieve these objectives, adequate canvas designs have been developed according to the different case studies examined; specifically, several cases have been analysed, starting from simple volumes up to complex geometries and even large dimensions. The input sources for the elaborations in Grasshopper can be multiple; for example, numerical cartography, geodata from Open Street Map and point clouds generated by airborne LIDAR sensors were analysed. The 3D models generated in this way have parametric characteristics that are useful for integration into Building Information Models (BIM) and Geographic Information Systems (GIS), for analysis and simulation, or for visualising projects from illustrations to photorealistic renderings.

**Key-words:** Grasshopper, 3D city model, Rhinoceros, Open Street Map, Point Cloud, Extrusion.

### 1. INTRODUCTION

The representation of the city indicates the study of the morphology and expressive language of the urban fabric, in relation to significant monuments and buildings. With the advent of the digital age, new systems for visualising and managing geodata within web platforms or specific Apps, such as Google Maps, Google Earth, Street View Map, Earthexplorer (United States Geological Survey - USGS) have enabled a new approach to urban experimentation and knowledge (Isikdag & Zlatanova, 2010; Li & Ratti, 2019). Parametric modelling is a useful tool for management and planning that can study and predict the multiple logics of urban expansion. The parameterization of buildings or individual objects can be achieved through the use of parametric software, which is able to collect information and distribute it graphically on multiple levels, providing a series of complex scenarios. For example, a building is the set of individual basic elements (such as walls, windows, pipes and floors, etc.) with certain technical and structural characteristics (Shirowzhan et al., 2020). Using the same basic elements, then, it is possible to produce diversified designs, i.e. a design that can be shared with the various professionals involved in the process. In this way, it is possible to enrich, insert, extract, update or modify the information model in an immediate and effective way. An open standardised data model and exchange format for storing 3D digital models of cities and landscapes is CityGML, which defines ways to describe most of the common 3D features and objects found in cities (such as buildings, roads, rivers, bridges, vegetation and street furniture) and the relationships between them. In particular, CityGML defines several standard Levels of Detail (LoD) for the representation of objects for different applications and purposes, such as simulations, urban data mining, facilities management and thematic surveys (Gröger et al., 2012; Dardanelli et al., 2017; Biljecki et al., 2018; Pepe et al., 2020).

---

<sup>1</sup> Polytechnic of Bari, via E. Orabona 4, 70125 Bari, Italy, [domenica.costantino@poliba.it](mailto:domenica.costantino@poliba.it),  
[aryanna997@gmail.com](mailto:aryanna997@gmail.com), [massimiliano.pepe@poliba.it](mailto:massimiliano.pepe@poliba.it)



In particular, 4 consecutive well-defined LODs, applicable both internally and externally can be identified: *i*) LOD0 - Highly generalised model; *ii*) LOD1 - Block/object extrusion model; *iii*) LOD2 - Realistic, but still generalised model; and *iv*) LOD3 - Highly detailed model (Kutzner et al., 2020).

A tool for parametric modelling of buildings and urban areas is Grasshopper, which is a plug-in implemented in Rhinoceros (also simply called Rhino) software (developed by Robert McNeel & Associates, USA). This plug-in consists of a programming language for the creation of geometries visualised through the Rhino software (Kos & Snoj, 2016). The algorithms are developed within a canvas that represents the working area. Within this workspace, two macro-classes are identified: *i*) parameters, which contain the information (numbers, vectors, geometries) and; *ii*) components that perform the operations such as translation, copy, subdivision, scale, etc. Application of parametric modelling in the urban field can be found in several recent works. Rakha & Reinhart, 2012 showed an urban analysis workflow using a Rhinoceros/Grasshopper massing tool; the tool uses terrain elevation models as part of the design process to subdivide sites and generate urban forms to explore parametrically. De Jesus et al., 2018 showed the first results of geometric modelling performed in the campus of the Federal University of Bahia (UFBA), using aerial laser scanning data, integrating QGIS, Rhinoceros and FME (Feature Manipulation Engine); in Rhinoceros software, it was possible to generate an extrusion of the geometric model and in particular using plug-ins named Heron and Meerkat. Fink & Koenig, 2019 discuss about of a holistic, digital urban design process aimed at developing a practical methodology for future projects; the urban design process presented in the paper includes analysis and simulation tools within Rhinoceros 3D and its Grasshopper plug-in as quality enhancement means that facilitate creative approaches throughout the project. Silva et al., 2020 have developed a method in order to facilitate designing and building curvilinear architectures and their supporting structures using simultaneously two design paradigms connected via parametric programming. Therefore, this paper is set in the context of geometric and semantic modelling in the urban environment using Rhinoceros/Grasshopper tools.

## 2. METHOD

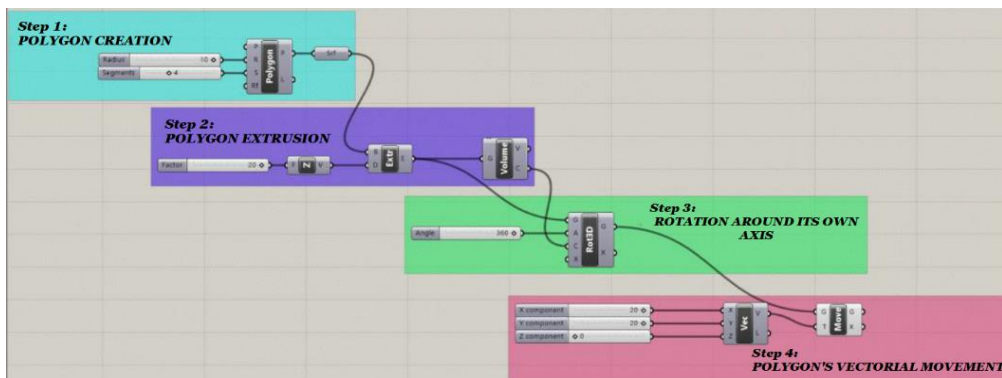
### 2.1. Design in Grasshopper and Rhinoceros

The parameterisation of the objects can be applied to different elements of the territory by means of the tools implemented in Rhino and Grasshopper. Indeed, programming in Grasshopper makes it possible to manage and model even complex geometries. Most of the Grasshopper interface is focused on the canvas, which is where the users performing the design of several elements and connecting them with wires. Grasshopper's components are written in Python, which is a popular language among computational designers due to its integration into many 3D modelling software and its relatively simple syntax (Peronato et al., 2017). Moreover, this environment allows one to use multiple 3D modelling functions and manage the entire design phase. For example, it is possible to build a model in Rhino and export it to a BIM (Li et al., 2012) or 3D-Geographic Information System (GIS) environment (Pepe et al., 2021). Grasshopper allows modelling using vector-type tools such as basic geometric and 3D shape sets (parametric primitives) are available that can be used to create complex objects through assembly, modification and deformation operations. It is also possible to create 3D shapes starting from two-dimensional forms and paths. In fact, through an extrusion operation, it is possible to generate the third dimension starting from a two-dimensional shape (open or closed) according to an axis that can have any inclination with respect to the starting plane. This last approach is widely used for modelling buildings in the urban environment both as prismatic solids and with rather complex 3D geometry. In order to highlight the potential of this Rhino/Grasshopper combination in urban modelling, different levels of detail and geometric complexity are discussed in the paper. In particular, 4 case studies are examined: *i*) the extrusion of simple and complex geometries; *ii*) the construction of 3D models from numerical cartographies; *iii*) the construction of 3D models using Open Street Map (OSM) data; *iv*) the construction of the 3D model from a point cloud of a church belonging to the cultural heritage and characterized by a complex geometry.

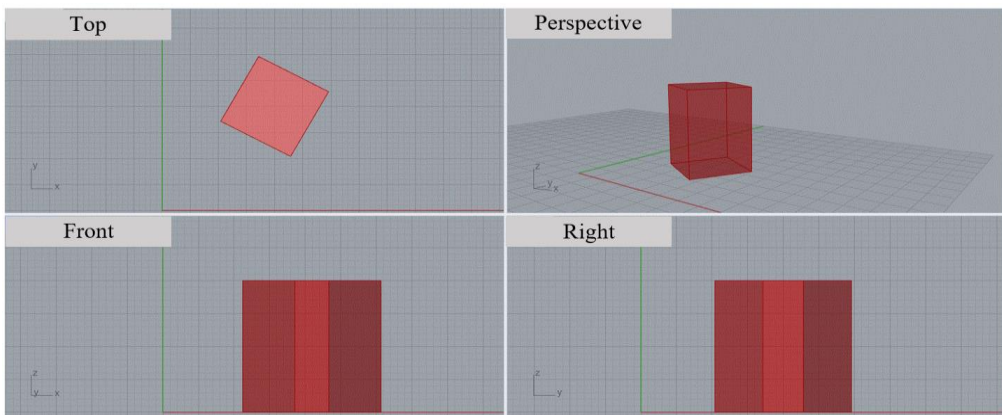
## 2.2. Extrusion of simple and complex geometries

The first research activity concerned the building of a rather simple three-dimensional geometry using Grasshopper. The resulting main design phases can be divided into the following activities: *i*) creation of the polygon; *ii*) extrusion of the polygon; *iii*) vector displacement of the geometry and; *iv*) rotation of the geometry around its own axis.

The first task involves the construction of a polygon on a regular square base. The code provides for the insertion in the canvas of the tool "Polygon", to which the desired number of sides (Segments) and the length of each side (Radius) can be attributed; in this way, Rhino defines the construction of a regular figure in the XY plane, centred on the origin of the axes. The next phase consists in the extrusion of the polygon by means of the tool "Extrude > Unit Z": the directional plane was then attributed through which the third dimension is obtained; in Rhino the square is developed along the Z axis characterizing the formation of a straight parallelepiped of variable height by assigning a certain value to the multiplication unit with the appropriate slider. A further attribute to be assigned is the angle at which the geometry produced is arranged in space. Through the "Rotate 3D" option, the construction can rotate around its axis according to the angle defined in the slider. Therefore, the polygon on Rhino will rotate around the XZ axis, arranging itself in space in the most appropriate way. Once built the 3D model, we can observe that it was still centred in the origin of the axes; at this stage, the objective of this third phase is to allow the figure to move in three-dimensional space. The last step, i.e. the vector movement of the solid was allowed through the "Move" tool, to which the three vector components X, Y, Z and their respective domains are associated. The representation of the canvas and the result of the modelling displayed in Rhino is shown in Fig. 1.



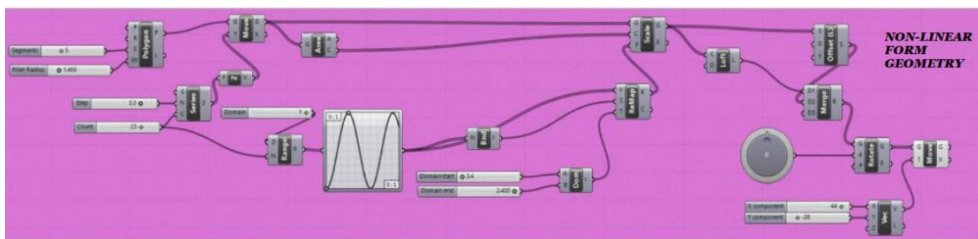
(a)



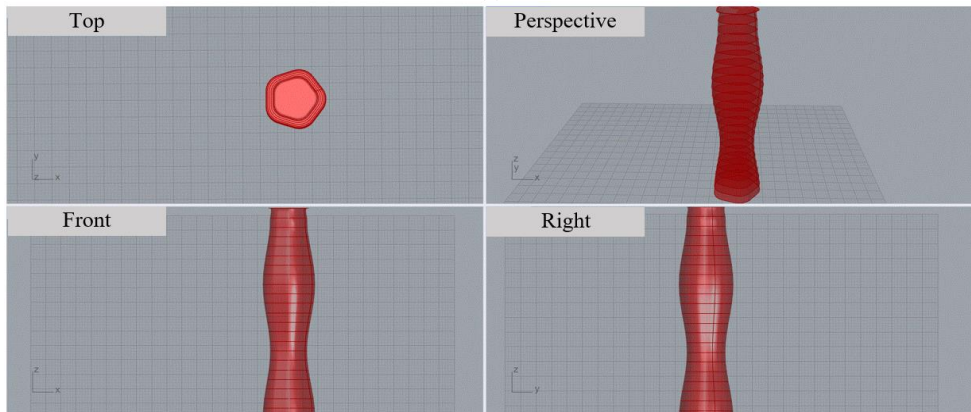
(b)

**Fig. 1.** Building of simple geometries using Grasshopper: code generated in the Grasshopper canvas (a); view from several perspectives, i.e. top, front, right and perspective view (b).

Once a rather simple solid was built, the possibility of realising complex 3D models was evaluated. The basic surface was acquired using the "Polygon" tool, through which it was possible to define the number of sides and relative dimensions: a pentagonal plan surface was chosen, with convex vertices using the "Fillet Radius" slider. Next, the number of floors of the building was identified and defined using the "Move > Series" command and the area ("Area") was attributed, defining the relative centres that make up, consequently, the central axis of the building itself. In order to set the sinusoidal shape of the walls, a "Graph Mapper" has been adopted, to which a domain ("Construct Domain") is associated that returns the diversified dimensions of each single floor, giving the required shape: everything is carried out by the "Scale/Offset Surface Looser" tool. Once the "Loft" surface has been applied, a first image of the tower has been reproduced; then, it has been possible to proceed with the union of the two geometries through the "Merge" command, generating a single complex. The tools "Rotate3D > Knob" and "Move > Vector XY" were used to allow the solid to rotate and move in space. The design realised in the canvas and the results of the model are reported in **Fig. 2**.



(a)



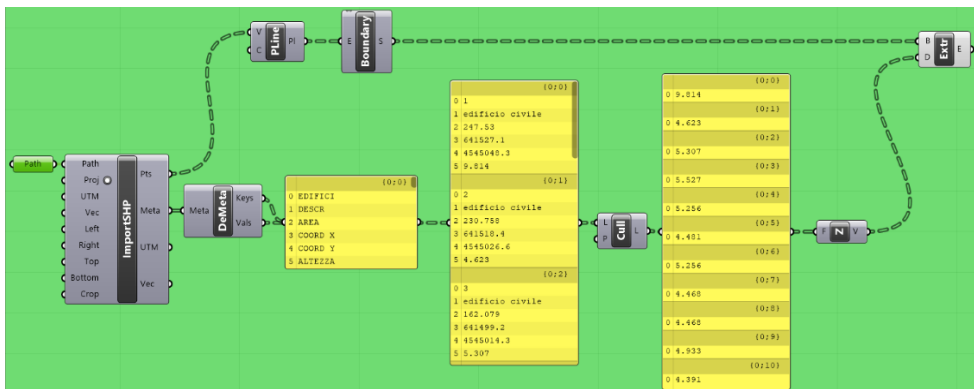
(b)

**Fig. 2.** Construction of non-linear geometries: code generated in the Grasshopper canvas (a); view from several perspectives: top, front, right, perspective (b).

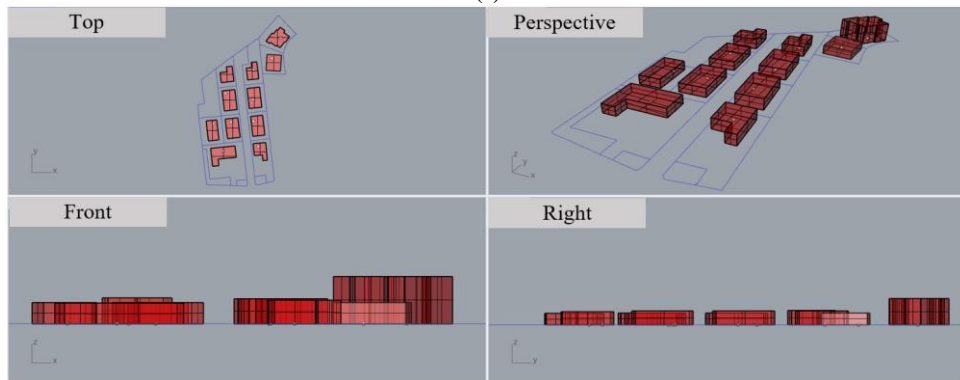
### 2.3. Building 3D models from numerical cartography

Using a cartography, it was possible to proceed to the design of 3D models, representing multiple buildings diversified by geometry and typology located in a precise spatial reference system. The area taken into consideration concerned part of the territory of the city of Palo del Colle (Bari, Italy); the aim of this task was to predict, starting from numerical cartography, the extrusion in space of some buildings constituting a residential area, i.e. to build in LOD1 model. The first step involved the acquisition of the regional technical map in ESRI shapefile format through the website dedicated to the thematic cartography of the Apulia region. Subsequently, using "Urbano" plugin (Dogan et al., 2020), it was possible to import this file through the use of "ImportSHP" tool: points corresponding to the vertices of each building will be returned in Rhinoceros. Subsequently, the code "Polyline>

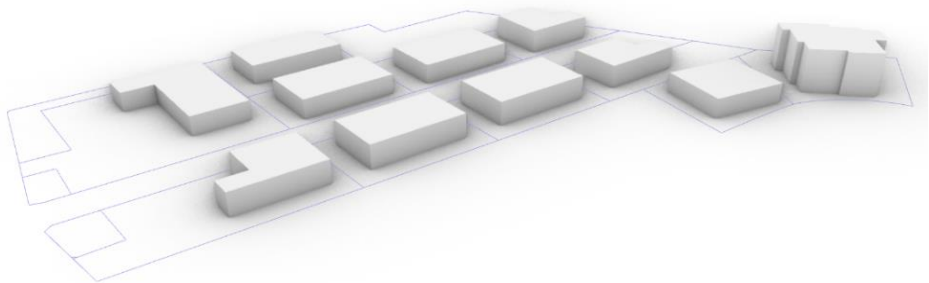
Boundary Surface" was linked to the "Points" parameter in order to recreate the base surface of each component belonging to the shapefile. Urbano plugin introduces a fully automated workflow to load in contextual GIS, OpenStreetMap and Google Places data to set up an urban mobility model; in addition, in the version 1.2, Urbano supports terrain and allows the construction of site models with 3D terrain, buildings and roads in easy way. In this case study, the aim was to extrude the building using the properties or better the values present in the "Metadata". In order to distinguish the numerical data from the corresponding descriptions, the tool "Deconstruct Metadata" has been inserted in such a way that, by means of a "Panel", the attributes for each building are clearly visible. Among all the characteristics, the one of main interest is that relative to the heights of the buildings, therefore the "Cull Pattern" command was inserted to remove the superfluous elements from the list. Finally, the civil dwellings were extruded by associating these values to the code "Extrude > Unit Z". The representation of the canvas and the realised 3D model are shown in **Fig. 3**.



(a)



(b)



(c)

**Fig. 3.** Building geometries from numerical cartography: code generated in the Grasshopper canvas (a); view from several perspectives: top, front, right, perspective (b); perspective view of buildings (c).

## 2.4. Building 3D models using Open Street Map

For further 3D design, geospatial data available on the OSM website were used. Since the model available from this web platform can be easily managed in the Rhinoceros/Grasshopper environment, the geospatial data are used for our purpose, i.e. to create a parametric 3D model at urban scale. The Area of Interest (AOI) can be identified through a manually adjustable window set on the OSM or by entering the relative coordinates geographic coordinates of the four vertices of the window itself. It should be emphasised that not all cities are covered with 3D models. Once the AOI was selected, the .osm file can be downloaded. OSM files are XML based and typically used to export an extent of the OSM GIS service into other applications. Once the file in .osm format was acquired, it was imported into the Grasshopper canvas using the following code: "File Path > Location > OSM Data" provided by the ELK tool (Webb, 2014). This step is performed by connecting the points together using the "Polyline" tool to outline the perimeter of the individual buildings. At the "OSM Data" command we set the "Create 3D Buildings" input to extrude the heights provided by the data acquired from the .osm file: in this phase not all the buildings of the study area will be extruded, but only the known ones. The contour surface was then created using "Geometry > Brep". An illustrative case reproduced in this project phase of part of the 'City' of London at in LOD1 is reported in Fig. 4.

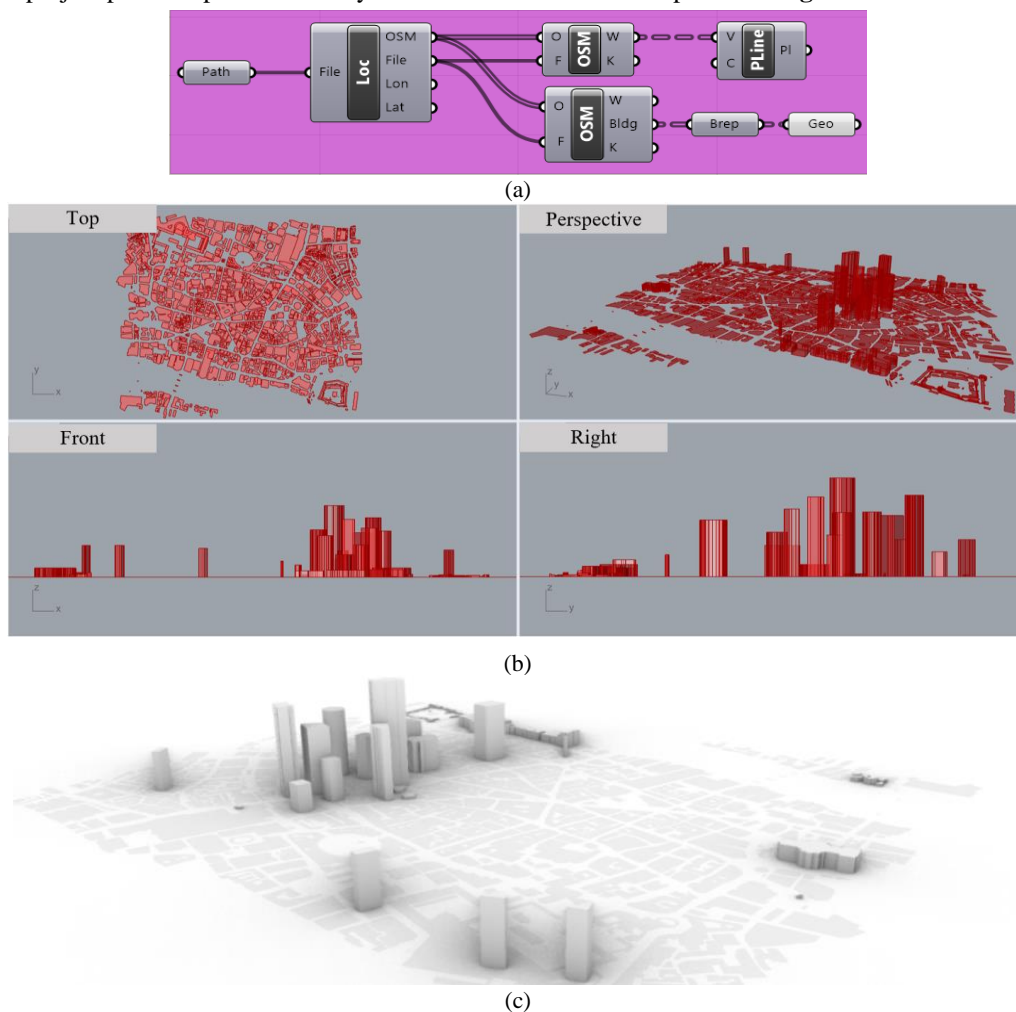


**Fig. 4.** Building 3D geometries from data obtained from Google Street Map: code generated in the Grasshopper canvas (a); view from several perspectives: top, frontal, right, perspective (b); perspective view of buildings in a portion of the City of London.



## 2.5. Building 3D models from point cloud

The structure identified for the 3D modelling of complex buildings concerns the Saint-André Cathedral, located in the city of Bordeaux, in the south-west of France, which is situated in an important historical urban centre dating back to the Enlightenment period and which was declared a UNESCO World Heritage Site in 2007.

The modelling involved the parametric modelling of the Saint-André Cathedral. This operation consisted of three phases: *i*) data collection; *ii*) acquisition and modification of the point cloud and; *iii*) Parametric modelling of the structure.

The dataset used for structure modelling was obtained from the point clouds generated by Airborne Laser Scanner-ALS sensors and a dataset of colour images generated by nadir and oblique cameras (Costantino et al., 2021). For data collection, a photogrammetric flight over the city of Bordeaux was carried out using a twin-engine aircraft (Partenavia P68C) at an altitude of 850 m above ground level. The hybrid sensor mounted on the aircraft was the "Leica CityMapper" specifically designed for aerial urban mapping. The main characteristics of the sensor are: *i*) pulse repetition rate up to 700 KHz; *ii*) programmable return pulses of up to 15 returns, including intensity, pulse width, area; *iii*) curved waveform and slope attributes; *iv*) full waveform recording option at down-sampled frequencies; *v*) oblique scanner, with various scanning patterns; *vi*) real-time LiDAR waveform analysis, including acquisition of waveform attributes.

The main data used in the geometric modelling of the structure was derived from the point cloud generated by the Leica Hyperion LiDAR ALS unit and available in LAS format. The survey produced a point cloud of 100,924 points, with a density on the horizontal surfaces (roofs and ground) of 7-8 pts/m<sup>2</sup> and georeferenced in the WGS84/UTM (World geodetic System/Universal Transverse of Mercator) zone 30 North projection, EPSG:32630 (Nicolai & Simensen, 2008; Dardanelli et al., 2020).

Using the Cloud Compare software (Girardeau-Montaut, 2014), the point cloud was cleaned from "noise" or better all the parts that do not contribute to the parametric modelling of the building, such as the vegetation surrounding the cathedral, were deleted (**Fig. 5**).

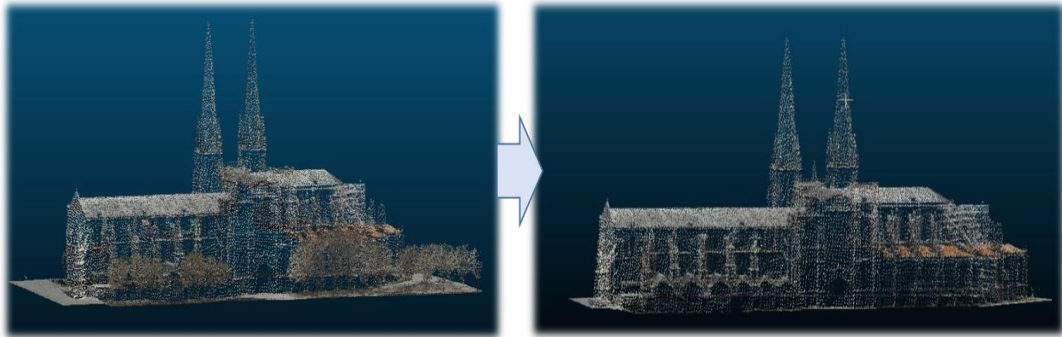
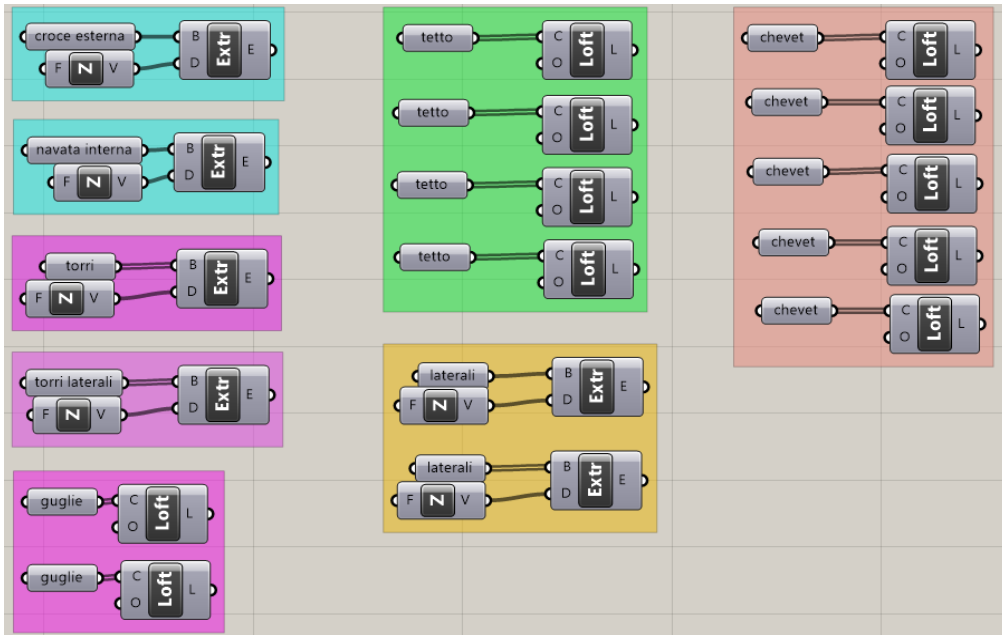


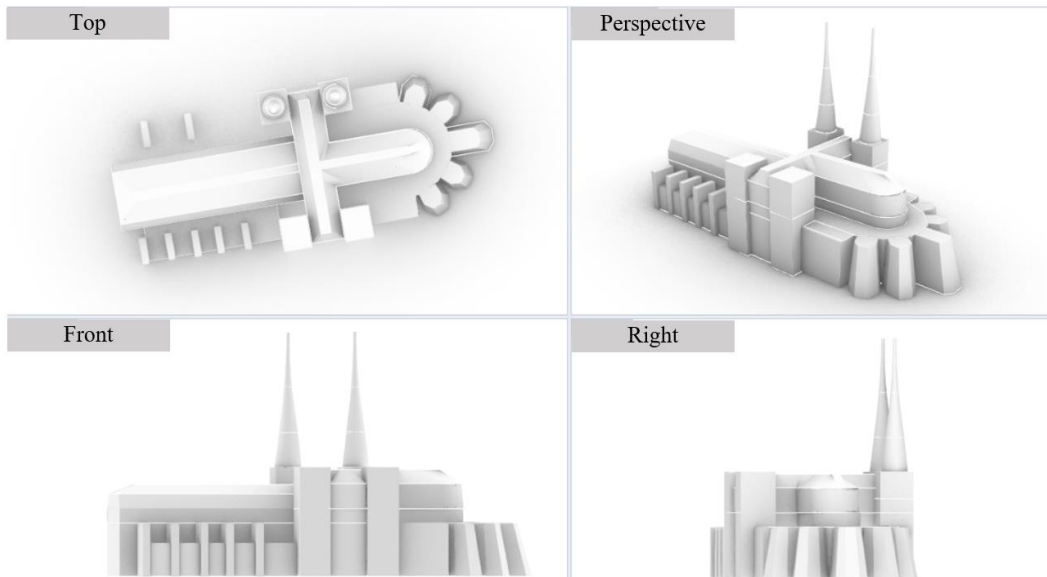
**Fig. 5.** Point cloud cleaned of "noise" and vegetation.

Subsequently, the point cloud was imported into Rhinoceros software. To create the parametric objects of the elements of the structure under consideration, Arena4D plug-in was used. Indeed, this latter plug-in also offers powerful point cloud manipulation tools, such as slicing, clipping, smoothing, lighting, magnification, colour ramping and exporting (Pepe & Costantino, 2021). In order to reconstruct the 3D model with different profiles, slicing command was used. In fact, this tool allows to cut the point cloud in several profiles. In Rhino environment, the different profiles were vectorised and interpolated by *Non Uniform Rational B-Splines* (NURBS) surfaces, which are mathematical representations of 3D geometry. This surface precisely defines any shape: from a simple line, to a circle, arc or curve, to the most complex free-form or organic 3D solid or surface.

In the first task, we extruded the central nave, the main towers located near the side entrances and those located along the sides of the cathedral. Then, the roof was built, which has a non-homogeneous conformation for all the layers involved; therefore, we opted for the use of the "Loft" tool, which has the objective of generating a surface along a series of selected curves. The same process was applied to generate the spires above the towers on the left-hand side of the structure and the five chevets at the top. The designed canvas and the result of the modelling in LOD2 are shown in **Fig. 6**.



(a)



(b)

**Fig. 6.** Building 3D geometries from ALS data: (a) code generated in the Grasshopper canvas for each element of the church (a); view from several perspectives: top, front, right, perspective of the building with complex geometry (Saint-André Cathedral, Bordeaux, France).



### **3. RESULTS AND DISCUSSION**

In this paper, the 3D semantic modelling approach using Rhinoceros v.7/Grasshopper software was addressed.

In the first phase, simple elements were modelled in order to identify the level of depth, automation and sharing of the 3D models generated in this environment. The codes generated in the Grasshopper canvas formed the basis for the subsequent, more complex phases. The management in this software can be implemented using multi-sources such as, for example, numerical cartography (ESRI shapefile) or point clouds in LAS format.

The parametric approach was applied to objects, such as buildings, which can be deduced from numerical cartography; different design alternatives were experimented until generating a code that allows the immediate import of the shapefile into Grasshopper. In this way, it was possible to create three-dimensional models quickest and simplest way. Moreover, through a specific study, it was ascertained that in the case of areas of interest of relevant importance, it is possible to choose for the acquisition of geospatial data through the Open Street Map website, as it returns directly and with extreme ease a file compatible with Rhinoceros/Grasshopper. From the analysis of the geo-data, it was possible to note that in the case study of the 'City' of London only few specific buildings underwent extrusion: the most renowned ones.

Finally, an experiment was carried out on urban buildings with a rather complex geometry starting from a cloud of points generated by an airborne ALS sensor. The modelling involved several long working phases and the use of different software such as Cloud Compare and Rhinoceros/Grasshopper. Despite the complexity of the geometry, the parameterization of the structure was quite faithful to the real model, i.e. the model represented by a point cloud. Once the parametric modelling has been carried out in Rhino, through the use of a specific plug-in called Rhino.Inside, it is possible to incorporate the model into Revit (BIM software developed by the Autodesk company).

In particular, through Rhino.inside.Revit it is possible to take advantage of an integration platform between Rhino and Revit. This add-on allows Rhino and the respective Grasshopper applications to be loaded, providing a collection of new components for interaction with Revit. Rhino.inside.Revit provides a set of tools for switching between Rhino free-form modelling and BIM modelling. Using this system, through design in the Grasshopper canvas it was possible to import the 3D model of the cathedral inside the Revit software.

### **4. CONCLUSIONS**

Programming and modelling in Rhinoceros and Grasshopper has enabled the building of high quality parametric 3D models. The different case studies have shown the ease and enormous capacity of this environment to design and plan at different levels of detail, from a single building to an entire city. Furthermore, it is possible to model even complex geometries, as shown in the case study of the Saint-André Cathedral in Bordeaux.

This process, based on the use of Rhinoceros and Grasshopper, will be increasingly used in the future to increase IT and technological efficiency in the management of individual buildings and, at the same time, of urban areas, factors which affect economic, social and, above all, environmental aspects. Furthermore, these tools represent the basic elements for the construction of 3D models suitable for subsequent analysis and cataloguing of geo-data in a BIM (or Heritage BIM-HBIM) or 3D GIS environment.

## REFERENCES

- Biljecki, F., Kumar, K., & Nagel, C. (2018). CityGML application domain extension (ADE): overview of developments. *Open Geospatial Data, Software and Standards*, 3(1), 1-17.
- Costantino D, Vozza G, Alfio VS, Pepe M. (2021) Strategies for 3D Modelling of Buildings from Airborne Laser Scanner and Photogrammetric Data Based on Free-Form and Model-Driven Methods: The Case Study of the Old Town Centre of Bordeaux (France). *Applied Sciences*, 11(22):10993.
- Dardanelli, G., Allegra, M., Giammarresi, V., Brutto, M. L., Pipitone, C., & Baiocchi, V. (2017). Geomatic Methodologies for The Study of Teatro Massimo in Palermo (Italy). *The International Archives of Photogrammetry, Remote Sensing and Spatial Information Sciences*, 42, 475.
- Dardanelli, G., Lo Brutto, M., & Pipitone, C. (2020). GNSS CORS network of the university of Palermo: design and first analysis of data. *Geographia Technica*, 15(1).
- De Jesus, E. G. V., de Amorim, A. L., Groetelaars, N. J., & Fernandes, V. O. (2018). Modeling cities for 3D\_GIS purposes. *International Archives of the Photogrammetry, Remote Sensing & Spatial Information Sciences*, 42(4).
- Dogan, T., Yang, Y., Samaranyake, S., & Saraf, N. (2020). Urbano: A tool to promote active mobility modeling and amenity analysis in urban design. *Technology/ Architecture+ Design*, 4(1), 92-105.
- Girardeau-Montaut D. (2014), CloudCompare. Available on line at: <http://www.danielgm.net/cc/>
- Gröger, G.; Kolbe, T.H. OGC City Geography Markup Language (CityGML) Encoding Standard; Open Geospatial Consortium Inc.: Wayland, MA, USA, 2012.
- Isikdag, U., & Zlatanova, S. (2010). Interactive modelling of buildings in Google Earth: A 3D tool for Urban Planning. In *Developments in 3D Geo-Information Sciences*, Springer, Berlin, Heidelberg, 52-70.
- Kos, B., & Snoj, L. (2016). On using Grasshopper add-on for CAD to MCNP conversion. *PHYSOR*, Sun Valley, USA.
- Kutzner, T., Chaturvedi, K., & Kolbe, T. H. (2020). CityGML 3.0: New functions open up new applications. *PFG—Journal of Photogrammetry, Remote Sensing and Geoinformation Science*, 88(1), 43-61.
- Li, H. Y., Du, S. B., & Sha, Z. H. (2012). BIM Application and Practice with Rhino—A Case Study of Steel Construction in Datong Library. In *Applied Mechanics and Materials*, Trans Tech Publications Ltd, Vol. 174, 2052-2056.
- Li, X., & Ratti, C. (2019). Using Google street view for street-level urban form analysis, a case study in Cambridge, Massachusetts. In *The Mathematics of Urban Morphology*, Birkhäuser, Cham, 457-470.
- Nicolai, R., & Simensen, G. (2008). The New EPSG Geodetic Parameter Registry. In 70th EAGE Conference and Exhibition incorporating SPE EUROPEC 2008 (pp. cp-40). European Association of Geoscientists & Engineers.
- Pepe, M., Costantino, D., Alfio, V. S., Angelini, M. G., & Restuccia Garofalo, A. (2020). A CityGML Multiscale Approach for the Conservation and Management of Cultural Heritage: The Case Study of the Old Town of Taranto (Italy). *ISPRS International Journal of Geo-Information*, 9(7), 449.
- Pepe, M.; Costantino, D.; Alfio, V.S.; Restuccia, A.G.; Papalino, N.M. Scan to BIM for the digital management and representation in 3D GIS environment of cultural heritage site. *Journal of Cultural Heritage*, 2021, 50, 115–125.
- Pepe, M., & Costantino, D. (2021). UAV photogrammetry and 3D modelling of complex architecture for maintenance purposes: The case study of the masonry bridge on the Sele river, Italy. *Periodica Polytechnica Civil Engineering*, 65(1), 191-203.
- Peronato, G., Kämpf, J. H., Rey, E., & Andersen, M. (2017). Integrating urban energy simulation in a parametric environment: a Grasshopper interface for CitySim (No. CONF).
- Shirowzhan, S., Tan, W., & Sepasgozar, S. M. (Eds.). (2020). Spatial big data, BIM and advanced GIS for smart transformation: city, infrastructure and construction. *MDPI*, Basel, Switzerland, Jul. 2020.
- Silva, N. F., Silva, L. M. F., & Lacroix, Í. (2020). Generating NURBS cladding and structures with parametric programming and BIM. *PARC Pesquisa em Arquitetura e Construção*, 11.
- Tarek Rakha, Christoph Reinhart. Generative urban modeling: a design workflow for walkability-optimized cities. Fifth National Conference of IBPSA-USA Madison, Wisconsin, August 1-3, 2012.
- Theresa Fink, Reinhart Koenig. City Information Modelling and Gis - Volume 3. Integrated Parametric Urban Design in Grasshopper /Rhinoceros 3D, Demonstrated on a Master Plan in Vienna.
- Webb, A, “Productive Hybrids: Folding Social Media as Urban Analysis”. (2014). *ACADIA 2014*, 75-80.

## Aims and Scope

**Geographia Technica** is a journal devoted to the publication of all papers on all aspects of the use of technical and quantitative methods in geographical research. It aims at presenting its readers with the latest developments in G.I.S technology, mathematical methods applicable to any field of geography, territorial micro-scalar and laboratory experiments, and the latest developments induced by the measurement techniques to the geographical research.

**Geographia Technica** is dedicated to all those who understand that nowadays every field of geography can only be described by specific numerical values, variables both of time and space which require the sort of numerical analysis only possible with the aid of technical and quantitative methods offered by powerful computers and dedicated software.

Our understanding of **Geographia Technica** expands the concept of technical methods applied to geography to its broadest sense and for that, papers of different interests such as: G.I.S, Spatial Analysis, Remote Sensing, Cartography or Geostatistics as well as papers which, by promoting the above mentioned directions bring a technical approach in the fields of hydrology, climatology, geomorphology, human geography territorial planning are more than welcomed provided they are of sufficient wide interest and relevance.

### Targeted readers:

The publication intends to serve workers in academia, industry and government. Students, teachers, researchers and practitioners should benefit from the ideas in the journal.

## Guide for Authors

### Submission

Articles and proposals for articles are accepted for consideration on the understanding that they are not being submitted elsewhere.

The publication proposals that satisfy the conditions for originality, relevance for the new technical geography domain and editorial requirements, will be sent by email to the address [editorial-secretary@technicalgeography.org](mailto:editorial-secretary@technicalgeography.org).

This page can be accessed to see the requirements for editing an article, and also the articles from the journal archive found on [www.technicalgeography.org](http://www.technicalgeography.org) can be used as a guide.

### Content

In addition to full-length research contributions, the journal also publishes Short Notes, Book reviews, Software Reviews, Letters of the Editor. However the editors wish to point out that the views expressed in the book reviews are the personal opinion of the reviewer and do not necessarily reflect the views of the publishers.

Each year two volumes are scheduled for publication. Papers in English or French are accepted. The articles are printed in full color. A part of the articles are available as full text on the [www.technicalgeography.org](http://www.technicalgeography.org) website. The link between the author and reviewers is mediated by the Editor.

### Peer Review Process

The papers submitted for publication to the Editor undergo an anonymous peer review process, necessary for assessing the quality of scientific information, the relevance to the technical geography field and the publishing requirements of our journal.

The contents are reviewed by two members of the Editorial Board or other reviewers on a simple blind review system. The reviewer's comments for the improvement of the paper will be sent to the corresponding author by the editor. After the author changes the paper according to the comments, the article is published in the next number of the journal.

Eventual paper rejections will have solid arguments, but sending the paper only to receive the comments of the reviewers is discouraged. Authors are notified by e-mail about the status of the submitted articles and the whole process takes about 3-4 months from the date of the article submission.

Indexed by: **CLARIVATE ANALYTICS**  
**SCOPUS**  
**GEOBASE**  
**EBSCO**  
**SJR**  
**CABELL**

**ISSN: 1842 - 5135 (Print)**  
**ISSN: 2065 - 4421 (Online)**

